Continuous flow optimisation of nanoparticle catalysts

Brendan L. Hall

Submitted in accordance with the requirements for the degree of
Doctor of Philosophy

The University of Leeds

Complex Particulate Products and Processes

School of Chemical and Process Engineering

September 2022

The candidate confirms that the work submitted is their own, except where work which has formed part of jointly authored publications has been included. The contribution of the candidate and the other authors to this work has been explicitly indicated below. The candidate confirms that appropriate credit has been given within the thesis where reference has been made to the work of others.

Chapter 2 - is based on work from a jointly authored publication: • Brendan L. Hall, Connor J. Taylor, Jamie A. Manson, Ricardo Labes, Alexander F. Massey, Robert Menzel, Richard A. Bourne and Thomas W. Chamberlain. "Autonomous optimisation of a nanoparticle catalysed reduction reaction in continuous flow." Chemical Communications (2021): 57, 4926-4929.

The work contained within this publication that is directly attributable to Brendan Hall was the experimentation, coding of the automated system and preparation of the manuscript. Connor Taylor aided in the development of the kinetic model which was used in Chapter 3 for benchmarking optimisation algorithms. Alexander F. Massey and Robert Menzel assisted in the interpretation of XAS data. Ricardo Labes, Richard A. Bourne and Thomas W. Chamberlain provided direction, general supervision and guidance during the preparation of this manuscript.

This copy has been supplied on the understanding that it is copyright material and that no quotation from the thesis may be published without proper acknowledgement. The right of Brendan Hall to be identified as author of this work has been asserted in accordance with the Copyright, Designs and Patents Act 1988.

© 2022 The University of Leeds and Brendan L. Hall

Acknowledgements

Firstly, I would like to thank Thomas Chamberlain and Richard Bourne for their supervision and guidance over the past 5 years. Their encouragement and advice, especially during some of the more challenging periods of this project has been invaluable.

I would also like to thank all of my iPRD colleagues I have had the pleasure of working with. Alastair Baker for bringing me enthusiastically into the world of research. Luke Power for being my ideas sounding board and a welcome distraction during some of my more mundane or frustrating research tasks. Zabeada Aslam from the Leeds electron microscopy and spectroscopy centre for providing nanoparticle TEM analysis. Claudio Avila for his help processing and analysing spectroscopic data. Alex Massey & Robert Menzel for their help interpreting my XPS data. Jamie and Adam for their programming advice/debugging clues. Sarah Boyall for helping me to solve some of the more challenging reactor issues encountered in this project and for taking over social responsibilities from Calum Birch – you both did an excellent job of organising events and bringing the group together. My masters and summer students: Tom H, Jinjie, Louis, Gintare and Niamh.

Also, everyone else who has made the University of Leeds such a great place to work over the past few years: Ollie, Holly, Ilias, Chris, Mary, Tom D, Tom S, Tom P, Tom N, Christiane, Beth, Nisha, Matt, Fernando, James, Micaela, Rosie, Sam, Alison, James, George and Pia. The members of the Chamberlain and Menzel group office/lab: Xiangyi, Damon, Bence, Anthony, Becky, Jamie, Rachel, Alex, Maha and Tom M for inviting me on socials, letting me use your coffee machine and always being up for a quick chat during the occasional mid-afternoon break – especially you Alex.

A special thanks to Connor Taylor for teaching us how to model our reactions and stay productive during the pandemic. For being one of the few along with Ricardo who would be there to keep me company during late nights in the lab/office, thank you both for your help with my first lead-author paper. Finally, the University of Leeds Caving society for all the adventures and memories.

Abstract

Continuous flow reactors offer a host of advantages over their more traditional batch counterparts. These include more controlled mixing, enhanced heat transfer and increased safety when handling hazardous reagents as only a small volume of material is present within the reactor at any one time. For these reasons, flow reactors are becoming increasingly popular for the synthesis of nanoparticle catalysts.

Recent advances in reactor technology and automation have transformed how chemical products are developed and tested. Automated continuous flow reactors have been coupled with machine learning algorithms in closed feedback loops, allowing vast areas of multi-dimensional experimental space to be explored quickly and efficiently,[1] significantly accelerating the identification of optimum synthesis conditions. While both reducing costs and improving the sustainability of process development.

This work describes the development of a novel two-stage autonomous reactor for the optimisation of nanoparticle catalysts by direct observation of their performance in a catalysed chemical reaction. The key advantage of this performance directed system is that no offline processing or analysis of the nanoparticles is required. Allowing both the nanoparticle properties and the nanoparticle catalysed reaction conditions to be optimised in tandem by an automated system with zero human intervention.

Chapter 1 introduces the principles and methods underlying this work with a focus on nanoparticle catalysts, flow reactor technologies and optimisation algorithms. Chapter 2 describes a self-optimising reactor capable of nanoparticle catalysed reaction optimisation. Chapter 3 shows the development of a reactor which was able to produce alloyed nanoparticle catalysts with tuneable composition. Chapter 4 describes a body of work surrounding the computational modelling of nanoparticle catalysed reactions for the evaluation of different optimisation algorithms. Chapter 5 concludes this project by presenting a two-stage reactor which was able to optimise both the physical properties of the nanoparticles as well as the conditions under which they were used to catalyse a reaction.

Table of Contents

Acknowledgements **1**

Abstract **2**

List of Figures **8**

List of Schemes **24**

List of Tables **24**

List of Abbreviations **27**

1 Chapter 1 Introduction **29**

1.1 Nanoparticles 29

1.1.1 Nanoparticle stability 30

1.1.2 Surface plasmon resonance 31

1.1.3 Nanoparticles in catalysis 32

1.1.4 Nanoparticle synthesis 33

1.2 Flow reactors 35

1.2.1 Mass transfer within continuous flow reactors 36

1.2.2 Tubular reactors 37

1.2.3 Continuous stirred tank reactors (CSTRs) 39

1.2.4 Flow control 40

1.2.5 Continuous flow reactors for nanoparticle catalyst synthesis 41

1.2.6 Continuous flow analysis 50

1.3 Reaction optimisation 52

1.3.1 One variable at a time (OVAT) 52

1.3.2 Design of experiment (DoE) 53

1.3.3 Simplex 55

1.3.4 Genetic algorithms 56

1.3.5 SNOBFIT 57

1.3.6 Bayesian optimisation 59
1.3.7 Multi-objective optimisation 60
1.4 Project aims and objectives 62
2 Chapter 2 Autonomous optimisation of a nanoparticle catalysed reduction reaction in continuous flow 64
2.1 The reduction of nitrophenol 64
2.1.1 HPLC investigation NP catalysed nitrophenol reduction 66
2.2 Gold nanoparticle catalyst 68
2.2.1 TEM particle size distributions (before/after reaction) 69
2.2.2 X-ray photoelectron spectroscopy (XPS) 70
2.2.3 UV-vis analysis 72
2.2.4 DLS analysis 73
2.2.5 Nanoparticle surface area calculation 73
2.3 Inline reaction monitoring 74
2.3.1 Nitrophenol and gold nanoparticle calibration 75
2.3.2 Spectral convolution 76
2.3.3 Spectral deconvolution 77
2.3.4 H_2 gas formation 78
2.3.5 Spectrometer temperature regulation 79
2.4 Self-optimising reactor 80
2.5 Self-optimisation of a nanoparticle catalysed reaction 82
2.5.1 Conditions generation function 84
2.5.2 Self-optimisation (with conditions generation function) 85
2.6 Conclusions 87
3 Chapter 3 Continuous flow synthesis of nanoparticle alloy catalysts 88
3.1 Introduction 88

3.2 Batch synthesis of AuAgNPs 92
3.3 Flow reactor development 92
3.3.1 Tubular PTFE reactor 93
3.3.2 Continuous flow synthesis with pre-formed AuNP solution 98
3.3.3 Ascorbic acid reducing agent 99
3.3.4 Sodium borohydride reducing agent 100
3.3.5 AuAgNP flow synthesis with sodium borohydride reducing agent 102
3.3.6 Tannic acid reducing agent 103
3.3.7 AuNP synthesis in a fReactor with preheating 105
3.3.8 Modified fReactor design 108
3.3.9 Continuous flow synthesis of AuAgNPs 110
3.3.10 TEM-EDS analysis of AuAgNPs 112
3.4 Summary and future work 114
4 Chapter 4 Modelling nanoparticle catalysis optimisation 116
4.1 Introduction 116
4.2 Kinetic model development 120
4.2.1 The Langmuir-Hinshelwood kinetic model 120
4.2.2 LH kinetic model fitting 123
4.2.3 Model extrapolation and scalarisation 125
4.3 Simulated optimisation 127
4.3.1 Genetic algorithm 127
4.3.2 Design of experiment 129
4.3.3 SNOBFIT optimisation 132
4.3.4 BOAEI optimisation 133
4.3.5 Single objective optimisation algorithm comparison 133
4.3.6 Effect of noise on optimisation algorithms 134

4.3.7 Multi-objective optimisation 136

4.4 Summary 138

5 Chapter 5 Two-stage, continuous flow nanoparticle catalysed reaction optimisation 140

5.1 Introduction and background 141

5.1.1 High-throughput experimentation 141

5.1.2 *In silico* modelling 143

5.1.3 Multistage flow synthesis and optimisation 144

5.2 Reactor development 148

5.2.1 Inline nitrophenol concentration monitoring 148

5.2.2 Spectra deconvolution 149

5.2.3 Two-stage reactor design 150

5.2.4 Conditions generation function 153

5.2.5 Reactor automation 154

5.3 Results 155

5.3.1 SNOBFIT optimisation 155

5.3.2 Bayesian optimisation 159

5.3.3 TEM analysis 161

5.4 Summary 162

6 Chapter 6 Conclusions and future work 163

7 Chapter 6 Materials and methods 166

7.1 Methods (chapter 2) 167

7.1.1 Reservoir solutions 167

7.1.2 Analytical methods 167

7.1.3 Reactor setup 170

7.1.4 Reactor component details 172

7.1.5 Experimental Methods 172
7.2 Methods (Chapter 3) 173
7.2.1 Analytical methods 173
7.2.2 Experimental Methods 173
7.3 Methods (chapter 4) 179
7.3.1 Experimental methods 179
7.4 Methods (Chapter 5) 179
7.4.1 Reservoir solutions 179
7.4.2 Analytical methods 180
7.4.3 Reactor setup 181
7.4.4 Table of components 182
7.4.5 Reactor component details 183
8 Appendix 185
8.1.1 TEM micrographs (before reaction) 185
8.1.2 TEM micrographs (after reaction) 186
8.1.3 Data from self-optimisation experiments 187
8.1.4 TEM micrographs and histograms for AuAgNPs 189
8.1.5 TEM-EDS analysis 195
8.1.6 Simulated test problem single objective optimisation comparison 197
8.1.7 Design of experiments 200
8.1.8 Single objective optimisation comparison with added noise 200
8.1.9 TS-EMO multi-objective optimisation 202
8.1.10 TEM micrographs and histograms for AuAgNPs 206
8.1.11 Data from self-optimisation experiments 212
9 References 216

List of Figures

Figure 1. Diagram showing electrostatic repulsion between two nanoparticles with negatively charged surface coatings and surrounding positive ions in solution. 30

Figure 2. Diagram showing steric repulsion between polymer-coated colloids. 31

Figure 3. A diagram describing the mechanism behind the phenomenon of surface plasmon resonance. An incident electric field causes electrons on the surface of the nanoparticles to oscillate, converting electromagnetic energy into heat. This can be observed as the absorption of specific wavelengths of light. 31

Figure 4. A reaction coordinate diagram describing how a catalyst increases the rate of a reaction via a reduction in activation energy. 32

Figure 5. A graph illustrating the events that take place during nanoparticle formation. As the concentration of metal atoms increases above the 'nucleation threshold' a nucleation event occurs resulting in a burst of very small nanoparticles forming in solution, this effectively results in a decrease in the concentration of monomer in solution to below the nucleation threshold where a subsequent growth process occurs. Adapted from.[36] 33

Figure 6. A plot showing the effect of flow rate on Reynolds number for standard laboratory scale flow reactors with an aqueous solution, the hashed lines indicate the boundaries between laminar, transitional, and turbulent flow regimes. 36

Figure 7. An idealised plug flow model assumes all the fluid in the reactor is moving at the same velocity. 37

Figure 8. Laminar flow results in Taylor dispersion characterised by a parabolic flow profile and a non-uniform flow velocity. 37

Figure 9. Segmented flow reactors significantly reduce axial mixing within tubular reactors, therefore, creating residence time distributions analogous to that of a plug flow reactor. The occurrence of recirculating currents within each droplet also results in better mixing. 38

Figure 10. (a) A CSTR composed of one reactor. (b) A CSTR composed of a series of 5 reactors all interconnected. (c) A plot describing the difference in the residence time distributions of 1 CSTR vs 5 CSTRs, if a pulse of low volume high concentration dye

was injected into the reactor/s after flushing with and followed by a solvent at a constant flow rate. 39

Figure 11. A diagram describing the single-phase reactor design presented by Huang and Gavriilidis et al. (Reproduced with permission from ref.[44] Copyright 2018, Elsevier. All rights reserved)..... 41

Figure 12. A diagram showing a reactor with multiple converging and diverging streams for enhanced mass transfer. (Reproduced with permission from ref.[71] Copyright 2005, ACS Publications. All rights reserved). 42

Figure 13. A diagram describing the design of a reactor capable of producing sub-nm sized nanoparticles (Reproduced with permission from ref.[72] Copyright 2008, ACS Publications. All rights reserved). 42

Figure 14. A two-stage single-phase reactor capable of producing AgNPs between 5-10 nm (Reproduced with permission from ref.[32] Copyright 2019, Royal Society of Chemistry. All rights reserved). 43

Figure 15. A diagram describing a segmented flow reactor for the synthesis of AuNPs (Reproduced with permission from ref.[77] Copyright 2020, Royal Society of Chemistry. All rights reserved)..... 44

Figure 16. A gas/liquid high-pressure/high-temperature flow reactor for the synthesis of Pd nanorods. (Reproduced with permission from ref.[78] Copyright 2016, Wiley. All rights reserved)..... 45

Figure 17. A micro reactor for the continuous flow synthesis of AuAgNP catalyst. (Reproduced with permission from ref.[79] Copyright 2008, Elsevier. All rights reserved). 46

Figure 18. A three-pump reactor setup for segmented flow synthesis of core/shell and core/double/shell AuAgNPs, a solution containing metal precursor, nanoparticle seeds and capping agent was in syringe A was mixed with a tetradecane carrier medium this was mixed with a solution of NaOH downstream before entering a heated reactor. (Reproduced with permission from ref.[80] Copyright 2011, Elsevier. All rights reserved). 47

Figure 19. An innovative example of inline UV-vis analysis for nanoparticle analysis. A movable flow cell allows researchers to decouple the effects of reactor flow rate and

residence time. (Reproduced with permission from ref.[98] Copyright 2019, Wiley & CO. All rights reserved)..... 51

Figure 20. A contour plot to showing how the OVAT approach can miss the true 'optimum'. Optimum conditions found using this technique are likely to be highly dependent on the starting conditions used. 53

Figure 21. This plot shows the arrangement of experiments within a three-variable design space, each point represents an experiment and the corners of the cube represent the upper and lower limits of the experiment..... 54

Figure 22. A Simplex optimisation performed on a 2D optimisation problem. An initial 3 experiments are performed generating a simplex with 3 points (a). These are then ranked from highest (1) to lowest (3) with the simplex reflected along vertex opposite the worst-performing conditions, this process is repeated until the optimal conditions are found..... 55

Figure 23. A diagram showing the process of optimisation using genetic algorithms, a population of individuals is evaluated and before the best performing individuals are selected for cross-over and mutation generating a new population. 56

Figure 24. A flow diagram describing the optimisation process for the SNOBFIT algorithm. The experiment is terminated once the experiment limit is reached. N_{eval} is the current number of points for the current iteration of experiments, N_{req} is the number of points required for each iteration. 57

Figure 25. Bayesian optimisation of an arbitrary function. The true response (solid black line) is predicted by the surrogate model (dashed line), the acquisition function (orange) calculates the trade-off between exploration and exploitation to find the points (brown/black dots) where both the model fit can be improved while also discovering the optimum. 59

Figure 26. A diagram describing the Pareto front for an arbitrary minimisation problem where $f_1(X)$ and $f_2(X)$ are two conflicting objectives. No points can access the region beyond the Pareto front which consists of a set of non-dominated solutions. 60

Figure 27. A hypothticlal plot demonstrating the process by which the TSEMO algorithm performs a multi-objective optimisation. A set of candidate experiments

generated along a predicted Pareto front, the experiment that archives the greatest increase in hypervolume is selected for the next experiment by the algorithm. 61

Figure 28. Flow diagram showing how individual aims contribute towards end goal of a fully integrated tandem reactor design for nanoparticle catalyst optimisation. 62

Figure 29. A graphical abstract depicting the approach developed to perform the automated optimisation of a gold nanoparticle catalysed nitrophenol reaction. 64

Figure 30. A schematic of the view inside the commercially available OceanOptics™ spectrometer assembly used in this work.[124] 65

Figure 31. A scanning kinetics plot for the reduction of 4-nitrophenol with sodium borohydride in the presence of AuNPs over 7.5 minutes. 66

Figure 32. Aminophenol calibration, gradient: 389, R^2: 0.999. 67

Figure 33. Nitrophenol calibration, gradient: 2375, R^2: 0.999. 67

Figure 34. The HPLC chromatograph for the reaction solution before the reduction reaction, nitrophenol was detected at 10.12 minutes (273 nm) with a peak area of 1348 (0.57 mM). 68

Figure 35. The HPLC chromatograph for the reaction mixture after the reduction reaction, aminophenol was detected at 3.37 min (273 nm) with a peak area of 213 (0.55 mM). 68

Figure 36. TEM micrographs of AuNPs synthesised using the method described in section 7.1.1.1. 69

Figure 37. Size distribution histogram for 120 manually sized AuNPs taken before they were used to catalyse the reduction of nitrophenol (15.7 ± 5.5 nm) from TEM micrographs shown in Section 8.1.1. 70

Figure 38. Size distribution histogram for 120 manually sized AuNPs taken after the nanoparticles were used to catalyse the reduction of nitrophenol (15.4 ± 5.9 nm) from TEM micrographs shown in Section 8.1.2. 70

Figure 39. XPS spectra of AuNPs, A) survey spectrum for AuNPs pre-catalysis, B) survey spectrum for AuNPs post-catalysis, C) high-resolution Au 4f spectra before and after catalysis, and D) high-resolution Au 4d spectra before and after catalysis. 71

Figure 40. UV-vis spectra of AuNPs synthesised in the study, peak absorption occurs at 530 nm. 72

Figure 41. DLS analysis of the AuNP solution prepared using the method described in 7.1.1.1, with plots showing the size distribution by percent intensity (top), volume (middle) and number (bottom). 73

Figure 42. A 3D plot showing how the absorption at the reactor outlet changes as the reaction conditions are changed in flow, the difference between transient and steady-state conditions can be observed in real-time. 74

Figure 43. Plot showing absorption bands for 5 nitrophenol calibration standards from 0.012 to 0.06 mM. 75

Figure 44. A calibration plot showing the integrated absorption values for nitrophenol calibration standards (adjusted to pH 10), between 350 - 450 nm, for 5 nitrophenol calibration standards from 0.012 to 0.06 mM. Gradient 26.439, Intercept 0.03344, R-squared value: 0.999. 75

Figure 45. UV-vis spectra of pure nitrophenol and pure AuNP solution compared to a nitrophenol and AuNP mixture. 76

Figure 46. Graph showing the difference between solutions of pure nitrophenol as a % of the experimental starting concentration (0.06 mM) and nitrophenol mixed with varying amounts of AuNPs within the ranges which would be expected during a self-optimising reaction. 77

Figure 47. Graph showing how a more accurate measurement of the nitrophenol concentration can be obtained by deconvolution of the combined nitrophenol and AuNP spectra. 78

Figure 48. A plastic cuvette containing aqueous $NaBH_4$ solution (2 mM) opened to the atmosphere (left). A flow cell containing aqueous $NaBH_4$ solution (2 mM) under 40 psi of pressure showing the formation of H_2 gas bubbles in a non-pressurised cuvette. ... 78

Figure 49. UV-vis spectrometer placed on top of an aluminium heating block regulated with a Eurotherm PID controller. 79

Figure 50. A fixed wavelength scan of water at 400 nm over 8.5 hours. The temperature of the device was maintained at 35 °C for the first 6 hours before investigating the effect of changing the temperature. 80

Figure 51. A simplified representation of the automated flow reactor used for the optimisation of a nanoparticle catalysed reaction. 81

Figure 52. A flow diagram describing the automated processes by which the nanoparticle catalysed nitrophenol reduction reaction was optimised. 82

Figure 53. A 3D plot showing the effect of changing pump flow rates (FR) on reaction conversion. 83

Figure 54. 3D Plot showing the effect of AuNP, $NaBH_4$ concentration and residence time on the yield of an AuNP catalysed nitrophenol reduction. 83

Figure 55. 3D plot showing the effect of changing three reaction variables on the conversion of nitrophenol to aminophenol. Each of the coloured spots in this diagram represents an experiment carried out by the reactor. 86

Figure 56. A reactor design for the continuous flow synthesis of AuAgNPs with control over composition. A reducing agent solution is pumped into a reactor with the metal precursors solutions of two different metals, a reduction reaction takes place leading to the formation of nanoparticles which are characterised by inline UV-vis spectroscopy. 88

Figure 57. A diagram showing the three categories of alloyed nanoparticles: core-shell (left), intermetallic (middle) and heterostructure (right). Nanoparticle alloys may be composed of two or more metals. 89

Figure 58. A STEM-XEDS micrograph showing the composition of Au/Ag/Au double-shell nanoparticles (Au = green, Ag = blue and oxygen = red). (Reproduced with permission from ref. [160] Copyright 2005, Royal Society of Chemistry. All rights reserved.) 90

Figure 59. STEM-EDS micrographs showing the variety of individual heterostructure nanoparticles that can be synthesised using a two-step thermal annealing procedure of metal precursor and block copolymer solutions deposited onto a flat substrate.[173] (A) monometallic nanoparticles, (B) bimetallic nanoparticles, (C) trimetallic and, (D) tetrametallic nanoparticles. (Reproduced with permission from ref [173]. Copyright 2010, American Association for the Advancement of Science. All rights reserved.) 91

Figure 60. Sample vials containing a range of AuAgNPs with increasing gold concentrations from left to right. 92

Figure 61. A plot showing the UV-vis spectra depending on the Au:Ag metal ratio of the nanoparticles. 92

Figure 62. A reactor diagram showing the initial system designed for the synthesis of AuNPs in flow, gold nanoparticle precursor solutions and sodium citrate reducing agent/capping ligand were pumped into a 5 mL PTFE tubular reactor heated to 100 °C. 93

Figure 63. A plot showing the integrated absorption values between 500 - 550 nm measured at the reactor outflow. 94

Figure 64. A diagram showing how the rate of reactor fouling increases as the number of nucleation sites for nanoparticle formation on the walls of the reactor increases, this eventually exceeds the rate of nanoparticle formation leading to a decline in nanoparticle yield. 94

Figure 65. A plot showing the relative rates of AuNP formation for each growth step, the absorbance values plotted are the integrated absorbance values between 500 and 550 nm. 95

Figure 66. An image showing gold nanoparticles accumulating to form solid gold on the reactor walls. 95

Figure 67. Due to an excess of backpressure on the aqueous side of the membrane separator, the diaphragm valve closes off on the organic side of the separator, causing both phases to be retained. 96

Figure 68. A graphical summary showing how optimising the rate of nanoparticle formation and fouling may lead to optimal steady-state conditions, without compromising nanoparticle quality. 97

Figure 69. A tubular continuous flow reactor which incorporates an AuNP seed solution stream for accelerated nanoparticle formation. 98

Figure 70. A plot showing the integrated absorption values between 500 - 550 nm measured at the reactor outflow for a reactor which uses preformed AuNPs as a catalyst for nanoparticle formation. 99

Figure 71. A reactor diagram showing nanoparticle precursor $HAuCl_4$ being pumped into a 5 mL PFA tubular reactor alongside a mixture of sodium citrate and ascorbic acid. 99

Figure 72. A plot showing the integrated absorption values between 500 - 550 nm measured at the reactor outflow for a reactor which used ascorbic acid to accelerate the rate of nanoparticle formation. 100

Figure 73. A reactor diagram showing nanoparticle precursor $HAuCl_4$ being pumped into a 0.5 mL PFA tubular reactor alongside a $NaBH_4$ solution. 101

Figure 74. A plot showing the integrated time-series absorption values between 500 - 550 nm, measured at the reactor outflow, for a reactor which uses $NaBH_4$ solution as a reducing agent. 101

Figure 75. The reactor T-piece before nanoparticle synthesis (left) and the reactor T-piece after nanoparticle synthesis (right) a small amount of fouling can be seen after nanoparticle synthesis. 102

Figure 76. A diagram showing a reactor designed for the synthesis of Au_xAg_{1-x} nanoparticles. Comprising of a PFA tubular reactor with a 0.5 mL volume. $HAuCl_4$ and $AgNO_3$ precursor solutions were pumped into the reactor alongside a $NaBH_4$ solution. 102

Figure 77. A photograph showing the nanoparticle solutions produced immediately after flow synthesis (Top) and one hour after synthesis (bottom), with black precipitate highlighted in the red box. 103

Figure 78. A reactor diagram showing nanoparticle precursor $HAuCl_4$ being pumped into a 5 mL PFA tubular reactor alongside a mixture of sodium citrate and tannic acid. 103

Figure 79. A plot showing the integrated time series absorption values between 500 - 550 nm, measured at the reactor outflow for a reactor which uses a mixture of sodium citrate and tannic acid as the reducing agent. 104

Figure 80. An image showing the PFA reactor tubing after approximately 1 hour of use, the internal wall of the first 30 cm of the reactor tubing is coated in metallic gold. . 104

Figure 81. (a)UV-vis spectra showing the AuNP solution formed in flow (red) and in batch (blue) and a photograph of the resulting solutions (b) left, showing the nanoparticles formed in flow and right, showing the nanoparticles formed in batch. 105

Figure 82. diagram showing annotated design of individual CSTR. 106

Figure 83. A photograph showing the fReactors used to synthesise AuNPs, cotton wool was used to insulate the tubing connections between the preheating fReactors and the main fReactor. 106

Figure 84. A reactor diagram showing a mixture of sodium citrate and tannic acid, as well as nanoparticle precursor $HAuCl_4$, being pumped through separate preheating fReactors and combined/mixed in a final fReactor for nanoparticle synthesis. 106

Figure 85. A plot showing the integrated absorption values between 500 - 550 nm measured at the reactor outflow for a fReactor system which uses a mixture of sodium citrate and tannic acid as the reducing agent. 107

Figure 86. An image showing 400 mL of AuNPs collected from the fReactor CSTR. 107

Figure 87. A plot showing overlapping UV-vis absorption spectra for nanoparticles synthesised during the steady-state period of the reactor's operation, no change in the nanoparticle's absorption properties were observed during this period. 108

Figure 88. A reactor diagram showing gold nanoparticle precursor $HAuCl_4$, being pumped into a series of 3 fReactors with a mixture of sodium citrate and tannic acid reducing agents at 100 °C. 108

Figure 89. The integrated UV-vis absorption profiles for total combined flow rates of 1,3 and 4 mL/min. 109

Figure 90. Clean fReactor (left) followed by stages 1, 2 and 3 (right), fouling was observed only within the first reactor of the series. 109

Figure 91. A diagram showing the reactor used to synthesise AuAgNPs. 110

Figure 92. A photograph of the AuAgNPs showing the effect of alloy composition on the colour of the nanoparticle solutions, with the samples from left to right increasing in Au composition. Far left 100% silver with samples increasing in gold content by 10% up to 100% gold on the far right. 110

Figure 93. UV-vis spectra corresponding to AuAgNP solutions synthesised using the CSTR cascade, changing the flow ratio of Au and Ag precursor solution pumped into the reactor. 111

Figure 94. A plot showing changing λ_{max} wavelength as the percentage of Au in the AuAgNPs was increased by 10% every 15 minutes, with pure silver nanoparticles at t=0 and pure gold nanoparticles at t = 2.5 hours. 111

Figure 95. A TEM micrograph showing an example of the AuAgNPs (40:60 Au:Ag) collected from the outlet of the flow reactor developed in this chapter, see Appendix, Section 8.1.4. 112

Figure 96. Time-series UV-vis absorption spectra integrated between 450 and 500 nm for AuNPs, AgNPs and a range of AuAgNP alloys formed in batch. 113

Figure 97. An example EDS spectrum for an AuAgNP sample with an Au:Ag ratio of 60:40. 114

Figure 98. Plot showing the fraction of nanoparticles containing Au (%) with the remainder made up of Ag from EDS analysis. 114

Figure 99. A summary of the approach used to compare optimisation algorithms in this chapter. A variety of algorithms were benchmarked using a reproducible, simulated reaction. The outcomes of these optimisation processes were then used to compare the efficacy of each algorithm. 116

Figure 100. Examples of unconstrained single-objective response surfaces, these types of functions are commonly used to benchmark optimisation algorithms. These algorithms are each named according to their shape or after their creators: a) Bird, b) Schweffel, c) Matayas, d) Zettl, e) Bukin, and f) Beal. 117

Figure 101. A convergence plot showing the averaged cumulative best fitness of each of the algorithms compared in this study, benchmarked using the Schwefel function with the butterfly algorithm[207] against seven other optimisation algorithms.[105,206,208–212] (Reproduced with permission from ref [207] Copyright 2018, Springer Science & Business Media. All rights reserved.) 118

Figure 102. A diagram showing the conversion of 4-nitrophenol to 4-aminophenol on the surface of a solid catalyst via the Langmuir-Hinshelwood model. Here H^- dissociates from $NaBH_4$ and on the surface of the catalyst, both components then react to form aminophenol which then desorbs. 121

Figure 103. A diagram showing the conversion of 4-nitrophenol to 4-aminophenol on the surface of a solid catalyst via the Eley–Rideal mechanism. Here only the

aminophenol adsorbs onto the surface of the catalysts before the other reacts with this adsorbed molecule without adsorbing itself. 121

Figure 104. A graphical summary of the approach used to generate the kinetic model in this chapter. 124

Figure 105. A plot showing predicted versus experimental kinetic profiles for a batch reduction of nitrophenol reaction. 124

Figure 106. A plot showing the predicted reaction conversion (mesh surface) under different nanoparticle concentrations and reactor residence times, with the concentration of NaBH4 held at 1.5 mM to aid visualisation. Experimental data (coloured points) are overlaid for comparison with the model, the red line shows the simulated kinetic reaction conversion versus time. 125

Figure 107. A plot showing the extrapolated model, a large flat plane is observed as 100% conversion is reached at high residence times and catalyst surface areas. 126

Figure 108. The response surface after scalarisation with weighting factors of 0.06 and 60 for the amount of catalyst used and residence time respectively. This scalarization process transforms the shape of the surface so that the most efficient conditions were a singular point (red marker) as opposed to an infinite surface. 127

Figure 109. A response surface showing the residence times and catalyst surface areas explored by the genetic algorithm, after 12 generations each with a population of 150, the optimum conditions are indicated with a red marker. 128

Figure 110. A plot showing the residence times and catalyst surface areas explored by the genetic algorithm, after 5 generations each with a population size of 10. The large red marker on this surface highlights the optimal conditions. 128

Figure 111. A two-level two-factor FFD with a centre point exploring the upper and lower limits of: (residence time, AuNP SA) on reaction efficiency. 130

Figure 112. A contour representation of the model created using FFD experimental design. 130

Figure 113. A two-level two factor FFD with additional experiments along the axis of the design space and a centre point exploring the effects of the variables: (residence time, AuNP SA) on reaction efficiency. 131

Figure 114. A contour representation of the model which includes quadratic terms created using an experimental design with points along the axis of the design space. 131

Figure 115. An overlay plot showing the 100 SNOBFIT experiments performed during the SNOBFIT optimisation. The optimal conditions are highlighted by the red dot. 132

Figure 116. An overlay plot showing the 100 experiments performed during the BOAEI experiment with the optimal conditions shown by the red marker. Note that the majority of experiments were conducted near the optimum point. 133

Figure 117. A convergence plot showing the cumulative running best conditions obtained using the 3 different types of single-objective optimisation algorithms explored in this chapter. 134

Figure 118. A parity plot showing the results of the predicted kinetic model relative to the experimental results..... 135

Figure 119. A convergence plot showing the cumulative running best conditions obtained with the addition of white gaussian noise for each of the 3 algorithms benchmarked in this chapter..... 135

Figure 120. A plot showing the trade-off curve between the two competing performance criteria (STY and E-factor), the LHC experiments (blue markers), Gaussian process model (purple crosses), Pareto experiments conducted by the algorithm (red crosses) and the Pareto front i.e. all of the points at which it was not possible to increase STY while also minimising E-factor (yellow circles). 137

Figure 121. A heatmap showing the effect of changing residence time and concentration on the efficiency of the reaction, the Pareto front is plotted as an overlay with each of the 30 Pareto experiments represented by red crosses. 138

Figure 122. A graphical representation depicting the concept of a two-stage performance directed nanoparticle catalysed reaction optimisation system. 140

Figure 123. A photograph of a ChemSpeed catalyst screening platform used to screen catalysts and reaction conditions in an automated fashion (Photo credit: Christopher Horbaczewskyj, University of York, 2021). 141

Figure 124. A reconfigurable multi-stage continuous synthesis and optimisation system (Reproduced with permission from ref.[254] Copyright 2018, American Association for the Advancement of Science. All rights reserved.) 145

Figure 125. UV-vis absorption calibration for solutions of 4-nitrophenol between 0.024-0.12 mM. 148

Figure 126. Calibration plots comparing calibrations taken between 375-425 nm (left) and 425-450 nm (right). 148

Figure 127. Plot showing UV-vis absorption spectra before and after deconvolution, a slight depression in absorption can be observed at 490 nm and ~580 nm, this is due to stronger light intensity provided in these areas from the stronger deuterium light source, this did not interfere with subsequent analysis as these regions of the spectrum were not analysed. 150

Figure 128. A diagram showing the initial two-stage reactor developed during this chapter of work. 150

Figure 129. A diagram showing the conventional use of a six-way switching valve, when the switching valve is in Position 1 the sample flows through the sample loop while the carrier phase flows to the column. When the valve is switched to position 2, the sample solution contained within the sample loop is injected onto the column. . 151

Figure 130. Diagram showing the reactor during stage one of an optimisation experiment, the secondary reactor is switched off and the nanoparticle stream bypasses the second reactor to save time and material. 152

Figure 131. Diagram showing the reactor during stage two of on optimisation experiment, the switching valve changes position and the K_2CO_3 pump is used to pump nanoparticles into the second reactor. 152

Figure 132. A flow diagram describing the automated processes by which the two-stage nanoparticle catalyst synthesis and screening reaction optimisation was performed. 154

Figure 133. (bottom) A figure showing the changing fixed wavelength absorption @ 400 nm throughout the first 20 experiments of the optimisation experiment, described further in section 5.3.1. Blue lines indicate when nanoparticle synthesis was taking place, orange lines indicate when the catalysed reaction was being performed. (top) Expanded region to highlight when steady-state conditions were achieved. 155

Figure 134. 3D plot showing results of a SNOBFIT optimisation exploring all possible Au:Ag ratios. The optimal reaction conditions identified in this optimisation are highlighted with a black star. 156

Figure 135. 3D plot showing results of second SNOBFIT optimisation exploring Au:Ag ratios between 0.9:0.1 and 1.0:0.0 Au:Ag with SNOBFIT. The optimal reaction conditions identified in this optimisation are highlighted with a black star. 157

Figure 136. A line plot showing the effect of changing Au:Ag ratio between 0.9-0.1 to 1.0-0.0 Au:Ag, for the conversion of nitrophenol to aminophenol, the error bars are based on 3 repeats taken @ an Au:Ag ratio of 0.97:0.03 with a standard deviation of 3.58% quoted as the error..... 158

Figure 137. 3D plot showing results of the BOAEI algorithm optimisation exploring Au:Ag ratios between 0.9-0.1 to 1.0-0.0 Au:Ag. The optimal reaction conditions identified in this optimisation are highlighted with a black star. 160

Figure 138. A convergence plot showing a comparison between the number of experiments taken to find the optimal conditions with the BOAEI and SNOBFIT algorithms..... 160

Figure 139. TEM images showing AuAgNP ratios of (a) 0.96:0.04,(b) 0.97:0.03, (c) 0.98:0.00,(d) 0.99:0.01(e) pure AuNPs and (f) 0.97:0.03 AuAgNPs after use in a catalytic reaction. 161

Figure 140. Histograms showing the size distribution of particle sizes for the optimal AuAgNPs with a ratio of 0.97:0.03 – Au:Ag..... 161

Figure 141. A plot showing the mean average and standard deviation range for the nanoparticles with Au:Ag ratios from 0.96:0.04 to 1.00:0.00 with steps of 0.01. 162

Figure 142. A reactor schematic describing in detail the reactor setup, the 4 pumps and the UV-vis detector in this schematic were connected to a computer to allow automated optimisation..... 170

Figure 143. Photograph showing a configuration of the flow reactor platform for the optimisation of a gold nanoparticle catalysed nitrophenol reduction. 171

Figure 144. Left: a photograph showing a 250 mL round-bottomed flask containing a 100 mL stirred reaction solution was recirculated through a quartz flow cell for continuous monitoring. Right: a diagrammatic representation of this setup. 179

Figure 145. A reactor schematic describing in detail the reactor setup, the 6 pumps and the UV-vis detector in this schematic were connected to a computer to allow automated optimisation. 182

Figure 146. Photograph showing a configuration of the flow reactor platform for the optimisation of a AuNP, AgNP and AuAgNP catalysed nitrophenol reduction. 182

Figure 147. TEM images used to obtain the size distribution histogram shown in Figure 36 (before reaction). 185

Figure 148. TEM images used to obtain the size distribution histogram shown in Figure 37 (after reaction). 186

Figure 149. A histogram describing the distribution of particle sizes for AgNPs. 189

Figure 150. TEM micrographs showing AgNPs. 189

Figure 151. A histogram describing the distribution of particle sizes for AuAgNPs with the ratio 0.2:0.8 – Au:Ag. 190

Figure 152. TEM micrographs showing AuAgNPs with the ratio with the ratio 0.2:0.8 – Au:Ag. 190

Figure 153. A histogram describing the distribution of particle sizes for AuAgNPs with the ratio 0.4:0.6 – Au:Ag. 191

Figure 154. TEM micrographs showing AuAgNPs with the ratio with the ratio 0.4:0.6 – Au:Ag. 191

Figure 155. A histogram describing the distribution of particle sizes for AuAgNPs with the ratio 0.6:0.4 – Au:Ag. 192

Figure 156. TEM micrographs showing AuAgNPs with the ratio with the ratio 0.6:0.4 – Au:Ag. 192

Figure 157. A histogram describing the distribution of particle sizes for AuAgNPs with the ratio 0.8:0.2 – Au:Ag. 193

Figure 158. TEM micrographs showing AuAgNPs with the ratio with the ratio 0.8:0.2 – Au:Ag. 193

Figure 159. A histogram describing the distribution of particle sizes for AuNPs. 194

Figure 160. TEM micrographs showing AuNPs. 194

Figure 161. An EDS spectrum obtained from a AgNP sample. 195

Figure 162. An EDS spectrum obtained from a 20:80 AuAgNP sample..... 195

Figure 163. An EDS spectrum obtained from a 40:60 AuAgNP sample..... 195

Figure 164. An EDS spectrum obtained from a 60:40 AuAgNP sample..... 196

Figure 165. An EDS spectrum obtained from an 80:20 AuAgNP sample..... 196

Figure 166. An EDS spectrum obtained from a AuNP sample. 196

Figure 167. A histogram describing the distribution of particle sizes for AuAgNPs with the ratio 0.96:0.04 – Au:Ag..... 206

Figure 168. TEM micrographs showing AuAgNPs with the ratio 0.96:0.04 – Au:Ag. 206

Figure 169. A histogram describing the distribution of particle sizes for AuAgNPs with the ratio 0.97:0.03 – Au:Ag..... 207

Figure 170. TEM micrographs showing AuAgNPs with the ratio with the ratio 0.97:0.03 – Au:Ag. 207

Figure 171. A histogram describing the distribution of particle sizes for AuAgNPs with the ratio 0.98:0.02 – Au:Ag..... 208

Figure 172. TEM micrographs showing AuAgNPs with the ratio with the ratio 0.98:0.02 – Au:Ag. 208

Figure 173. A histogram describing the distribution of particle sizes for AuAgNPs with the ratio 0.99:0.01 – Au:Ag..... 209

Figure 174. TEM micrographs showing AuAgNPs with the ratio with the ratio 0.99:0.01 – Au:Ag. 209

Figure 175. A histogram describing the distribution of particle sizes for AuNPs. 210

Figure 176. TEM micrographs showing AuNPs. 210

Figure 177. A histogram describing the distribution of particle sizes for AuAgNPs with the ratio 0.97:0.03 – Au:Ag after use in a catalysed reaction. 211

Figure 178. TEM micrographs showing AuAgNPs with the ratio 0.97:0.03 – Au:Ag after use in a catalysed reaction. 211

List of Schemes

Scheme 1. The nanoparticle catalysed reduction of 4-nitrophenol to 4-aminophenol with $NaBH_4$ under room temperature conditions. 65

Scheme 2. Examples of the reactions optimised by the reconfigurable self-optimising multistage reactor. 1. Nucleophilic aromatic substitution (S_NAr), 2. C-C cross-coupling, 3. reductive amination, 4. olefination, and 5. photo redox catalysis, reproduced from.[252] 146

List of Tables

Table 1. A summary of the advantages and disadvantages of different pumps used for continuous flow chemistry and references to continuous flow studies employing each pump type. 40

Table 2. A summary of nanoparticle catalysts and nanoparticle alloys synthesised in continuous flow. 48

Table 4. A table showing the deconvoluted peak positions for the Au 4f and Au 4d high-resolution XPS spectra before and after catalysis. 72

Table 5. Table showing two sets of samples, pure nitrophenol and nitrophenol mixed with varying amounts of AuNPs within the range that would be expected during the self-optimising reaction. 76

Table 6. Upper and lower bounds of reactor flow rates (mL/min), nitrophenol was set as a ratio of the other flow rates so that a constant starting concentration of 0.6 mM nitrophenol was pumped into the reactor. 82

Table 7. The lower and upper variable bounds used for the optimisation in this study. 85

Table 8. A summary of the factors influencing the rate of reactor fouling and the rate of nanoparticle formation in continuous flow reactors. 96

Table 9. The mean average sizes and standard deviation size variation for the AuAgNPs sampled in this chapter. 112

Table 10. A table showing the number of optimisation experiments and amount of time required to reach the reaction yields stated in the final column of each reaction, reproduced from.[254] 147

Table 11. Design space for first SNOBFIT optimisation exploring all possible Au:Ag ratios. 156

Table 12. Design space for second SNOBFIT optimisation exploring Au:Ag ratios between 0.9-0.1 to 1.0-0.0. 157

Table 13. A table outlining the design space for the BOAEI algorithm. 159

Table 3. The solvent elution gradients used in the HPLC method to determine the extent of nitrophenol to aminophenol conversion. 168

Table 14. A table showing the name and purpose of the reactor components shown in Figure 141. 171

Table 15. Volumes of metal precursor added to sodium citrate solution. 174

Table 16. Flow rates of metal precursor and reducing agent used to synthesise AuAgNPs in 0.5 mL PFA reactor with sodium borohydride in continuous flow. 176

Table 17. Number of fReactors and the flow rates used to determine the requirements for steady-state conditions. 177

Table 18. Flowrates of metal precursor and reducing agent used to synthesise AuAgNPs in continuous flow. 178

Table 19. Table showing the volumes of precursor added to a tannic acid/sodium citrate solution. 178

Table 20. A table showing the name and purpose of the reactor components shown in Figure 144. 182

Table 21. Table showing raw data for optimisation performed without conditions generation function. 187

Table 22. Table showing experiments performed during the optimisation. 188

Table 23. A list of simulated experiments based on a LH kinetic model. Showing mean average changes in reaction efficiency (20 runs) for the BOAEI and genetic algorithms and a single run for the SNOBFIT algorithm. 197

Table 24. A table showing the initial conditions and reaction efficiencies for a FFD exploring the upper and lower limits of residence time, AuNP SA on reaction efficiency. 200

Table 25. A table showing the initial condition and reaction efficiencies for a FFD with additional experiments along the axis of the design exploring the upper and lower limits of residence time, AuNP SA on reaction efficiency. 200

Table 26. A list of simulated experiments based on a LH kinetic model. Showing mean average changes in reaction efficiency (20 runs) for the BOAEI and genetic algorithms and a single run for the SNOBFIT algorithm with added white Gaussian noise. 200

Table 27. A table showing the reaction conditions, STY and E-factors for experiments performed during the multi-objective TS-EMO optimisation. 202

Table 28. Table showing raw data for optimisation performed with AuAgNP range (0.0:1.0 – 1.0:0.0, Au:Ag). 212

Table 29. Table showing experiments performed with AuAgNP range (0.9:0.1 – 1.0:0.0, Au:Ag) using the SNOBFIT algorithm. 213

Table 30. Table showing line profile experiments performed between a AuAgNP range of 0.9:0.1 – 1.0:0.0, Au:Ag. 214

Table 31. Table showing experiments performed with AuAgNP range (0.9:0.1 – 1.0:0.0, Au:Ag) with a Bayesian optimisation algorithm (BOAEI)..... 215

List of Abbreviations

AuNPs – Gold Nanoparticles

AgNPs – Silver Nanoparticles

AuAgNPs – Gold/Silver Nanoparticle Alloys

BOAEI – Bayesian Optimiser with Adaptive Expected Improvement

BPR – Back Pressure Regulator

CCD – Charge Coupled Device

CFD – Computational Fluid Dynamics

CSTR – Continuous Stirred Tank Reactor

DoE – Design of Experiment

DLS – Dynamic Light Scattering

DFT – Density Functional Theory

EDS – Energy Dispersive X-ray Spectroscopy

ER – Eley-Rideal

FEP – Fluorinated Ethylene Propylene

FFD – Full Factorial Design

FR – Flow Rate

GA – Genetic Algorithm

GC – Gas Chromatography

GP – Gaussian Process

HPLC – High Performance Liquid Chromatography

HTS – High Throughput Screening

LH – Langmuir-Hinshelwood

LHC – Latin Hypercube

LHS – Latin Hypercube Sampling

NMR – Nuclear Magnetic Resonance

NIR – Near-Infrared

ODE – Ordinary Differential Equation

OVAT – One Variable at A Time

PFA – Perfluoroalkoxy Alkane

PID – Proportional, Integral, Derivative

PTFE – Polytetrafluoroethylene

PEEK – Polyether Ether Ketone

PVP – Polyvinylpyrrolidone

SA – Surface Area

SPR – Surface Plasmon Resonance

SAXS – Small-Angle X-ray Scattering

XPS – X-ray Photoelectron Spectroscopy

SOBO – Single Objective Bayesian Optimisation

STY – Space Time Yield

SNOBFIT - Stable Noisy Optimization by Branch and Fit

TEM – Transmission Electron Microscopy

TS-EMO - Thompson Sampling Efficient Multi-objective Optimisation

TSC – Trisodium Citrate

UV-vis – Ultraviolet-Visible

λ_{max} – Maximum Absorption Wavelength

XANES – X-ray Absorption Near Edge Structure

Chapter 1 Introduction

1.1 Nanoparticles

Optimising the catalytic properties of nanoparticle catalysts can be a challenging and time-consuming task. Unlike homogeneous organic or metal-complex based catalysts, nanoparticles typically present as a non-discrete distribution of structures. These structures can be infinitely modified, providing many variables to explore.

Additionally, the performance of nanoparticle catalysts depends on both the intrinsic properties of the nanoparticles and the experimental conditions under which the reactions are performed.[2] Therefore, it is important to not only compare each discrete catalyst system but also each system under different reaction conditions. The difficulty of implementing such an approach arises from the sheer number of experiments required to thoroughly explore reaction conditions in this way. Particularly when using methods which rely on labour-intensive offline performance comparisons.

Continuous flow reactors have become attractive platforms for nanoparticle development. Flow reactors offer a more scalable alternative to more conventional batch synthesis of nanoparticles.[3] Continuous reactors are also easily automatable, *e.g.* when equipped with inline analytical techniques, feedback control systems can be implemented allowing autonomous reaction optimisation to take place. These self-optimising reactors also employ machine learning algorithms to accomplish this task more efficiently,[4] leading to higher yields and accelerated process development timelines.[5]

This project describes a novel approach with the potential to significantly accelerate nanoparticle catalyst development. Demonstrating a system capable of quantitative online assessment of nanoparticle catalytic activity in real-time, which allows nanoparticle catalysts to be developed in a self-optimising fashion.

This first chapter introduces the essential concepts required to understand continuous flow nanoparticle optimisation. Namely, the basic properties of colloidal nanoparticles, nanoparticle synthesis methods, different types of continuous flow reactors, flow regimes, flow equipment and finally an explanation of the types of optimisation algorithms which can be used to optimise reactions in these systems.

1.1.1 Nanoparticle stability

Colloidal nanoparticles possess high energy surfaces making them attractive candidates for catalysis. However, in the absence of other factors, this also presents a thermodynamic driving force towards aggregation. To prevent this, nanoparticle suspensions contain stabilising agents such as polymers, surfactants or charged compounds which coat the surface of nanoparticles preventing aggregation.

Charged capping agents prevent aggregation through electrostatic repulsion, causing the nanoparticles to repel one another due to having the same surface charge (Figure 1). As charged capping agents such as sodium citrate form relatively weak bonds with nanoparticle surfaces, they can easily be exchanged with more strongly binding capping ligands allowing nanoparticle functionalisation.

These functionalised nanoparticles are particularly useful in biological applications. For example, in the detection of viruses, antibodies can be bound to the surface of gold nanoparticles (AuNPs) allowing them to bind to the spike protein of the COVID19 virus, resulting in aggregation of the nanoparticles. This leads to a colour change from red to purple/blue indicating a positive test result.[6] Other biological applications of functionalised nanoparticles include microscopic image enhancement of pathogens and cancerous cells,[7–9] drug delivery and oncology.[10–13]

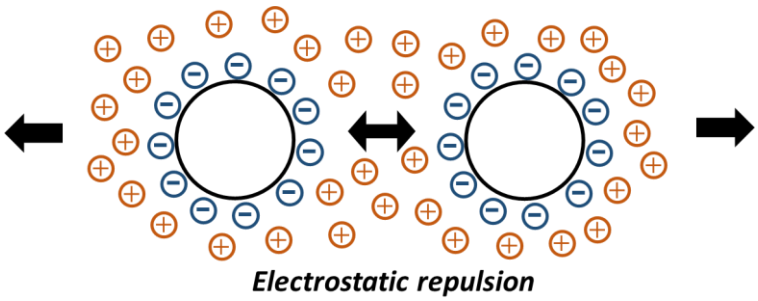

Figure 1. Diagram showing electrostatic repulsion between two nanoparticles with negatively charged surface coatings and surrounding positive ions in solution.

Organic capping agents such as surfactants or polymers *e.g.*, polyvinyl propylene (PVP) can also prevent aggregation through steric repulsion. When two polymer capped particles come into contact an entropic driving force, arising from increased local osmotic pressure and a reduction in the number of possible configurations of the surface polymers (excluded volume effect), causes the particles to repel (Figure 2).[14] Such capping agents are typically used during the synthesis of smaller and more catalytically

active nanoparticles, as these are typically less stable and require strongly bound capping agents to prevent agglomeration.[15]

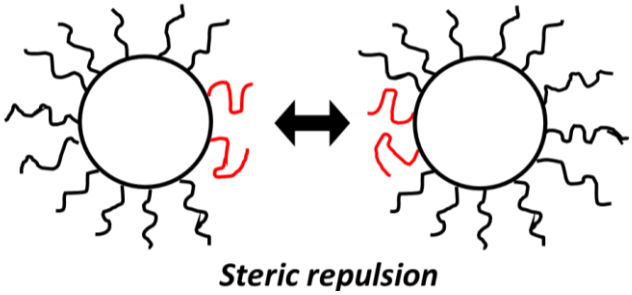

Figure 2. Diagram showing steric repulsion between polymer-coated colloids.

1.1.2 Surface plasmon resonance

Some metal nanoparticles have distinct ultraviolet/visible (UV-vis) absorption spectra, this is due to a phenomenon called surface plasmon resonance. Surface plasmon resonance occurs when an external electromagnetic field such as UV and visible light causes the electrons on the surface of the nanoparticles to oscillate collectively (Figure 3). These surface electrons will oscillate at a range of frequencies depending on the size, shape and composition of the nanoparticles.[16]

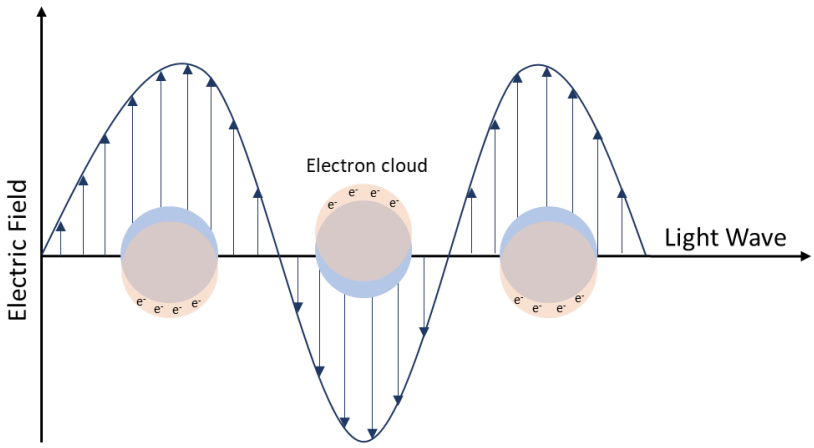

Figure 3. A diagram describing the mechanism behind the phenomenon of surface plasmon resonance. An incident electric field causes electrons on the surface of the nanoparticles to oscillate, converting electromagnetic energy into heat. This can be observed as the absorption of specific wavelengths of light.

In the case of AuNPs, the frequencies of light absorbed range from ~520-550 nm giving AuNP solutions a characteristic ruby red colour. For nanoparticles, the maximum wavelength of the peak observed in the absorption spectrum is dependent on the size of the nanoparticles, as AuNPs increase in size the maximum wavelength of the absorption peak also increases.[17] Aggregation causes this frequency to shift to even higher wavelengths causing the nanoparticle solutions to appear purple.[18]

1.1.3 Nanoparticles in catalysis

A catalyst is any substance which increases the rate of a chemical reaction without being consumed. A catalytic increase in reaction rate is caused by a decrease in activation energy, meaning more molecules in the reaction possess the required energy to undergo a reaction, see Figure 4.

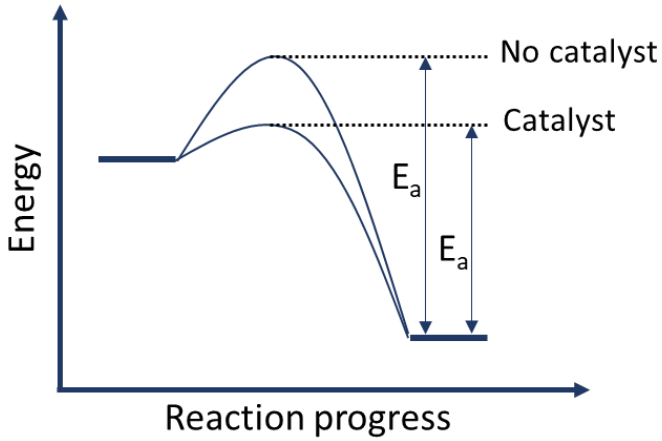

Figure 4. A reaction coordinate diagram describing how a catalyst increases the rate of a reaction via a reduction in activation energy.

Despite being unreactive in the bulk phase, metals such as gold, silver, palladium and platinum have been demonstrated as excellent catalysts in a wide variety of chemical transformations, such as photocatalytic water splitting,[19] hydrogenations,[20] oxidations[21] and cross-coupling reactions.[22] Owing to their high energy surfaces and extremely high surface atom to volume ratios.[23]

Gold and silver nanoparticles have shown particular efficacy as catalysts for redox reactions such as in the reduction of methylene blue[24] or nitro aromatic compounds.[25] One patent describes the use of AuNPs as catalysts for the oxidation of CO to CO_2 under ambient conditions, example applications for this patent could include fire escape hoods or catalytic converters.[26] AuNPs have also proven effective catalysts for reactions involving carbon-carbon bond formation.[27]

Simple redox reactions such as the reduction of nitro aromatic compounds are commonly used as screening reactions to assess the catalytic activity of AuNPs. The kinetics of these reactions can be monitored with UV-vis spectroscopy and take place in aqueous solution at room temperature, allowing quick comparison between different nanoparticles. The catalytic properties of AuNPs are highly dependent upon their size. Activity is typically inversely proportional to particle size[28] as solutions containing

smaller nanoparticles have a larger catalytic surface area than solutions containing larger nanoparticles with the equivalent mass of catalyst.

It is possible to create very small nanoparticles between 2-5 nm in diameter[29] or with more complicated techniques even smaller nanoparticles can be made.[30] However, smaller nanoparticles are not always more catalytically active than larger ones. It has been reported that gold nanoparticles with a diameter of ~3 nm were more catalytically active than nanoparticles of 1.7 nm for the reduction of 4-nitrophenol with sodium borohydride.[31] This may have been due to differences in the ability of the reactant molecules to bind to the smaller nanoparticles. As nanoparticles become smaller their surfaces also become less crystalline, meaning the surface is less ordered for catalysis. An optimal 'sweet spot' may exist where nanoparticles are small enough to maximise their surface area to volume ratio but still crystalline enough for catalysis.

1.1.4 Nanoparticle synthesis

Solution-based precipitation methods are used to synthesise nanoparticles in continuous flow.[32] These methods produce nanoparticles from homogenous solutions of the corresponding metal salt or salts. The metal ions in the salt solution are reduced to metal atoms by either chemical,[33] electrochemical[34] or thermal reduction,[3] the amount of metal atoms increases until the solution becomes supersaturated, at which point the metal atoms cluster to form nuclei and grow to form nanoparticles (Figure 5).[35]

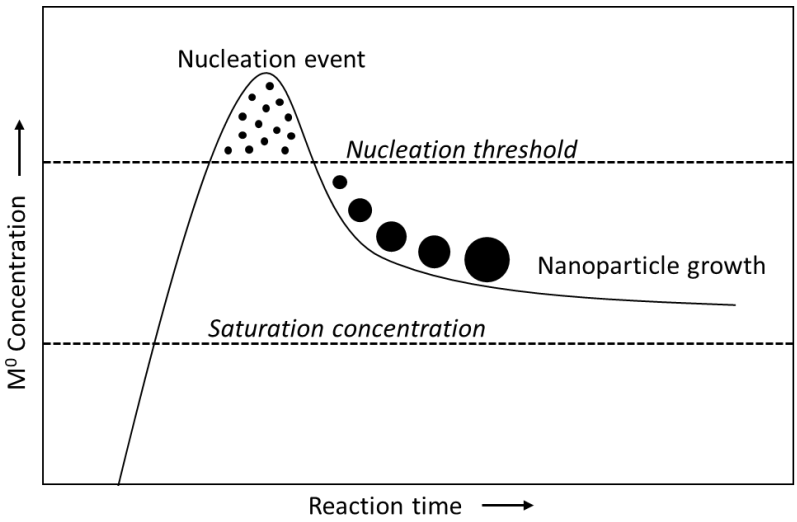

Figure 5. A graph illustrating the events that take place during nanoparticle formation. As the concentration of metal atoms increases above the 'nucleation threshold' a nucleation event occurs resulting in a burst of very small nanoparticles forming in solution, this effectively results in a decrease in the concentration of monomer in solution to below the nucleation threshold where a subsequent growth process occurs. Adapted from.[36]

Most modern methods for AuNP synthesis have been developed from the 'Turkevich' method published in 1951.[37] This reaction involves the reduction of tetrachloroauric acid ($HAuCl_4$) with sodium citrate ($Na_3C_6H_5O_7$) and is a reliable method for the production of stable monodisperse citrate capped AuNPs. This method has since been adapted to produce AuNPs with a high degree of control over size by combining other reducing agents with the sodium citrate reductant and capping agent.[33]

The underlying mechanisms for the Turkevich reaction have recently been investigated by Polte *et al.* using a combination of X-ray absorption near edge structure (XANES) and small-angle X-ray scattering (SAXS) to monitor the rate of Au^{3+} ion reduction alongside the rate of nanoparticle growth and the number of nanoparticles in solution. Their findings suggest AuNPs form through several steps beginning with the formation of many smaller AuNPs which undergo coalescence and Oswald ripening to form a smaller number of larger particles.[38]

Other methods for the synthesis of AuNPs can be carried out at room temperature and involve the use of stronger reducing agents such as ascorbic acid or sodium borohydride. These methods produce smaller nanoparticles with wider size distributions, they also require the presence of strongly binding capping agents such as polysorbate or polyvinylpyrrolidone (PVP) to ensure nanoparticle stability.[15] A concise review summarising the most recent methods for nanoparticle synthesis has been written by M. Sengani *et. al.*[39]

Continuous flow reactors provide a promising alternative to batch reactors. Their smaller dimensions and precise geometries can offer enhanced heat and mass transfer properties. Using these methods, it may be possible to continuously produce nanoparticles with more consistent properties and narrower size distributions.

1.2 Flow reactors

Traditional methods of chemical/materials manufacturing use batch reactions as a primary means of synthesis. These methods typically involve charging reactants, solvents and reagents into a reaction vessel for a fixed amount of time while stirring and optionally heating or cooling the reaction mixture. This has been the standard method of chemical synthesis for hundreds of years and is still the most popular method for chemical/materials manufacturing today.

Flow reactors are an alternative method of chemical/materials manufacturing. Continuous flow manufacturing involves pumping solutions of reactants/reagents into a continuous stream where they undergo a reaction for an amount of time defined by the volume of the reactor and the total combined flow rate. The advantages of using this type of reactor include being less constrained to producing an amount of product defined by the size of the reactor; increased safety as only a small amount of material is reacting at any one time; more efficient heat transfer between the reactor walls and the reaction mixture and more defined mixing lead to more consistent conditions across the reactor. Conversely, a major limitation of these reactors is that they are prone to blocking with reactions which involve solids, these reactors can also lack versatility and are typically designed for specific reactions/processes.

In the context of this project the main justification for using continuous reactors is that they are relatively simple to automate. By connecting the reactors pumps/reactor temperature controls and integrated analysis to a central control unit it becomes possible to monitor and control a reaction with relative ease. With the dawn of artificial intelligence and development of optimisation algorithms it has become possible to create reactors which are able to optimise their conditions to meet set targets, such as increased yield and/or selectivity towards a specific product.

This section outlines the basic engineering concepts underpinning mixing within these reactors, different types of continuous reactor, ways of controlling flow rates within flow reactors, a review of reactors used for nanoparticle synthesis and methods of analysis in continuous flow reactors.

1.2.1 Mass transfer within continuous flow reactors

Effective mass transfer is important for the formation of nanoparticles with consistent properties and narrow size distributions. The mass transfer properties within a reactor can be described by the Reynolds number (Re). This dimensionless number indicates the type of flow pattern that occurs within a reactor. A Reynolds number below 2000 indicates laminar flow, a transitional phase exists between 2000 and 3000 and turbulent flow regimes are indicated by Reynolds numbers beyond 3000. The Reynolds number can be calculated for a tubular reactor using equation (1) where: pipe diameter = D, average flow velocity = v, fluid density = ρ and dynamic viscosity = μ.[40]

$$Re = \frac{Dv\rho}{\mu} \tag{1}$$

The plot shown in Figure 6 describes the flow rates required to obtain turbulent flow regimes in standard laboratory scale tubular reactors with water at room temperature. At this scale flow reactors typically run at flow rates well below 50 mL/min falling firmly within a laminar flow regime, where diffusive mass transfer and conductive heat transfer dominate. The rate of heat and mass transfer under a laminar regime is inversely proportional to the square of the characteristic channel size, meaning under these conditions narrower tubular reactors provide more effective mixing.[41]

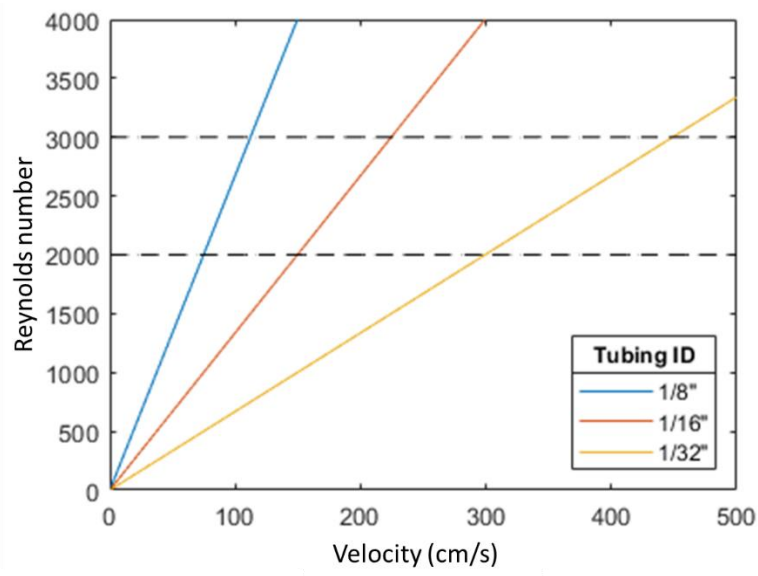

Figure 6. A plot showing the effect of flow rate on Reynolds number for standard laboratory scale flow reactors with an aqueous solution, the hashed lines indicate the boundaries between laminar, transitional, and turbulent flow regimes.

1.2.2 Tubular reactors

In continuous flow chemistry, residence time describes the amount of time spent by reagents in a flow reactor under steady-state conditions. This can be calculated by dividing the volume of the reactor by the flow rate of the reagents. This description of residence time holds true for theoretical plug flow reactors (Figure 7), which assume all the fluid within the flow reactor is moving at the same velocity

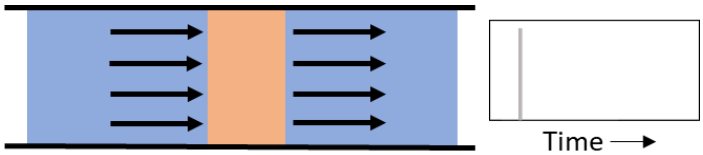

Figure 7. An idealised plug flow model assumes all the fluid in the reactor is moving at the same velocity.

Laminar flow is more realistic and can be used to describe residence times as a distribution of times a molecule could spend in a flow reactor. Fluids moving through a tubular reactor under a Laminar flow regime are described as an infinitesimal number of layered concentric cylinders running parallel to the walls of the reactor. Shear forces between these layers emanating from the inner surface of the reactor result in a characteristic parabolic velocity profile (Figure 8), also known as Taylor dispersion. [42]

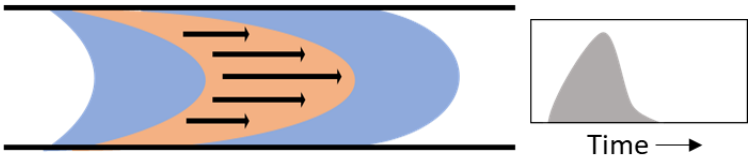

Figure 8. Laminar flow results in Taylor dispersion characterised by a parabolic flow profile and a non-uniform flow velocity.

A large degree of Taylor dispersion can be detrimental to some nanoparticle synthesis methods, particularly those involving long growth periods. As a wide residence time distribution may produce nanoparticles with a size distribution proportional to the residence time distribution of the reactor. Because nanoparticles produced in a flow reactor with significant Taylor dispersion will have spent different amounts of time experiencing the latter growth stages of the formation process.

More recently reactors with segmented flow regimes have been developed for nanoparticle synthesis. In these reactors, nanoparticles are formed within slugs of liquid held together with surface tension and separated by an immiscible liquid or gas, in effect creating a stream of discrete miniature batch reactors.[43–47] Residence time distributions

within these reactors are extremely narrow. Internal recirculation also occurs within the droplets promoting mixing. Segmented flow (Figure 9) has also been shown to prevent/slow reactor fouling during the flow synthesis of nanoparticles.[48]

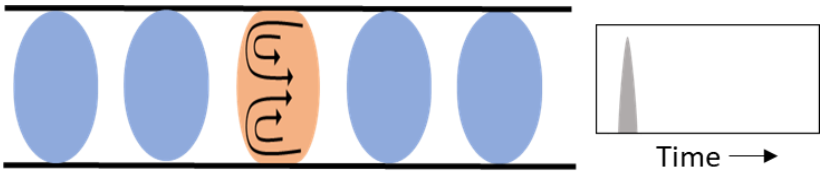

Figure 9. Segmented flow reactors significantly reduce axial mixing within tubular reactors, therefore, creating residence time distributions analogous to that of a plug flow reactor. The occurrence of recirculating currents within each droplet also results in better mixing.

However, there are also significant drawbacks associated with these reactors. As droplet surface tension weakens in reactors with wider channels, it becomes harder to implement these synthesis methods at larger scales. The flow rates of gas/liquid segmented flow reactors can be difficult to control due to pressure fluctuations within the reactor when changing flow rates. For liquid/liquid phase segmented flow reactors there is potential for accumulation of nanoparticles at the phase interface or phase transfer of reagents between the polar and non-polar phases, this may be desirable for ligand exchange or purification[49] but can pose an issue for nanoparticle synthesis. Additional issues with segmented flow regimes include complications with downstream processing, which are particularly difficult to deal with in telescoped reactor systems as it can be difficult to ensure mixing occurs uniformly downstream without first removing the segmenting medium, this is discussed further in Chapter 3.

Single-phase coiled polymer PTFE and PFA reactors with narrow internal diameters (1/32") have been found to reduce the extent of axial dispersion in studies by Hone[50] and Jensen.[51–53] The extent of axial dispersion (D_s) in a straight pipe was derived by Taylor[54] and later modified by Aris[55] to give equation (2) where D_m is the diffusion coefficient in liquid systems this can be considered negligible due to the small diffusion pathway present in these narrow-channelled reactors, d_t is the tube diameter, u is the mean velocity and k is a coefficient describing the extent of dispersion attributed to the geometry of the reactor.

$$D_s = D_m + k\frac{d_t^2 u^2}{192\, D_m} \tag{2}$$

The value of k is lower for reactors with smaller amounts of dispersion due to their geometry. For example, the coiled reactor tubes used in this project provide flow regimes with an altered parabolic velocity profile due to the formation of Dean vortices caused by centrifugal forces. This increase in radial mixing reduces the extent of dispersion in the reactor, thus creating a flow regime with plug flow characteristics.

1.2.3 Continuous stirred tank reactors (CSTRs)

Mixing in continuous flow reactors can be further enhanced through the incorporation of active mixing, this can be achieved in continuous systems through the use of continuous stirred tank reactors (CSTRs). These reactors have been employed in a range of applications including heterogenous catalysis,[56] biocatalysis[57] and nanoparticle synthesis.[58]

The simplest CSTR design is composed of a batch reactor where reagents are continuously charged into and discharged out of the reactor at a specific rate. This type of CSTR design is problematic, however, as a large portion of the reaction solution leaves the reactor soon after entering. To get around this, multiple batch reactors can be joined in series where the reacting solution flows from one reactor to the next creating a residence time distribution closer to plug flow conditions (Figure 10).

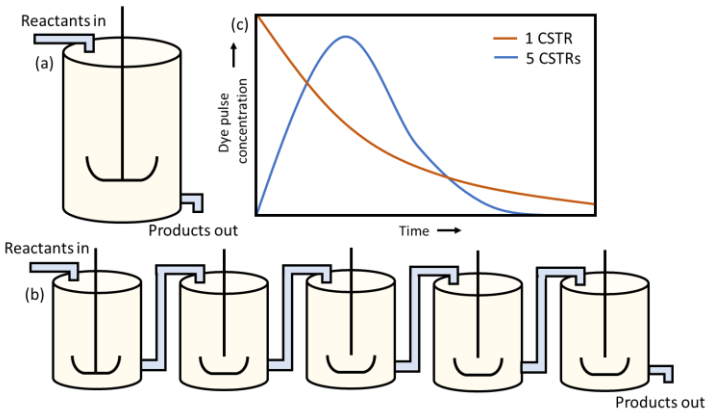

Figure 10. (a) A CSTR composed of one reactor. (b) A CSTR composed of a series of 5 reactors all interconnected. (c) A plot describing the difference in the residence time distributions of 1 CSTR vs 5 CSTRs, if a pulse of low volume high concentration dye was injected into the reactor/s after flushing with and followed by a solvent at a constant flow rate.

In modelled CSTR flow reactors mixing is assumed to be perfect, meaning reactants are instantly dispersed within the reactors upon entering. However, it is important to remember that without consideration during the design of these reactors, mixing may not be instantaneous due to the presence of dead zones, bypass zones and density differences in multiphasic reactions.

1.2.4 Flow control

Precise control over fluid movement is required to maintain a consistent flow regime within these reactors. In self-optimising flow reactors, this is especially important, as flow control governs both residence time and reagent stoichiometry, impacting the reproducibility of reactor conditions.

This flow control can be provided by a variety of different pumps, Table 1 presents a summary of the advantages and disadvantages associated with the main pump types used in continuous flow reactors. Each of the types of pumps below can be controlled with a serial communication interface allowing for integration into automated systems.

Table 1. A summary of the advantages and disadvantages of different pumps used for continuous flow chemistry and references to continuous flow studies employing each pump type.

Pump type and Refs.	**Advantages**	**Disadvantages**
Syringe ([59–61])	- Mechanical components of pump are separate from liquids in contact with the inert syringe - Able to pump at very low flow rates	- Tend to stall when used with reactors under back pressure - Syringes need to be refilled periodically
Piston ([62–64])	- Able to operate at very high pressures - Highly accurate 0.01 mL/min flow resolution	- Easily blocked by small particulates/dust - Cavitation can cause unstable flow profile
Peristaltic ([65,66])	- Able to pump slurries and gases. - Self-priming - Liquids only in contact with cheap/inert tubing material	- Low back pressure tolerance. - Tubing needs to be replaced relatively often - Pulsing flow profile.
Gear ([67,68])	- Highly accurate - Self-priming - Can handle low viscosity liquids	- Easily blocked by solids - Expensive - Components require regular replacement
Mass flow controller ([69,70])	- Can pump either liquid or gas - Not prone to cavitation	- Cannot pump slurries - Requires reservoir/s to be under pressure

1.2.5 Continuous flow reactors for nanoparticle catalyst synthesis

In recent years there has been a large increase in the number of research articles presenting continuous flow reactors for the synthesis of nanoparticles. The simplest flow reactor design for nanoparticle synthesis is a single-phase tubular reactor, Huang and Gavriilidis *et al.* have described such a reactor for the synthesis of AuNPs.[44] In this work the authors used two syringe pumps to separately pump gold precursor ($HAuCl_4$) and trisodium citrate solution into a 2.5 m long tubular reactor, the reactor was submerged in a heated/stirred oil bath and the outlet of the reactor was kept under 2.75 bar pressure to prevent the solution within the reactor from boiling, a diagram showing this reactor setup is shown in Figure 11 below.

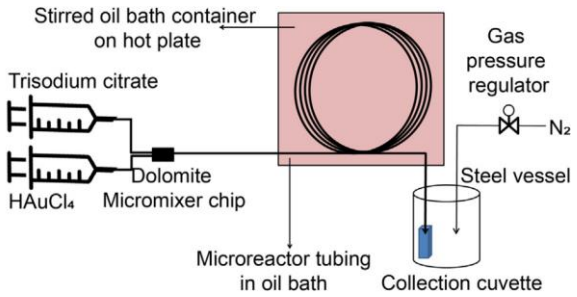

Figure 11. A diagram describing the single-phase reactor design presented by Huang and Gavriilidis et al. (Reproduced with permission from ref.[44] Copyright 2018, Elsevier. All rights reserved).

A variety of experiments were performed using this reactor design investigating the influence of surface area to volume ratio, reactor material, flow rate and temperature on the size and polydispersity of the resulting nanoparticles. Reactors with higher surface area to volume ratios produced smaller nanoparticles on average, this was likely due to reactor fouling, as nanoparticles adhered to the reactor walls increasing the number of nucleation events within the reaction solution. Of the materials tested, fluorinated ethylene propylene (FEP), fused silica, polytetrafluoroethylene (PTFE) and polyether ether ketone (PEEK), little difference in nanoparticle size was observed other than for FEP which produced much larger nanoparticles on average than the rest of the materials tested. However, larger particles were observed among many smaller particles, this may have been caused by larger particles becoming unstuck from the reactor walls. Slower flow rates were found to result in nanoparticle solutions with higher conversion rates, as longer residence times were required for the reaction to reach completion within the reactor. Finally, higher temperatures resulted in the formation of smaller nanoparticles with narrower size distributions as more precursor ions would have the energy required to undergo reduction and nucleation at these temperatures.

More complex single-phase reactors with enhanced mixing characteristics have also been reported. In 2005 Wagner and Köhler presented a reactor consisting of multiple parallel converging and diverging channels which provided a more turbulent flow regime than could be obtained using a conventional tubular reactor (Figure 12).[71]

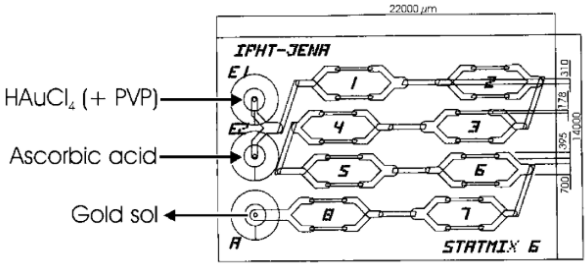

Figure 12. A diagram showing a reactor with multiple converging and diverging streams for enhanced mass transfer. (Reproduced with permission from ref.[71] Copyright 2005, ACS Publications. All rights reserved).

The glass chip reactor was made hydrophobic via silanization with trichloro(1H,1H, 2H,2H-perfluoro-octyl)silane. The reactor produced nanoparticle sizes ranging from 5-50 nm, with significantly less fouling observed in the reactor post silanization.

In 2008 Tsunoyama and Tsukuda *et al.* reported a reactor consisting of 32 parallel channels each with dimensions less than 100 µm (Figure 13).[72] These channels contained separate streams of $HAuCl_4$ and $NaBH_4$ which converged in an alternating fashion mixing upon lamination and compression of the streams. Interestingly using this reactor it was possible to synthesize nanoparticles smaller than particles produced using an equivalent batch process,[15] this was likely due to the highly efficient diffusional mixing within the very narrow reactor channels. The AuNPs produced during this study proved to be effective catalysts for the oxidation of 4-(hydroxymethyl)phenol. These reactors were able to synthesise nanoparticles with reproducible properties, however, the microscale chip reactors used in these studies lack the scalability offered by more conventional tubular reactors.

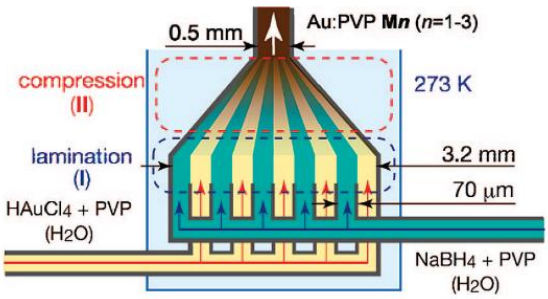

Figure 13. A diagram describing the design of a reactor capable of producing sub-nm sized nanoparticles (Reproduced with permission from ref.[72] Copyright 2008, ACS Publications. All rights reserved).

In 2017 Wu and Torrente-Murciano *et al.* published a paper describing a simple helical tubular rector design for the synthesis of silver nanoparticles (AgNPs) with narrow size distributions.[60] Two years after this publication the same authors published a second paper demonstrating that by separating the nucleation and growth processes of nanoparticle formation AgNPs could be produced with control over nanoparticle size.[73] The reactor for nanoparticle growth consisted of two stages, in the first reactor nanoparticle seed formation took place, these nanoparticles were then pumped into a second reactor with milder conditions which encouraged nanoparticle growth (Figure 14). The size of the nanoparticles was controlled by altering the concentration of precursor added in the second stage of the synthesis process. The degree of nanoparticle growth was monitored by observing the shift in λ_{max} UV-vis absorption to higher wavelengths and confirmed with TEM microscopy to produce nanoparticles with sizes ranging from 5-10 nm ± ~1.5 nm.

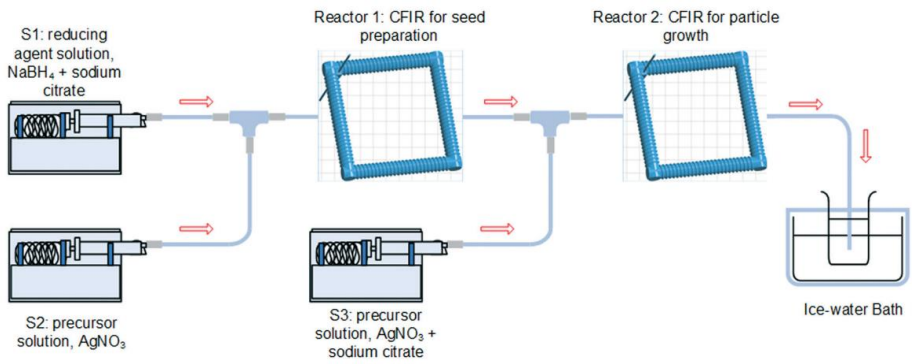

Figure 14. A two-stage single-phase reactor capable of producing AgNPs between 5-10 nm (Reproduced with permission from ref.[32] Copyright 2019, Royal Society of Chemistry. All rights reserved).

Reactor fouling is one of the most significant limitations of nanoparticle synthesis in single-phase continuous flow reactors. This is particularly the case in self-optimising systems as fouling which occurs during previous reactions may detrimentally influence nanoparticle formation in future experiments. Several studies have attempted to minimise fouling using techniques such as coaxial flow,[74,75] ultrasonics[76] and hydrophobic (perfluoro-octyl)silane) reactor wall treatment.[71]

However, one of the more effective techniques for the prevention of reactor fouling is segmented flow. Reactors which adopt this method of synthesis typically premix reaction reagents before a separate immiscible solution is pumped into the flow path to create several discrete reactor droplets.

1.2.5.1 Segmented flow reactors

The reactor shown in Figure 15 is an example of a two-phase segmented flow reactor designed for the synthesis of AuNPs by Panariello and Gavriilidis *et al.*[77] In this reactor citrate capped AuNPs were synthesised using a modified Turkevich method. Aqueous precursor reagents were pumped through a T-piece and pre-mixed in a short coil of tubing before passing through a second T-piece where the precursor mixture was separated by immiscible slugs of heptane. These segmented slugs of reaction mixture were then pumped into a reactor coil submerged in a 90 °C oil bath, here the precursor solutions underwent conversion to nanoparticles. At the end of the reactor, the collection reservoirs were placed under pressure with N_2 gas to provide the reactor with enough back pressure to prevent boiling of the heptane or reaction solution within the heated reactor coil. Finally, the nanoparticles could either be collected for analysis or directed to a waste container using an adjustable valve, this allowed the nanoparticles to be collected for analysis without the need to depressurise the reactor.

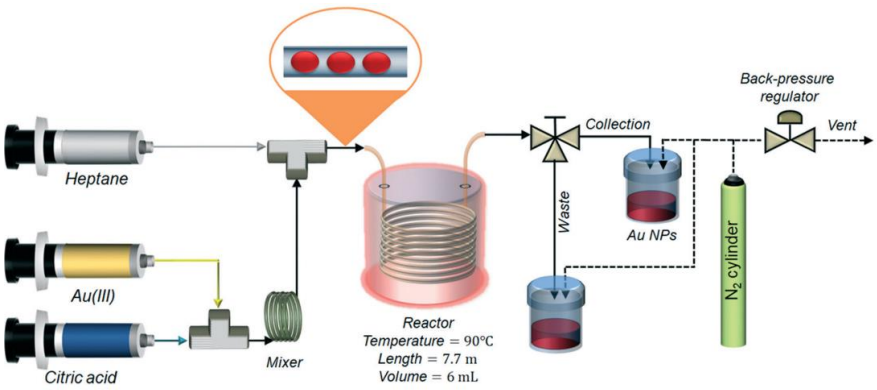

Figure 15. A diagram describing a segmented flow reactor for the synthesis of AuNPs (Reproduced with permission from ref.[77] Copyright 2020, Royal Society of Chemistry. All rights reserved).

The anti-fouling properties of this reactor worked on the principle that the hydrophobic ethylene tetrafluoroethylene (ETFE) reactor walls were preferentially wetted by the hexane segmenting phase. Droplets containing the reaction solution were prevented from touching the reactor walls. The authors found they were able to produce nanoparticles with narrower size distributions than was possible with previous single-phase reactor designs, likely due to nanoparticles being unable to attach, grow and then dislodge from the reactor walls or influence nucleation within the reactor. In addition, as each droplet of reaction solution experienced virtually no dispersion throughout the reactor the residence times for each droplet were extremely narrow leading to further improvements in particle size distribution.

Segmented flow reactor designs have also been used in the synthesis of palladium nanorods. Sebastian and Jensen *et al.* designed a high-pressure/high-temperature segmented flow reactor with air as the segmenting phase (Figure 16).[78] The high-pressure air mixture was used to provide oxygen to the reaction solution for oxidative etching, which the authors propose is a requirement for anisotropic nanoparticle growth. By controlling the reactor temperature and pressure the authors were successfully able to control the shape of the nanoparticles produced.

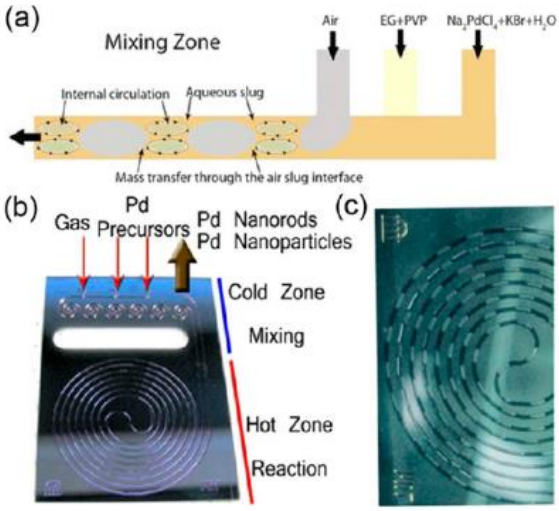

Figure 16. A gas/liquid high-pressure/high-temperature flow reactor for the synthesis of Pd nanorods. (Reproduced with permission from ref.[78] Copyright 2016, Wiley. All rights reserved).

By performing this reaction in a microreactor the authors were able to significantly improve the safety and reproducibility of the synthesis method. The use of air as the segmenting phase also provided the advantages of less waste as no immiscible liquid was required and simplification of the process as there was no requirement for post-process separation.

Although the nanorods produced using this reactor were shown to possess superior catalytic performance compared with an equivalent quantity of conventional carbon-supported palladium catalyst with a turnover frequency (TOF) of 6297 mol mol^{-1} hr^{-1} *vs.* 1542 mol mol^{-1} hr^{-1} respectively. The performance of these palladium nanorod catalysts was still significantly worse when compared with a commercially available $PdCl_2$ catalyst with a TOF of 38220 mol mol^{-1} hr^{-1}.

1.2.5.2 Nanoparticle alloy synthesis in continuous flow

Changing the composition of an alloyed nanoparticle catalyst can also greatly affect catalytic performance, this is discussed in more detail in Chapter 3, including different

types of nanoparticle alloy catalysts and proposed rationale for their superior catalytic performance. Several studies have explored the synthesis of nanoparticle alloys in continuous flow. Two key studies demonstrate the continuous flow synthesis of gold-silver nanoparticle (AuAgNP) alloys. Köhler *et al.* presented one of the first articles proposing such a method for AuAgNP flow synthesis. In this study solutions of $HAuCl_4$ and $AgNO_3$ were injected into a micro reactor along with a solution of ascorbic acid reducing agent and an 'effector solution' containing a PVA polymer capping agent and buffer to modify the properties of the resulting nanoparticles (Figure 17).[79]

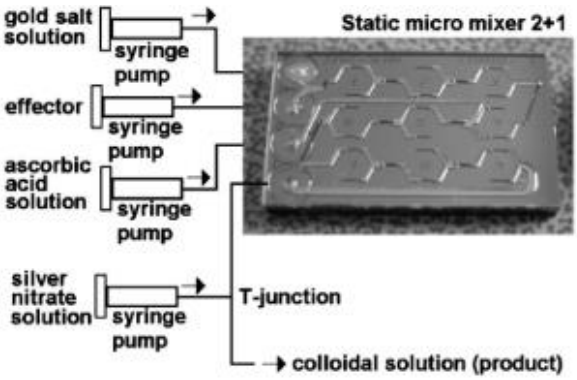

Figure 17. A micro reactor for the continuous flow synthesis of AuAgNP catalyst. (Reproduced with permission from ref.[79] Copyright 2008, Elsevier. All rights reserved).

This study also included a second reactor designed to generate core/shell AuAgNPs in a two-stage process forming AuNP or AuAgNP cores in the first reactor stage, which were later coated with silver in the second reactor forming core/shell nanoparticles. By increasing the concentration of Ag precursor in the second stage of the reactor the size of the nanoparticles could also be increased. This size increase was also accompanied with an increase in size distribution, however, which was likely due to parallel nucleation and growth processes occurring within the second reactor stage.

The AuAgNP catalysts produced during this study were compared in a rhodamine B dye bleaching reaction with a potassium peroxodisulphate bleaching agent. Significant increases in catalytic activity were observed for the AuAg core Ag shell nanoparticles compared with Au core Ag shell nanoparticles.

Knauer and Köhler *et al.* later proposed a segmented flow reactor for the synthesis of similar AuAgNPs.[80] A study by Knauer *et al.* further explored the use of segmented flow reactors for the synthesis of core/shell nanoparticles and core/double-shell AuAgNPs. These nanoparticles were synthesised using the reactor shown in Figure 18.

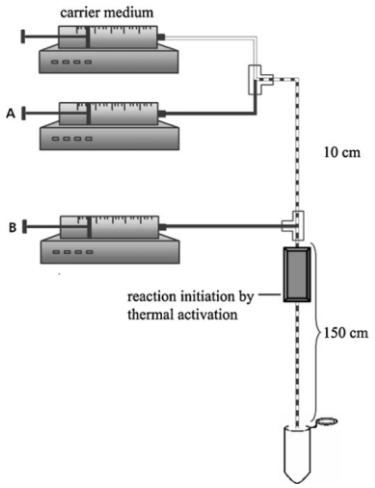

Figure 18. A three-pump reactor setup for segmented flow synthesis of core/shell and core/double/shell AuAgNPs, a solution containing metal precursor, nanoparticle seeds and capping agent was in syringe A was mixed with a tetradecane carrier medium this was mixed with a solution of NaOH downstream before entering a heated reactor. (Reproduced with permission from ref.[80] Copyright 2011, Elsevier. All rights reserved).

Au core Ag shell nanoparticles were formed by adding a batch synthesised AuNP suspension to a solution of $AgNO_3$ with an ascorbic acid reductant and cetyltrimethylammonium bromide (CTAB) capping agent. These were then separated into uniform slugs with a carrier medium (tetradecane) by converging both streams at a T-piece junction, a third syringe was used to add a solution of 11 mM NaOH to the reaction stream at a second T-piece which was heated to 80 °C to initiate the reduction of Ag^+ to Ag^0 on the surface of the AuNPs to form the Au/Ag core/shell nanoparticles. Au/Ag/Au core/double-shell nanoparticles were formed by repeating this procedure but with the newly formed Au/Ag core/shell nanoparticles as the nanoparticle seed solution instead of pure AuNPs and a solution of $HAuCl_4$ instead of $AgNO_3$.

The UV/vis absorption spectra were as expected for the AuNP seeds and the Au/Ag core/shell nanoparticles, however, interestingly the absorption profile for the Au/Ag/Au core/double-shell nanoparticles reached a peak absorption at much higher wavelengths of approximately 650 nm appearing dark blue. To rule out the possibility of particle aggregation the authors also performed TEM analysis of the Au/Ag/Au core/double-shell nanoparticle which showed the nanoparticles as discrete agglomerated particles. Indicating a significant change in the resonance conditions of the nanoparticles demonstrating a wider range of wavelengths can be absorbed by AuAgNPs than previously assumed.

A summary of studies which present methods for the continuous flow synthesis of nanoparticles is presented in Table 2. Due to the vast amount of work conducted so far in this area the table focuses primarily on nanoparticle alloy synthesis.

Table 2. A summary of nanoparticle catalysts and nanoparticle alloys synthesised in continuous flow.

Material	Size (nm)	Structure	Precursor/s	Reductant/s	Solvent	Capping agent	Temp. (° C)	Reactor type	Ref.
PdPt	20-30	Core-shell	$PdCl_2$, H_2Cl_6Pt	Ascorbic acid	H_2O	CTAB	96 °C	Oil bath heated PTFE tubing	81
AuAg	2-5	Intermetallic	$AgNO_3$, $HAuCl_4$	C. Platycladi extract	H_2O	C. Platycladi extract	70 °C	Oil bath heated PTFE tubing	82
PtFeCu/Carbon	1.5-2.1	Intermetallic	H_2PtCl_6, $CuCl_2$, $FeCl_3$	$H_3N.BH_3$	H_2O, Ethylene glycol	Polyethylene glycol	RT	Microchip reactor	83
AuPd/ TiO_2	3-4	Intermetallic	$HAuCl_4$, $PdCl_2$	$NaBH_4$	H_2O	PVA	RT	3D printed helical reactor	84
PdNi	20-30	Hetero-structure	$Ni(ac)_2$, $Pd(ac)_2$	Benzyl Alcohol	Benzyl Alcohol	Oleylamine	204 °C	Microwave heated CSTRs	85
RhAg	3-4	Intermetallic	$RhCl_3$, $AgNO_3$	Ethylene glycol	Ethylene glycol	PVP	120 °C	3D printed mixer / oil bath heated PTFE reactor	86
Au	30-40	Monometallic	$HAuCl_4$	Ascorbic acid	H_2O	PVP	RT	Microchip reactor	71

Material	Size (nm)	Structure	Precursor/s	Reductant/s	Solvent	Capping agent	Temp. (° C)	Reactor type	Ref.
Au/Ag/Au	40-50	Double core shell	$HAuCl_4$, $AgNO_3$	Ascorbic acid	H_2O	CTAB	80 °C	Water bath heated Segmented flow tubular reactor	80
$AuPd/TiO_2$	3-5	Intermetallic	K_2PdCl_4, $HAuCl_4$	$NaBH_4$	H_2O	PVA	RT	PFA tubular reactor	87
PdPtFe/ Al_2O_3	2-3	Intermetallic	H_2PtCl_2, $FeCl_3$, $PdCl_2$	EtOH	EtOH	N/A	500 °C	Stainless-steel high-pressure tubular reactor	88
AuAg	4-7	Core-shell	$HAuCl_4$, $AgNO_3$	Ascorbic acid	H_2O	PVA	RT	Microchip mixer and PTFE tubing	79
Au	8-30	Monometallic	$HAuCl_4$	Sodium citrate/ Citric acid	H_2O	Citrate	90 °C	Oil bath heated PTFE tubing	77
Ag	5-10	Monometallic	$AgNO_3$	$NaBH_4$, Na citrate	H_2O	$NaBH_4$, Citrate	60 °C/ 90 °C	Oil bath heated PTFE tubing	73
Ag	3-7	Monometallic	$HAuCl_4$	$NaBH_4$	H_2O	TTABr	100 °C	microchip reactor	89

1.2.6 Continuous flow analysis

A diverse range of basic analytical instrumentation can be integrated into continuous reactors and used to monitor reactor state, providing information such as temperature, pH, turbidity, pressure and conductivity. These techniques are used heavily in industry to ensure consistency of conditions used during chemical manufacturing; these are often implemented within Proportional, Integral, Derivative (PID) control systems which allow processes to self-adjust when conditions deviate from a desired setpoint. These are useful for maintaining desirable conditions within a rector but fail to reveal any information about the underlying chemical process.

More complex forms of integrated analysis have also been integrated into continuous flow systems for monitoring chemical processes and have enabled the development of self-optimising reactors. Techniques such as high-performance liquid chromatography (HPLC) or gas chromatography (GC) can be used for the quantification of chemical species and work by extracting a small portion of the continuous reaction stream to process offline.[90] HPLC and GC offer high precision and accuracy when quantifying known compounds within a reaction, however, can be time-consuming to implement due to the need for method development and calibration, suffer from poor time resolution and cannot identify unknown species within a reaction.

Online chromatography is therefore often coupled with other techniques such as near-infrared (NIR) spectroscopy and mass spectrometry to allow the elucidation of molecules in real-time.[91] Inline nuclear magnetic resonance (NMR) allows relatively accurate quantification of the components of a reaction as well as the identification of unknown compounds in a reaction.[92] However, the integration of high-resolution NMR spectrometers into flow reactors is costly and impractical for most research groups.

The use of integrated reactor analysis in nanoparticle synthesis is an evolving field, with particle characterisation techniques such as online dynamic light scattering (DLS) beginning to emerge.[93] However, at the time of writing most, if not all, self-optimising reactors for the synthesis of metal nanoparticles have employed UV-vis spectroscopy as their primary means of analysis.[94] Particularly for the optimisation of quantum dot nanoparticle fluorescence and absorbance properties, these systems have employed a range of algorithms and reactor types.[58,95–97] Figure 19 presents an example of such work by Abdel-Latif and Abolhasani *et al.* whereby a segmented stream of quantum dot

nanoparticles was synthesised continuously and monitored using a movable fibreoptic UV-vis absorbance/fluorescence flow cell.[98]

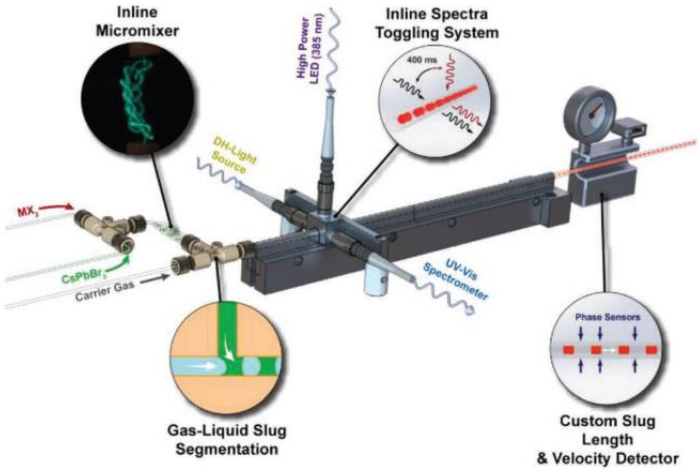

Figure 19. An innovative example of inline UV-vis analysis for nanoparticle analysis. A movable flow cell allows researchers to decouple the effects of reactor flow rate and residence time. (Reproduced with permission from ref.[98] *Copyright 2019,* Wiley & CO. *All rights reserved).*

These studies demonstrate that self-optimising analysis can be effectively used to optimise the optical properties of nanoparticles, however, due to the limitations of the analytical capabilities of these reactors, catalytic nanoparticle properties have not yet been optimised in such systems. Continuous monitoring of the reactions catalysed by nanoparticles is a challenging task, conventional means of reaction monitoring such as online HPLC or GC can be damaged as catalytic particles accumulate or become trapped within the fine channels of these instruments, adversely affecting further analysis.

UV-vis spectroscopy has a multitude of advantages as a quantitative inline analytical technique, the main two advantages are that UV-vis spectroscopy is non-intrusive and continuous, allowing constant monitoring of reactor streams with sub-second resolution. UV-vis absorption spectroscopy is particularly applicable to nanoparticle systems due to the phenomenon of SPR which can change in response to changes in nanoparticle size/shape/composition.[99] The limitations of inline UV-vis spectroscopic analysis however are that overlapping signals make it difficult to differentiate between different chemical species, only a limited range of concentrations can be observed for a set path length and the solutions also need to be transparent.

1.3 Reaction optimisation

The efficiency and profitability of chemical processes are highly dependent on the input conditions used. Many parameters such as temperature, reagent concentration, reaction time and, in the context of this project, nanoparticle catalyst properties can be changed to improve or worsen the outcome of a chemical reaction. Optimising these parameters is a challenging task, as there are an infinite number of reaction conditions under which a reaction can be performed. Optimisation algorithms can reduce the number of experiments required to obtain a satisfactory reaction outcome given the range of conditions available. There is no single approach to optimisation and trial and error is often required to determine the most suitable method for a given application, a systematic approach to selecting the best optimisation method for the improvement of nanoparticle catalysed reactions is discussed in Chapter 4. This section gives a broad overview of various optimisation algorithms which have been adopted by chemists.

1.3.1 One variable at a time (OVAT)

One variable at a time (OVAT) is one of the most common forms of optimisation used by chemists. Using this approach, it is possible to see how changing one variable such as temperature affects how a system responds in terms of a chosen performance indicator, for example, yield, E-factor or cost. Then once the 'optimal' temperature has been found, a second reaction variable such as the reaction catalyst concentration will then be varied at this temperature. This approach is the most intuitive form of optimisation but provides limited insight into the relationships between different variables.

For example, J. Wang *et al.*[100] used an OVAT approach to optimise a heterogeneously catalysed aldol condensation between acetophenone and benzaldehyde over a calcium oxide catalyst to increase yield. They first varied the catalyst loading between 5 and 60 wt. % with 20 wt. % identified as the optimal catalyst loading, yield was monitored keeping all other variables constant. Once the 'best' catalyst loading was found this variable was held constant while the temperature was varied between 30 and 65 °C with the highest temperature of 65 °C found to give the highest yields. Finally, acetophenone/benzaldehyde ratios between 1:1.1 to 1:2.0 were explored, with a ratio of 1:15 giving the highest yields. This led to the conclusion that a reaction with an acetophenone/benzaldehyde ratio of 1:1.5, a 20 wt. % catalyst loading at 65 °C would

give the highest possible reaction yields within this design space, however, this was unlikely to be the case as most of the chemical reaction space was unexplored during these experiments.

The OVAT approach will indicate how different factors influence responses such as yield in the example above, however, in chemical systems a large number of interdependent variables can affect the outcome of a reaction. Therefore, the 'optimum' conditions found through an OVAT approach can often be far from the true optimum. The contour plot shown in Figure 20 describes how the optimal conditions discovered using this approach may vary depending on the chosen starting conditions.

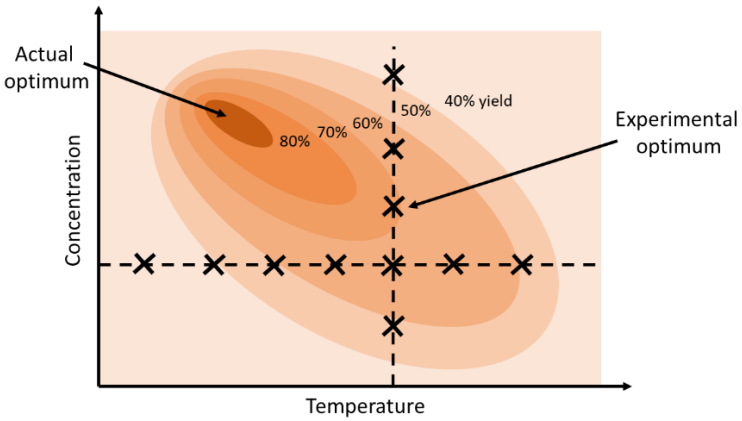

Figure 20. A contour plot to showing how the OVAT approach can miss the true 'optimum'. Optimum conditions found using this technique are likely to be highly dependent on the starting conditions used.

1.3.2 Design of experiment (DoE)

Design of experiment (DoE) is a statistical approach used to determine how various input parameters affect response variables using a minimal number of experiments. The relationships between variables and responses are fitted to, for example linear, quadratic, logarithmic or polynomial mathematical models. DoE also identifies the extent of the synergistic and antagonistic variable interactions present in a design space. The DoE approach is particularly powerful when optimising chemical systems where there is limited understanding of the interactions between reaction variables and responses such as yield and E-factor.[101]

Unlike OVAT where each variable is explored independently, the DoE approach allows the entire experimental design space to be mapped out efficiently using a minimal number of experiments. This is because in each sequential experiment multiple factors are changed simultaneously. These experiments can be arranged differently (design

selection) depending on the number of variables and the number of experiments which are reasonable to carry out.

A commonly used DoE design is a 3-factor central composite design, the 3-dimensional experimental space explored by this design is shown in Figure 21 This allows a good compromise between the exploration of chemical space and the efficient use of resources. This design investigates the upper and lower limits of each factor, intermediate conditions and finally, three or more repeats are taken at the central point, the order of the experiments is also randomised to avoid order bias. The limits of the design space need to be carefully selected so they do not exceed the physical limitations of the reactor material and consider factors such as the solubility/stability of any chemical species in the reaction. Using DoE software such as MODDE, multiple 3D heat maps can be used to convey the interactions between variables in a system.[102]

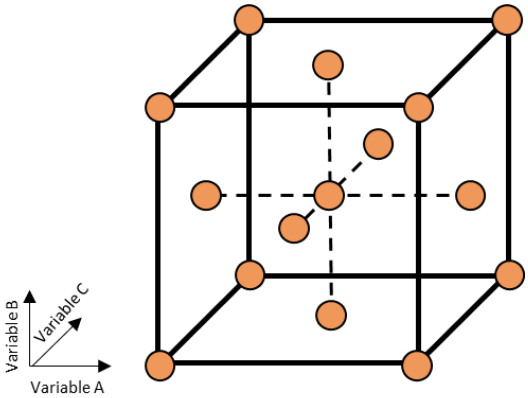

Figure 21. This plot shows the arrangement of experiments within a three-variable design space, each point represents an experiment and the corners of the cube represent the upper and lower limits of the experiment.

DoE is commonly used as an efficient starting point for understanding a chemical design space, it provides a lot of information about a system with only a few experiments, helping to identify which variables are most important. One of the main limitations of DoE arises from the fact that the number of experiments required for a comprehensive DoE study increases exponentially as the number of variables increases. Fractional designs can be used when the number of experiments becomes impractical, however, these can provide misleading data and further experiments may be required to deconvolute any confounded interactions.

With every variable added the number of potential experiments can increase by an order of magnitude. Using the methods discussed so far it would be necessary to carry out an unfeasible number of experiments to fully explore a chemical system with more than

three variables at finitely spaced intervals. Therefore, more efficient self-optimising methods are available which can explore more complex design space with fewer experiments.

1.3.3 Simplex

A simplex is a polyhedral formed from n+1 vertices (where, in the context of the optimisation, n is the number of variables). The Simplex optimisation method was one of the first optimisation algorithms, published in 1962 by Spendley *et al.*[103] Using a 2-dimensional optimisation as a visual example, the Simplex algorithm first performs 3 experiments forming a triangular simplex. The responses for each of the experiments are then ranked from best to worst. The simplex is reflected along the vertex opposite the worst-performing conditions generating a new point, this process is repeated until the optimal conditions are found, see Figure 22. Higher-dimensional space can also be explored using the Simplex algorithm by generating, for example, a 3D polygon with 4 points and 4 sides, the conditions are then reflected away from the worst-performing conditions.

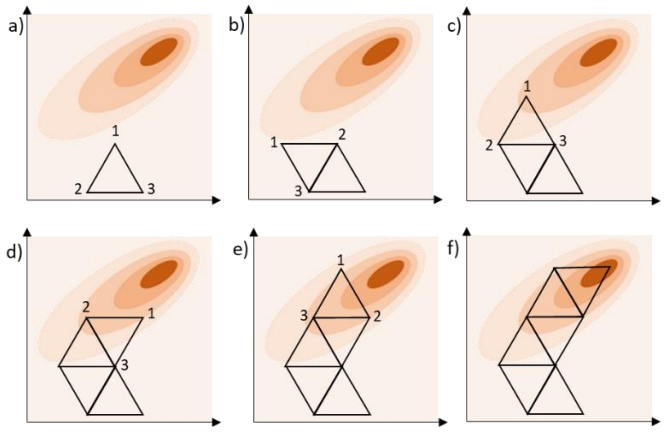

Figure 22. A Simplex optimisation performed on a 2D optimisation problem. An initial 3 experiments are performed generating a simplex with 3 points (a). These are then ranked from highest (1) to lowest (3) with the simplex reflected along vertex opposite the worst-performing conditions, this process is repeated until the optimal conditions are found.

Nelder and Mead later modified the original Simplex method to adaptively contract and expand the reflected polygons both internally and externally, significantly reducing the number of experiments required to reach the optimum conditions.[104] Simplex methods are effective for systems with a single optimum, however, for systems with multiple optima the probability of discovering the optimal conditions is highly dependent on the starting point, these methods also don't include noise handling capabilities.

1.3.4 Genetic algorithms

Genetic algorithms mimic the theory of evolution in nature and fall within the category of global optimisers. Global algorithms can handle experimental noise and escape local optima making them vastly superior to local optimisers for noisy systems with multiple potential optima. Each iteration of a genetic algorithm is comprised of a population of 'individuals', each consisting of a combination of input parameters (genes) and a response. After each iteration, the individuals with the worst responses are removed and the best performing individuals are used to create the next population. The new individuals in the new population can be formed from the surviving individuals from the previous population by one of two mechanisms. Cross-over: where the input parameters from two different well-performing individuals are swapped, and mutation: where one of the input parameters of an individual is changed (Figure 23).[105]

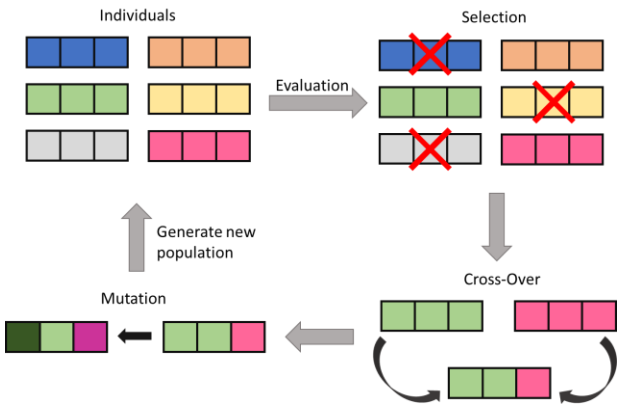

Figure 23. A diagram showing the process of optimisation using genetic algorithms, a population of individuals is evaluated and before the best performing individuals are selected for cross-over and mutation generating a new population.

Recently genetic algorithms were used during the autonomous optimisation of AuNPs and AuAgNPs where the goal was to obtain desirable morphologies such as spheres, nanooctahedrons and nanorods.[99] In this study a custom-built rotational reaction stage was used to house several reactors allowing parallel experiments to be rapidly performed. Ten generations of experiments each with a population of 15 were performed for each type of AuNP synthesis. The positions of multiple peaks within the UV-vis spectra were used to predict changes to the particle shape, this was later confirmed by TEM. For each type of nanoparticle, the observed spectra improved after each generation demonstrating the effectiveness of this type of algorithm.

1.3.5 SNOBFIT

Despite the success of genetic algorithms these algorithms require many experiments to achieve successful results making them unsuitable in some applications. The Stable Noisy Optimisation by Branch and Fit (SNOBFIT) optimisation algorithm is an example of a global optimiser with a more targeted approach, often requiring far fewer experiments to discover optimum conditions while also exploring the entire design space.[106]

SNOBFIT is a derivative-free optimisation algorithm, meaning no gradient information is required for the objective function to be optimised, hence its application in self-optimising reactors. This algorithm generates a disperse set of initial experiments from which it then generates a combination of linear and quadratic surrogate models to predict the optimal conditions. Surrogate models are mathematical approximations of the relationships between variables and responses in a system based on empirical data, these are useful when the exact physical relationships between each of the variables/responses in a system are not well understood. Once a surrogate model has been established, SNOBFIT aims to improve these models while finding the optimal conditions and exploring new experimental design space. Figure 24 presents a flow chart describing the process by which SNOBFIT performs an optimisation.

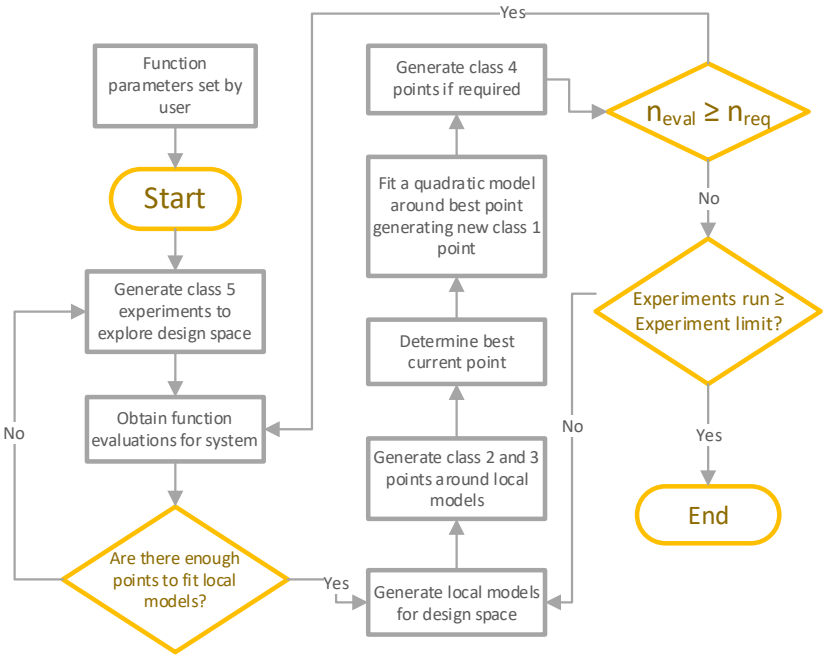

Figure 24. A flow diagram describing the optimisation process for the SNOBFIT algorithm. The experiment is terminated once the experiment limit is reached. N_{eval} is the current number of points for the current iteration of experiments, N_{req} is the number of points required for each iteration.

The algorithm can generate experiments which fall into one of five classifications described below:

- **Class 1:** An experiment performed at the minima of the quadratic model in the current best local optima identified by the algorithm.
- **Class 2:** These experiments are generated around existing local models to improve the accuracy of the optimisation.
- **Class 3:** These points are generated around models which are non-local.
- **Class 4:** These experiments are performed in the regions of chemical space least explored by the algorithm. The probability of generating class 4 experiments can be set by the user depending on the type of system being optimised.
- **Class 5:** These are the experimental conditions generated at the start of the optimisation to build the initial surrogate models, the number of class 5 experiments is dependent on the number of variables.

In the context of nanoparticle synthesis, SNOBFIT was used by S. Krishnadasan *et al.*[97] for the optimisation of fluorescent CdSe quantum dots. These were synthesised by separately injecting solutions of CdO and Se into a continuous microfluidic reactor at different temperatures. The injection rates and reactor temperature were adjusted to yield quantum dots with desirable optical properties. While optimising the properties of the quantum dot nanoparticles in this case it was necessary to reduce the entire emission spectrum from each experiment to a single scalar value. This was accomplished via a process called optimisation by scalarisation where the values for emission intensity with distance from the desired emission wavelength were combined to give a single scalar 'dissatisfaction coefficient', where a value of zero denotes complete satisfaction and one complete dissatisfaction. The system was then able to generate nanoparticles of the highest emission intensity for a range of wavelengths.

SNOBFIT has been a popular choice of algorithm for self-optimising flow reactors due to its proven track record in this area. Other examples of reactions optimised using SNOBFIT include the continuous flow methylation of methyl nicotinate with aqueous methylamine,[107] Claisen-Schmidt condensation between acetone and benzaldehyde,[108] synthesis of EGFR kinase inhibitor AZD9291,[5] synthesis of o-xylene C_{60} adducts[109] and semi-hydrogenation of 2-methyl-3-butyn-2-ol to 2-methyl-3-buten-2-ol.[110]

1.3.6 Bayesian optimisation

Recently Bayesian optimisation has become very popular in the automated optimisation of chemical systems due to its ability to discover optimal conditions with relatively few experiments.[111] This type of derivative-free global optimisation uses a probabilistic surrogate model of the true response surface alongside an acquisition function to decide which experimental conditions to run after each iteration.

Firstly, an initial set of experiments (normally 2n+1 the number of variables) are selected using a stratified sampling method such as a Latin hypercube (LHC) design .[112] These sampling methods can be superior to random sampling as they ensure an even spread of sample points across all potential values. The results of the initial experiments are then used to build a surrogate model. Once the initial surrogate model is in place an acquisition function calculates the areas where the surrogate model predicts the best conditions and areas of greatest uncertainty. The objective of the acquisition function is to select the conditions which both improve the accuracy of the model by reducing the amount of uncertainty (exploration) and discover the optimal conditions (exploitation).[113] The trade-off between exploration and exploitation can be user adjusted before optimisation, a description of this process is shown in Figure 25.

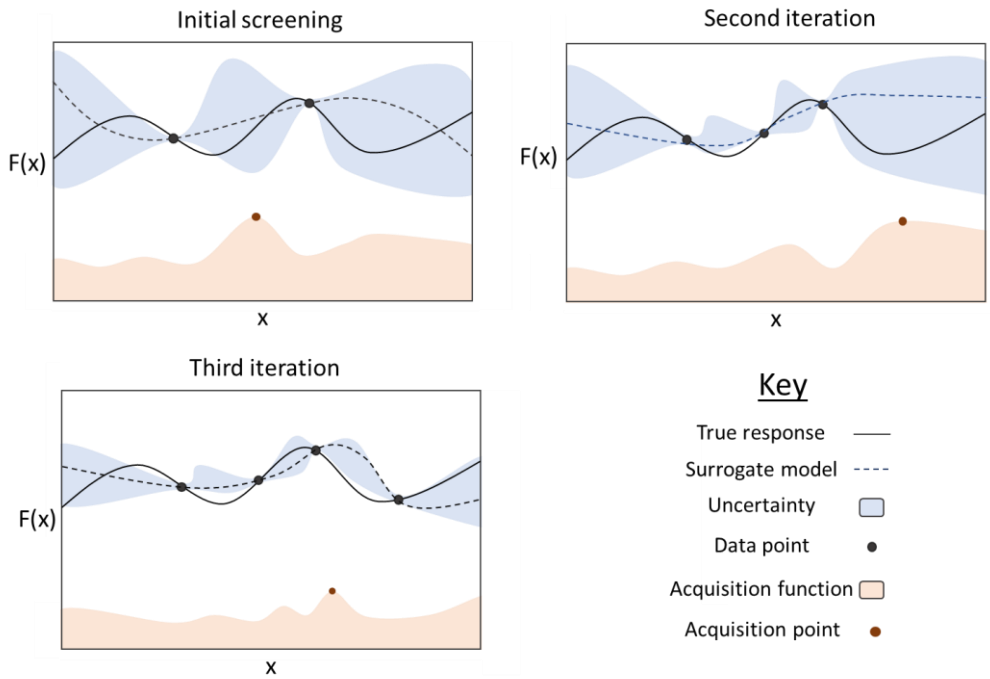

Figure 25. Bayesian optimisation of an arbitrary function. The true response (solid black line) is predicted by the surrogate model (dashed line), the acquisition function (orange) calculates the trade-off between exploration and exploitation to find the points (brown/black dots) where both the model fit can be improved while also discovering the optimum.

1.3.7 Multi-objective optimisation

The algorithms discussed so far fall into the category of single objective optimisers. In chemical manufacturing, it is often important to consider multiple competing economic and environmental factors. Whereas synthesis chemists will often focus on product yield and purity, process chemists/engineers will also be concerned about reaction efficiency in terms of, for example, the time required for the reaction to complete, the cost of reagents/waste and the amount of energy required to heat, cool and mix a reaction.

Often, when attempting to optimise multiple objectives it becomes apparent that some objectives cannot be improved without adversely affecting other aspects of the reaction, as conflicting process metrics can be located in different areas of design space. One solution to this problem is to merge multiple objectives into a single objective.[114] However, this results in the discovery of one of many potential optima excluding other valid solutions.

The Pareto front (Figure 26) is a set of non-dominated optimisation solutions to multiple competing objectives which cannot be improved without detrimentally affecting other reaction metrics. Some algorithms, for example, genetic algorithms can be modified to perform multi-objective optimisations by favouring solutions which fall closer to the Pareto front, however, this approach requires many experiments.

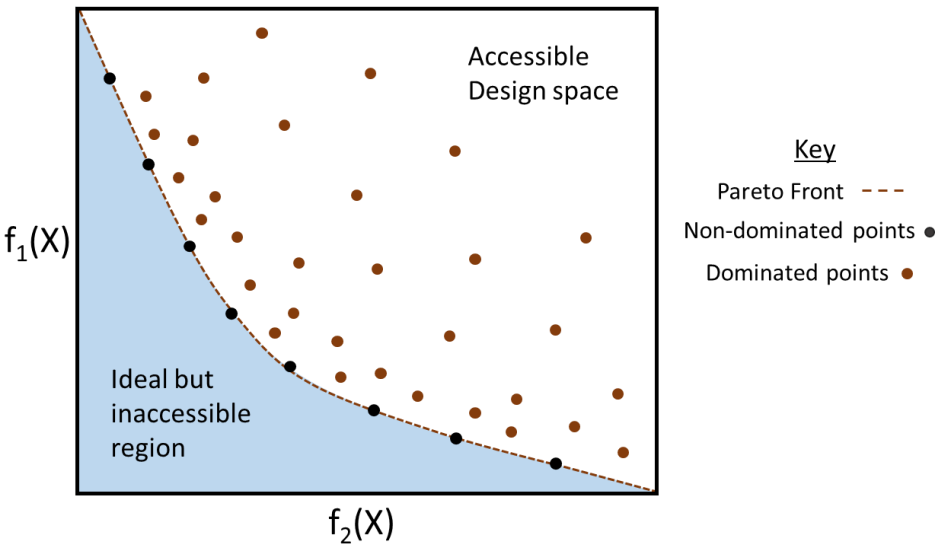

Figure 26. A diagram describing the Pareto front for an arbitrary minimisation problem where $f_1(X)$ and $f_2(X)$ are two conflicting objectives. No points can access the region beyond the Pareto front which consists of a set of non-dominated solutions.

Nanoparticle catalysts are only used in small amounts but as they are often composed of precious metals, it is desirable to optimise these catalysts in as few experiments as possible. The Thompson Sampling Efficient Multi-Objective (TSEMO) algorithm has recently been used able to identify the trade-off between Space-Time Yield (STY) and conversion in a palladium catalysed Sonogashira reaction with only 100 optimisation experiments in under 13 hours.[115]

The TSEMO algorithm first builds a surrogate model of the design space using data points obtained with a stratified sampling method such as a LHC design, analogous to the first stage of Bayesian optimisation. The next stage of the TSEMO optimisation is relatively computationally demanding, as the algorithm uses genetic algorithms to generate over 4000 possible Gaussian process (GP) functions to find a surrogate model which best fits the experimental data. The location of the Pareto front is predicted based on the best fitting surrogate model and a set of candidate experiments are generated along this front. These experiments are then ranked from best to worst in terms of expected hypervolume improvement, which is the volume between the current set of non-dominated points and a reference point set far away from the Pareto front. The highest-ranking experiment is then performed and the process is repeated ensuring an even spread of points along the Pareto front is obtained upon termination of the algorithm, see Figure 27.[116]

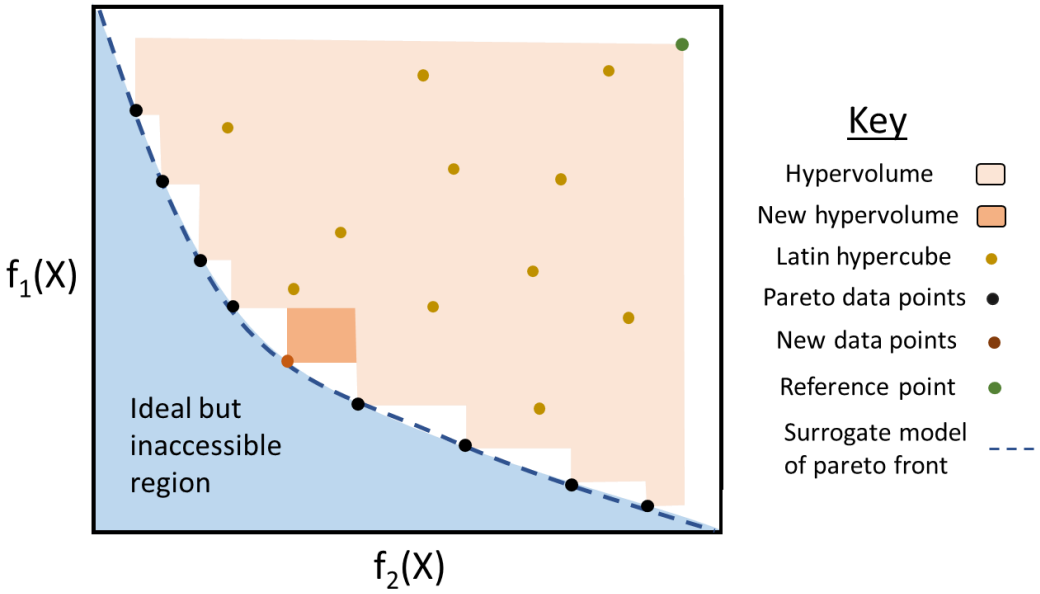

Figure 27. A hypothticlal plot demonstrating the process by which the TSEMO algorithm performs a multi-objective optimisation. A set of candidate experiments generated along a predicted Pareto front, the experiment that archives the greatest increase in hypervolume is selected for the next experiment by the algorithm.

1.4 Project aims and objectives

This project aims to streamline the process of nanoparticle catalyst and nanoparticle catalysed reaction optimisation, using a two-stage performance directed continuous flow self-optimising system. This system will synthesise nanoparticles in stage one of the reactor, altering their composition in a controlled manner, the nanoparticles will then be pumped directly into a second reactor to observe how they perform in a reaction. This process will be repeated iteratively with the aid of optimisation algorithms, which will tune the catalysts produced in the first stage of the reactor based on their catalytic activity in the second stage of the reactor.

This approach differs from other approaches as it allows completely autonomous optimisation and comparison of catalytic nanoparticles without the need for reaction benchmarking in offline experiments. Once the conditions which produce the most active catalyst have been found, the nanoparticle stream can be collected and analysed using a suite of characterisation techniques to fully understand the structure/performance relationship of the materials generated during the optimisation. Figure 28 shows a flow diagram describing how each chapter of this thesis fits into the broad aim of this project to study homogenous nanoparticle catalysts in a 2-stage self-optimising reactor system.

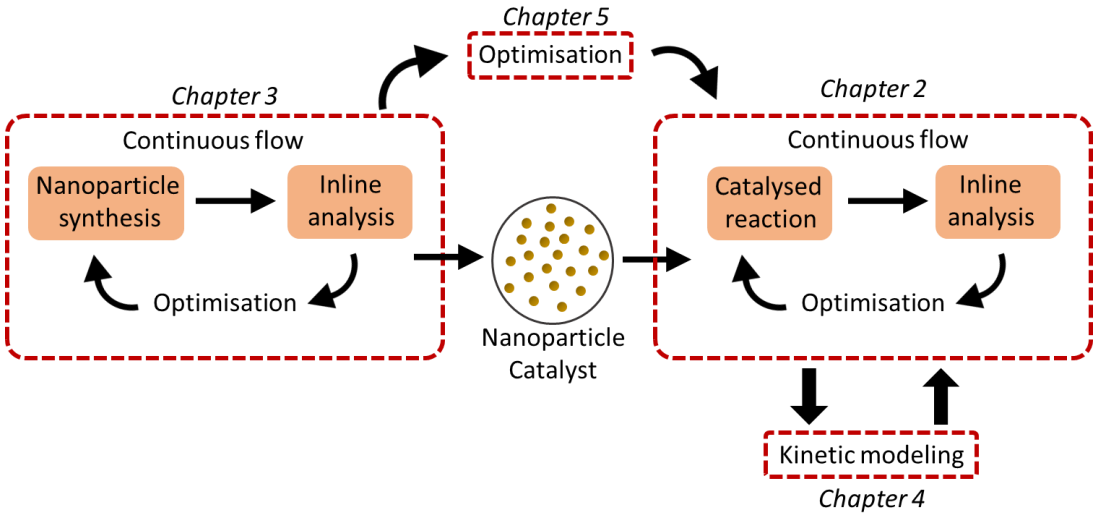

Figure 28. Flow diagram showing how individual aims contribute towards end goal of a fully integrated tandem reactor design for nanoparticle catalyst optimisation.

This project's aim will be achieved upon completion of the 4 parts covered in chapters 2-5 of this thesis:

- Chapter 2: A nanoparticle catalysed reaction will be optimised in continuous flow with gold nanoparticles synthesised in batch. The nanoparticles will be pumped into the continuous reactor from a storage reservoir. This work will show for the first time that nanoparticle catalysed reactions can be optimised in a self-optimising flow reactor.
- Chapter 3: A reactor capable of producing nanoparticles with tuneable properties will be developed. Focusing on the synthesis of bimetallic nanoparticle alloys. The nanoparticles will be monitored using inline UV-vis spectroscopy to confirm the consistency and composition of the nanoparticles.
- Chapter 4: A kinetic model will be developed based on data obtained during stage 1 of the project. The kinetic model will allow the simulation of a nanoparticle catalysed reaction. The simulated nanoparticle catalysed reactions will then be used to benchmark several different optimisation algorithms.
- Chapter 5: The reactors developed in stages 1 and 2 will be combined to create a fully autonomous multistage reactor capable of nanoparticle catalyst optimisation.

Chapter 2

Autonomous optimisation of a nanoparticle catalysed reduction reaction in continuous flow

In this chapter an automated continuous flow reactor system, equipped with inline analysis, was developed for the closed-loop optimisation of a nanoparticle catalysed reaction. The system was used to optimise the conditions of a gold nanoparticle catalysed nitrophenol reduction reaction, towards maximum conversion. The data obtained from this optimisation was then used to generate a kinetic model of the reaction, enabling the prediction of reaction outcomes under different experimental conditions, a graphical summary of the approach is shown in Figure 29. In combination with methods for the continuous flow synthesis of nanoparticles, this approach could significantly accelerate the development timeline for nanoparticles in catalytic applications.

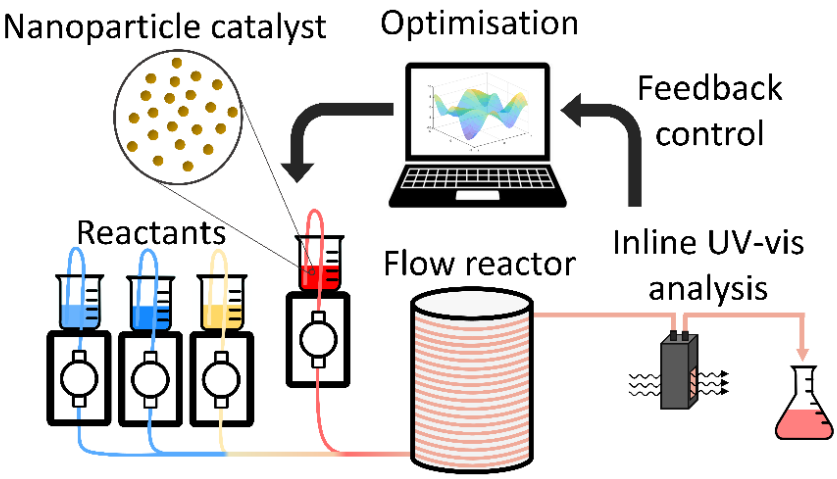

Figure 29. A graphical abstract depicting the approach developed to perform the automated optimisation of a gold nanoparticle catalysed nitrophenol reaction.

2.1 The reduction of nitrophenol

Reduction of nitroarenes to their corresponding amines is one of the most important transformations in fine chemical/pharmaceutical manufacturing,[117] the process of converting nitrobenzene to aniline in Europe alone, takes place on a 500,000 ton per annum scale.[118] The aqueous solution-based nanoparticle catalysed reduction of nitrophenol with $NaBH_4$ reducing agent (Scheme 1) in particular, is a prevalent reaction within the literature.[119–121] As a result, this reaction is commonly used as a benchmark to compare the catalytic activity of different nanoparticle catalysts.[122]

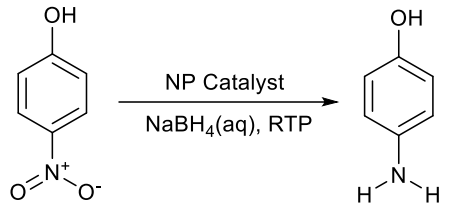

Scheme 1. The nanoparticle catalysed reduction of 4-nitrophenol to 4-aminophenol with $NaBH_4$ under room temperature conditions.

The reduction of nitrophenol was first identified as a suitable reaction for the comparison of nanoparticle catalysts by Pal *et al.*,[123] where it was used to compare the catalytic performance of different silver nanoparticle catalysts. In this study, the authors found that the reaction followed pseudo-first-order kinetics when an excess of $NaBH_4$ is used and that no change in nanoparticle size/structure was observed after the reaction.

The reaction, which occurs on the surface of metal nanoparticle catalysts, can be performed under room temperature conditions and monitored with UV-vis spectroscopy. The UV-vis spectrometer used in this project comprised of a CCD (Charge-coupled device) detector array, a tungsten/deuterium light source, fibre optic cables. The reaction media was pumped through a 1 cm path length flow cuvette (CVF-Q-10) in a flow cuvette holder, all supplied by OceanOptics™, see section 7.1.2.5 for further details. This type of flow cell was chosen as it gave a cleaner absorption spectra than alternative flow configurations e.g., shining the light directly through the tubing or using a z-flow cell configuration.

The UV-vis detector assembly contained an arrangement of mirrors which reflected broad-spectrum light onto a diffraction grating, which split the incoming light into its constituent wavelengths along a linear array CCD sensor array, so each sensor pixel corresponded to a specific wavelength, a diagram of this setup is shown in Figure 30.

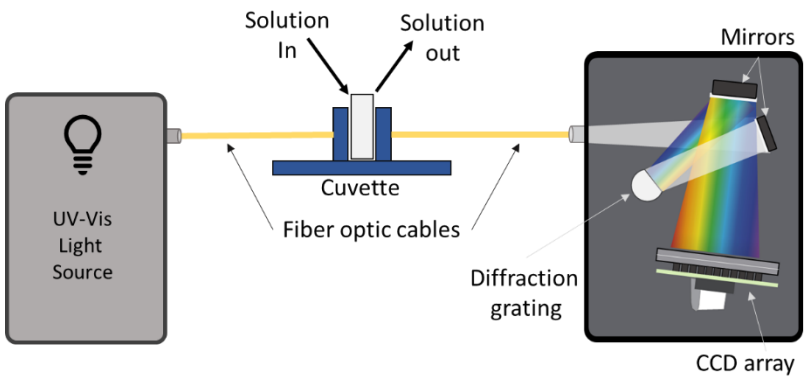

Figure 30. A schematic of the view inside the commercially available OceanOptics™ spectrometer assembly used in this work.[124]

The slightly basic conditions, resulting from the dissociation of sodium borohydride in an aqueous solution results in deprotonation of 4-nitrophenol to 4-nitrophenolate, which absorbs light strongly between 350 and 450 nm. The corresponding reduction product 4-aminophenol absorbs light in a lower wavelength region. Therefore, the conversion of nitrophenol to aminophenol can be accurately monitored with UV-vis spectroscopy. Figure 31 shows a typical set of transient UV-vis absorption spectra collected over time during a gold nanoparticle catalysed nitrophenol reduction reaction, see section 7.1.5.1 for method.

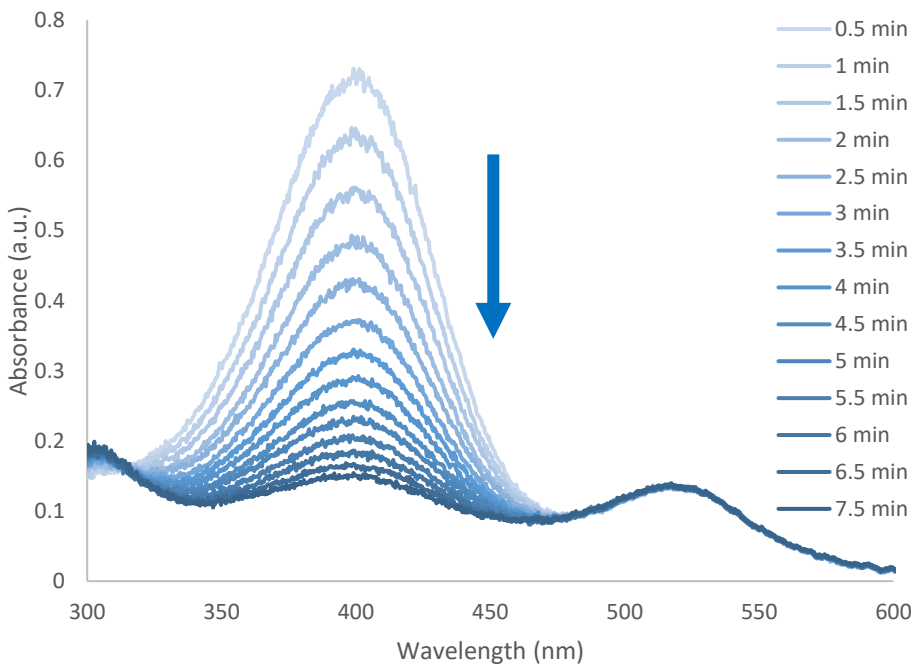

Figure 31. A scanning kinetics plot for the reduction of 4-nitrophenol with sodium borohydride in the presence of AuNPs over 7.5 minutes.

2.1.1 HPLC investigation NP catalysed nitrophenol reduction

To confirm aminophenol was the sole product of the nitrophenol reduction reaction in this study, a batch experiment was performed and analysed with HPLC, see sections 7.1.2.1 and 7.1.2.2 for method. First a calibration was performed with analytical grade nitrophenol and aminophenol, for method see section 7.1.1.

The calibration curves are shown in Figures 32 and 33. For aminophenol a calibration gradient of 389 was measured with an R^2 value of 0.999 and a retention time of 3.34 min. A calibration gradient of 2375 was measured for nitrophenol with an R^2 value of 0.999 and a retention time of 10.17 min.

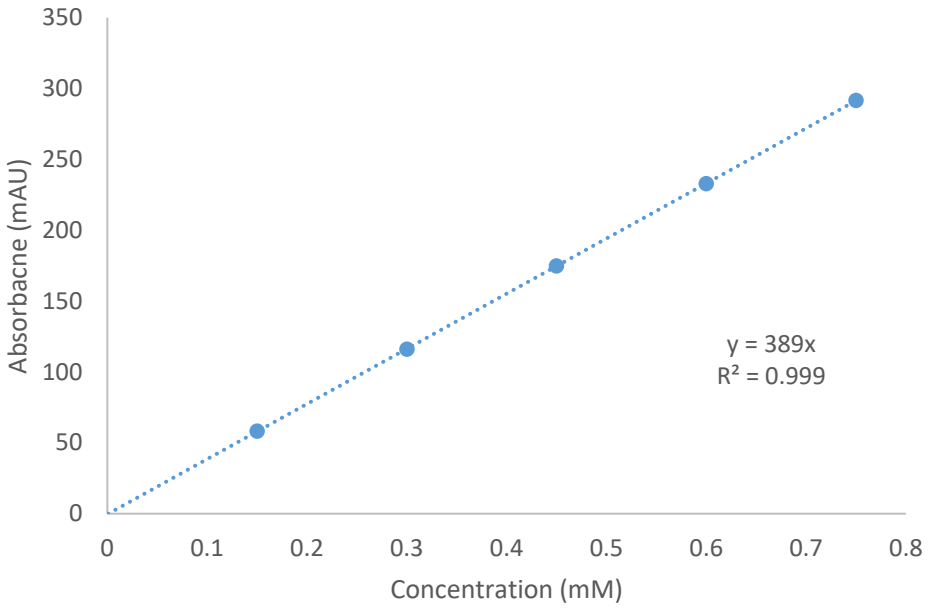

Figure 32. Aminophenol calibration, gradient: 389, R^2: 0.999.

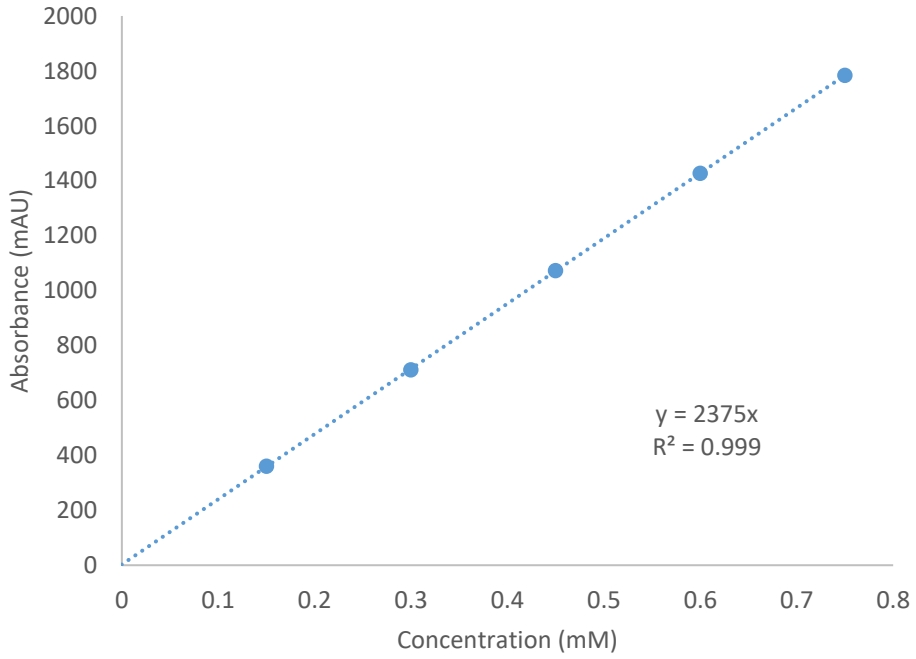

Figure 33. Nitrophenol calibration, gradient: 2375, R^2: 0.999.

Based on the HPLC analysis of the reaction mixture before reducing agent was added (Figure 34), the theoretical maximum concentration that could be achieved during the reaction was 0.57 mM. A final solution concentration of 0.55 mM of aminophenol was measured by HPLC after the reduction reaction (Figure 35), which corresponds to a 98% yield, with no other peaks observed in the HPLC chromatograph.

2.1.1.1 HPLC before reduction (Nitrophenol only)

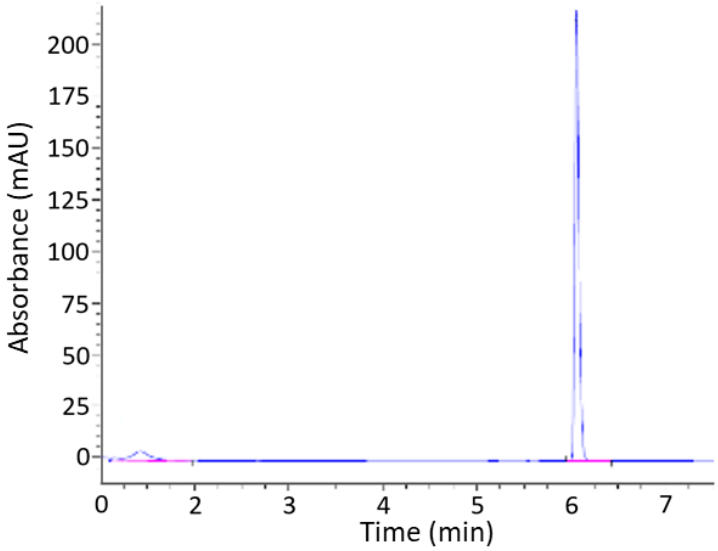

Figure 34. The HPLC chromatograph for the reaction solution before the reduction reaction, nitrophenol was detected at 10.12 minutes (273 nm) with a peak area of 1348 (0.57 mM).

2.1.1.2 HPLC after reduction (Aminophenol only 98% yield)

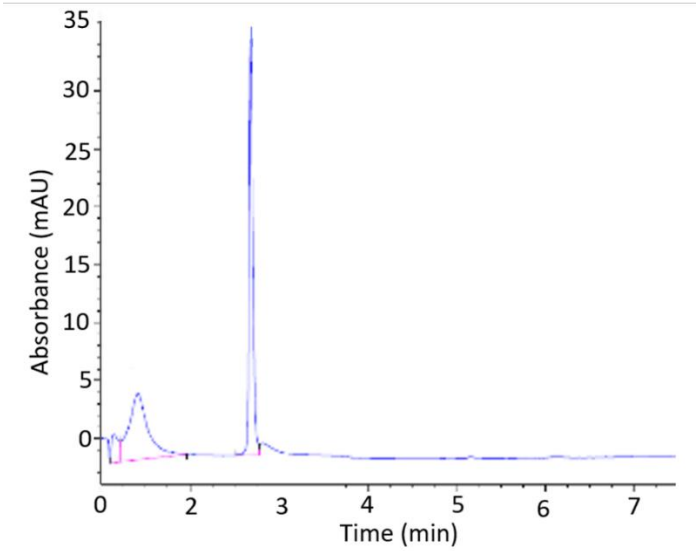

Figure 35. The HPLC chromatograph for the reaction mixture after the reduction reaction, aminophenol was detected at 3.37 min (273 nm) with a peak area of 213 (0.55 mM).

2.2 Gold nanoparticle catalyst

In this chapter the objective was to demonstrate that nanoparticle catalysed reactions can be explored in a continuous flow self-optimising system. Gold nanoparticles were synthesised in batch and pumped through the reactor under different conditions. The method used to synthesise these nanoparticles was later developed for continuous flow in Chapter 3.

The AuNP catalysts were synthesised using a standard Turkevich protocol adapted from N.G. Bastus *et. al.* [17] confirmed by TEM to be 15.8 ± 5.6 nm in size, see Figure 36, all TEM micrographs can be found in Appendix sections 8.1.1 and 8.1.2.

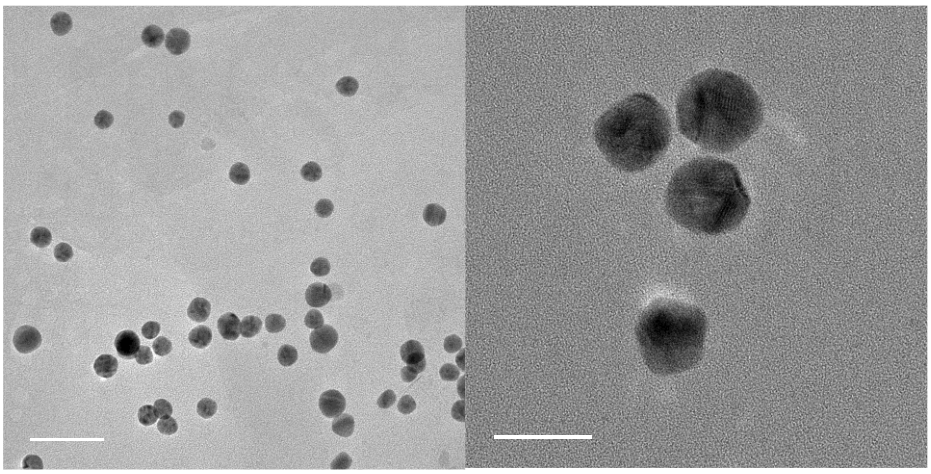

Figure 36. TEM micrographs of AuNPs synthesised using the method described in section 7.1.1.1.

This method was chosen as it produces stable, quasi-spherical nanoparticles with a high degree of monodispersity. The nanoparticles were also citrate-stabilized; a loosely bound citrate capping layer prevented agglomeration while allowing reaction species to easily access the surface of the nanoparticle for catalysis.

Control experiments were carried out to confirm that no significant changes to the nanoparticle size, shape and/or oxidation state occurred during the reduction of nitrophenol reaction. TEM and XPS analysis were performed on AuNPs synthesised using the protocol outlined in Section 7.1.1.1 both before and after they were used to catalyse the reduction of nitrophenol reaction described in Section 7.1.5.2.

2.2.1 TEM particle size distributions (before/after reaction)

TEM analysis of the AuNPs was performed before and after the nanoparticles were used to catalyse the reduction of nitrophenol to aminophenol. The resulting micrographs (see sections 8.1.1 and 8.1.2) confirmed the shape of the nanoparticles remained quasi-spherical even after they were used as catalysts. The size distribution plots are shown in Figure 37 (before catalysis) and Figure 38 (after catalysis) confirm there was no measurable change to the size of the nanoparticles during the reduction reaction.

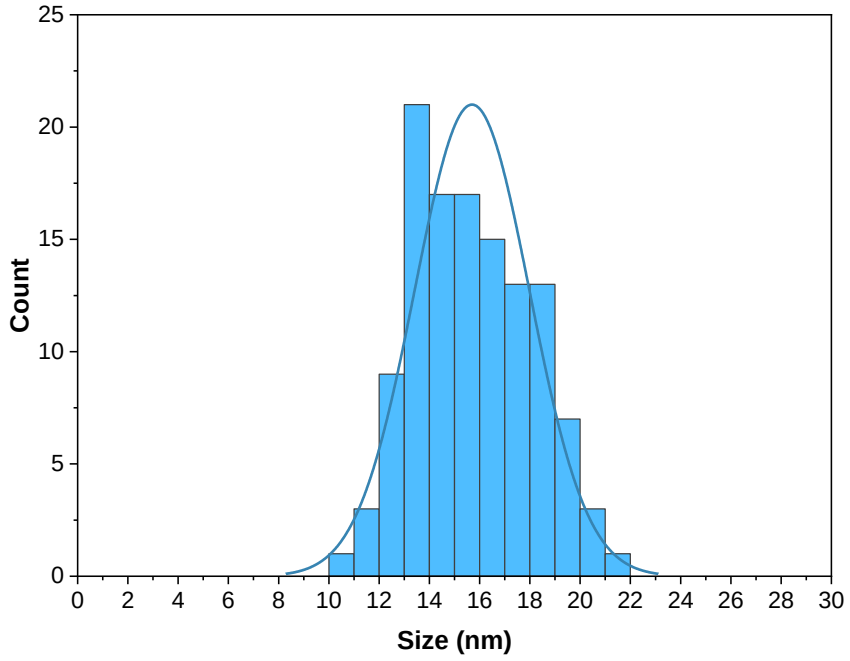

Figure 37. Size distribution histogram for 120 manually sized AuNPs taken before they were used to catalyse the reduction of nitrophenol (15.7 ± 5.5 nm) from TEM micrographs shown in Section 8.1.1.

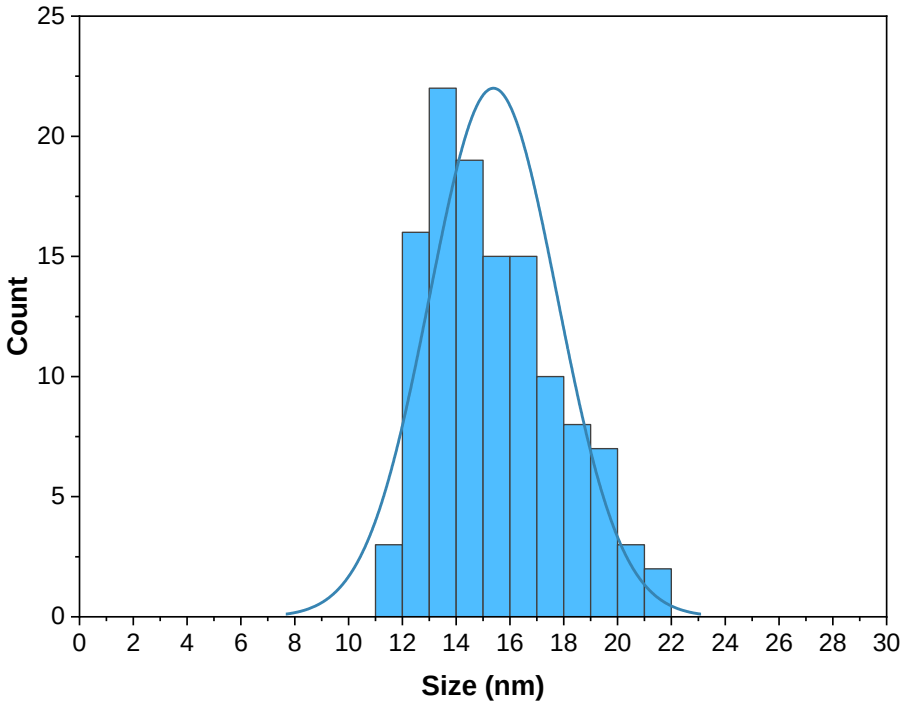

Figure 38. Size distribution histogram for 120 manually sized AuNPs taken after the nanoparticles were used to catalyse the reduction of nitrophenol (15.4 ± 5.9 nm) from TEM micrographs shown in Section 8.1.2.

2.2.2 X-ray photoelectron spectroscopy (XPS)

XPS survey measurements of the AuNPs before and after catalysis confirmed the presence of metallic gold in both samples, as indicated by the prominent Au 4d and Au 4f peaks (Figure 39 A and B). Both samples also showed pronounced XPS peaks for

carbon and oxygen, confirming the presence of organic capping agents (citrate) at the nanoparticle surfaces. Trace amounts of Na and Cl were observed in the XPS survey spectra, indicating minor residues of sodium chloride (a by-product of the Au nanoparticle synthesis) in the samples.

The Au 4f high-resolution XPS spectra of both samples show the typical gold peaks at 84.2 eV and 87.9 eV, assignable to the Au $4f_{7/2}$ and Au $4f_{5/2}$ spin-orbit splitting, respectively (Figure 39 (C)). For both samples, the symmetric nature and the characteristic position of both peaks indicate that gold is only present in its metallic state. It is well-known that the gold $4f_{7/2}$ peak for Au(0) has a characteristic binding energy of 84.2 eV, as observed here for both samples.[125,126] Further, the presence of Au(I) and Au(III) can be excluded as this would give rise to clear distortion of the peak symmetries and large shifts in characteristic binding energy for the Au $4f_{7/2}$ peak to 85.6 eV and 86.5 eV, respectively.[127]

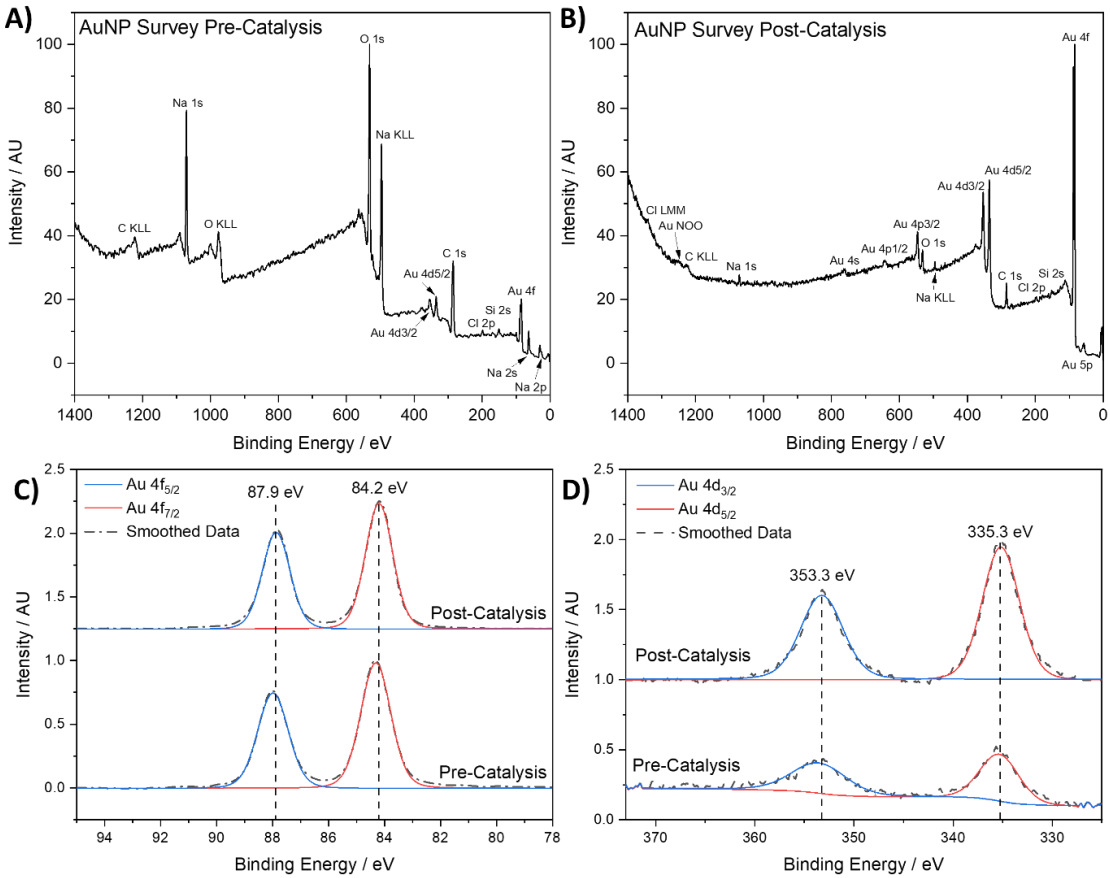

Figure 39. XPS spectra of AuNPs, A) survey spectrum for AuNPs pre-catalysis, B) survey spectrum for AuNPs post-catalysis, C) high-resolution Au 4f spectra before and after catalysis, and D) high-resolution Au 4d spectra before and after catalysis.

Comparing the high-resolution peaks of pre- and post-catalysis samples, no significant changes in peak position or peak symmetry were observed for the Au 4f and Au 4d high-resolution spectra (Table 3). These XPS findings indicate that no permanent change in Au oxidation was induced during the reaction, with the active nanoparticle surface atoms remaining in their metallic Au(0) state even after prolonged reaction times.

Table 3. A table showing the deconvoluted peak positions for the Au 4f and Au 4d high-resolution XPS spectra before and after catalysis.

Peak	Peak Position / eV	
	Pre-catalysis	Post-catalysis
Au $4f_{7/2}$	84.3	84.2
Au $4f_{5/2}$	88.0	87.9
Au $4d_{5/2}$	335.3	335.2
Au $4d_{3/2}$	353.3	353.2

2.2.3 UV-vis analysis

Figure 40 shows the UV-vis spectra corresponding to the AuNPs synthesised using the method described in section 7.1.1.1. The absorption profile is non-symmetric and peaks at 530 nm, N.B. the AuNPs absorb light in the same UV-vis region as nitrophenol. The steps taken to remove the Au spectra from the convoluted profiles are described in section 2.3.3.

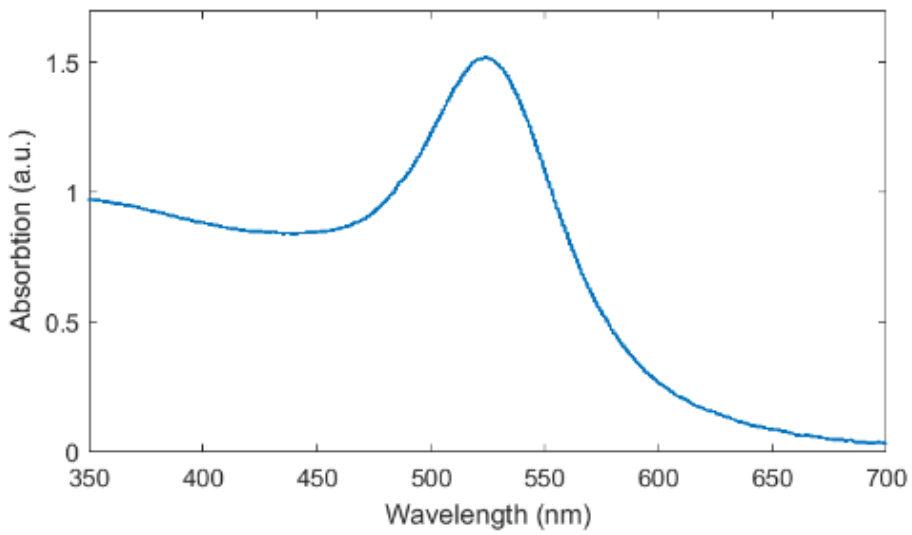

Figure 40. UV-vis spectra of AuNPs synthesised in the study, peak absorption occurs at 530 nm.

2.2.4 DLS analysis

After confirming the nanoparticles remained the same size before and after they were used to catalyse the reduction of nitrophenol. DLS analysis was used to further characterise the size of the nanoparticles synthesised in section 7.1.1.1. The size distribution profiles by intensity, volume and number are shown in Figure 41. The recorded Z-average diameter was 25.74 nm with a standard deviation of 16.05 nm, (count rate: 160.7 kcps and polydispersity index: 0.210).

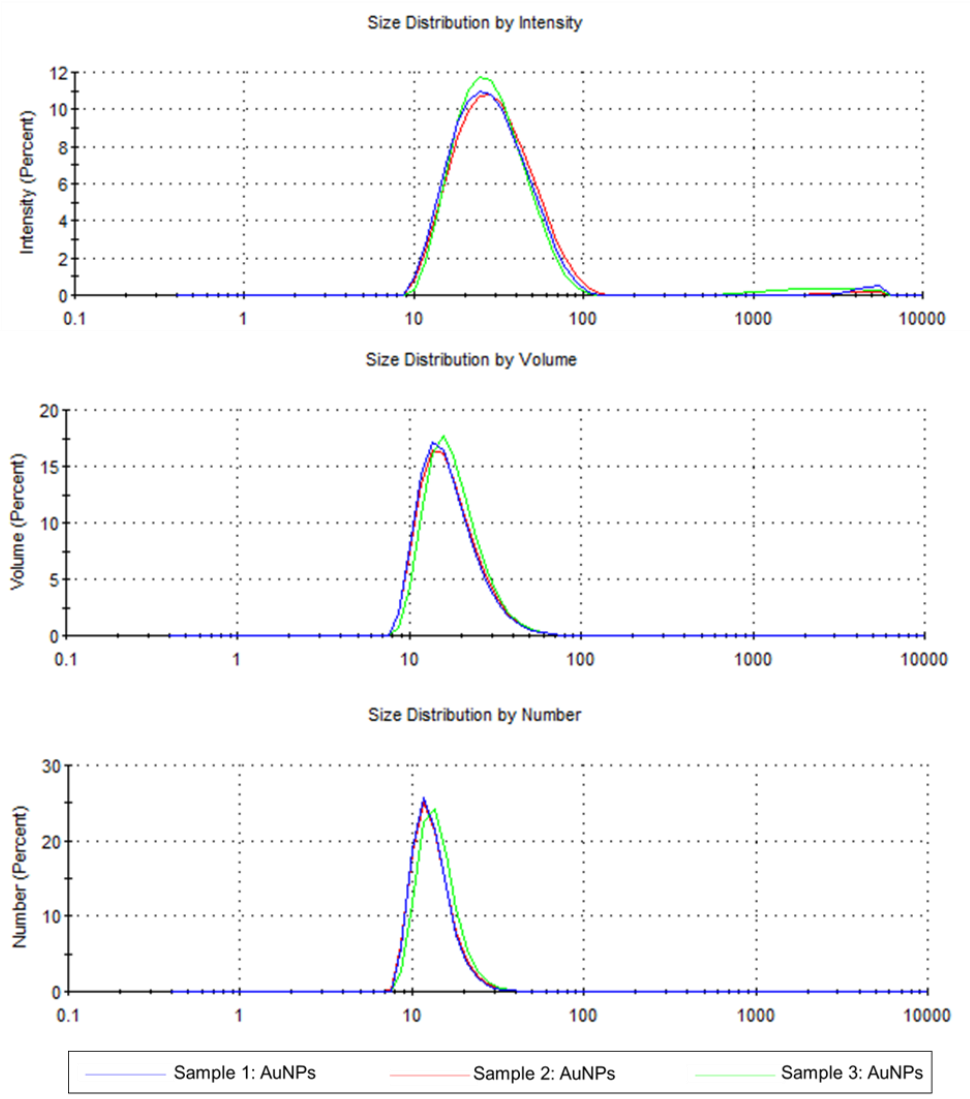

Figure 41. DLS analysis of the AuNP solution prepared using the method described in 7.1.1.1, with plots showing the size distribution by percent intensity (top), volume (middle) and number (bottom).

2.2.5 Nanoparticle surface area calculation

The active surface area of the Au nanoparticles (S) was calculated using a geometric approximation which assumed that all the gold nanoparticles (AuNPs) were the same

size, with a 'spherical', FCC structure, see equation (3). Where r was the average AuNP radius (7.85 nm, determined by TEM analysis, see section 2.2.1), C_{Au} was the concentration of Au atoms in a given reaction and a is the FCC unit cell length for bulk Au (0.407 nm), where each unit cell contains 4 atoms.[128] The number of atoms contained within each AuNP was calculated by dividing the nanoparticle volume by the unit cell volume and multiplying by 4. Dividing Avogadro's constant (N_A) by the average number of atoms contained within each AuNP gives the number of nanoparticles per mol of Au atoms, multiplying this value by the nanoparticle surface area gives a correlation constant with the units ($m^2\ mol^{-1}$). This constant was multiplied by the concentration of Au atoms in the reaction to give S for each reaction ($m^2\ L^{-1}$).

$$S = \frac{N_A}{\left(\left(\frac{\frac{4}{3}\pi r^3}{a^3}\right)\cdot 4\right)} C_{Au} 4\,\pi\, r^2 \tag{3}$$

2.3 Inline reaction monitoring

Inline UV-vis spectroscopy was used to determine the concentration of nitrophenol at the outlet of the reactor. This was beneficial as it allowed for real-time monitoring (one reading per second) of reagent concentrations, see Figure 42. It was therefore possible to constantly monitor the system for issues such as pump failure and ensure efficient use of the reactor by allowing accurate determination of the point at which steady-state had been reached.

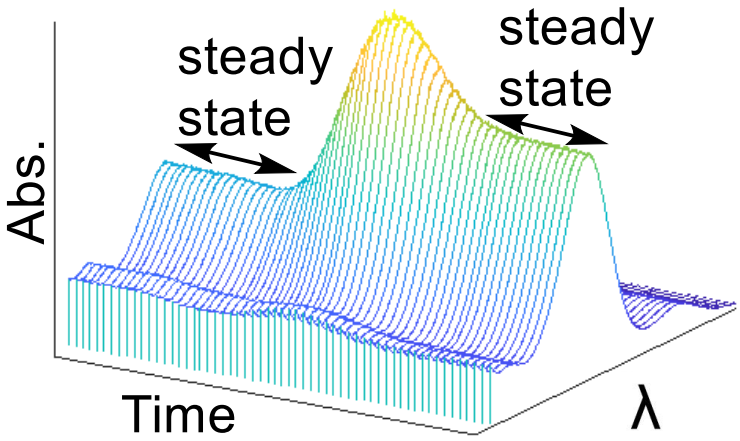

Figure 42. A 3D plot showing how the absorption at the reactor outlet changes as the reaction conditions are changed in flow, the difference between transient and steady-state conditions can be observed in real-time.

2.3.1 Nitrophenol and gold nanoparticle calibration

Nitrophenol solutions with the concentrations: 0.012, 0.024, 0.036, 0.048 and 0.06 mM were analysed with UV-vis absorption spectroscopy to obtain the absorption profiles shown in Figure 43. The corresponding calibration gradient obtained by integrating the absorption values between 350 and 450 nm is shown in Figure 44.

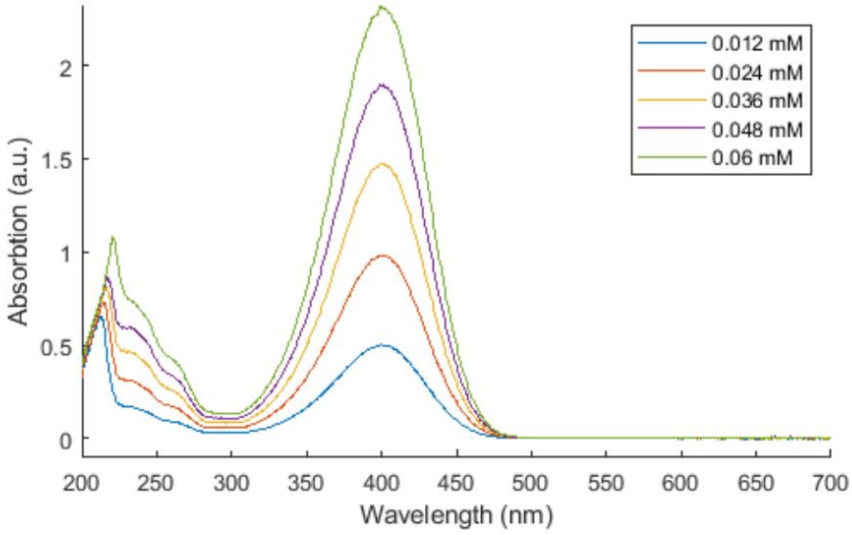

Figure 43. Plot showing absorption bands for 5 nitrophenol calibration standards from 0.012 to 0.06 mM.

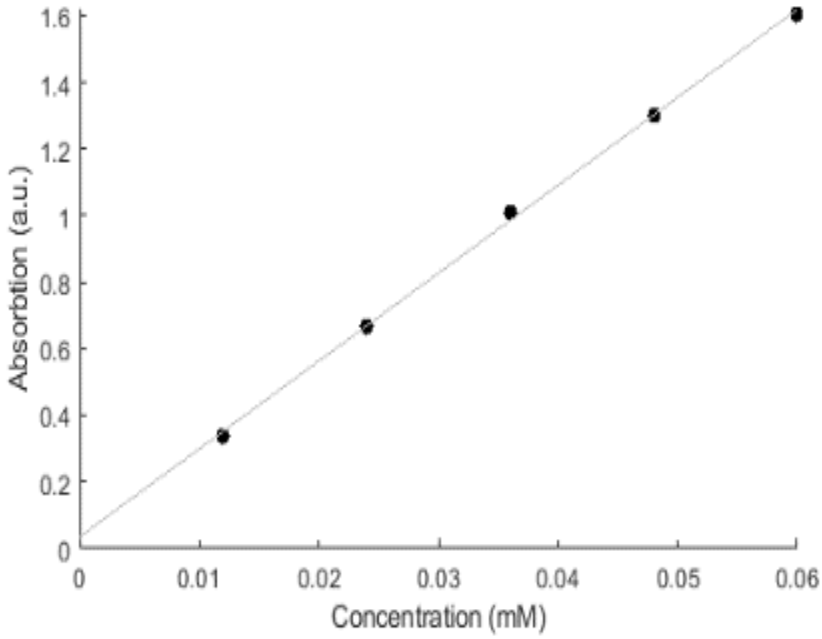

Figure 44. A calibration plot showing the integrated absorption values for nitrophenol calibration standards (adjusted to pH 10), between 350 - 450 nm, for 5 nitrophenol calibration standards from 0.012 to 0.06 mM. Gradient 26.439, Intercept 0.03344, R-squared value: 0.999.

2.3.2 Spectral convolution

Due to an overlap between the plasmon resonance of the AuNP catalysts and the nitrophenol absorption bands, it was not possible to use the raw UV-vis spectroscopy data for accurate quantification of reagent concentrations. Figure 45 shows an example of this additive effect, which results in convoluted UV-vis spectra. The broad absorption band of the AuNPs artificially inflates the nitrophenol absorption profile between 350 and 450 nm in the combined spectra.

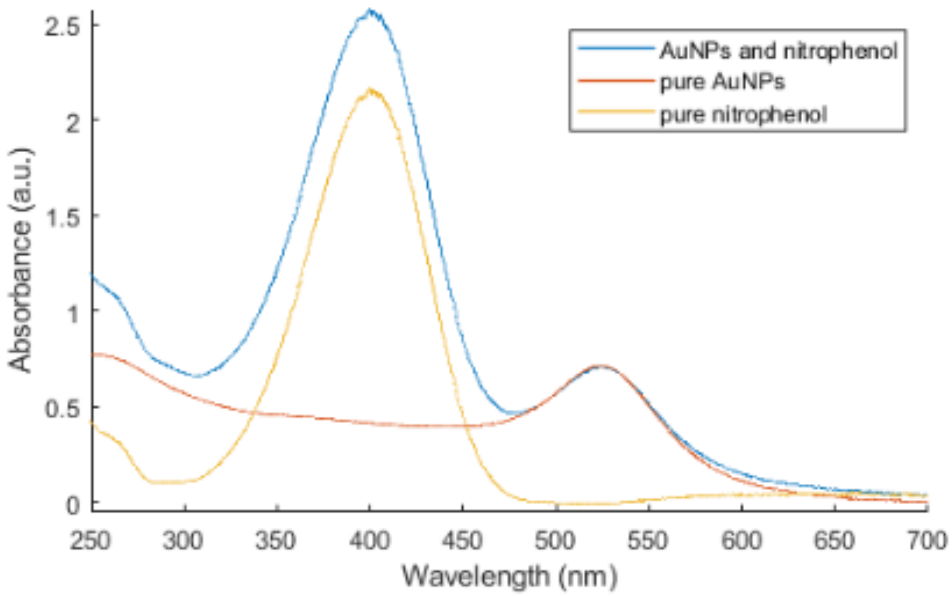

Figure 45. UV-vis spectra of pure nitrophenol and pure AuNP solution compared to a nitrophenol and AuNP mixture.

The data in Table 4 below presents a comparison of concentration data from two sets of samples containing a range of nitrophenol concentrations. One set shows the absorption values for a range of pure nitrophenol concentrations and another shows samples containing the same concentrations of nitrophenol but mixed with varying amounts of AuNP catalyst, within a range that would be expected within the range used during the -self-optimisation reactions. The concentrations are quoted as a % of the experimental starting concentration (0.06 mM).

Table 4. Table showing two sets of samples, pure nitrophenol and nitrophenol mixed with varying amounts of AuNPs within the range that would be expected during the self-optimising reaction.

Theoretical input conc. (%)	**Pure nitrophenol (%)**	**Nitrophenol + AuNPs (%)**
R^2	0.999	0.968

20	21	37
40	42	48
60	63	76
80	82	87
100	101	121

The effect of convolution can be seen in the graph shown in Figure 46. During this experiment, we found that measuring the concentration by integrating the absorption values between 350 and 450 nm without further processing of the data could lead to an error of up to 20 %.

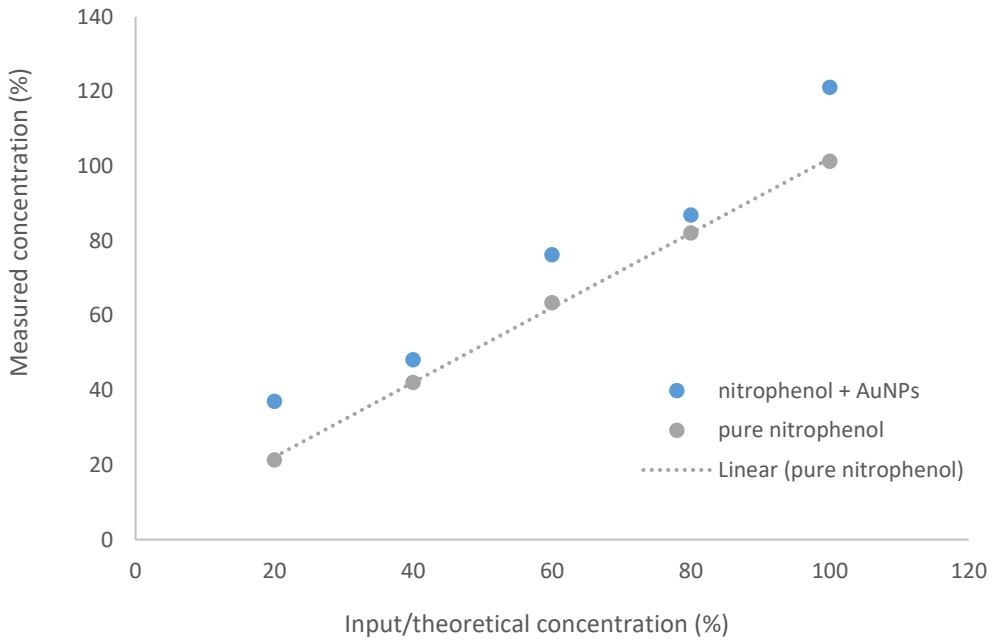

Figure 46. Graph showing the difference between solutions of pure nitrophenol as a % of the experimental starting concentration (0.06 mM) and nitrophenol mixed with varying amounts of AuNPs within the ranges which would be expected during a self-optimising reaction.

2.3.3 Spectral deconvolution

This systematic error was resolved using a deconvolution technique proposed by Sutherland, T. *et. al.*[129] Nitrophenol (purple line, Figure 47) does not absorb light at wavelengths >500 nm and AuNPs (aq.) have a broad UV-vis absorption band which typically peaks between 500-560 nm. Therefore, it was possible to generate a prediction of the underlying AuNP abortion band by scaling an AuNP reference spectra to match

the peak intensity in the measured spectrum between 500-560 nm (orange line, Figure 47). This predicted spectrum could then be subtracted from the overall absorption spectrum to obtain a more accurate representation of how the absorption spectrum would appear without the AuNP (aq.) absorption band (yellow line, Figure 47).

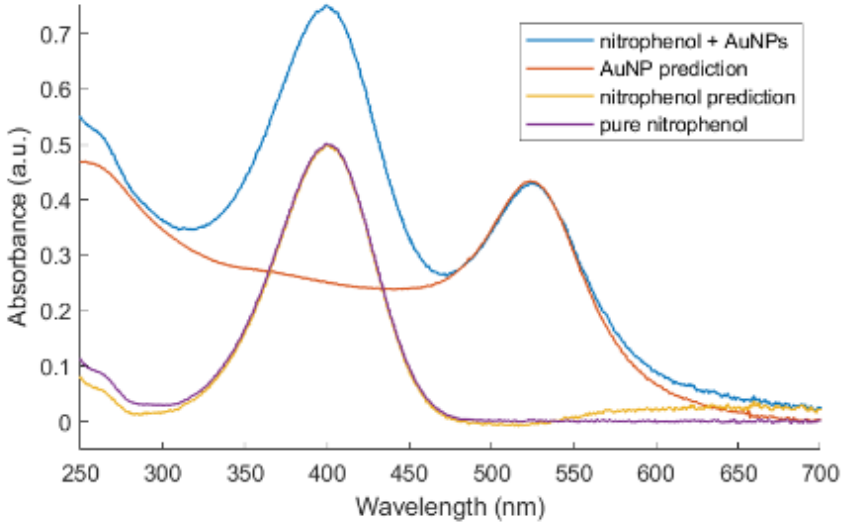

Figure 47. Graph showing how a more accurate measurement of the nitrophenol concentration can be obtained by deconvolution of the combined nitrophenol and AuNP spectra.

2.3.4 H_2 gas formation

$NaBH_4$ can react with water to form H_2, this gas formation presented a major problem for the system, as gas bubbles forming on the windows of the UV-cuvette (Figure 48) disrupted the inline analysis and bubbles forming in the reactor tubing made it impossible for the reactor to steady-state conditions.

Figure 48. A plastic cuvette containing aqueous $NaBH_4$ solution (2 mM) opened to the atmosphere (left). A flow cell containing aqueous $NaBH_4$ solution (2 mM) under 40 psi of pressure showing the formation of H_2 gas bubbles in a non-pressurised cuvette.

To resolve this issue the $NaBH_4$ reservoir solution was kept ice cold, adjusted to pH 10 with dropwise addition of a sodium hydroxide solution (0.1 M), then filtered through an inline gas/liquid separator before entering the pump. A back pressure of 40 psi was also maintained in the flow reactor and the flow cell.

2.3.5 Spectrometer temperature regulation

The UV-vis spectrometer in this project was sensitive to changes in ambient temperature. This signal drift could be corrected by performing regular baseline corrections, however, in the self-optimising system the spectrometer needed to obtain accurate readings throughout an entire optimisation (several hours).

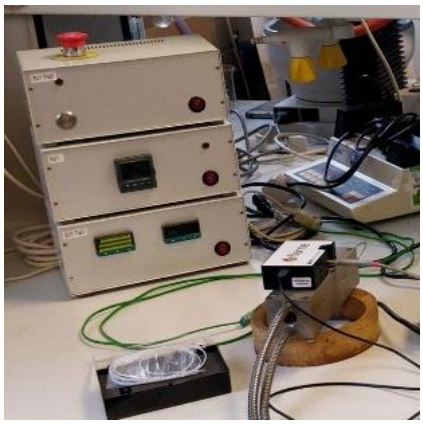

Figure 49. UV-vis spectrometer placed on top of an aluminium heating block regulated with a Eurotherm PID controller.

To prevent baseline drift caused by changes in ambient temperature the spectrometer was placed on top of an aluminium heating block (Figure 49), maintained at a temperature of 35 °C with a PID temperature regulator, thermal paste was applied between the spectrometer and the heating block to aid heat transfer. Figure 50 shows the stabilised absorption readings of a cuvette containing water, taken over 6 hours at 35 °C. The effect of reducing the temperature down to 30 °C and then up to 37.5 °C was then tested, revealing a significant decline in baseline signal at lower temperatures and an increase in baseline signal at higher temperatures.

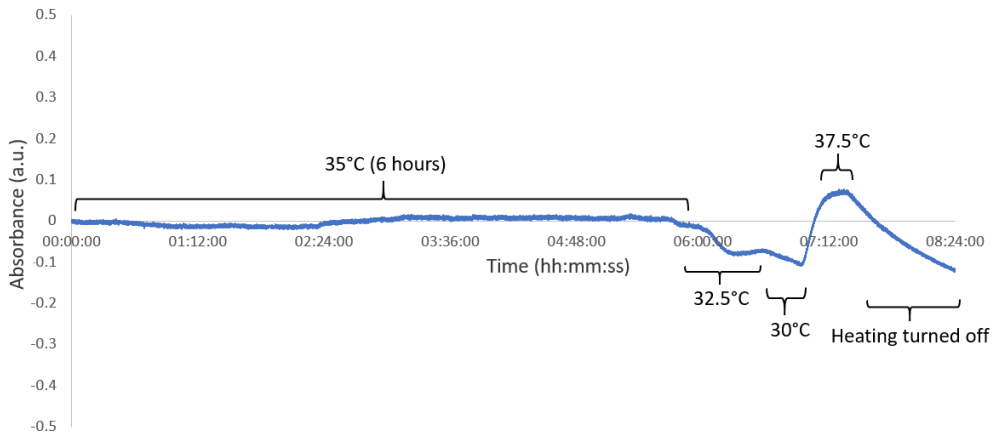

Figure 50. A fixed wavelength scan of water at 400 nm over 8.5 hours. The temperature of the device was maintained at 35 °C for the first 6 hours before investigating the effect of changing the temperature.

2.4 Self-optimising reactor

The general workflow of this approach was as follows: a window of user-defined operating conditions was determined for the system. Automated HPLC pumps then pumped nanoparticles and reagents into a tubular reactor. The reactor outlet stream was analysed with UV-vis spectroscopy. The resulting analysis data was reduced to a single scalar value describing the reaction output variable to be optimised, for example conversion or yield. These data were then fed to an optimisation algorithm which determined the next array of conditions to be set.

A schematic of the self-optimising reactor is shown in Figure 51 (specific component details are described in section 7.1.4). Altering the pump flow rates allowed different concentrations of reagents as well as different residence times to be explored. A water dilution pump was also included to increase the range of conditions that could be attained by the system, as not all combinations of factors could be achieved without a diluent *i.e.*, particular concentrations and residence times. The reactor pumps were controlled via a wired connection to a computer and a standard RS-232 serial communication protocol, the reactor was then automated with code written in MATLAB. The global optimisation algorithm SNOBFIT[106] was used to optimise the reaction, demonstrating the platform's ability to explore a wide range of reaction variables within a selected design space.

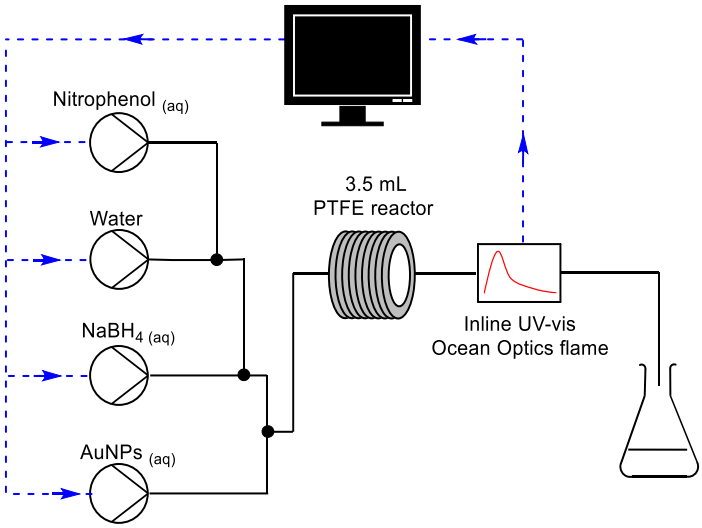

Figure 51. A simplified representation of the automated flow reactor used for the optimisation of a nanoparticle catalysed reaction.

Aqueous solutions of nitrophenol (0.6 mM), $NaBH_4$ (10 mM) and AuNPs (0.17 mM) were prepared and stored in reservoirs before being pumped into the tubular flow reactor (PTFE, 0.8 mm ID, 3.5 mL). The initial concentration of 4-NP (0.06 mM) was kept the same for each experiment to simplify analysis.

The reaction was monitored with an OceanOptics inline UV-vis spectrometer and interpreted using ChemiView[130] software, which allowed real-time monitoring of nitrophenol concentration and verification of steady-state conditions. The UV-vis spectroscopy data were deconvoluted and used to determine reaction conversion. The reaction conversion of each optimisation experiment was fed into the SNOBFIT algorithm and the next array of conditions was then automatically set by the reactor. This automated process was repeated iteratively until an optimum solution was obtained. The automated optimisation process is described in the flowchart shown in Figure 52.

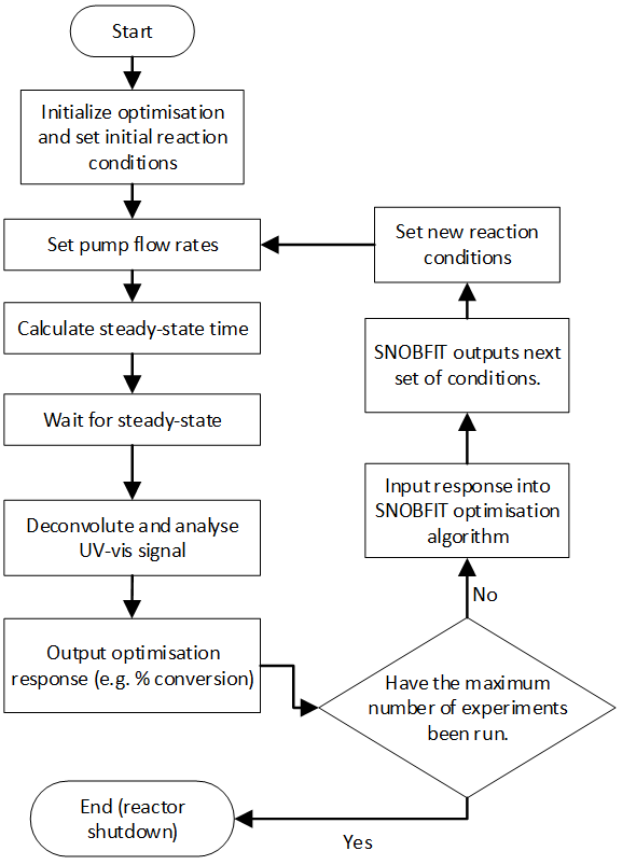

Figure 52. A flow diagram describing the automated processes by which the nanoparticle catalysed nitrophenol reduction reaction was optimised.

2.5 Self-optimisation of a nanoparticle catalysed reaction

After correcting for spectral convolution, 20 self-optimisation experiments were performed initially, the range of flow rates explored in these experiments are shown in Table 5. The preparation methods used to make up the reactor reservoirs are described in Section 7.1.1.

Table 5. Upper and lower bounds of reactor flow rates (mL/min), nitrophenol was set as a ratio of the other flow rates so that a constant starting concentration of 0.6 mM nitrophenol was pumped into the reactor.

	Water	$NaBH_{4(aq.)}$	AuNPs
min	0.1	0.25	0.05
max	2.5	2	0.5

Initially, the system was optimised in terms of pump flow rates. Figure 53 shows the design space explored during the initial self-optimisation of an AuNP catalysed nitrophenol reduction and the responses obtained. The flow rates of the pumps for each experiment and the corresponding conversion under steady-state conditions were plotted in real-time during the optimisation. Higher conversions were observed when

less water was pumped into the reactor and at higher AuNP solution flow rates. The concentration of $NaBH_4$ appeared to have less of an effect on the reaction conversion.

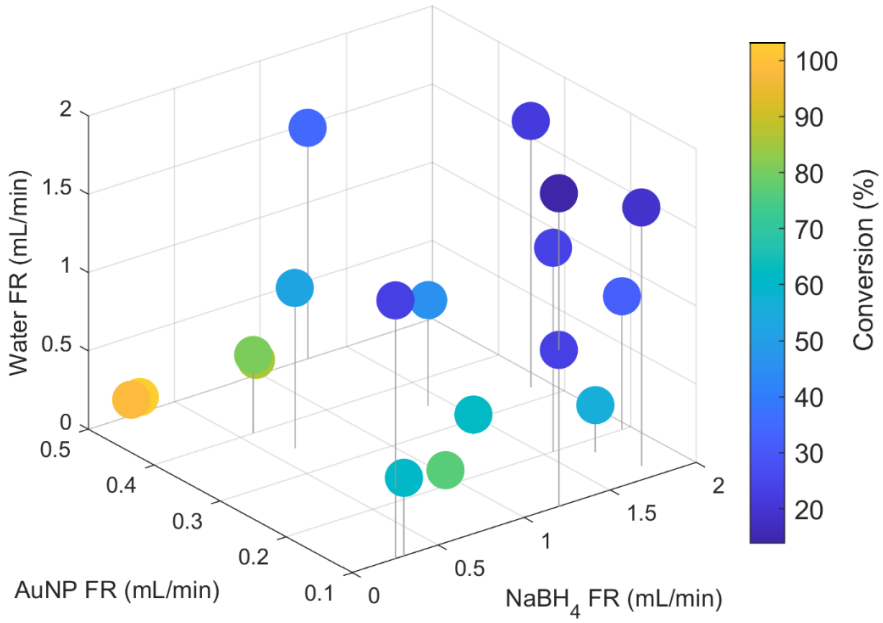

Figure 53. A 3D plot showing the effect of changing pump flow rates (FR) on reaction conversion.

To allow a more intuitive interpretation of the results, the pump flow rates were translated into reagent concentrations and residence times then replotted in Figure 54. This plot indicated that increasing the residence time, and AuNP catalyst concentration led to increased reaction conversion, however, changes in $NaBH_4$ concentration showed less of an effect.

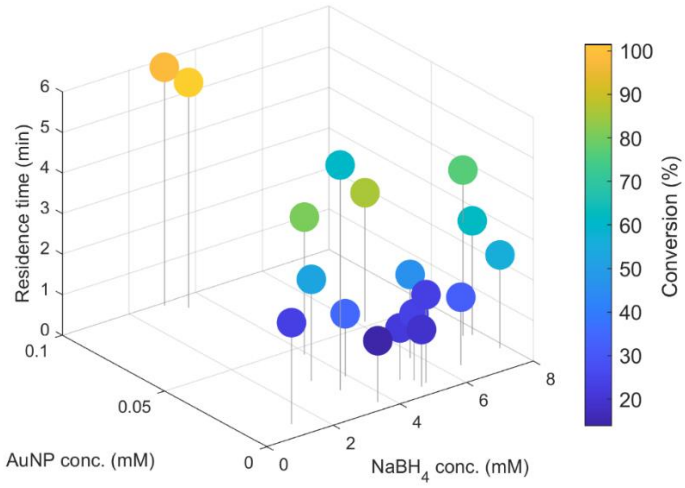

Figure 54. 3D Plot showing the effect of AuNP, $NaBH_4$ concentration and residence time on the yield of an AuNP catalysed nitrophenol reduction.

This plot also revealed a mathematical bias towards lower residence times and lower AuNP concentrations. This was because the pumps were set to flow at discrete intervals within set limits, therefore the spacing between potential residence times increased at lower flow rates, meaning there were fewer potential experiments present in these areas of the design space.

To mitigate this a new function was incorporated into the automation code, which allowed flow rates to be back calculated depending on the desired reaction conditions. This ensured an even spacing of the potential experiments that could be selected by the optimisation algorithm within the defined design space. This was called the 'conditions generation function' and was used to calculate pump flow rates based on nanoparticle surface area, reducing agent concentration and residence times.

2.5.1 Conditions generation function

The total flow rate was calculated by dividing the reactor volume by the residence time, see equation (4).

$$Total\ FR = \frac{Reactor\ volume}{Residence\ time} \tag{4}$$

The starting concertation of nitrophenol was 0.06 mM for every experiment. The nitrophenol stock solution concentration was 0.6 mM, therefore, the flow rate of nitrophenol could be calculated by multiplying the total reactor FR by 0.1, see equation (5).

$$Nitrophenol\ FR = Total\ FR\ \times 0.1 \tag{5}$$

The fraction of the total flow rate that should be allocated to $NaBH_4$ to allow a specific concentration of $NaBH_4$ to be pumped into the reactor was calculated by dividing the desired reactor concentration of $NaBH_4$ by the concentration of $NaBH_4$ in the stock solution reservoir, this fraction was then multiplied by the total flow rate to give the final $NaBH_4$ pump flow rate equation (6).

$$NaBH_4\ FR = \frac{NaBH_4\ conc.\ \times\ Total\ FR}{NaBH_4\ stock\ conc.} \tag{6}$$

A similar approach was taken to calculating AuNP flow rates where the desired surface area of nanoparticles in the reactor (AuNP SA) was determined by dividing the product of the surface area correlation coefficient, desired NP surface area and total flow rate by the concentration of AuNPs (mols of Au L^{-1}) in the stock solution reservoir equation (7).

$$AuNP\ FR = \frac{3880\ \times\ AuNP\ SA \times\ Total\ FR}{AuNP\ stock\ conc.} \quad (7)$$

A water pump was used to make up the remaining solution volume required to give the required total reactor flow rate for the desired residence time. This was calculated by subtracting the combined flow rates of the AuNP, nitrophenol and $NaBH_4$ solutions from the total flow rate equation (8).

$$Water\ FR = Total\ FR - (AuNP\ FR + NaBH_4\ FR + Nitrophenol\ FR) \quad (8)$$

2.5.2 Self-optimisation (with conditions generation function)

After integration of the conditions generation function, the design space could be explored evenly within the conditions shown in Table 6. A total of 29 optimisation experiments were performed in under 2.5 hours, the results are displayed in Figure 55. A trend toward the highest conversion (95 %) was found at longer residence times (3 min) and higher $NaBH_4$/AuNP concentrations: 2.1 mM and 0.04 mM respectively.

Table 6. The lower and upper variable bounds used for the optimisation in this study.

	AuNP SA (m^2L^{-1})	$NaBH_4$ (mM)	Res. time (min)
max	0.16	2.5	3
min	0.04	0.5	1

These results fit well with the findings of previously reported studies,[119,131] where the rate of the reaction was found to increase when higher concentrations of $NaBH_4$ were used and the length of time the reaction was allowed to proceed was increased. These studies did not directly compare different concentrations of the same catalyst, however, based on the Langmuir-Hinshelwood kinetic model, increasing the surface area of catalyst available in the system should increase the rate of reaction by increasing the number of sites for catalysis. The results shown in Figure 55 clearly show these trends,

the highest conversion (95% conversion) was found in the corner of the design space providing evidence of the system's capability for nanoparticle catalysed reaction optimisation. In addition, as the global optimisation algorithm explored a wide range of design space, it was possible to use this data set to identify kinetic parameters and obtain a high degree of understanding of the reaction system (discussed in chapter 4).

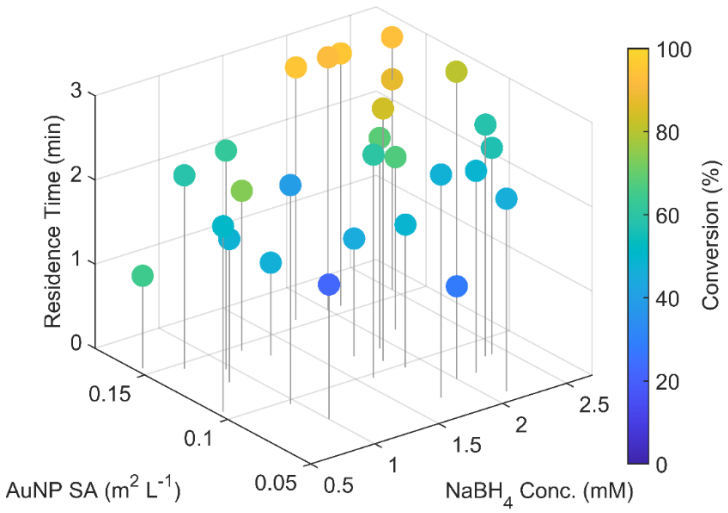

Figure 55. 3D plot showing the effect of changing three reaction variables on the conversion of nitrophenol to aminophenol. Each of the coloured spots in this diagram represents an experiment carried out by the reactor.

The data obtained from this optimisation was also used to generate kinetic reaction models. Allowing the prediction of rection outcomes performed using conditions not explored during the optimisation, either within or beyond the design space, discussed in detail in Chapter 4.

Although this was the first paper to describe a flow reactor which uses homogeneous nanoparticles as catalysts, an analogous heterogenous packed bed reactor has been investigated. In a 2016 paper by Nischang *et.al.* the authors describe a heterogenous packed bed reactor with nanoparticles adhered to the walls of a capillary-based flow reactor. The authors of this paper investigated changing sodium borohydride concentration and residence time on the conversion of nitrophenol to aminophenol. The findings of which were broadly in agreement with the results obtained this project, nitrophenol conversion was shown to increase with increasing sodium borohydride concentration and reactor residence time.[132]

2.6 Conclusions

In summary, a continuous flow reactor platform was developed and successfully demonstrated for the efficient optimisation of a nanoparticle catalysed reaction. The AuNP catalyst was analysed both before and after use in a reduction reaction with TEM and XPS analysis, then further size characterised with DLS. An inline UV-vis spectroscopy analytical method was developed which allowed live monitoring and accurate determination of the reaction conversion by deconvolution of overlapping absorption spectra.

Automated reactor controls and a self-optimising feedback loop were integrated into an automated flow reactor system. The effect of changing residence times, sodium borohydride concentrations and AuNP surface area were explored using a conditions generation function to translate the desired reaction conditions into pump flow rates and the global optimisation algorithm SNOBFIT to direct the system toward the highest possible reaction conversion.

The system was able to identify the optimum reaction conditions for maximum 4-NP conversion within a set operating window. Demonstrating the first proof-of-principle investigation automated optimisation of nanocatalysis in flow, this work allows the next step of the project. Where this system is incorporated into a flow reactor capable of nanoparticle synthesis, enabling rapid determination of the conditions required for producing optimal catalytic nanoparticles as well as the best conditions for the catalysed reaction.

The results described in this chapter have been published in the RSC's Chemical Communications Journal.[133]

Chapter 3

Continuous flow synthesis of nanoparticle alloy catalysts

This chapter describes the development of continuous flow reactors for the synthesis of gold nanoparticles (AuNPs) and gold-silver nanoparticle alloys (AuAgNPs). Reactor fouling presented a significant challenge during the initial development of this system, the effects of fouling were mitigated through careful choice of reagent concentrations and reaction conditions. The composition and consistency of the nanoparticles produced were monitored with inline UV-vis spectroscopy. A graphical summary of the approach is shown in Figure 56.

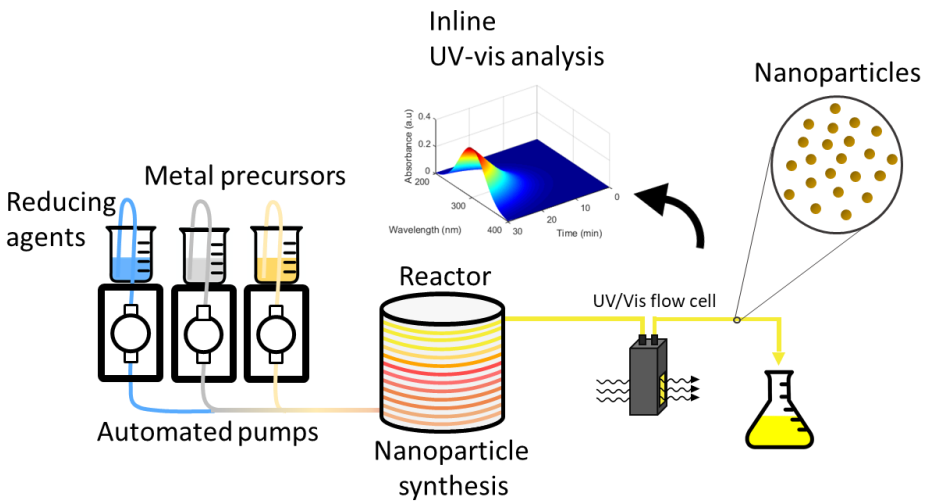

Figure 56. A reactor design for the continuous flow synthesis of AuAgNPs with control over composition. A reducing agent solution is pumped into a reactor with the metal precursors solutions of two different metals, a reduction reaction takes place leading to the formation of nanoparticles which are characterised by inline UV-vis spectroscopy.

3.1 Introduction

Alloyed metallic nanoparticles possess unique and tuneable optical,[134] magnetic[135] and catalytic properties.[136–138] Alloyed nanoparticle catalysts have also been shown to possess superior properties compared to their mono-metallic counterparts.[139] For example, core-shell nanoparticle catalysts with a ferromagnetic iron core and a more catalytic outer shell, can be magnetically separated from a reacting solution and recycled,[140] this has also been demonstrated for heterostructured magnetic nanoparticles.[141,142] In the cases where precious metals are used, such as ruthenium, platinum or palladium, bimetallic nanoparticles could potentially offer a cheaper alternative to monometallic nanoparticles, where only the reactive surface layer of these particles is composed of rare earth metals.[143]

This superior catalytic activity can be attributed to synergistic effects which occur between the different metals in the nanoparticles.[144] Introducing a second metal, may result in changes to the surface-structural and/or electronic properties of the nanoparticles, enhancing their catalytic properties.[145] For example, in the case of hydrogen evolution reactions, computational studies have shown that nanoparticles which adsorb hydrogen neither too strongly nor too weakly, possess the highest catalytic activities.[146,147] In subsequent experimental studies, the absorption properties of nanoparticle catalysts have been tuned by adjusting the ratios of their constituent metals, leading to significant increases in activity when compared to their monometallic counterparts.[34,148,149]

Combining metals in nanoparticles has also been shown to improve activity by protecting them from oxidation or poisoning. Conventional platinum nanoparticles undergo significant CO poisoning when used to catalyse the oxidation of formic acid.[150] CO in this case is produced during an undesirable side reaction, which has been evidenced to occur on platinum atom ensembles (an area of the nanoparticle surface with continuous monometallic neighbouring sites).[151] In cases where intermetallic PtPb, PtPd or PtBi nanoparticles are used, these ensembles are less prevalent, meaning a significant increase in catalytic performance is observed due to reduced catalyst poisoning.[152–154]

Nanoparticle alloys can be broadly categorised into three main structural categories, shown diagrammatically in Figure 57: intermetallic, where the constituent metals are evenly interspersed within each nanoparticle;[155] core-shell, where one metal is contained within the core of a nanoparticle with the subsequent metal layer/s of other metal/s coated on the outside of the core[156] and heterostructure, these nanoparticles are composed of metals which are joined at an interface or interfaces within the particle.[157]

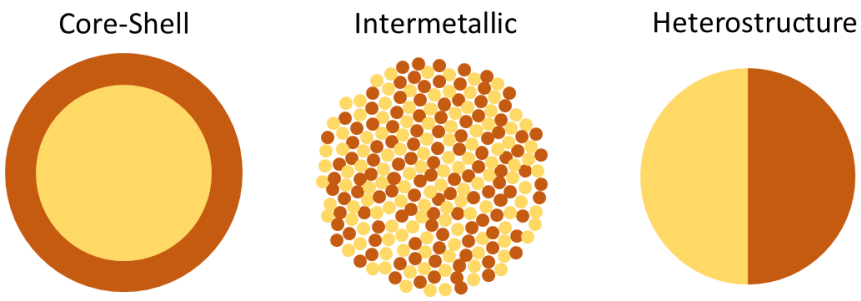

Figure 57. A diagram showing the three categories of alloyed nanoparticles: core-shell (left), intermetallic (middle) and heterostructure (right). Nanoparticle alloys may be composed of two or more metals.

Core/shell nanoparticle alloys are typically synthesised in solution, using a seeded growth approach.[158–161] In a study by Marzan *et. al.* multi-layered Au/Ag core/shell and Au/Ag/Au double-shell nanoparticles were synthesised in batch. This was accomplished by successive separate addition of Au and Ag metal precursor solutions to a reducing/capping agent solution.[162] The structure of nanoparticles such as these can be confirmed with high-resolution STEM-XEDS analysis, see Figure 58.

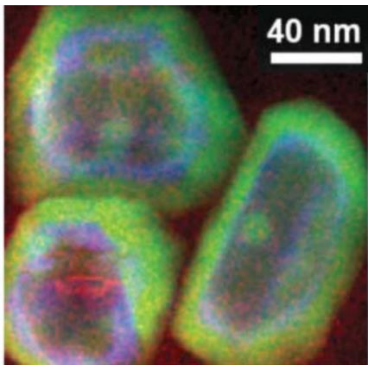

Figure 58. A STEM-XEDS micrograph showing the composition of Au/Ag/Au double-shell nanoparticles (Au = green, Ag = blue and oxygen = red). (Reproduced with permission from ref. [162] *Copyright 2005, Royal Society of Chemistry. All rights reserved.)*

There are two approaches commonly used to create intermetallic nanoparticles. The first is to synthesise nanoparticles using a solution-based co-reduction method, which produces nanoparticles with controlled sizes but a disordered arrangement of different metals. These nanoparticles are then later annealed at high temperatures to form an ordered structure.[163–168] The second approach is to use a solution-based co-reduction method to directly form an ordered arrangement of metals within the nanoparticle.[169–173]

Under these conditions, the formation of intermetallic nanoparticles can be thermo-dynamically favourable. At high temperatures, disordered alloys are energetically favoured, due to an associated increase in entropy. Complementary d-d orbital interactions between different transition metals can also lead to an increase in enthalpy. Therefore, the combination of these factors results in an overall reduction of Gibbs free energy, leading to the formation of ordered intermetallic nanoparticle structures.[174]

With a high degree of control, it is possible to create heterostructure nanoparticles with multiple different metals separated by discrete interfacial boundaries. In a 2016 study by Mirkin *et. al.*,[175] individual heterostructure nanoparticles were synthesised within nanosized reactors using a two-step annealing process. This was accomplished by depositing an ‘ink’ solution containing block copolymers and metal precursors, as

hemispherical domes, onto a flat substrate (*e.g.*, a silicon wafer) using dipped pen nanolithography. These domes, termed nanoreactors by the authors, were then heated to 120 °C under an argon atmosphere for 48 hours, then to 500 °C under an H_2 atmosphere for 12 hours, resulting in the reduction and coalescence of the reduced metal precursor ions. This long-term thermal treatment leads to a thermodynamically stable configuration of the constituent metals. Depending on the compatibility of the elements, these nanoparticles can be heterostructured, intermetallic or both, see Figure 59.

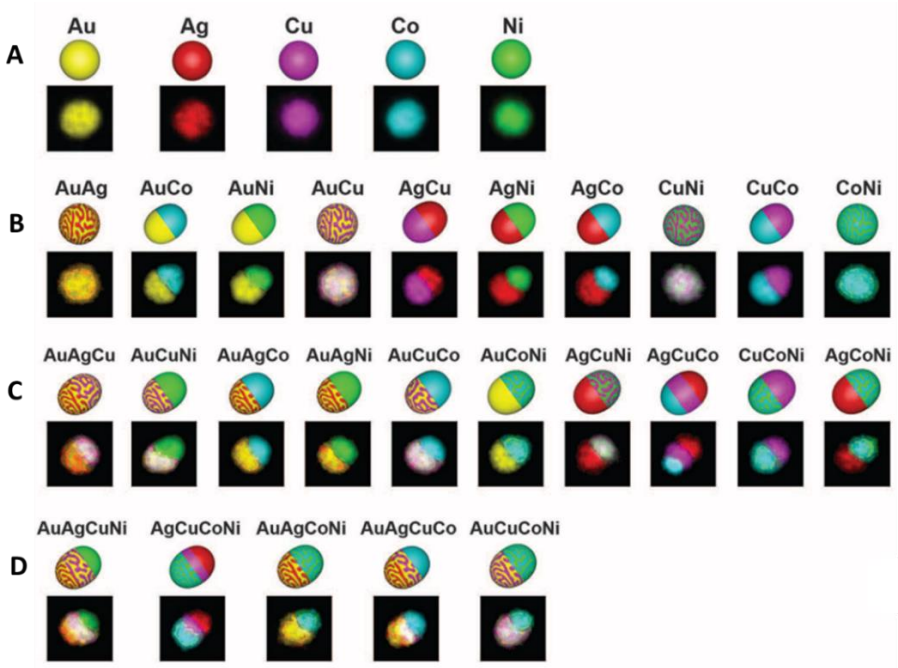

Figure 59. STEM-EDS micrographs showing the variety of individual heterostructure nanoparticles that can be synthesised using a two-step thermal annealing procedure of metal precursor and block copolymer solutions deposited onto a flat substrate.[175] *(A) monometallic nanoparticles, (B) bimetallic nanoparticles, (C) trimetallic and, (D) tetrametallic nanoparticles. (Reproduced with permission from ref* [175]*. Copyright 2010, American Association for the Advancement of Science. All rights reserved.)*

This chapter presents work surrounding the development of continuous flow reactors for nanoparticle catalyst synthesis, using AuAgNPs as an example system. Compared to AuNPs, AuAgNPs have shown higher degrees of catalytic activity in the gas phase oxidation of carbon monoxide with molecular O_2, under room temperature conditions.[176] For AuAgNPs with segregated regions of Au and Ag surface sites, a convincing theory for this superior catalytic performance is that the Ag sites effectively absorb and activate O_2, while neighbouring gold sites adsorb CO.[177] Oxygen transfer to the CO molecules can therefore easily occur between these neighbouring sites, resulting in a high rate of conversion. AuAgNPs have also proven effective for the catalytic oxidation of glycerol,[178] as well as the reduction of nitroaromatic compounds.[179]

3.2 Batch synthesis of AuAgNPs

Before developing continuous flow methods for the synthesis of AuAgNP alloys, these nanoparticles were first synthesised in batch using a method adapted from Rioux *et. al.*,[158] described in Section 7.2.2.1. This method uses a similar approach to the protocol used to synthesise AuNPs in Chapter 2 but incorporates an additional $AgNO_3$ silver precursor solution. The method produces clear coloured solutions containing AuAgNPs ranging from yellow (predominantly silver) to red (predominantly gold), see Figure 60.

Figure 60. Sample vials containing a range of AuAgNPs with increasing gold concentrations from left to right.

The UV-vis spectra of the AuAgNPs (normalised to maximum peak intensity) are presented in Figure 61 below. These results and many other studies have found that the λ_{max} value can be linearly correlated to the ratio of gold and silver contained within the nanoparticle solutions.[161,162,180–184] The presence of a single peak in each absorption spectrum, rather than two peaks, indicates that an alloyed nanoparticle species was formed rather than a mixture of discrete monometallic gold and silver nanoparticles.[185]

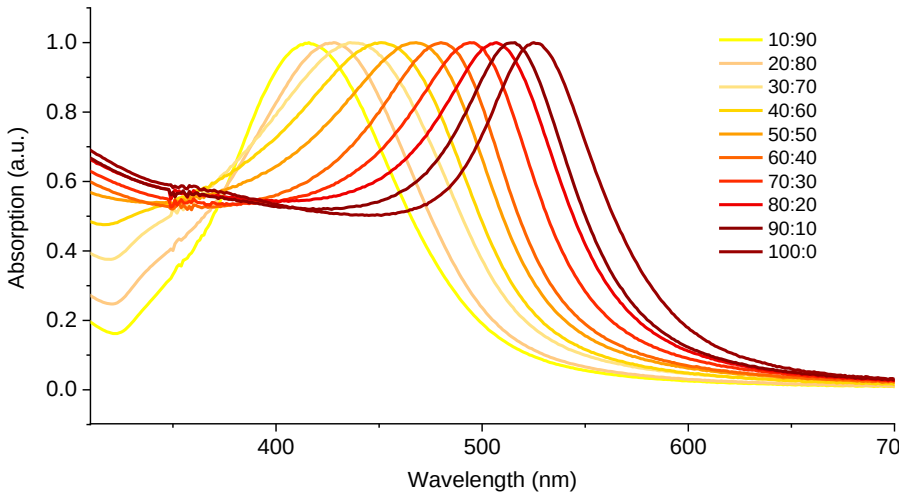

Figure 61. A plot showing the UV-vis spectra depending on the Au:Ag metal ratio of the nanoparticles.

3.3 Flow reactor development

Continuous flow methods have been previously developed for the production of AuAgNPs.[79,80,82] However, these methods were either incompatible with multistage

reactors or not designed for the continuous production of nanoparticles over several hours, as would be required for this project. Therefore, in this chapter continuous methods were first developed for the synthesis of AuNPs, to gain an understanding of nanoparticle flow synthesis, before developing more complex methods for the continuous synthesis of AuAgNPs. Multiple reactor configurations and chemistries were explored to determine the best method for synthesising nanoparticles with consistent properties and a high rate of conversion over a long period of time.

3.3.1 Tubular PTFE reactor

Reactors developed early in the project were constructed from 1/32" ID PTFE tubing, these reactors are commonly used for lab-scale continuous synthesis of organic molecules. Unfortunately, these did not produce a consistent stream of AuNPs and failed to reach steady-state conditions as the reactors were highly prone to fouling. Figure 62 shows a diagram of an early reactor design in the project, where solutions of reducing agent/capping ligand (sodium citrate) and gold precursor ($HAuCl_4$) were pumped into a 5 mL tubular reactor heated to 100 °C, with a 40-psi back pressure regulator to prevent the solvent (water) from boiling and bubbles forming within the flow cuvette and reactor.

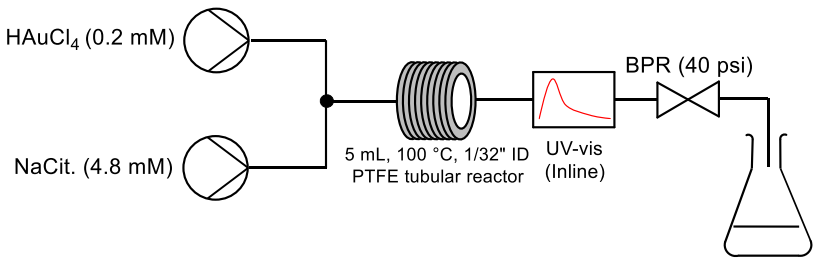

Figure 62. A reactor diagram showing the initial system designed for the synthesis of AuNPs in flow, gold nanoparticle precursor solutions and sodium citrate reducing agent/capping ligand were pumped into a 5 mL PTFE tubular reactor heated to 100 °C.

This reactor was based on a study by Gavriilidis *et. al.*[44] and was constructed from translucent PTFE tubing and ETFE T-pieces, allowing any fouling in the reactor to be observed easily through the tubing. A detailed description of the reactor and method can be found in Section 7.2.2.2. The reactor outflow stream was monitored with inline UV-vis absorbance spectroscopy, for over one hour, giving time-series data proportional to the concentration of AuNPs in the reaction solution, (full wavelength absorption spectra were taken once per second, then integrated between 500 – 550 nm) this data is shown in Figure 63 below.

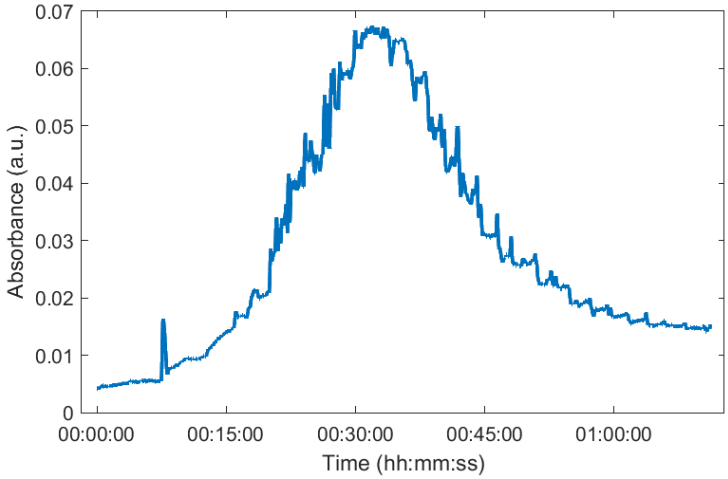

Figure 63. A plot showing the integrated absorption values between 500 - 550 nm measured at the reactor outflow.

This plot shows nanoparticle yield increasing steadily over the first 30 minutes of the reaction. The reactor then failed to reach steady-state and a significant decline in conversion was observed over the next 30 minutes. This was due to a significant build-up of fouling on the internal walls of the reactor, an increase in conversion accelerated until the rate of fouling in the reactor exceeded the rate of nanoparticle formation, at which point accelerated fouling and a decline in nanoparticle conversion was observed, see Figure 64.

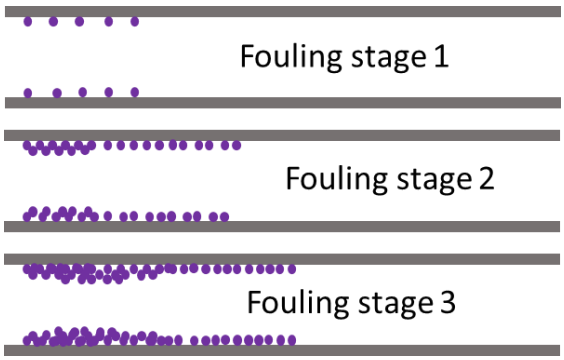

Figure 64. A diagram showing how the rate of reactor fouling increases as the number of nucleation sites for nanoparticle formation on the walls of the reactor increases, this eventually exceeds the rate of nanoparticle formation leading to a decline in nanoparticle yield.

The increasing rate of nanoparticle formation within the first 30 minutes of this experiment was likely due to the presence of catalytic nanoparticles adhered to the reactor tubing.[186] To confirm this, time-series UV-vis absorption spectra were obtained from AuNPs seeded growth studies in batch, a solution of AuNPs was synthesised in batch followed by successive addition of further precursor and reducing agent after each reaction had reached completion (see Section 7.2.2.3 for detailed methodology). These results showed that in the absence of seed AuNPs the amount of time taken for the Au^{3+} precursor solution to reach full conversion to nanoparticles was nearly twice as long as

when seed nanoparticles were present in the solution (Figure 65), this is supported by similar results in the literature.[187,188]

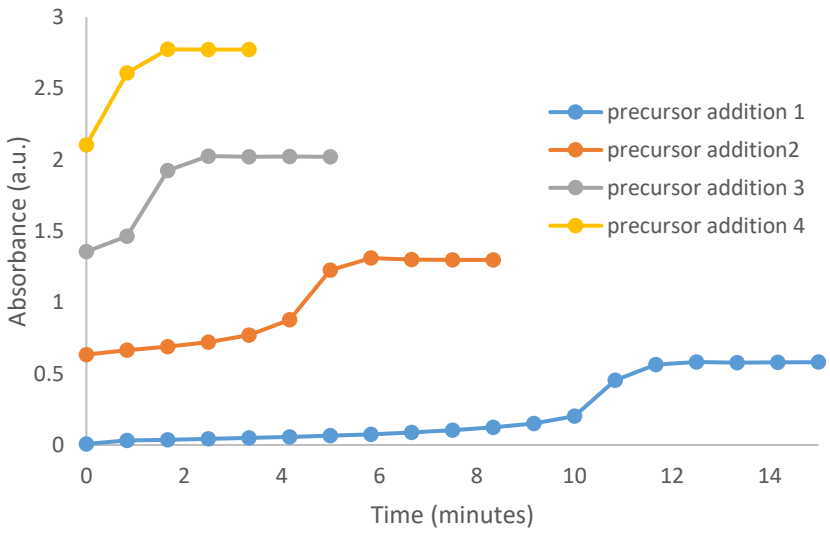

Figure 65. A plot showing the relative rates of AuNP formation for each growth step, the absorbance values plotted are the integrated absorbance values between 500 and 550 nm.

Initially fouling presented as a light pink coating on the walls of the reactor, this coating would then turn dark purple, before eventually developing a metallic gold appearance. This was likely due to the adsorption of AuNP nuclei on the walls of the reactor accumulating, growing and merging to form gold in the bulk phase, see Figure 66.

Figure 66. An image showing gold nanoparticles accumulating to form solid gold on the reactor walls.

For this project, it was essential for the self-optimising reactor to produce nanoparticles in a way that was not influenced by previous conditions in the reactor and reach steady-state conditions indefinitely, to ensure that the results of the optimisation were reproducible. However, the complete prevention of fouling during continuous flow nanoparticle synthesis is a challenging task. Many other studies have adopted segmented flow regimes in their reactors to reduce fouling.[48,64,189] But for this system both phases would need to be separated before entering the next stage of the reactor, adding dead volume and the need for a phase separator within the reactor design.

Commercially available, membrane-based phase separators have been used in other studies to separate phases in segmented flow reactors.[190,191] However, these types of phase separators were unsuitable for the reactor system in this project. Membrane separators use a diaphragm-based backpressure regulator to delicately balance the backpressure of both the aqueous and organic streams. During initial tests, an excess of backpressure at the aqueous outlet from the adjoining secondary reactor, caused the diaphragm to close off on the organic outlet. This resulted in both phases being retained on the aqueous side of the separator, as shown in Figure 67.

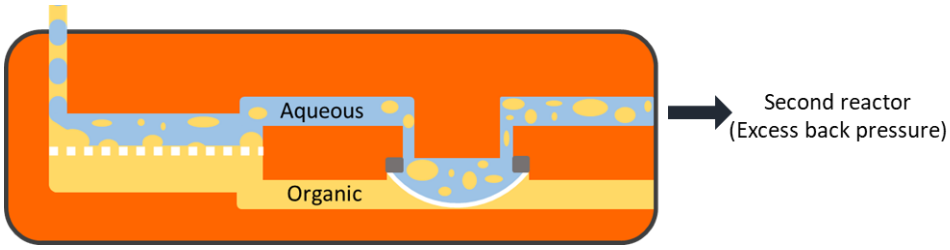

Figure 67. Due to an excess of backpressure on the aqueous side of the membrane separator, the diaphragm valve closes off on the organic side of the separator, causing both phases to be retained.

Therefore, instead of preventing the occurrence of fouling completely, the rate of fouling was limited as much as possible. This was accomplished by maximising the rate of nanoparticle formation while preventing nanoparticles from forming on the reactor walls. Table 7 presents the major factors which influence the rate of reactor fouling and the rate of nanoparticle formation.

Table 7. A summary of the factors influencing the rate of reactor fouling and the rate of nanoparticle formation in continuous flow reactors.

Rate of fouling	**Rate of NP formation**
Reactor wall smoothness	Reducing agent strength
Segmented flow	Presence of seed solution
Reactor surface area to volume ratio	Concentration of metal precursor
Flow reactor design	Reactor temperature

Tubing materials such as PFA have been found to foul less than tubing made from other materials such as PTFE.[192] The flow reactor design and type/extent of mixing can also influence the extent of reactor fouling.[193] The reactor surface area to volume ratio has a significant influence over reactor fouling, by lowering the surface area to volume ratio of the inside of the reactor, the amount of reacting solution exposed to the reactors internal surface is reduced, presenting fewer opportunities for the nanoparticles to form on the reactor walls.

Increasing the concentration or reduction potential of the reducing agents used in nanoparticle synthesis can increase the rate of nanoparticle formation, leading to the production of smaller more catalytically active nanoparticles.[194] As the formation of nanoparticles is an autocatalytic process, the presence of a seed solution may also help to accelerate the rate of nanoparticle formation. Finally, increasing the reaction temperature and reagent concentrations can accelerate the rate of nanoparticle formation by increasing the frequency of collisions between reactants. A graphic summarising the effect of these approaches is shown in Figure 68.

Once the nanoparticles have fully formed in solution, adsorption to the walls of the reactor becomes less likely. This is evidenced by the observation that no fouling was seen beyond the initial section of the reactor. Therefore, increasing the rate of nanoparticle formation in solution, rather than on the walls of the reactor was equally important for achieving steady-state conditions.

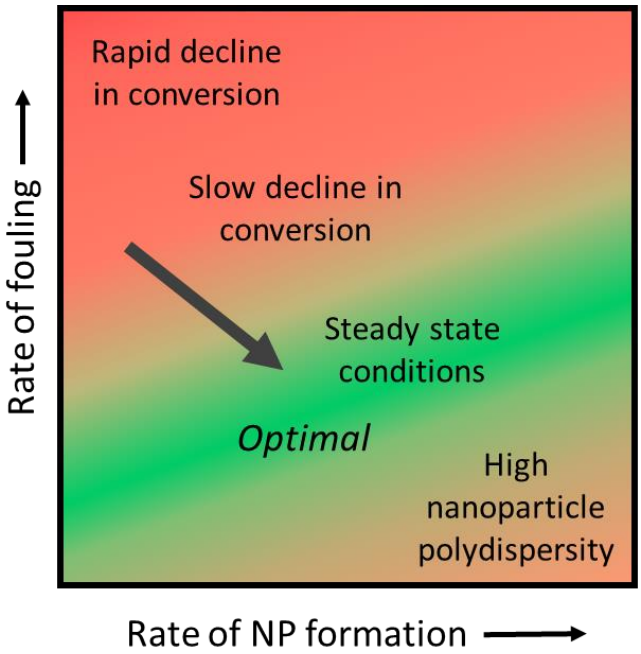

Figure 68. A graphical summary showing how optimising the rate of nanoparticle formation and fouling may lead to optimal steady-state conditions, without compromising nanoparticle quality.

Figure 68 presents the theory that increasing the rate of nanoparticle formation and decreasing the rate of reactor fouling, can lead to steady-state conditions. However, increasing the rate of nanoparticle formation too much can impact the uniformity and size distribution of nanoparticles produced. Therefore, it was important to balance the requirement to limit reactor fouling with the need to produce nanoparticles with

homogeneous physical properties. This chapter presents the development of an optimal strategy for achieving steady-state conditions in continuous NP synthesis.

3.3.2 Continuous flow synthesis with pre-formed AuNP solution

As AuNP formation is an autocatalytic process, the rate of nanoparticle formation could be increased by pumping a pre-formed nanoparticle solution into the reactor, with the nanoparticle precursor and reducing agent. This approach has also been used previously in the synthesis of core-shell AuAgNP alloys[80] and as a nanoparticle growth strategy in the continuous synthesis of AgNPs.[195]

The diagram shown in Figure 69, presents a reactor which includes a stream of preformed AuNPs, being pumped into the reactor alongside a $HAuCl_4$ metal precursor and sodium citrate reducing agent solution (see Section 7.2.2.4 for method).

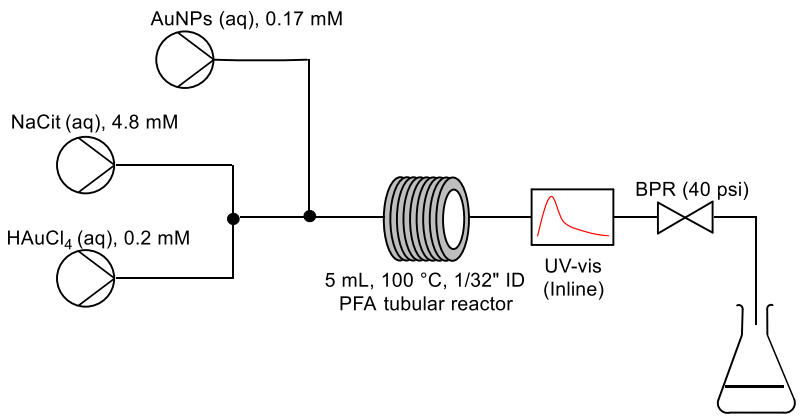

Figure 69. A tubular continuous flow reactor which incorporates an AuNP seed solution stream for accelerated nanoparticle formation.

The plot shown in Figure 70 shows an overall increase in precursor conversion compared to the reactor presented in 3.3.1. This was likely because the pre-formed nanoparticles, which were injected into the reactor along with the precursors, provided a preferential/catalytic surface for the reduction of Au^{3+} ions. The addition of a seed solution increased the rate of nanoparticle formation, but not significantly enough to prevent reactor fouling, which was observed after approximately 15 minutes. As steady-state could not be achieved using this approach, alternative methods were explored.

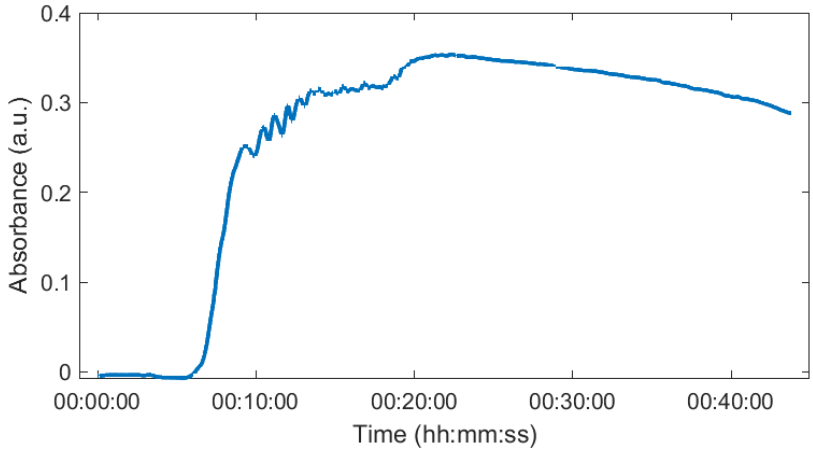

Figure 70. A plot showing the integrated absorption values between 500 - 550 nm measured at the reactor outflow for a reactor which uses preformed AuNPs as a catalyst for nanoparticle formation.

3.3.3 Ascorbic acid reducing agent

The reducing agent strength greatly influences the rate of Au^{3+} reduction. Stronger reducing agents with greater redox potentials rapidly reduce Au^{3+} ions, increasing the rate of nanoparticle formation.[196] Ascorbic acid is a stronger reducing agent than sodium citrate and has been used in previous studies to reduce $HAuCl_4$ in continuous flow.[71]

Ascorbic acid was added to a sodium citrate solution to accelerate the rate of nanoparticle formation by promoting nucleation within the solution, instead of the walls of the reactor. The diagram in Figure 71 below, shows a reactor with two inlet streams, one for $HAuCl_4$ and the other for a mixture of sodium citrate and ascorbic acid (see Section 7.2.2.5 for method).

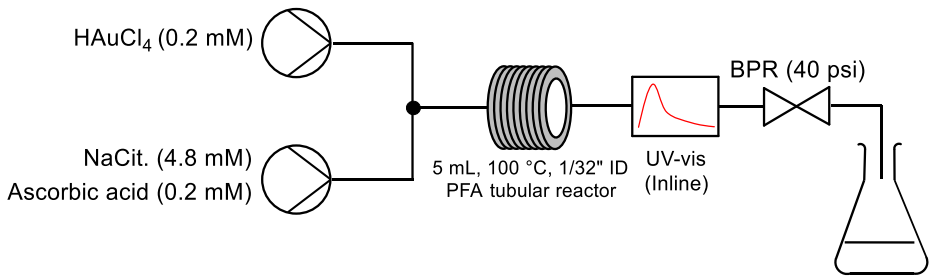

Figure 71. A reactor diagram showing nanoparticle precursor $HAuCl_4$ being pumped into a 5 mL PFA tubular reactor alongside a mixture of sodium citrate and ascorbic acid.

This modification led to improvements in the system's ability to maintain steady-state conditions, (see Figure 72) supporting the hypothesis that a decline in conversion could be avoided by increasing the kinetics of nanoparticle formation. The reactor required approximately an hour (6 reactor volumes) to reach maximum conversion, then the next several hours a decline in reaction conversion was observed.

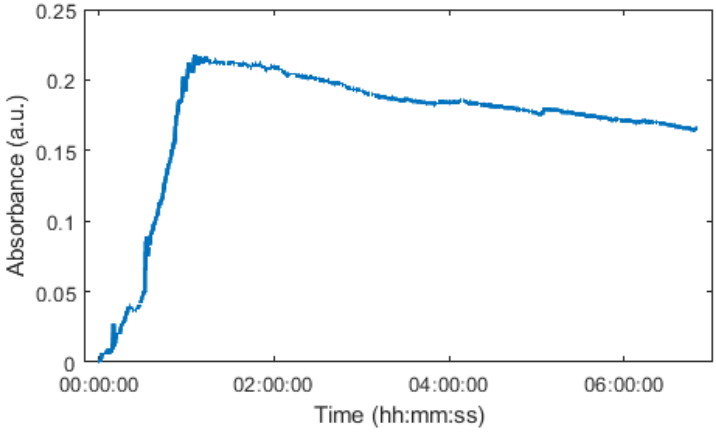

Figure 72. A plot showing the integrated absorption values between 500 - 550 nm measured at the reactor outflow for a reactor which used ascorbic acid to accelerate the rate of nanoparticle formation.

As this method required over an hour and several reactor volumes to reach steady state, it was likely that some fouling was required to catalyse the reduction of $HAuCl_4$. Therefore, because the reactor could not maintain steady-state conditions or reach high conversions without the presence of some reactor fouling, further attempts to reach steady-state conditions were made with stronger reducing agents.

3.3.4 Sodium borohydride reducing agent

$NaBH_4$ is a very strong reducing agent and has been used in the synthesis of highly catalytically active and colloidally stable gold nanoparticles. Similar to sodium citrate, $NaBH_4$ can act as both a reducing agent and a capping agent. The rate of formation of these nanoparticles was very fast, with the nanoparticle solution appearing to reach full conversion instantaneously upon mixing at room temperature. A method developed by Larm *et. al.* for the synthesis of AuNPs with $NaBH_4$,[197] was translated to flow with the reactor shown in Figure 73.

Due to the rapid kinetics of this reaction, the reactor was shortened to 0.5 mL. The total combined flow rate of the reactor was increased to 6 mL/min improving space-time yield, see Section 7.2.2.6 for method details.

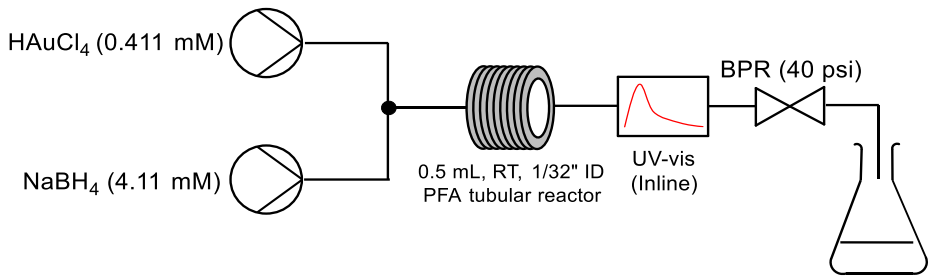

Figure 73. A reactor diagram showing nanoparticle precursor $HAuCl_4$ being pumped into a 0.5 mL PFA tubular reactor alongside a $NaBH_4$ solution.

This reactor proved capable of operating under steady-state conditions for over 30 minutes (Figure 74), producing approximately 200 mL of colloidally stable catalytic AuNPs. In the study by Larm *et. al.*, these nanoparticles were significantly more active than nanoparticles produced using weaker reducing agents, this is likely due to the smaller average size of the nanoparticles formed and the absence of any strongly binding capping agent which could restrict reactants from accessing the catalyst surface.

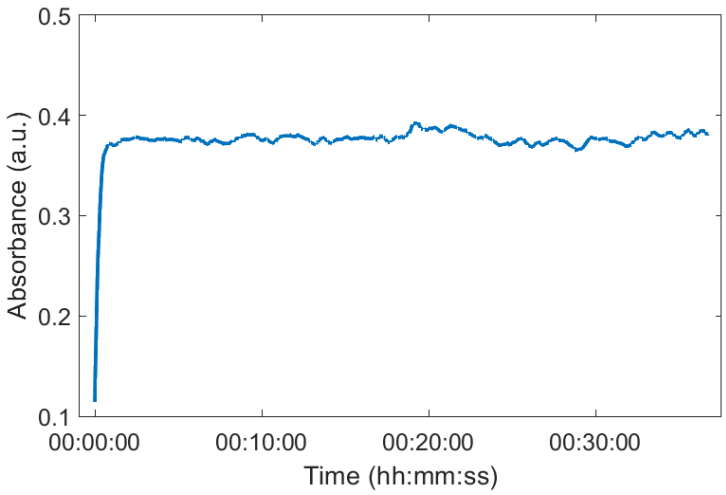

Figure 74. A plot showing the integrated time-series absorption values between 500 - 550 nm, measured at the reactor outflow, for a reactor which uses $NaBH_4$ solution as a reducing agent.

Only a small amount of fouling was observed within the reactor T-piece after a litre of nanoparticle solution was produced (Figure 75). This indicated that the nanoparticle formation reaction had reached near 100% completion before leaving the T-piece of the reactor.

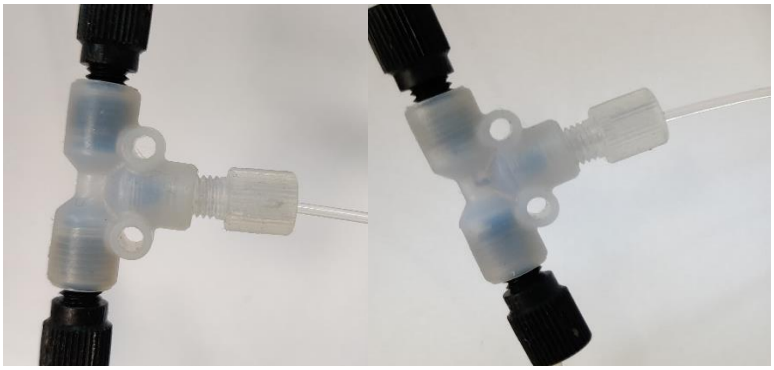

Figure 75. The reactor T-piece before nanoparticle synthesis (left) and the reactor T-piece after nanoparticle synthesis (right) a small amount of fouling can be seen after nanoparticle synthesis.

Nanoparticles formed rapidly in this system, meaning wait times between experiments of only a few minutes allowing efficient screening of reaction design space. This method was next developed for the synthesis of gold-silver nanoparticle alloys.

3.3.5 AuAgNP flow synthesis with sodium borohydride reducing agent

The nanoparticle synthesis method discussed in Section 3.3.4, has also been used previously for the synthesis of bimetallic Au_xAg_{1-x} nanoparticles. In a study by Baker *et. al.*, the authors found alloys of Au and Ag to be significantly more catalytically active than their monometallic counterparts in nitrophenol reception reactions, with the higher catalytic performance observed with AuAgNP alloys than pure AuNPs or AgNPs.[197]

The flow reactor in this section of the report was adapted from the study above, incorporating an additional silver precursor salt solution ($AgNO_3$). See Section 7.2.2.7 for a detailed description of the experimental method.

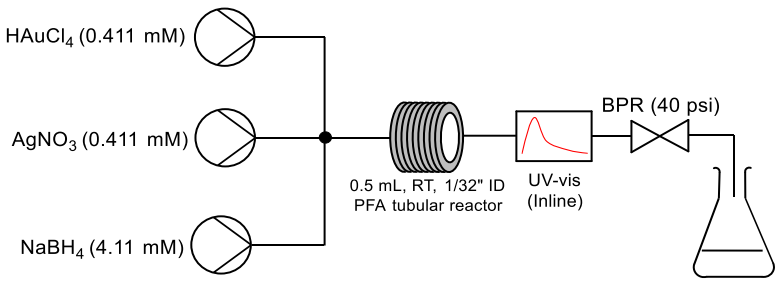

Figure 76. A diagram showing a reactor designed for the synthesis of Au_xAg_{1-x} nanoparticles. Comprising of a PFA tubular reactor with a 0.5 mL volume. $HAuCl_4$ and $AgNO_3$ precursor solutions were pumped into the reactor alongside a $NaBH_4$ solution.

Samples were collected for AuAgNPs with alloy ratios ranging from 0:1 to 1:0 Au:Ag in increments of 0.1. Figure 77 shows the nanoparticle solutions immediately after

synthesis and 1 hour after synthesis, within 1-hour nanoparticle solutions containing between 50 and 70% Ag had begun to aggregate to form a black precipitate. To increase the long-term stability of the nanoparticles, milder reducing agents were explored during the next stage of method development.

Figure 77. A photograph showing the nanoparticle solutions produced immediately after flow synthesis (Top) and one hour after synthesis (bottom), with black precipitate highlighted in the red box.

3.3.6 Tannic acid reducing agent

Tannic acid is a stronger reducing agent than ascorbic acid but weaker than $NaBH_4$. It has been used in the synthesis of smaller more catalytically active AuNPs than is possible using the traditional Turkevich protocol, which uses only sodium citrate. An AuNP synthesis method which employed tannic acid was originally presented in the seminal work of Mühpfordt in 1982.[198] This synthesis method has the benefit that it does not require toxic reagents or strongly binding capping agents, which would inhibit the performance of nanoparticles in catalytic or medical applications.

The diagram presented in Figure 78 shows an aqueous mixture of tannic acid and sodium citrate being pumped into a tubular reactor alongside $HAuCl_4$, for full experimental details see Section 7.2.2.8.

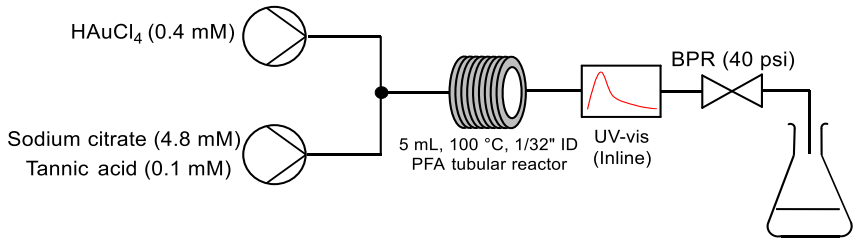

Figure 78. A reactor diagram showing nanoparticle precursor $HAuCl_4$ being pumped into a 5 mL PFA tubular reactor alongside a mixture of sodium citrate and tannic acid.

The reactor reached steady-state conditions for over 50 minutes, with little change in the UV-vis absorption spectra over this period, see Figure 79. After approximately one-hour fouling was observed on the first 30 cm of the reactor tubing (Figure 80).

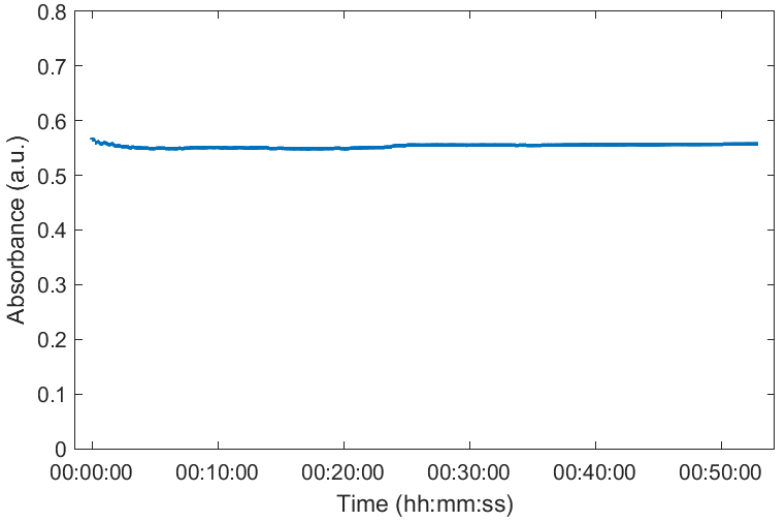

Figure 79. A plot showing the integrated time series absorption values between 500 - 550 nm, measured at the reactor outflow for a reactor which uses a mixture of sodium citrate and tannic acid as the reducing agent.

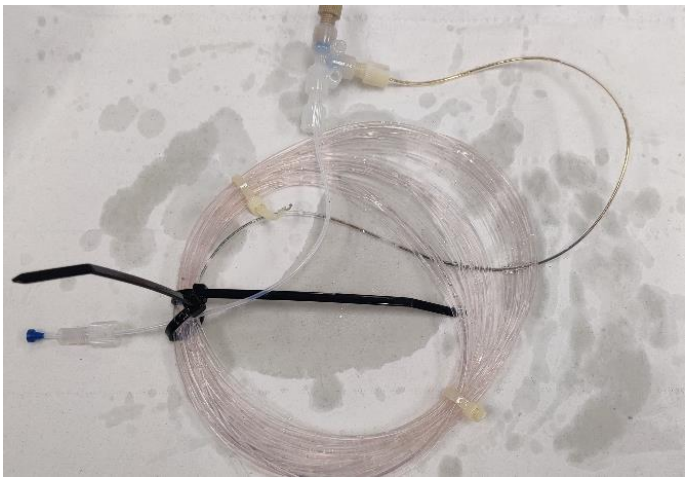

Figure 80. An image showing the PFA reactor tubing after approximately 1 hour of use, the internal wall of the first 30 cm of the reactor tubing is coated in metallic gold.

The nanoparticle solution leaving the reactor also appeared brown, in comparison to nanoparticles synthesised using the same synthetic method in batch (see Section 7.2.2.9 for batch method). This observation, coupled with a wide UV-vis absorption peak, indicated a wide nanoparticle size distribution and/or agglomeration of the nanoparticles, see Figure 81. The synthesis of AuNPs was likely affected by the build-up of fouling on the first section of the reactor.

To prevent reactor fouling from affecting the size distribution/dispersion of the nanoparticles formed within the flow reactor, it was necessary to either eliminate reactor

fouling completely or decrease the internal surface area to volume ratio of the flow reactor. This would mean that less of the reaction solution was in contact with the reactor walls during the reaction. This reduction in internal reactor surface area was achieved through the use of CSTRs.

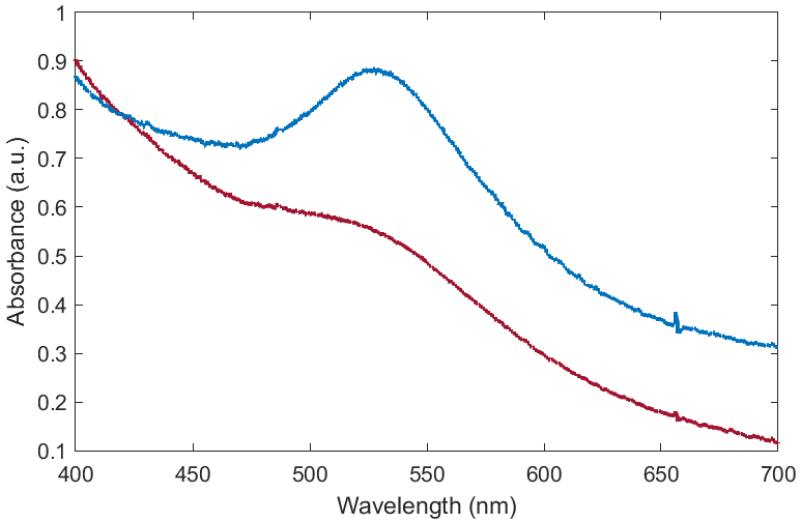

(a)

(b)

Figure 81. (a)UV-vis spectra showing the AuNP solution formed in flow (red) and in batch (blue) and a photograph of the resulting solutions (b) left, showing the nanoparticles formed in flow and right, showing the nanoparticles formed in batch.

3.3.7 AuNP synthesis in a fReactor with preheating

Miniature CSTRs have emerged as alternative continuous reactors for nanoparticle synthesis and multiphasic reactions.[58,199,200] These reactors possess lower surface area to volume ratios, without compromising on mass transfer due to active mixing within each CSTR, which ensures a high degree of solution homogeneity throughout the reactor.[57] Recently miniature CSTR reactors have been used to synthesise silica[200] and InP/ZnS quantum dot nanoparticles.[58]

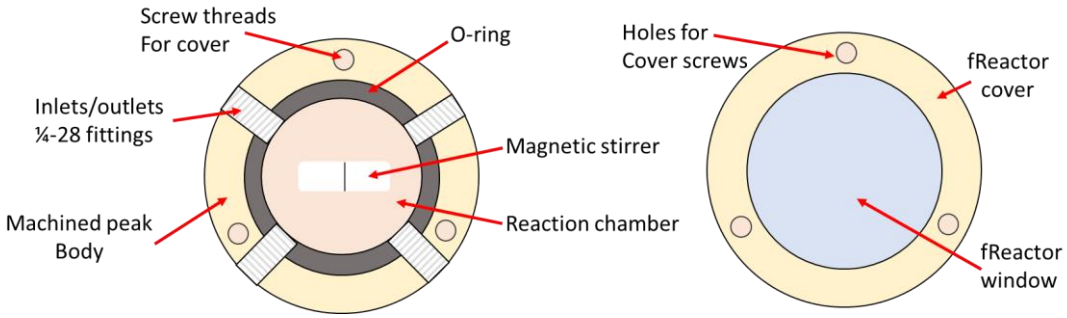

Figure 82. diagram showing annotated design of individual CSTR.

Herein, AuNPs were synthesised using commercially available miniature CSTR reactors (fReactors^{TM}),[57] consisting of reactor modules with an internal volume of 1.55 mL (including stirrer bar), pressure rated to 9 bar, the fReactors can have up to 4 ports liquids to move into and/or out of the reactor, see Figure 82 and Figure 83.

Figure 83. A photograph showing the fReactors used to synthesise AuNPs, cotton wool was used to insulate the tubing connections between the preheating fReactors and the main fReactor.

The reactants were preheated to 100 °C in separate fReactors, before converging within a final fReactor where the nanoparticle formation reaction took place. The connecting tubes between the preheating fReactors and the main reactor were insulated with glass fibre to prevent heat loss. A diagram of the reactor is presented in Figure 84, see Section 7.2.2.10 for full experimental details.

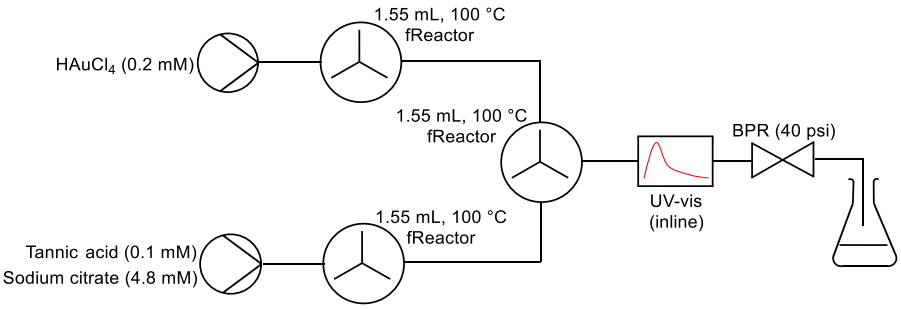

Figure 84. A reactor diagram showing a mixture of sodium citrate and tannic acid, as well as nanoparticle precursor $HAuCl_4$, being pumped through separate preheating fReactors and combined/mixed in a final fReactor for nanoparticle synthesis.

Figure 85 shows time series inline UV-vis absorption spectra values integrated between 500-550 nm. Approximately 30 minutes into the reaction the reducing agent pump stalled, leading to a brief spike in absorption due to an increase in nanoparticle concentration, this was quickly corrected. The reactor then returned to steady-state conditions.

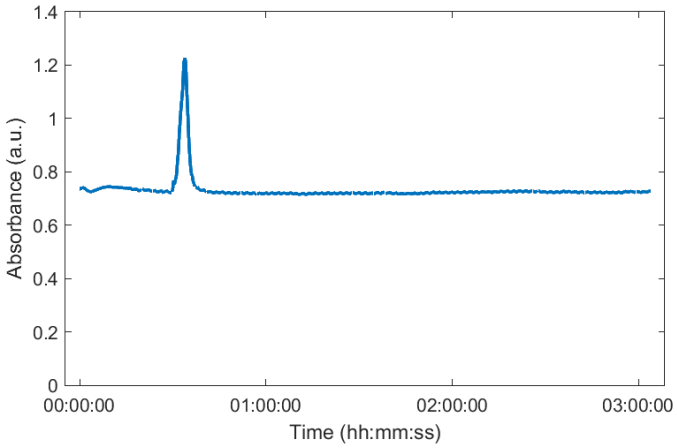

Figure 85. A plot showing the integrated absorption values between 500 - 550 nm measured at the reactor outflow for a fReactor system which uses a mixture of sodium citrate and tannic acid as the reducing agent.

After the conditions of the reactor returned to normal no change in the UV-vis absorption profile was observed for a further 2.5 hours. This indicated that the system was capable of producing nanoparticles with consistent properties over a significant period of time. Figure 86 shows 400 mL of AuNP solution collected from the flow reactor over this period.

Figure 86. An image showing 400 mL of AuNPs collected from the fReactor CSTR.

Figure 87 shows an overlay plot of all of the UV-vis absorption spectra (resolution = one second) taken after 1 hour into the experiment, with an insert to show the spectra in 3D with time as the 3rd axis. This figure confirms that the nanoparticles produced from this reactor were consistent, the narrow peak width also indicates the nanoparticles possessed a relatively narrow size distribution.[201]

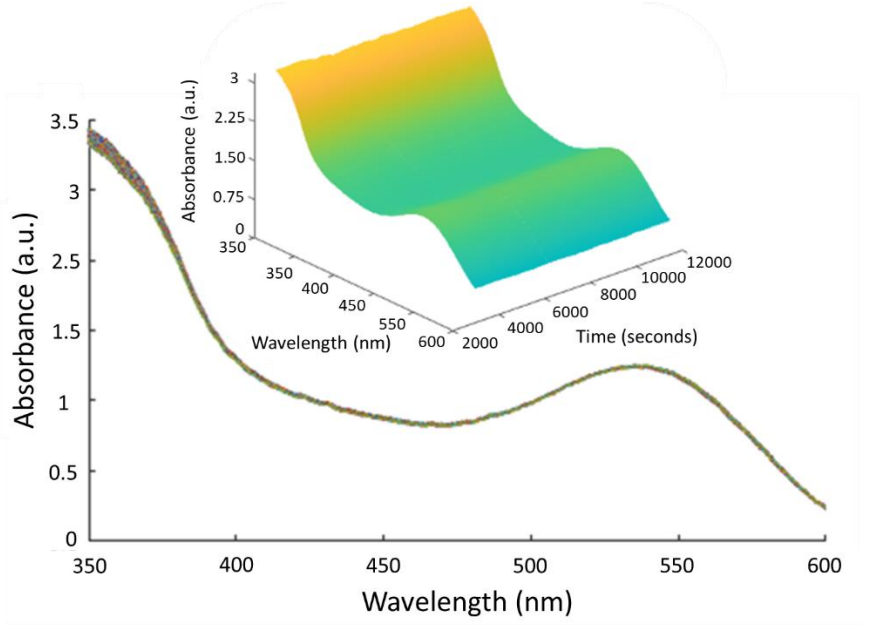

Figure 87. A plot showing overlapping UV-vis absorption spectra for nanoparticles synthesised during the steady-state period of the reactor's operation, no change in the nanoparticle's absorption properties were observed during this period.

3.3.8 Modified fReactor design

A near-instantaneous colour change from pale yellow to ruby red was observed through the window of the first fReactor in the CSTR series. This indicated that the reaction reached completion within only a few seconds. To ensure full conversion of the nanoparticle precursor solution, two additional fReactors were added. Because of the rapid heat transfer from the fReactors to the reacting solution, the preheating fReactors were found to be unnecessary and removed.

The reactor in Figure 88 shows the final reactor design used to synthesise AuNPs, a CSTR cascade made up of three fReactors in series. This reactor was tested with the precursor and reducing agent solutions pumped through the reactor with equal and total combined flow rates of 1, 3 and 4 mL/min. The reactor was flushed with water between each experiment, full experimental details can be found in Section 7.2.2.11.

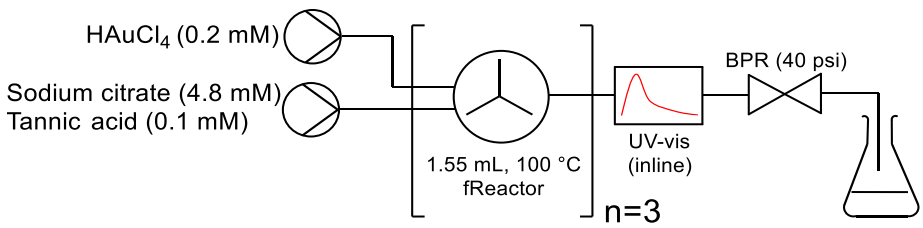

Figure 88. A reactor diagram showing gold nanoparticle precursor $HAuCl_4$, being pumped into a series of 3 fReactors with *a mixture of sodium citrate and tannic acid reducing agents at 100 °C.*

Figure 89 shows the time taken for the reactor to reach steady-state conditions at different combined total flow rates/residence times. Full conversion was reached within 8 minutes for all flow rates but within 3 minutes when reagents were pumped through the reactor with a total combined flow rate of 4 mL/min. This was equivalent to a residence time of 1.16 min for the reactor, minimising wait times between steady-state periods.

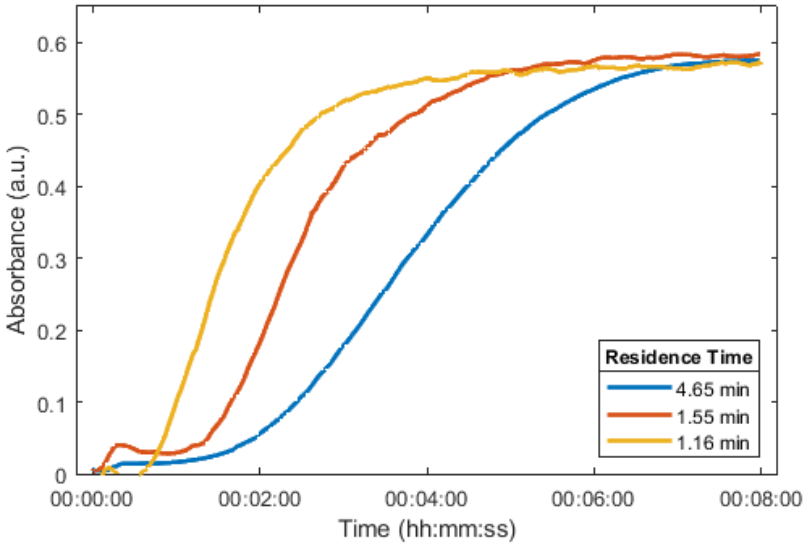

Figure 89. The integrated UV-vis absorption profiles for total combined flow rates of 1,3 and 4 mL/min.

Reactor fouling was observed only within the first fReactor of the series (Figure 90), however, this build-up was very gradual and did not significantly affect the UV-vis absorption properties of the nanoparticles produced by the CSTR. This indicated that the fouling within these CSTRs while using the nanoparticle synthesis method described above, had little to no influence over the properties of the nanoparticles produced by the reactor.

Figure 90. Clean fReactor (left) followed by stages 1, 2 and 3 (right), fouling was observed only within the first reactor of the series.

3.3.9 Continuous flow synthesis of AuAgNPs

To synthesise nanoparticles with different Au/Ag metal ratios, an additional $AgNO_3$ silver precursor stream was added to the flow reactor, see Figure 91. The separate solution reservoirs of $HAuCl_4$ and $AgNO_3$ were both made up to 0.4 mM and pumped into CSTRs heated to 100 °C, the flow ratios of these two streams were changed while maintaining a total combined flow rate of 2 mL/min. Sodium citrate (4.8 mM) was also pumped into the reactor as a reductant and stabiliser along with tannic acid (0.1 mM) at 1.5 mL/min. Finally, a K_2CO_3 solution (10 mM) was simultaneously pumped into the reactor at 0.5 mL/min. This was used as a pH mediator, K_2CO_3 has been found in previous studies to help reduce the nanoparticle size distribution of the particles produced using this method.[33] Experimental details can be found in Section 7.2.2.12.

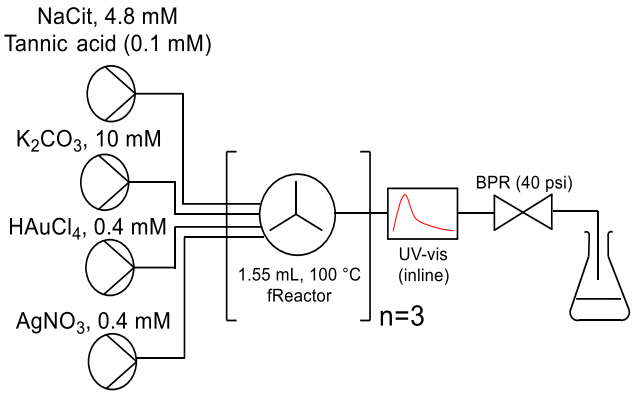

Figure 91. A diagram showing the reactor used to synthesise AuAgNPs.

A photograph showing the range of AuAgNP solutions that could be synthesised using the reactor setup described above is shown in Figure 92. The colour that can be observed for the different alloy ratios ranges from yellow (pure silver nanoparticles) and various shades of orange (Au:Ag nanoparticle alloys) to red (pure gold nanoparticles).

Figure 92. A photograph of the AuAgNPs showing the effect of alloy composition on the colour of the nanoparticle solutions, with the samples from left to right increasing in Au composition. Far left 100% silver with samples increasing in gold content by 10% up to 100% gold on the far right.

The UV-vis absorption spectra for the array of nanoparticles presented in Figure 92 are shown below in Figure 93. In previous studies, the presence of a single peak rather than

two discrete peaks has been found to indicate that the nanoparticles form an alloyed species rather than discrete silver and gold nanoparticles, a finding which has been further confirmed with TEM, EDS and EXAFS analysis.[159,202] In the case that a solution of pure AgNPs and AuNPs are mixed two peaks form.

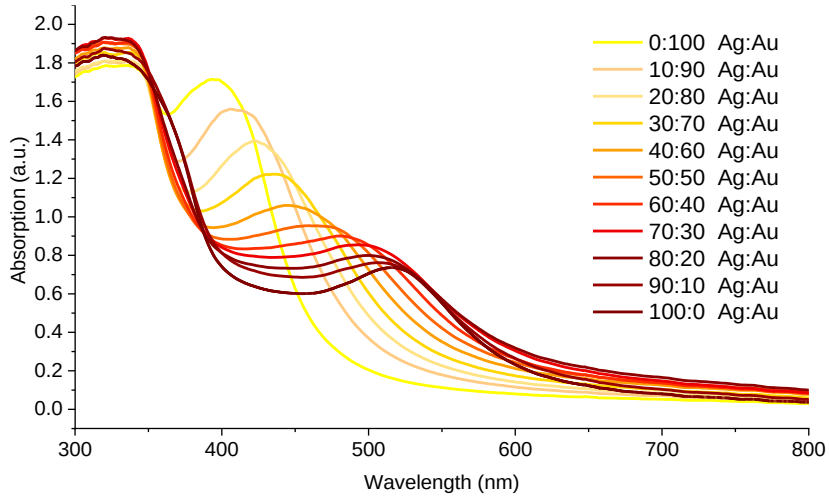

Figure 93. UV-vis spectra corresponding to AuAgNP solutions synthesised using the CSTR cascade, changing the flow ratio of Au and Ag precursor solution pumped into the reactor.

The λ_{max} wavelength of the absorption spectra was tracked, to monitor changing nanoparticle composition in the reactor and confirm steady-state conditions, at a variety of metal precursor pump flow rate ratios over 2.5 hours. Figure 94 shows the changing λ_{max} wavelength during an experiment where the ratio between the gold and silver solutions being pumped into the reactor was changed by 10% every 15 minutes, from 1:0 to 0:1 Ag:Au in increments of 0.1. Confirming the capability of the reactor to synthesise a range of AuAgNP alloys without any decline in conversion due to reactor fouling.

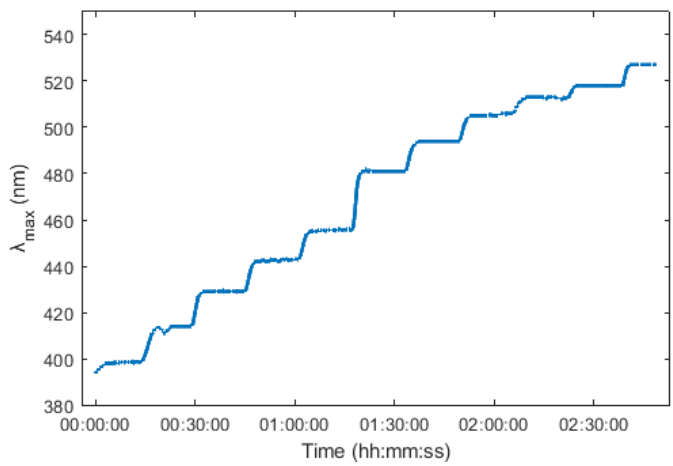

Figure 94. A plot showing changing λ_{max} wavelength as the percentage of Au in the AuAgNPs was increased by 10% every 15 minutes, with pure silver nanoparticles at t=0 and pure gold nanoparticles at t = 2.5 hours.

3.3.10 TEM-EDS analysis of AuAgNPs

A range of AuAgNP samples from Section 3.3.9 were analysed with TEM-EDS to determine the size distribution, shape and composition of the nanoparticles in each sample. Figure 95 shows an example TEM image of the gold-silver nanoparticle alloys synthesised in continuous flow. A comprehensive analysis of the TEM images with histograms corresponding to each sample can be found in the Appendix (Section 8.1.4).

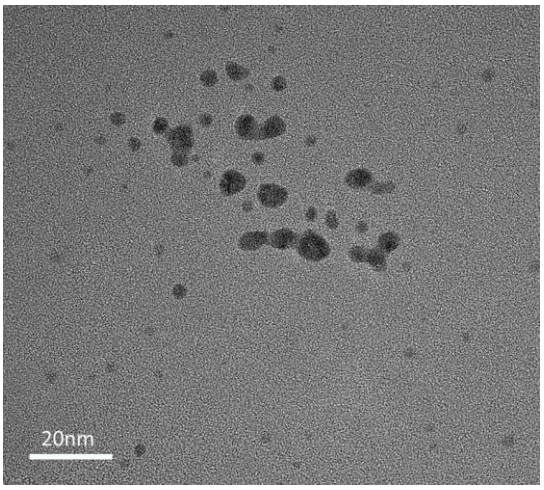

Figure 95. A TEM micrograph showing an example of the AuAgNPs (40:60 Au:Ag) collected from the outlet of the flow reactor developed in this chapter, see Appendix, Section 8.1.4.

TEM analysis was performed on nanoparticles with metal ratios between 0:1-1:0 Au/Ag at intervals of 0.2. Table 8 shows the mean and standard deviation size ranges for each AuAgNP sample. With the exception of the pure AgNPs, the nanoparticle alloys all fell within a similar size range with a mean average size of 6 +/- 2.3 nm. The nanoparticles were mostly spherical, some aggregation was observed although it is possible that this aggregation occurred during sample prep as the nanoparticle suspensions dried on the TEM sample grids.

Table 8. The mean average sizes and standard deviation size variation for the AuAgNPs sampled in this chapter.

NP alloy ratio (Au:Ag)	Mean average size	Standard deviation (+/- nm)
0.0:01	12.06	5.45
0.2:0.8	6.22	2.59
0.4:0.6	4.12	1.84
0.6:0.8	5.72	2.68
0.8:0.2	5.64	1.24
01:0.0	7.91	3.31

The larger pure AgNPs likely formed due to the slower rate of Ag^+ reduction compared to $AuCl_4^-$, as Ag^+ ions possess a lower redox potential,[203] providing fewer nucleating particles and more opportunities for nanoparticle growth.

To confirm this theory, a kinetic study was performed in batch, comparing the growth rates of nanoparticle alloys with different ratios of Au and Ag, see experimental Section 7.2.2.13. Time-series UV-vis absorption spectra integrated between 450 and 500 nm were recorded for AuNPs, AgNPs and a range of AuAgNP alloys, see Figure 96.

These results show that AgNPs are formed relatively slowly in solution, taking over 2 minutes to form and stabilise in solution. In comparison, AuAgNPs were fully reduced at the same rate as AuNPs, when placed under the same reduction conditions. This is likely because the rapidly formed AuNPs acted as a catalyst for the reduction of Ag^+.

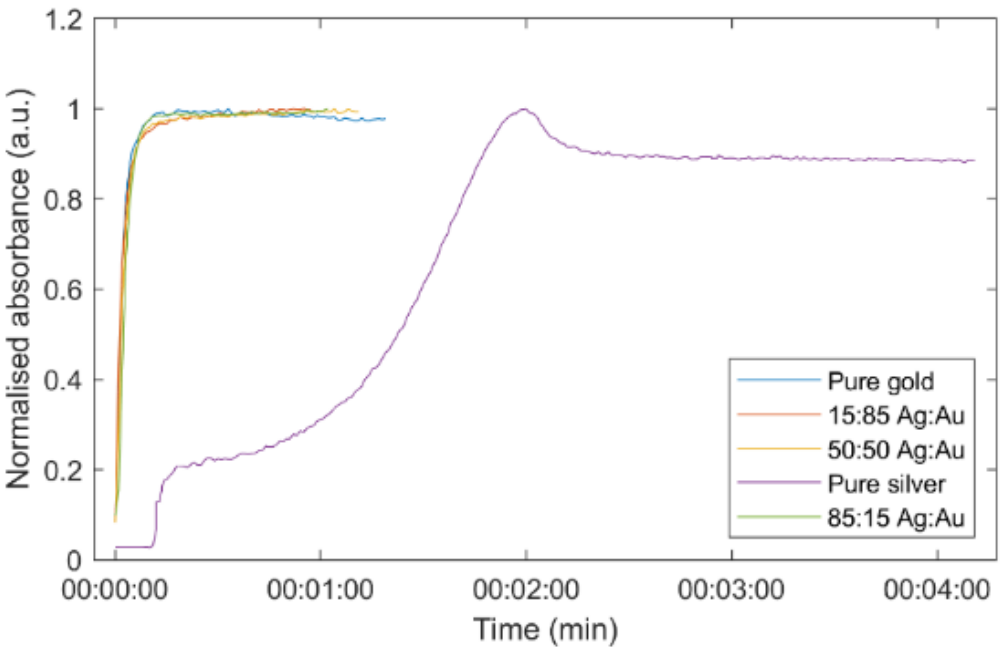

Figure 96. Time-series UV-vis absorption spectra integrated between 450 and 500 nm for AuNPs, AgNPs and a range of AuAgNP alloys formed in batch.

Energy-dispersive X-ray spectroscopy (EDS) was also used during TEM analysis to further determine the amount of Au and Ag contained within each sample, a multi-polynomial model was used for the background correction and a Brown-Powell model (a semi-empirical ionisation cross-section model) was used to determine the relative ratios of each metal. An example EDS spectrum from a sample containing AuAgNPs with a metal ratio of 60:40 Au:Ag is shown in Figure 97.

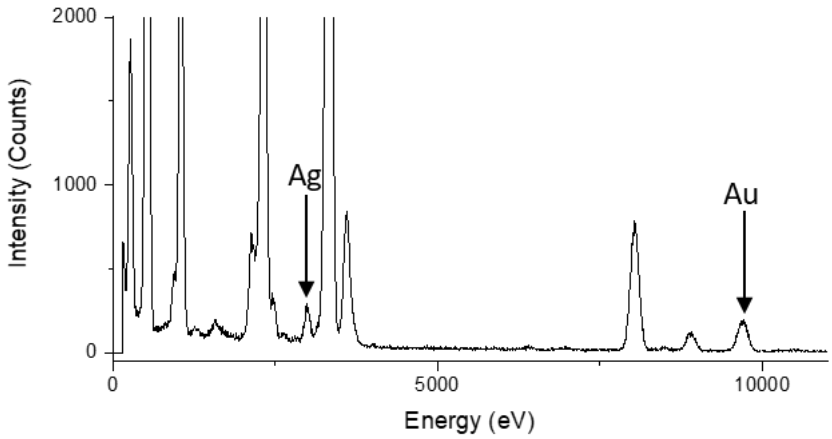

Figure 97. An example EDS spectrum for an AuAgNP sample with an Au:Ag ratio of 60:40.

When all of the relative metal ratios determined using the EDS data were compared, a near-linear relationship was observed between the fraction of gold in the sample and the ratio of different metal precursors used to synthesise the nanoparticles, see Figure 98.

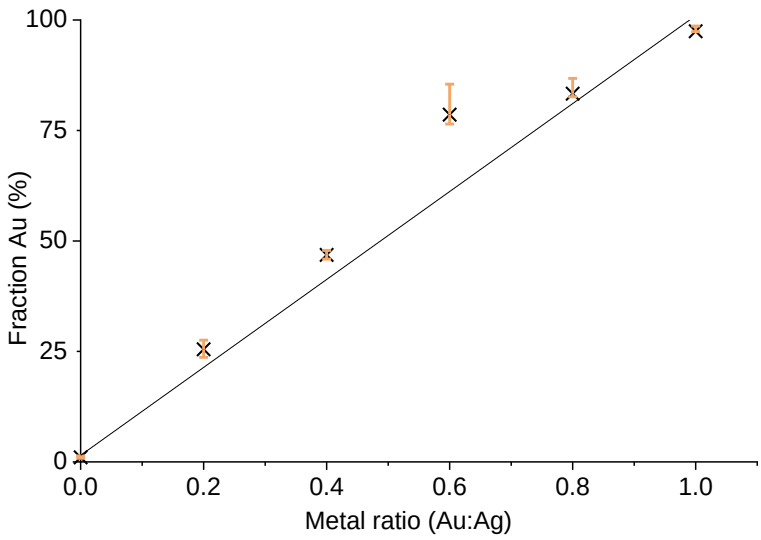

Figure 98. Plot showing the fraction of nanoparticles containing Au (%) with the remainder made up of Ag from EDS analysis.

3.4 Summary and future work

A synthetic route for the synthesis of AuNPs and AuAgNPs with different Au:Ag ratios were developed for continuous flow. The procedure was tested in batch, before being transferred to continuous flow for use in a self-optimising system. The issue of fouling was overcome through a combination of increasing the reaction rate of nanoparticle formation in solution and strategies to reduce the rate and influence of fouling on the reactor walls.

Previous work has shown that AuNPs, AgNPs and AuAgNPs can be synthesised using continuous flow methods, however, these articles tend to adopt segmented flow strategies to avoid issues related to reactor fouling. Despite the prevalence and effectiveness of segmented flow regimes in the literature, these were avoided due to the complications associated with implementing such a system in a telescoped reactor system.

This chapter describes, to the best of the author's knowledge, the first reported non-segmented continuous flow method of gold-silver nanoparticle synthesis. Where the flow reactor's ability to produce nanoparticle catalysts consistently over several hours, without a decline in conversion due to reactor fouling, was proven with continuous monitoring with inline UV-vis spectroscopy.

Several reactor design iterations and nanoparticle synthesis methods were attempted before reaching the final reactor design. These included changing the PFTE reactor tubing material to smoother PFA tubing, then from a tubular reactor to a CSTR cascade. The synthesis of AuNPs was attempted using different reducing agents, ascorbic acid, sodium borohydride and finally tannic acid. Tannic acid was able to reduce gold and silver metal ions while also producing stable nanoparticle suspensions.

Continuously monitored batch reactions for the synthesis of AgNPs required over 2 minutes to fully convert to nanoparticles. However, under the same reaction conditions, AuNPs and AuAgNPs reached 100% conversion only 20 seconds after the reaction reagents were mixed. These kinetic experiments confirmed that the reactor was capable of producing nanoparticle solutions with a 100% conversion rate during the synthesis of either pure AuNPs or AuAgNP alloys but not pure AgNPs.

Nanoparticle samples from the final reactor iteration were analysed with TEM-EDS which showed the nanoparticles possessed a mean average size of 6 ± 2.3 nm with the exception of the pure silver nanoparticles which were slightly larger (12.1 ± 5.4 nm). EDS confirmed the nanoparticles contained a ratio of gold and silver to be proportional to amounts of Au and Ag metal precursor introduced into the flow reactor.

The next stage of this work will involve implementing this reactor and nanoparticle synthesis method into a tandem self-optimising system. Where the nanoparticles synthesised in the first reactor stage are pumped into a second reactor for performance-based optimisation in a pharmaceutically relevant reaction.

Chapter 4

Modelling nanoparticle catalysis optimisation

The optimisation of a chemical or material synthesis method requires the iterative process of performing experiments to determine the effect of different reaction parameters on a desired outcome such as reaction efficiency and/or product quality. Several common optimisation strategies were discussed in section 1.3 of the introduction. Choosing which algorithm to use in each case can be a difficult decision, owing to a large number of available optimisation algorithms. In this chapter, a systematic computational approach was developed to compare a range of optimisation algorithms commonly used in self-optimising flow reactors, a summary of which is shown in Figure 99.

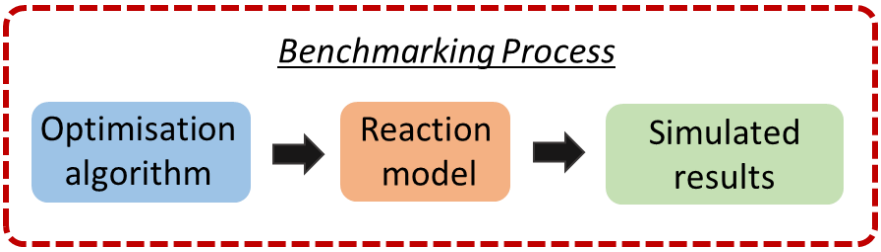

Figure 99. A summary of the approach used to compare optimisation algorithms in this chapter. A variety of algorithms were benchmarked using a reproducible, simulated reaction. The outcomes of these optimisation processes were then used to compare the efficacy of each algorithm.

4.1 Introduction

As discussed in Chapter 1, Section 1.3 optimisation algorithms have become a major technology used to solve many problems which have multiple possible solutions, often with complex economic and performance interactions. In a survey of experts from a variety of industries including power generation, aerospace, automotive construction and software, respondents reported the difficulty of choosing one technique over others as one of the most difficult challenges faced by their organisations.[204]

To solve this challenge researchers have become interested in developing methods which allow different algorithms to be efficiently and effectively compared/ benchmarked.[205,206] Benchmarking of optimisation algorithms involves the fair and systematic comparison of either: the same algorithm with different hyperparameters; different implementations/versions of the same algorithm or different optimisation algorithms on a series of test problems.[207]

During their initial development, before they are used in specific applications, these algorithms are normally compared using benchmark functions. These functions are purely mathematical and computationally cheap to evaluate. For example, the Matyas benchmarking function, which has no local minima other than the global one, is shown in equation (9). The optimisation is performed with x values ranging from -10 to 10 and the optimum of this function is 0 when both x_1 and x_2 equal 0.

$$f(x) = 0.26(X_1^2 + X_2^2) - 0.48x_1x_2 \tag{9}$$

There are a variety of benchmark functions available, however, there is no standardised set to be used for the purpose of comparing optimisation algorithms. Common practice is to compare optimisation algorithms with a diverse range of benchmark functions such as the ones shown in Figure 100.

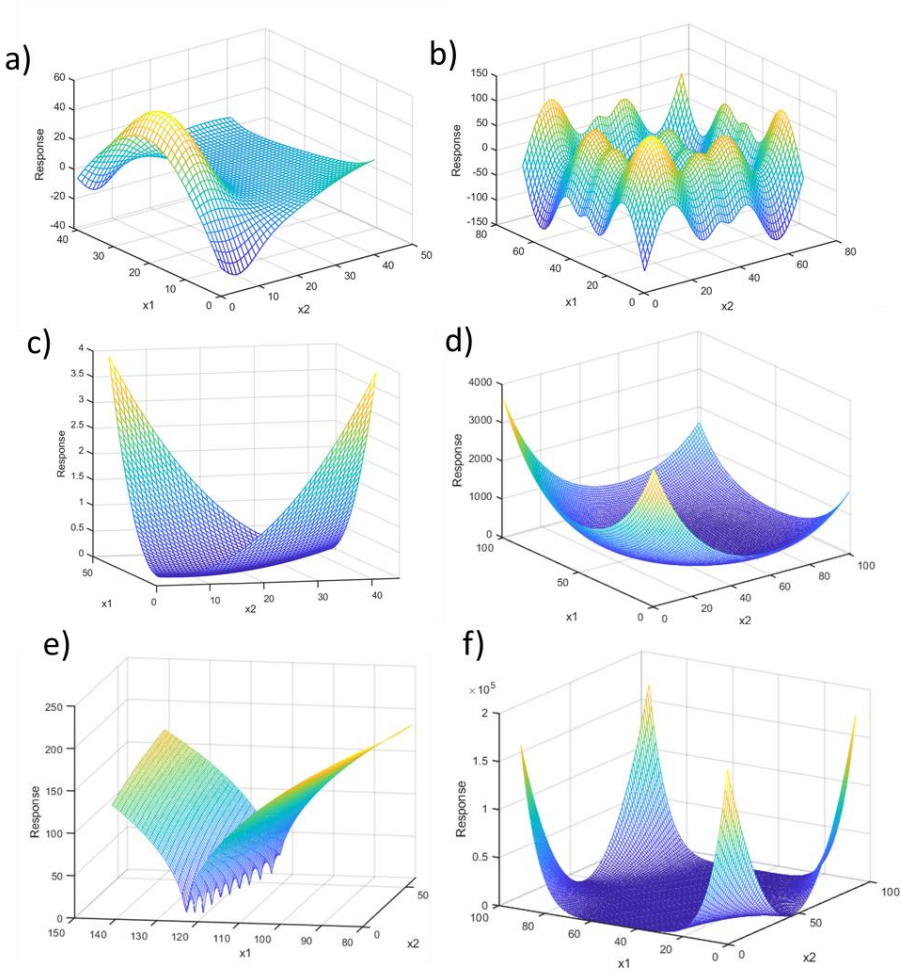

Figure 100. Examples of unconstrained single-objective response surfaces, these types of functions are commonly used to benchmark optimisation algorithms. These algorithms are each named according to their shape or after their creators: a) Bird, b) Schweffel, c) Matayas, d) Zettl, e) Bukin, and f) Beal.

In a study by S. Arora and S. Singh, 30 benchmark functions including the Matyas and Schwefel functions were used to evaluate the butterfly global optimisation algorithm (an algorithm inspired by the food foraging behaviour of butterflies). In this study, the butterfly algorithm was compared against other similar metaheuristic algorithms which mimic natural phenomena, such as the honey bee algorithm.[208] During this process the number of function evaluations required to optimise various test functions were compared for the different algorithms. In the case that there were the test functions contained multiple local optima both the number of local optima found and the ability of the algorithm to escape local optima avoiding premature convergence were also investigated.[209]

The evaluation approach used in this study was based on a general framework proposed by Shilane *et al.* Where 100 optimisation iterations were performed with each of the optimisation algorithms within every benchmarking function. As the algorithms tested in this study followed stochastic processes, 30 Monte Carlo runs were performed for each of the algorithms/benchmarks. The best, mean, median, standard deviation and worst results for each optimisation were recorded and compared in each case.

Convergence plots were used to visualise the comparative performance of the optimisations in this study. Convergence plots show the running best optimisation value recorded after each function evaluation. The convergence plot showing how each of the algorithms performed with the Schweffel function is shown in Figure 101.

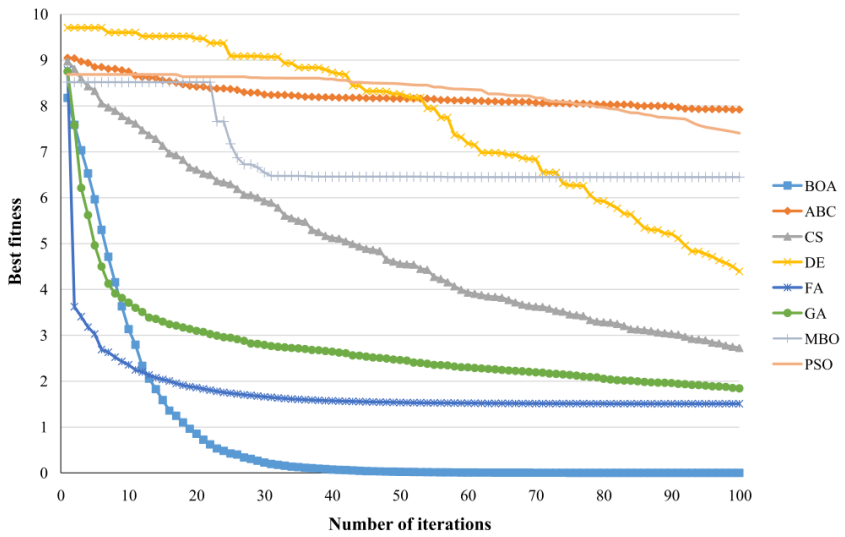

Figure 101. A convergence plot showing the averaged cumulative best fitness of each of the algorithms compared in this study, benchmarked using the Schwefel function with the butterfly algorithm[209] against seven other optimisation algorithms.[105,208,210–214] (Reproduced with permission from ref [209] Copyright 2018, Springer Science & Business Media. All rights reserved.)

The authors found that in most cases the butterfly algorithm significantly outperformed other similar algorithms during benchmarking experiments, this was in terms of both accuracy and the number of iterations required to reach the optima, particularly in cases involving noisy surfaces.[215]

However, it should not be concluded from the results of studies such as this that one algorithm is "better" than the other optimisation algorithms tested. As often is it the case that for any algorithm an observed increase in performance over one type of problem class is offset by decreases in performance over another class.[216] For this reason, it is important when selecting algorithms for a specific purpose, that the algorithms are benchmarked using functions which reflect their intended application. As synthetic benchmark functions are not typically designed to mimic real chemical space, it is instead more appropriate to use kinetic models to benchmark optimisation algorithms in the context of benchmarking chemical reaction optimisation algorithms.

In 2020 the Lapkin group published a paper comparing 6 single and multi-objective algorithms designed to find optimum reaction conditions with a minimal number of iterations. In this study, the group evaluated the: Nelder-Mead Simplex,[217] SNOBFIT,[106] single objective Bayesian optimisation (SOBO),[218] GRYFFIN,[219] TSEMO[220] and Deep Reaction Optimisation (DRO)[221] algorithms. These benchmarking functions were based on the kinetic models for an S_NAr and C-N cross-coupling reaction, with the input variables of catalyst concentration, temperature, residence time and concentrations. The objectives were space-time yield, E-factor for the S_NAr and yield and cost for the C-N cross-coupling reaction.

Both simulated reactions were run through 50 iterations with each of the optimisation algorithms. On average the Bayesian optimisation algorithms (TSEMO, GRYFFIN and SOBO) showed the best performance in terms of finding the most optimal points after 50 experiments, with TSEMO showing the best-in-class performance in terms of total hypervolume discovered upon termination of the optimisation run in both of the reactions.[222] However, as previously discussed, an optimisation strategy well suited to one problem will be inherently bad for another – this is commonly referred to within the optimisation community as the principle of "no free lunch".[216] It is therefore important to understand both the strengths and weaknesses of each type of optimisation algorithm. Developing workflows which allow efficient and cheap evaluation of optimisation algorithms is one way of gaining this understanding.

4.2 Kinetic model development

Kinetic models allow the prediction of reaction rates under different conditions. These models are normally determined by obtaining time-series concentration data throughout a reaction under a range of conditions.[223,224] This kinetic data can be obtained by periodically or continuously analysing a batch reaction using a quantitative analytical technique such as HPLC,[225] GC,[226] UV-vis spectrocopy,[131] or NMR[227] to determine the concentrations of different compounds in these samples over time. Continuous flow platforms have also been used to determine kinetic model parameters in a range of reactions by sampling the reactor outlet stream for different residence times at a range of steady-state conditions[50,228] or using transient conditions.[229] This approach has even been used to determine the kinetics of a heterogeneously catalysed hydrogenation reaction.[230]

4.2.1 The Langmuir-Hinshelwood kinetic model

The heterogeneously catalysed reduction of nitrophenol is currently widely accepted to follow Langmuir-Hinshelwood (LH) kinetics.[119,131,231–234] The LH model is described by equation (10) below, where: S is a factor relating to the number of active sites in the system (in this case the estimated surface area of the AuNPs in the reaction), k is the rate constant, C_{Nit} and C_{BH_4} represent the concentrations of the nitrophenol and sodium borohydride species respectively, and K_{Nit} and K_{BH_4} are the adsorption coefficients of nitrophenol and sodium borohydride respectively.

$$v = \frac{d\left[C_{aminophenol}\right]}{dt} = -\frac{d[C_{Nit}]}{dt} = -\frac{d[C_{BH4^-}]}{dt}$$
$$= \frac{k \cdot S \cdot K_{Nit}[C_{Nit}]K_{BH4^-}[C_{BH4^-}]}{(1 + K_{Nit}[C_{Nit}] + K_{BH4^-}[C_{BH4^-}])^2} \qquad (10)$$

This model consists of several steps occurring in parallel, these steps are represented by the LH model diagram shown in Figure 102. In a mechanism proposed by Wunder *et al.*, BH_4^- ions react on the surface of the nanoparticles forming BO_2^-, H_2O and H^-. The H^- ions then react with surface adsorbed 4-nitrophenol (Nit) forming 4-aminophenol and water, finally these products desorb from the nanoparticles back into solution. The diffusion, adsorption and desorption processes are assumed to be fast relative to the reduction of 4-nitrophenol which is the rate-limiting step.[131]

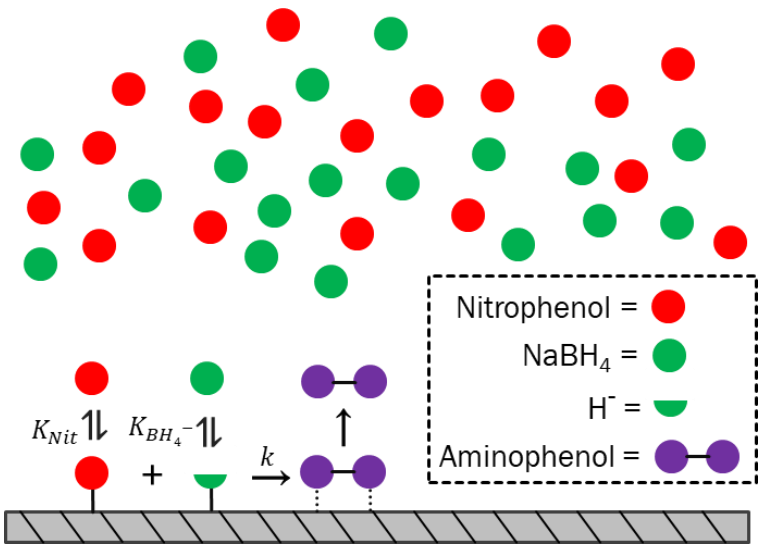

Figure 102. A diagram showing the conversion of 4-nitrophenol to 4-aminophenol on the surface of a solid catalyst via the Langmuir-Hinshelwood model. Here H^- dissociates from $NaBH_4$ and on the surface of the catalyst, both components then react to form aminophenol which then desorbs.

The Eley–Rideal (ER) model has been proposed as an alternative mechanism for the nanoparticle catalysed reduction of nitrophenol.[235,236] However, a much larger body of research and more recent studies which specifically investigate the kinetics of reduction of nitrophenol on heterogeneous catalysts, provide evidence supporting the theory that this reaction takes place via a LH mechanism.[119,131,231–234] The key difference between these two models is that only one of the reactant molecules is adsorbed onto the catalyst surface in the ER mechanism. The other reactant molecules react with the adsorbed molecules without adsorbing to the catalyst surface, see Figure 103.

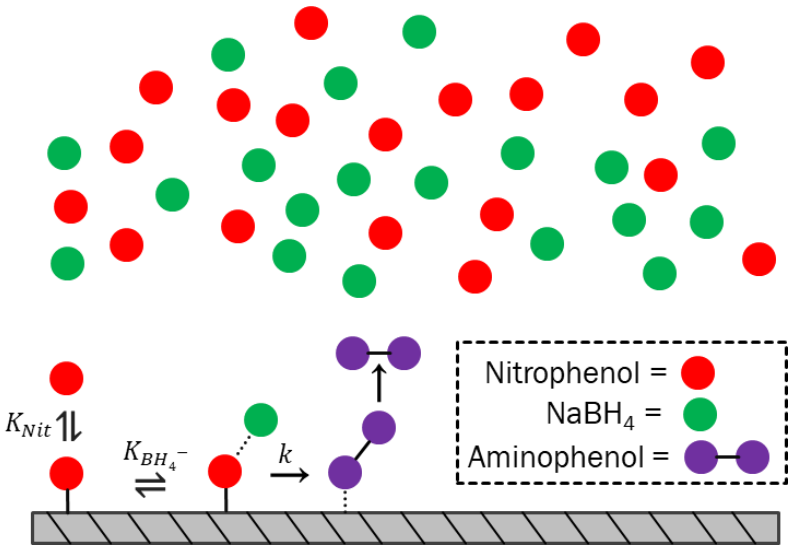

Figure 103. A diagram showing the conversion of 4-nitrophenol to 4-aminophenol on the surface of a solid catalyst via the Eley–Rideal mechanism. Here only the aminophenol adsorbs onto the surface of the catalysts before the other reacts with this adsorbed molecule without adsorbing itself.

Reaction conversion can be monitored continuously using UV-vis spectroscopy, the absorption profile @400 nm (corresponding to nitrophenol) decays linearly with concentration as the reaction proceeds. Previous studies and work conducted in Section 2.1.1, have confirmed that this reaction proceeds from nitrophenol to aminophenol with no stable intermediates or side products.[237]

Equation (11) describes how the apparent rate constant k_{app} is normally obtained when benchmarking catalysts using this reaction, this value is commonly used to compare the activity of different catalyst species. A_0 corresponds to the absorbance of nitrophenol at the start of the reaction just after the reagents are mixed and A_t corresponds to the absorbance of nitrophenol at time (t) during the reaction. When $NaBH_4$ is present in excess the reaction proceeds via pseudo-first-order kinetics,[122] allowing k_{app} to be obtained by taking the gradient of ln (A_t/A_0) plotted against time.

$$\ln\left(\frac{A_t}{A_0}\right) = -k_{app} \cdot t \qquad (11)$$

The model in this case can be confirmed using one of two methods. Either, by changing the concentration of nitrophenol while keeping the concentrations of the catalyst and $NaBH_4$ constant or by changing the concentration of $NaBH_4$ while keeping the concentrations of the catalyst and nitrophenol constant.

In cases where a surface catalysed reaction proceeds via an ER mechanism and the hydride ions adsorb onto the surface of the catalyst, k_{app} values would be expected to increase as the concentration of nitrophenol increases. As the two starting reagents would not be competing for surface sites on the catalyst, meaning the rate of reaction would increase as the concentration of nitrophenol increases.

Whereas, in the cases where surface catalysed reactions proceed via an LH mechanism, the k_{app} values would be expected to decrease as the concentration of nitrophenol increases beyond the concentration of $NaBH_4$. This is due to saturation of surface sites with nitrophenol preventing hydride ions from adsorbing onto the surface of the catalyst.

In a kinetic study for the catalytic reduction of nitrophenol with AuNPs by Thawarkar *et al.*,[232] researchers found that k_{app} values decreased as nitrophenol concentrations were increased beyond the concentration of $NaBH_4$ in solution, while subsequently

increasing upon an increase in the concentration of $NaBH_4$. Thus, supporting the theory that this reaction takes place via a LH mechanism.

4.2.2 LH kinetic model fitting

The benchmarking function used to evaluate the optimisation algorithms in this chapter was based on the LH kinetic model. A kinetic fitting methodology was developed to determine the absorption coefficients and rate constants of the AuNP catalysed nitrophenol reduction reaction optimised previously in Chapter 2.

The LH model is a rate equation which allows one to determine the rate of change of reactant/product concentration as a function of the concentration and temperature of a reaction. As a reaction proceeds the concentration of reactants/products decrease and increase respectively, therefore the rate of reaction changes throughout the reaction. This meant that the LH kinetic model alone could not be used to predict the reaction outcome.

A Runge-Kutta solver function (MATLAB ODE15s) was used to generate kinetic reaction profiles from the LH model described in differential equation (10). Different kinetic parameters were applied iteratively to the LH model using a genetic algorithm,[238] after each iteration a set of predicted reaction conversions for the reaction conditions performed in Chapter 2 were generated and compared against the actual conversion data using kinetic fitting software developed by Taylor *et al*.[239]

$$SSE = \sum_{x=1,2,3,\ldots,n} (E_x - S_x)^2 \tag{12}$$

A genetic algorithm was then used to minimise the sum of squared error (SSE) in equation (12), where: E_x and S_x were experimental and simulated data points from each experiment (x) and n was the total number of experiments, generating the following rate constants: k = 2.46 $M^{-1}s^{-1}$, K_{Nit} = 12.17 and K_{BH_4} = 1.47. Upon identifying the kinetic parameters for this reaction, it was possible to create a kinetic model. This allowed for the prediction of reaction conversion under different experimental conditions, both in lab experiments and *in silico.* A summary of this approach is shown in Figure 104.

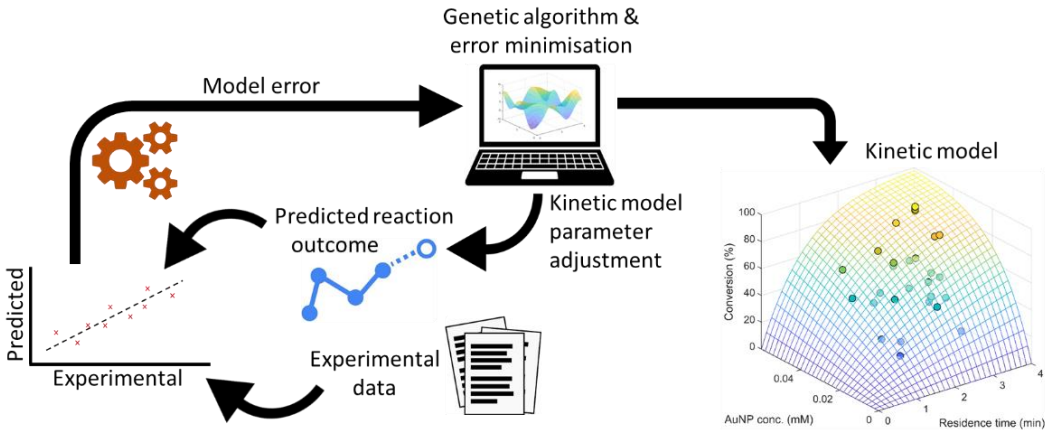

Figure 104. A graphical summary of the approach used to generate the kinetic model in this chapter.

The model was validated by predicting the reaction kinetics of a AuNP catalysed 4-NP reduction reaction performed in a batch reactor, with a two-fold increase in 4-NP concentration compared to the flow optimisation study, *i.e.*, using conditions outside of the range used to generate the data set that was used to create it. The resulting extrapolated reaction kinetics showed good agreement with the model prediction, with a residual error of only ±1.85%, see Figure 105 (experimental method described in section 7.3.1).

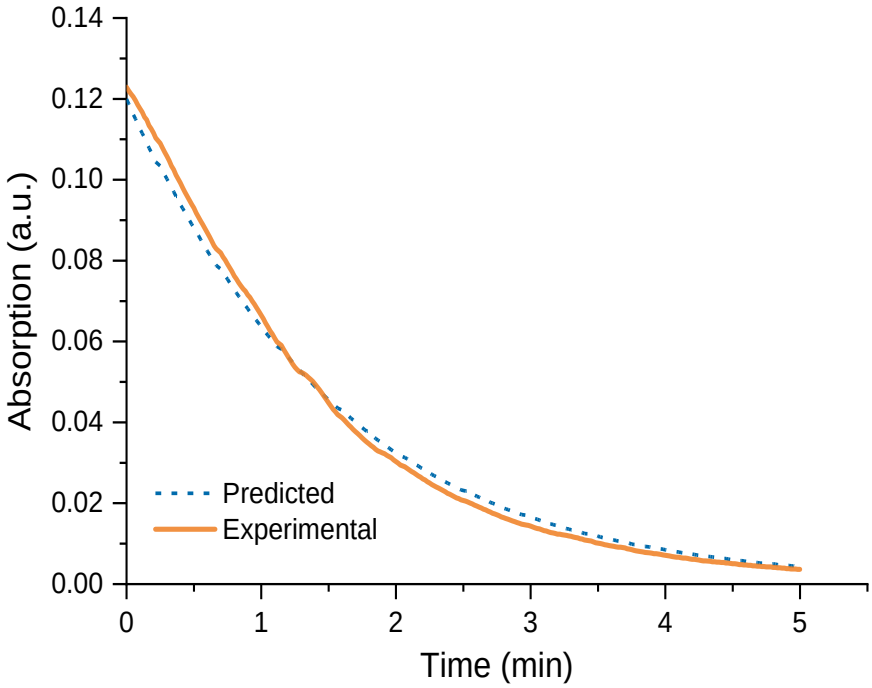

Figure 105. A plot showing predicted versus experimental kinetic profiles for a batch reduction of nitrophenol reaction.

The surface plot shown in Figure 106 describes how reaction conversion changes with respect to nanoparticle concentrations and residence time, with a nitrophenol starting

concentration of 0.6 mM. Experimental data points were also included in Figure 104 for comparison with the simulated surface. Increasing both the residence time (min) and nanoparticle surface area ($m^2 L^{-1}$) resulted in higher reaction conversion, Lin *et. al.* found similar results when modifying the size of Al_2O_3 supported AuNPs between 3.8 and 8.2 nm.[31]

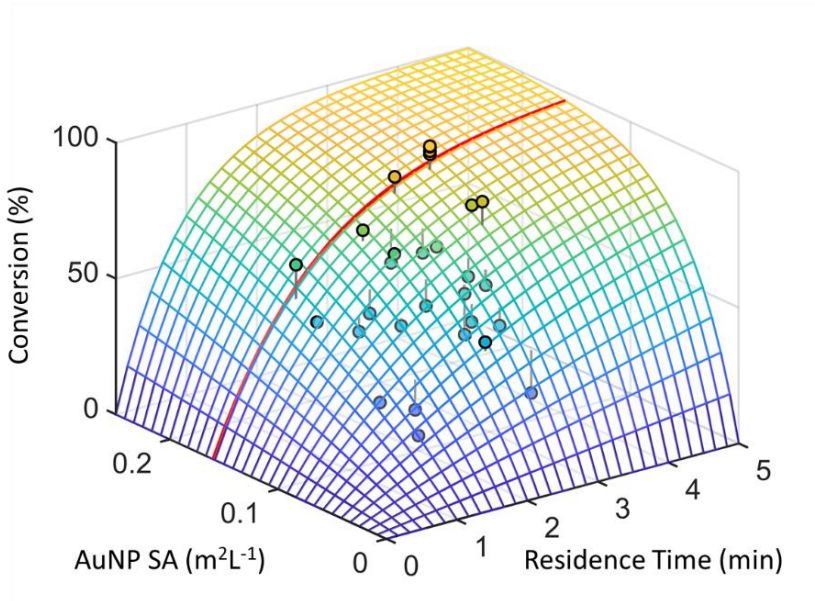

Figure 106. A plot showing the predicted reaction conversion (mesh surface) under different nanoparticle concentrations and reactor residence times, with the concentration of NaBH4 held at 1.5 mM to aid visualisation. Experimental data (coloured points) are overlaid for comparison with the model, the red line shows the simulated kinetic reaction conversion versus time.

4.2.3 Model extrapolation and scalarisation

The kinetic model was extrapolated beyond the existing data set to predict reaction outcomes outside the experimental data range. This extrapolated model is presented in Figure 107 relative to the experimental data. This 3D plot shows that with enough time and catalyst, the reaction always reached 100% conversion with an infinite plateau beyond the point at which enough catalyst and residence time was provided for the reaction to proceed.

Maximizing reaction conversion for a predictable response surface such as this would be trivial for most optimisation algorithms, as the maximum conversion value is reached by maximising the input variables. An alternative approach to solve this problem was to modify the response surface to reflect reaction efficiency as well as reaction conversion.

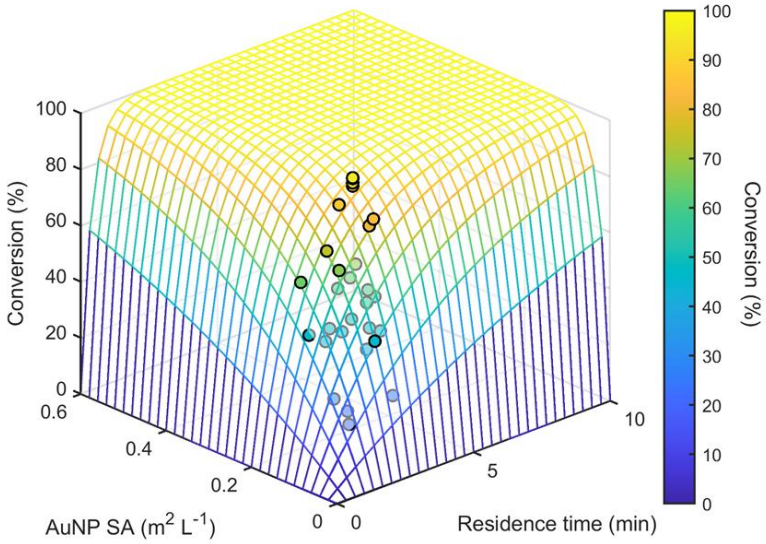

Figure 107. A plot showing the extrapolated model, a large flat plane is observed as 100% conversion is reached at high residence times and catalyst surface areas.

This approach is known as optimisation by scalarisation and was achieved by applying weighting factors to each of the input variables, see equation (13).

$$reaction\ efficency = conversion - ((res.time \times\ 0.6) + catalyst\ conc. \times 60)) \tag{13}$$

In this example weighting factors 0.06 and 60 were chosen for residence time and catalyst concentration respectively. These weighting factors were selected to create a symmetrical response surface and prevent the optimisation algorithm from favouring one variable over the other. In a study by Fitzpatrick *et. al.*, a scalarisation function was used to reduce resource consumption while maximising reaction conversion. In this study weighting factors were added to allow the importance of different terms within their scalarisation equation to be increased or decreased.[240] In real-world applications these weighting factors could be composed of values relating to actual market/production costs. This would enable the determination of conditions which allow the process to run as cost-effectively as possible.

Figure 108 shows the response surface after scalarisation, the surface shape was transformed so that conditions which gave full conversion with excess use of catalyst or residence time received a lower reaction efficiency rating. The surface was also scaled to show the responses relative to the optimal response in terms of % reaction efficiency. The optimal conditions were found using a brute force approach, a computationally expensive 2000x2000 grid search, which explored 4,000,000 catalyst

surface areas and residence times between 0 and 0.6 and between 0 and 10 minutes respectively found the optimal conditions to be: 3.7 minutes and 0.248 m^2L^{-1}.

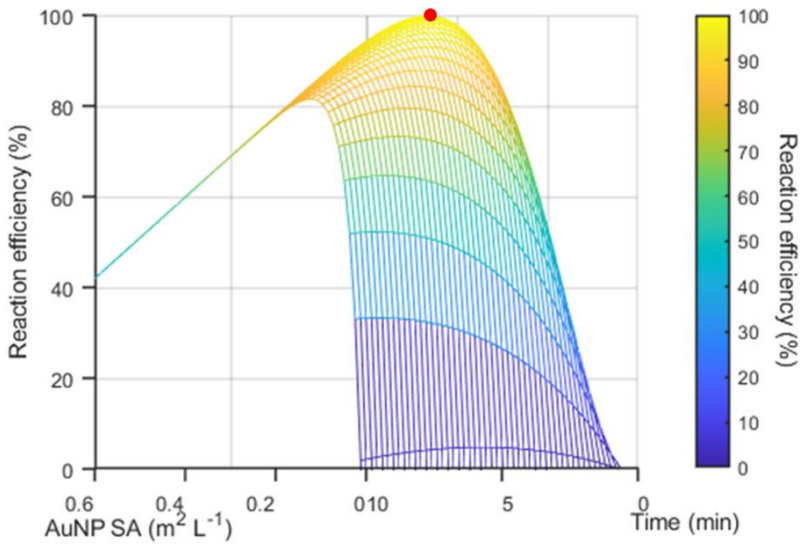

Figure 108. The response surface after scalarisation with weighting factors of 0.06 and 60 for the amount of catalyst used and residence time respectively. This scalarization process transforms the shape of the surface so that the most efficient conditions were a singular point (red marker) as opposed to an infinite surface.

4.3 Simulated optimisation

After developing an *in silico* test problem representative of the reaction explored in this project, it was possible to compare the performance of different optimisation algorithms in a way that would require less time and resources than conducting actual experiments but which would achieve similar results. Four different types of algorithm, all of which have previously proven effective in self-optimising flow reactors, were then benchmarked using this simulated reaction: SNOBFIT,[241] Bayesian,[242] TSEMO[115] and genetic[243] algorithms, comparing the number of function evaluations required to reach the optimal conditions and how close these conditions were to the 'true optimum'.

4.3.1 Genetic algorithm

Genetic algorithms are particularly useful for problems that are cheap to evaluate and have multiple optima. They have been used previously in continuous flow material synthesis and optimisation platforms.[242,244] The performance of these algorithms depends largely on the number of generations and the population size of each generation. Bigger population sizes with more generations tend to lead to more optimal results. After 12 generations each with a population size of 150, MATLAB's inbuilt genetic algorithm[238] found the conditions for 99.9% reaction efficiency (Figure 109).

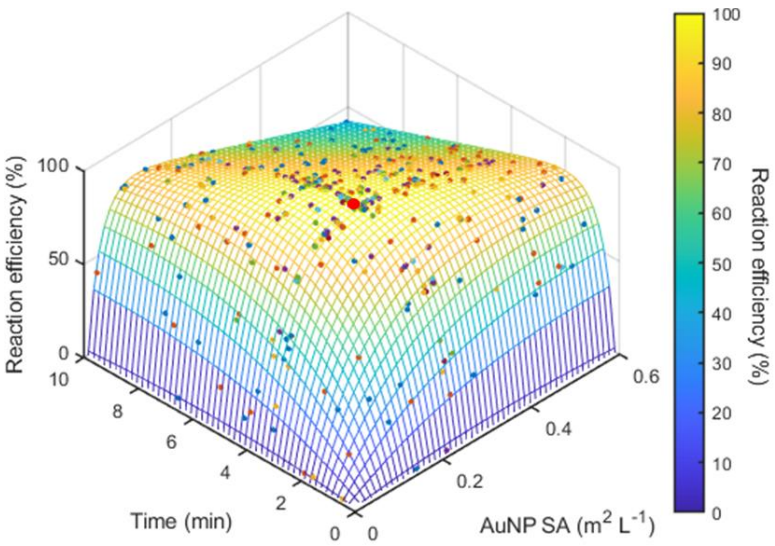

Figure 109. A response surface showing the residence times and catalyst surface areas explored by the genetic algorithm, after 12 generations each with a population of 150, the optimum conditions are indicated with a red marker.

However, most examples of self-optimising reactors are presented with fewer than 100 experiments, as this is a comfortable compromise between performing enough experiments to converge on optimal conditions without using an excessive amount of reactor time and chemicals. Therefore, in this benchmarking chapter the maximum number of function evaluations was set at 100 for each optimisation algorithm. Figure 110 shows the experiments performed by the genetic algorithm after 5 generations each with a population size of 10.

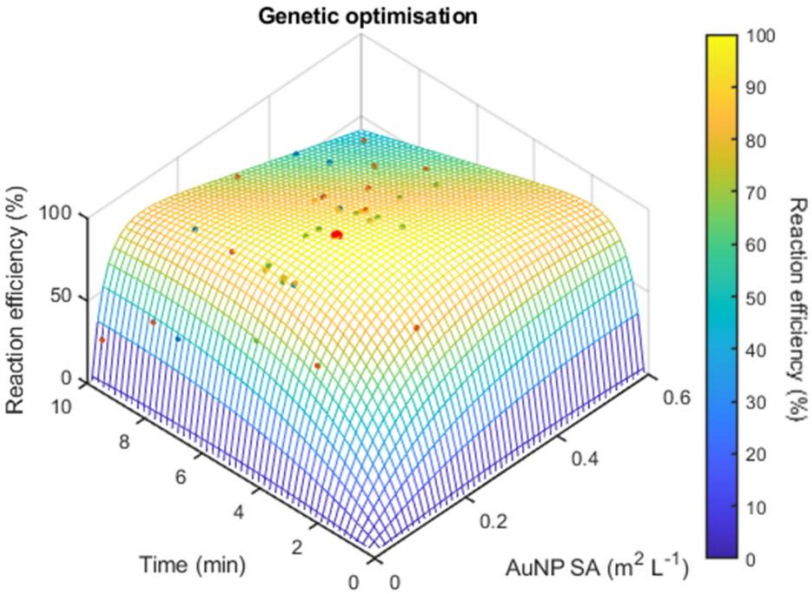

Figure 110. A plot showing the residence times and catalyst surface areas explored by the genetic algorithm, after 5 generations each with a population size of 10. The large red marker on this surface highlights the optimal conditions.

The best function evaluation in this case (reaction efficiency: 98.9%) was found with a catalyst surface area of 0.212 and a residence time of 6.347 (highlighted with a red marker in Figure 110). GA optimisation approaches fall under the umbrella of evolutionary algorithms and are best suited to the optimisation of systems which are cheap to evaluate, possess complex unpredictable response surfaces and multiple local minima. Finding applications in areas such as image analysis,[245] antenna[246] and game[247] design.

4.3.2 Design of experiment

Design of Experiment (DoE) approach was evaluated next, this approach is well established in many applications including reaction optimisation and is used to establish variable response relationships with a minimal number of experiments.[102] Factorial designs are commonly used in both academia and industry to screen experimental design space, as these methods are simple to set up and straightforward to interpret.[248,249] An experiment with a full factorial design (FFD) explores every possible variable combination of upper and lower limit values, this design can also include a centre point. Equation (14) shows the factorial design model for a 2 basic level 2 factor FFD design, where X_1 is residence time, X_2 is AuNP SA and b represents the model fitting coefficients for each parameter, the magnitude of b in each case reflects how much of an effect each variable has on the response.

$$y = b_0 + b_1X_1 + b_2X_2 + b_{1,2}X_1X_2 \qquad (14)$$

A 2 level 2 factor FFD is shown in Figure 111, 4 experiments exploring the upper and lower limits of each variable and an experiment exploring the centre point, the centre point experiment would typically be performed in triplicate to determine the reproducibility of the experimental method if the data was obtained experimentally.

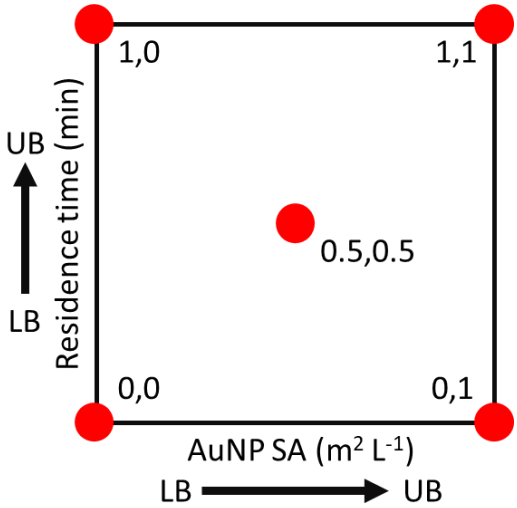

Figure 111. A two-level two-factor FFD with a centre point exploring the upper and lower limits of: (residence time, AuNP SA) on reaction efficiency.

Figure 112 shows a contour plot representation of the model predicted using data obtained using an FFD design. The FCC method is a minimalistic design which focuses on conserving resources and in this case provided a model with a poor fit to the actual kinetic model with an R-squared value of 0.476.

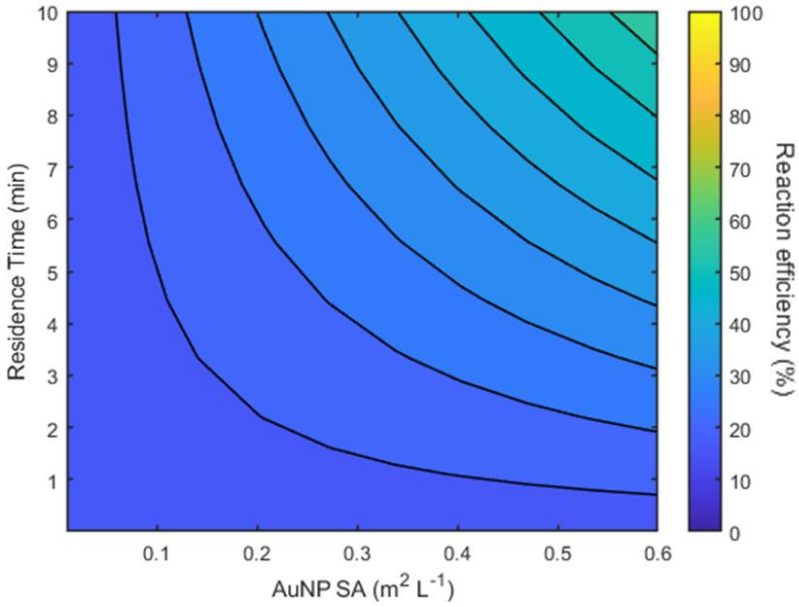

Figure 112. A contour representation of the model created using FFD experimental design.

Better fitting experimental designs typically include more quadratic terms and give more tightly fitted model predictions for response surfaces with significant degrees of curvature. To properly account for the curvature of the response surface the experimental design was modified to include points along the axis of the design space (Figure 113), quadratic terms were then added to the model to improve the fit equation (15).

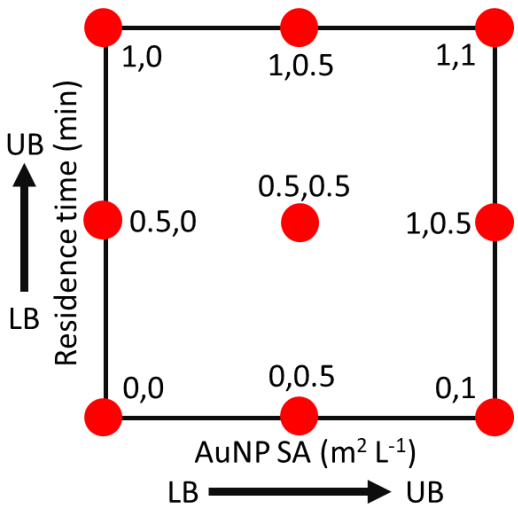

Figure 113. A two-level two factor FFD with additional experiments along the axis of the design space and a centre point exploring the effects of the variables: (residence time, AuNP SA) on reaction efficiency.

$$y = b_0 + b_1X_1 + b_2X_2 + b_{1,2}X_1X_2 + b_{1,1}X_1^2 + b_{2,2}X_2^2 \quad (15)$$

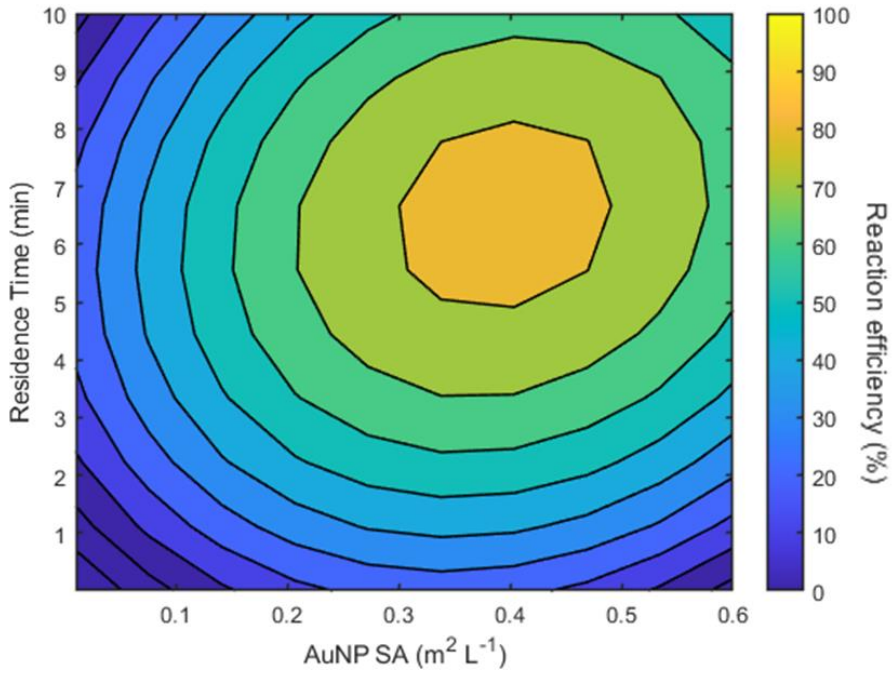

Figure 114. A contour representation of the model which includes quadratic terms created using an experimental design with points along the axis of the design space.

The fit of this predicted model (Figure 114) was significantly higher with an R-squared value of 0.821, however, the model still failed to accurately represent the true response surface. DoE investigations offer a crude but useful estimation of reaction trends while highlighting which variables have the greatest effect on the response. Despite the usefulness of DoE, its main limitation becomes apparent with increasing experimental complexity, as the number of required experiments increases exponentially as a function

of the number of levels to the power of the number of independent variables (factors). More advanced DoE methods have been developed which use iterative search algorithms to reduce the number of required experiments and minimise the variance between the model values and actual data.[250] These advanced DoE's are similar to iterative optimisation algorithms such as Stable Noisy Optimization by Branch and FIT (SNOBFIT)[106] or Bayesian Optimiser with Adaptive Expected Improvement BOAEI, which are typically more focused on seeking the optimal conditions.

4.3.3 SNOBFIT optimisation

SNOBFIT overcomes the issues encountered so far with inaccurate model generation or the requirement for excessive experimentation, through the generation of multiple linear and quadratic surrogate models. These models are used to predict optimal design parameters for further experiments which improve the accuracy of the model. As SNOBFIT creates multiple competing models, it is more likely to find the true optimal conditions if there are multiple competing optima. This algorithm was used in the first reported self-optimising system, a system which aimed to fine-tune the optical properties of CdSe quantum dot nanoparticles.[97] A total of 100 SNOBFIT experiments were performed achieving a 99.9% reaction efficiency with a residence time of 228 seconds and a AuNP SA of 0.2400 m^2L^{-1} (Figure 115, red marker = optimal conditions).

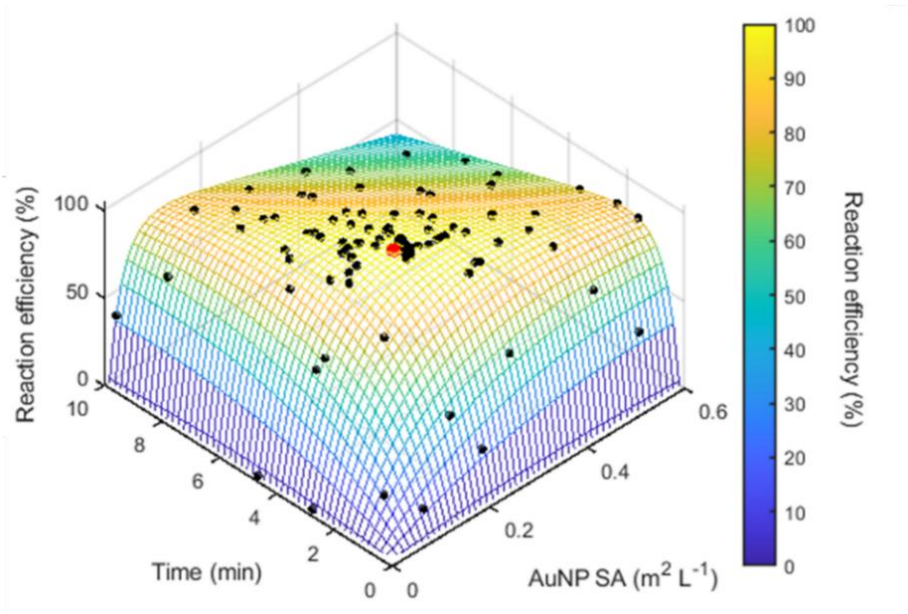

Figure 115. An overlay plot showing the 100 SNOBFIT experiments performed during the SNOBFIT optimisation. The optimal conditions are highlighted by the red dot.

This algorithm was able to reach 98.73% reaction efficiency after only 16 experiments. However, due to the exploratory nature of this global optimisation algorithm, many

experiments were performed outside of the optimal region and 74 experiments were performed before the algorithm was able to reach 99.9% reaction efficiency.

4.3.4 BOAEI optimisation

Bayesian algorithms also create surrogate models using sampled data, these algorithms build Gaussian process models which, when combined with an acquisition function, allow the optimisation to improve iteratively.[111] Figure 116 shows 100 experiments performed using the Bayesian algorithm BOAEI.

This algorithm automatically adapts the extent to which it explores regions of experimental space with high levels of model uncertainty. This algorithm displayed a more targeted approach performing far more experiments in the optimal region. Achieving a 99.9% reaction efficiency after only 6 experiments with a residence time of 4 minutes 9 seconds and a AuNP SA of 0.235 m^2L^{-1}.

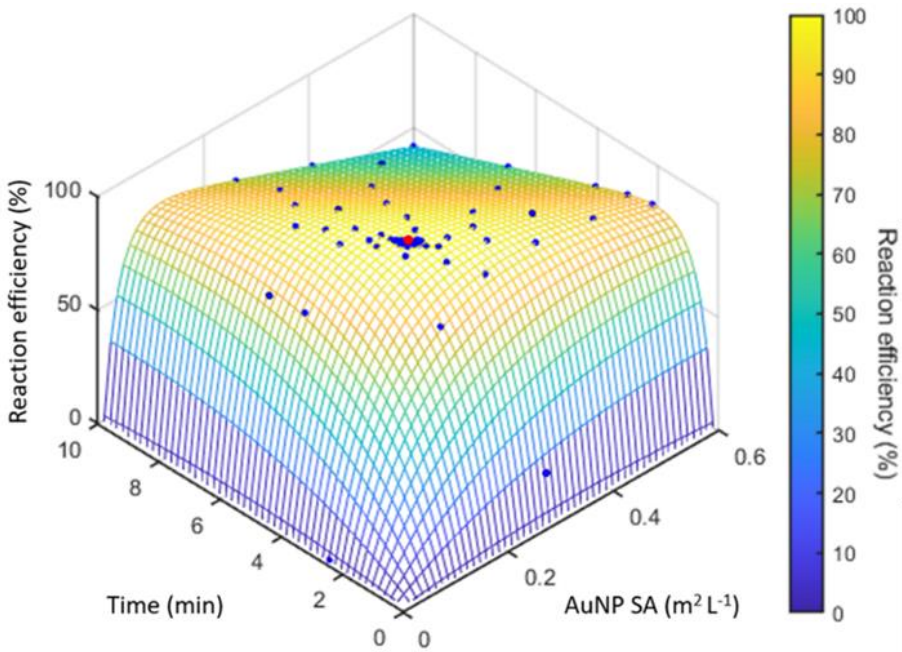

Figure 116. An overlay plot showing the 100 experiments performed during the BOAEI experiment with the optimal conditions shown by the red marker. Note that the majority of experiments were conducted near the optimum point.

4.3.5 Single objective optimisation algorithm comparison

The performance of each of the single objective genetic, SNOBFIT and BOAEI optimisation algorithms was compared using the following approach. Each algorithm was given an evaluation budget of 100. The single objective optimisation algorithms were each run 20 times and averaged to ensure the results were statistically significant.

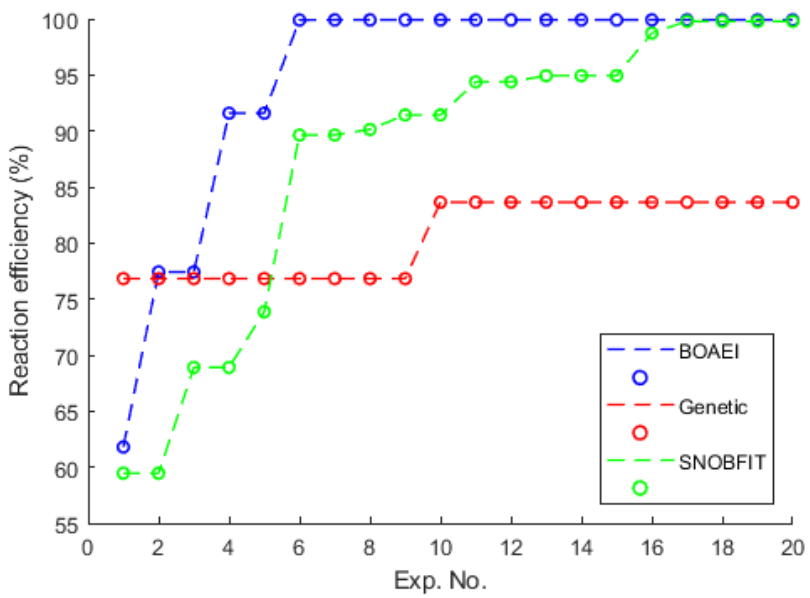

Figure 117. A convergence plot showing the cumulative running best conditions obtained using the 3 different types of single-objective optimisation algorithms explored in this chapter.

The results of this simulated comparative study are shown in the convergence plot in Figure 117. These results show that the BOAEI algorithm significantly outperforms both the SNOBFIT and genetic algorithms, with the genetic algorithm showing the worst performance. It is possible that the combination of gaussian process model and acquisition function used by the BOAEI algorithm were better suited to the optimisation of this type of reaction than other optimisation algorithms. Bayesian optimisation algorithms have also shown superior performance in other studies which use both real reactions and kinetic models to benchmark the performance of different algorithms.[111,222,251]

4.3.6 Effect of noise on optimisation algorithms

The benchmarking comparisons discussed so far in this chapter were all performed in the absence of noise. Despite the heightened level of control which is gained from performing chemical reactions within automated continuous flow reactors, there is still a small amount of error inherent within these systems. To determine the approximate error between the model and the experimentally obtained results, the results predicted using the kinetic model were compared against the results which were obtained experimentally. The parity plot in Figure 118 shows how the experimental results compare to the predicted results, a mean error of 8.37% was recorded with a standard deviation of +/- 6.65%.

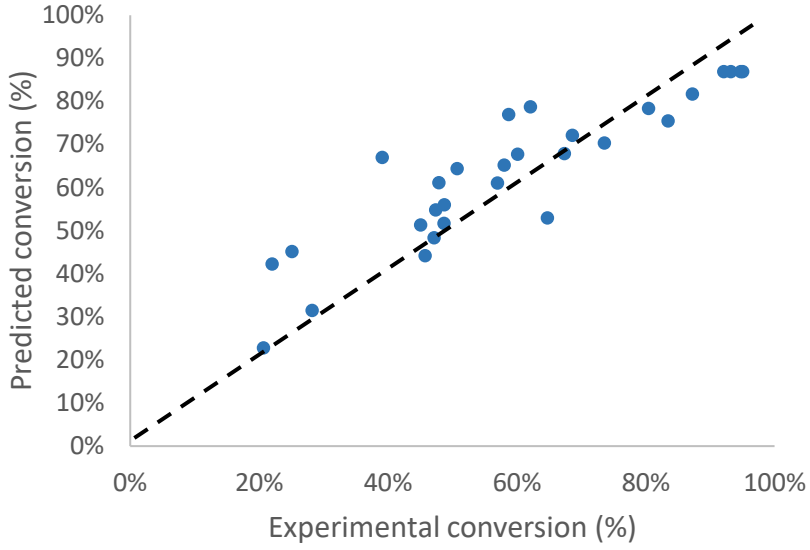

Figure 118. A parity plot showing the results of the predicted kinetic model relative to the experimental results.

To investigate how well the different algorithms benchmarked so far in this chapter performed when noise was incorporated into the response surface, 8.37% error in the form of white gaussian noise was artificially added to each kinetic model response after each iteration. The noise was later removed from the data after the optimisation to determine which algorithms were better able to discover the true optimum conditions under noisy conditions.

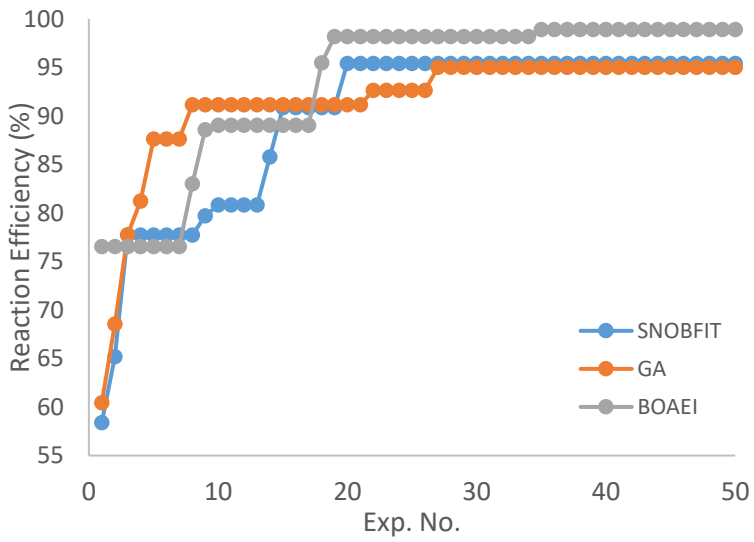

Figure 119. A convergence plot showing the cumulative running best conditions obtained with the addition of white gaussian noise for each of the 3 algorithms benchmarked in this chapter.

The convergence plot shown in Figure 119 above shows the cumulative best optimisation values obtained throughout 50 simulated experiments averaged across 20 runs. The genetic and SNOBFIT algorithms rapidly discovered the conditions required for ~90% reaction efficiency in less than 10 experiments but were unable to find the

conditions required for 95% reaction efficiency after 50 experiments. The BOAEI algorithm was able to discover the true reaction conditions for near 100% reaction efficiency despite the presence of 8.37% noise during the simulations. Although both SNOBFIT and BOAEI are designed to work effectively with noisy data. The BOAEI algorithm also has built in features for automatic hyperparameter tuning. This means that during an optimisation it is able to adjust the extent to which the next experiment is aiming to improve the level of certainty of the model or identify regions of optimal performance. It is likely that the algorithm determined the region of optimal performance with a high degree of certainty then adjusted it's hyperparameters to concentrate further experiments in this area. Thus, leading to more experiments being performed around the area of optimal performance meaning a higher probability of discovering the true optimal reaction conditions.

4.3.7 Multi-objective optimisation

So far in this chapter, a scalarisation approach has been used to optimise multiple objectives within a single objective design space. This allowed the optimisation algorithms to maximise conversion while also minimising the residence time and quantity of catalyst used. However, optimal conditions obtained in these cases were heavily dependent on the weighting factors applied to the input variables. In a manufacturing context, the cost of chemical feedstocks, solvents, catalysts and plant operations are likely to vary significantly over time, depending on resource availability and market forces.[252]

Therefore, a more useful optimisation might highlight all of the optimal points at which 100% conversion is achieved while also minimising the cost of the process, this would avoid the need to re-run optimisations each time there is a significant change in operation/resource costs. This is known as the Pareto front. Pareto-optimisation aims to identify a trade-off curve, which in this case would comprise of a series of non-dominated points at which maximum conversion can be achieved with minimal use of resources.[253] To find such a trade-off, two new objectives were used: E-factor and space-time yield (STY). E-factor is usually defined as the total mass of waste produced by a process (including solvents and auxiliary reagents) divided by the total mass of product produced.[254]. In this case, E-factor was modified to describe the amount of catalyst used during this process versus the amount of product produced and was

defined as the amount of catalyst used per minute divided by the amount of aminophenol produced per minute, a lower value meaning that more product was produced with less catalyst. STY was defined as the amount of product produced per minute per volume of reactor, a higher value meaning more aminophenol being produced per unit time/volume of reactor. The goal of this optimisation was to maximise STY while minimising E-factor. As these two objectives were mutually exclusive, a multi-objective optimisation algorithm could be used to identify the trade-off between these two factors.

The Thompson Sampling Efficient Multi-Objective (TS-EMO) optimisation algorithm[220] was configured to maximise STY while minimising E-factor. This algorithm works by first sampling a large area of chemical space using a LHC sampling method (in this case 100 initial experiments), the TS-EMO algorithm then creates a surrogate Gaussian process (GP) model from which further experiments (30 experiments in this case) were performed to identify the Pareto front by maximising the hypervolume of each iteration of solutions. Figure 120 shows the resulting trade-off between these two responses.

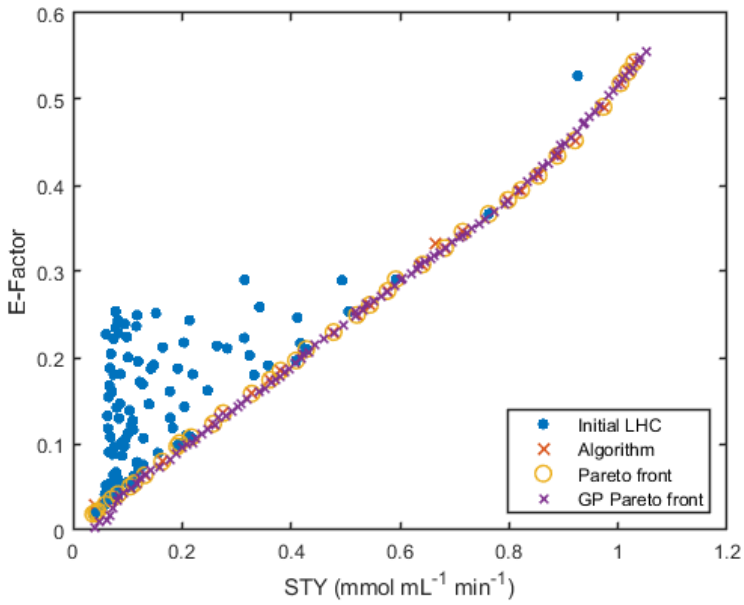

Figure 120. A plot showing the trade-off curve between the two competing performance criteria (STY and E-factor), the LHC experiments (blue markers), Gaussian process model (purple crosses), Pareto experiments conducted by the algorithm (red crosses) and the Pareto front i.e. all of the points at which it was not possible to increase STY while also minimising E-factor (yellow circles).

When plotted on a heatmap of the response surface the Pareto front can be seen on the ridgeline (Figure 121) where 100% conversion is reached but without excess wasted catalyst. The data obtained from an optimisation such as this could then be used to find the optimum conditions for maximum reaction efficiency. It should be noted that the

values obtained along this Pareto front are on the 'cliff-edge' of the response surface, to improve the robustness of this process the catalyst concentration and/or residence time can be increased slightly beyond the optimal ridge.

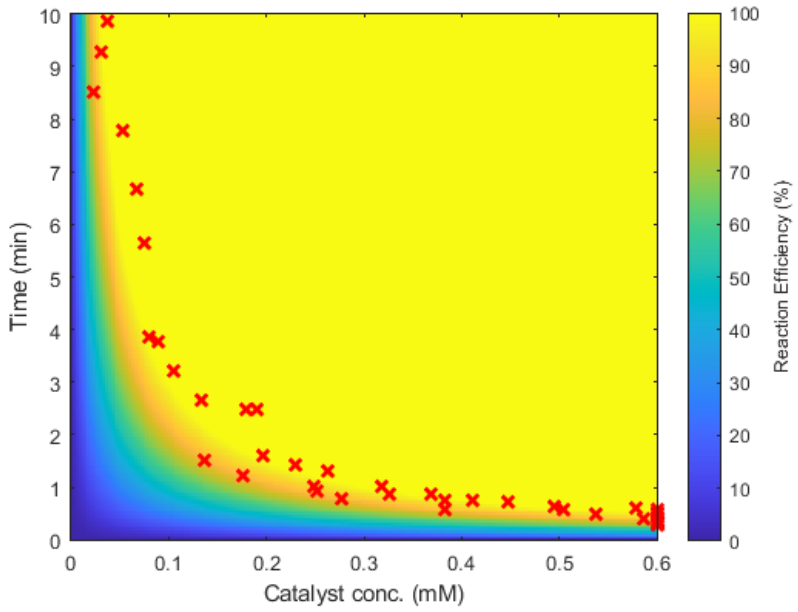

Figure 121. A heatmap showing the effect of changing residence time and concentration on the efficiency of the reaction, the Pareto front is plotted as an overlay with each of the 30 Pareto experiments represented by red crosses.

4.4 Summary

In summary, this chapter presents a benchmarking framework for the evaluation of algorithms in nanoparticle catalysed reaction optimisation. Four different optimisation algorithms (a genetic algorithm (GA), SNOBFIT, BOAEI and TS-EMO) were used to optimise a simulated nanoparticle catalysed reaction. The simulated reaction was based on a LH kinetic model fitted to data obtained during an optimisation experiment performed in Section 2.5.2. The kinetic model was generated by employing ODE solvers and a genetic optimisation algorithm to iteratively tune kinetic parameters until the predicted reaction values closely matched experimental data. Once generated the kinetic model was further validated by predicting the outcome of a scale-up reaction performed in batch.

Of the single objective optimisation algorithms, the GA showed the worst performance in terms of the number of experiments required to reach the optimal conditions, as this method required multiple generations and large population sizes to obtain the most optimal results, significant improvements were made with each generation of conditions and not after each iteration. In the benchmarking kinetic study in this chapter, the

response surface was relatively predictable and uncomplex. For more complex response surfaces for example when optimising the physical properties of heterogenous catalysts,[255] a genetic algorithm may be more appropriate but only if it is possible to also perform many experiments.

The SNOBFIT algorithm has historically been a popular choice of algorithm for self-optimising flow reactors[5,97,133,241,242,256] due to its proven ability to optimise systems with inherent noise and multiple local minima. This algorithm performed well when optimising the kinetic model developed in this chapter, discovering near-optimal conditions in just 16 experiments, however, requiring many more (74) experiments to reach 99.9% reaction efficiency.

The BOAEI algorithm showed the best performance reaching 99.9% conversion after only 6 experiments. Bayesian optimisation algorithms are becoming more dominant within the literature as the algorithms of choice for reaction optimisation. Similar comparative studies have found this type of algorithm to outperform both other algorithms[222] and human experts[111] in terms of accuracy and the number of iterations required to find a global optimum.

Finally, the multi-objective optimisation algorithm (TS-EMO) has previously proven more effective than similar multi-objective optimisation algorithms when applied to benchmarking functions[220] and kinetic models.[257] TS-EMO was able to identify the minimum amount of catalyst and residence time required to reach near 100% reaction efficiency across the entire design space, thus providing a range of optimum conditions.

This benchmarking approach offers a simple *in silico* approach to algorithm comparison, without the need for hundreds of labour and resource-intensive experiments. This enables chemists to make an informed decision on the best choice of algorithm while better understanding the strengths and weaknesses of each optimisation strategy. This is particularly important as the field of optimisation is constantly evolving and methods which allow new algorithms to be objectively and efficiently compared with the current state of the art algorithms would allow faster progress to be made in a variety of fields. In the context of chemical and material sciences benchmarking processes such as this could be further developed into strategies for the optimisation of more complex systems involving the development of nanoparticle catalysts,[258,259] multiple stages[115,260] and discrete/continuous variables.[261,262]

Chapter 5

Two-stage, continuous flow nanoparticle catalysed reaction optimisation

Self-optimising reactors have previously been used to produce nanoparticles with desirable optical properties.[95,97,242,263,264] This chapter describes a self-optimising flow system which was able to optimise the performance of a nanoparticle catalysed reaction, by exploring both the nanoparticle catalyst composition and the conditions of the catalysed reaction. Previously in chapters 2 and 3, reactors capable of continuous flow nanoparticle synthesis and nanoparticle catalysed reaction optimisation were developed separately. In this chapter, these concepts were combined to produce a system which optimised both the catalytic performance of the nanoparticles and the nanoparticle catalysed reaction conditions. This was achieved by flowing nanoparticles synthesised in one reactor directly into a catalysed reaction performed in a secondary reactor, the degree of reaction conversion in the second reactor was used to assess the catalytic performance of the nanoparticles and direct an optimisation algorithm to improve the nanoparticles in an informed way, see Figure 122.

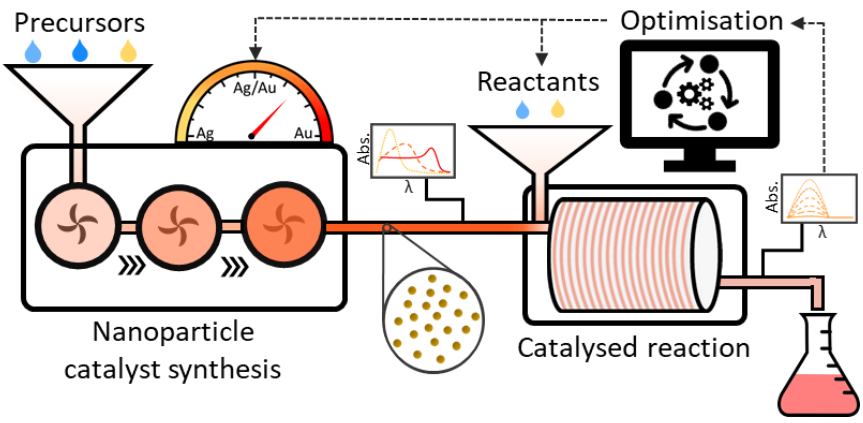

Figure 122. A graphical representation depicting the concept of a two-stage performance directed nanoparticle catalysed reaction optimisation system.

This two-reactor system was demonstrated through the optimisation of a nitrophenol reduction reaction with a bimetallic AuAgNP catalyst. The composition of the nanoparticles was adjusted within the first reactor (CSTR cascade), these nanoparticles were then telescoped into a secondary (tubular) reactor, where their catalytic performance was assessed in a 4-nitrophenol reduction reaction. Both the nanoparticle composition and reaction conditions for the reduction of nitrophenol (residence time and nanoparticle to reducing agent ratio) were optimised and both stages of the reaction

were monitored with inline UV-vis spectroscopy. This approach allowed rapid assessment of catalytic efficacy (< 10 min per experiment) of different nanoparticle catalyst compositions under a variety of reaction conditions.

5.1 Introduction and background

5.1.1 High-throughput experimentation

High-throughput screening (HTS) methodologies have become standard within industry and are becoming more common within academic research. These methods harness automation and data analysis techniques to determine the best reaction conditions for a range of chemical reactions.[265,266] These platforms are capable of performing many experiments in parallel with accurate automated dispensing of often difficult to handle powders, viscous liquids, suspensions or waxes, into parallel reaction/formulation vessels where the constituent components are then mixed and heated according to the specifications of the experimentalist, providing a faster turnaround of experiments, greater control and reproducibility.[267] For example, in 2011 AstraZeneca invested in a suite of ChemSpeed parallelised automated screening platforms,[268] an example of a ChemSpeed platform is shown in Figure 123.

Figure 123. A photograph of a ChemSpeed catalyst screening platform used to screen catalysts and reaction conditions in an automated fashion (Photo credit: Christopher Horbaczewskyj, University of York, 2021).

These screening platforms allowed AstraZeneca to determine the optimal combination of metal/ligand for organometallic catalysts, solvent, additives and conditions for their

manufacturing processes. Predetermined quantities of catalyst, solvents and reagents were automatically dispensed into vials contained within 96 well plates. These reaction mixtures were then placed under an inert atmosphere, shaken and heated at a specific rate/temperature. The solutions were then analysed using conventional methods such as HPLC to determine the best catalyst/reaction conditions to move forward with. AstraZeneca quoted a time to return of investment of fewer than 6 months after employing these devices.

Syngenta, an agrochemicals manufacturer, has also employed HTS platforms for the development of its products. In 2017 researchers at Syngenta concluded that the cost of a particular product could be reduced significantly if an existing emulsifier was replaced with a cheaper alternative. High-throughput technologies were employed to prepare potential product formulations with blends of alterative emulsifier types and concentrations. Laboratory and image analysis tests were then performed on each sample to determine the dispersion properties, rheological suitability and emulsion stability of the resulting formulations. A statistical modelling software package was used to analyse the resulting data, from this analysis an area of overlap between acceptable dispersion, rheological and stability properties was identified. Further work was then undertaken within this area of design space. Over 350 experiments were performed by the high-throughput platform within 15 days, leading to the successful development of a new product with significantly reduced costs.[269]

In the context of heterogeneous catalyst screening, R. Laine *et. al.* developed a HTS platform for mixed metal oxide NO and unburnt hydrocarbon oxidation catalysts as an alternative to platinum-based catalysts used in emission control devices. In this study 48 different mixed-metal oxide powders were packed into a library plate which allowed NO, O_2, C_3H_8 and N_2 gasses to pass over the powders at 300 °C. The resulting gasses (N_2O, NO_2, CO, and CO_2) were then analysed with IR. Using this high throughput screening method, the authors identified a set of $Ce_{1-x}Zr_xO_2$ and Al_2O_3-$Ce_{1-x}Zr_xO_2$ oxidation catalysts as potential candidates for both NO_x reduction and propane/propene oxidation with comparable activities to Pt/Al_2O_3 catalysts.[270]

All of these automated HTS examples were able to explore large parameter spaces by performing orders of magnitude more experiments than would be feasibly possible using more traditional and labour-intensive methods. In addition to reductions in costs and time, due to the high precision of the robotic instruments and reduced probability

of human error, the data obtained would likely also be more accurate and reliable. Most importantly for routine screening experiments, these HTS systems lower the individual cost per experiment, meaning a larger design space can be explored and more repeats can be taken to improve the statistical validity of the data obtained. The main drawbacks of these high-throughput screening approaches are high initial investment costs for specialist equipment and the initial setup costs can be high meaning these techniques are unsuitable for procedures that require complex processes which regularly change. Finally, there is a requirement for experimentalists using these technologies to possess specialist/multidisciplinary skills, in addition automating experimental procedures can sometimes take longer than carrying them out in a more traditional manner, particularly if only a small number of experiments is required. In the case of catalyst screening, high-throughput screening platforms are also normally limited by the requirement for pre-existing catalyst libraries (which could take days to prepare if not already available).

5.1.2 *In silico* modelling

In silico methods for optimising heterogeneous catalysis are not limited by the constraints of pre-existing catalyst libraries or pre-determined reaction conditions.[271,272] These techniques can also provide an understanding of catalytic processes over a wide range of length and time scales.[273] Multiscale modelling of heterogenous reactions is an evolving field with multiple possible approaches, but a bottom-up approach is commonly used to model these reactions. Using a bottom-up approach, heterogeneous catalysts are assumed to be relatively uniform on a molecular length scale, with a repeating surface structure. Elementary processes are specified for the catalytic reaction of interest, the binding energies associated with interactions between the catalyst active sites, reactants, intermediates and products can then be predicted using density function theory (DFT) calculations, giving reaction rate constants and output metrics such as the number of product molecules produced per active site per unit time - turnover frequency (TOF).

Yang and Muckerman *et. al.* used such an approach to model the reaction kinetics of a water-gas shift reaction ($CO + H_2O \rightarrow CO_2 + H_2$) over a Cu/ZnO nanoparticle catalyst. The heterogeneous nanoparticle catalyst was modelled as a homogenous and atomically flat ZnO surface covered in Cu ‘nano islands’. Their DFT simulated results showed that

catalytic activity increased linearly with an increase in the total number of Cu edge sites.[274]

This approach provides a prediction of the process in a local environment as a function of input variables such as the partial pressures of reactants/products in gaseous reactions and temperature under uniform conditions.[146] However, to improve accuracy, these local models need to be integrated into a higher-level model, considering differences in conditions that are likely to exist more globally within the reactor, such as mass transfer into and out of a porous heterogeneous catalyst support material. Sutton and Savara *et. al.* integrated a DFT kinetic model of a CO oxidation reaction ($2CO + O_2 \rightarrow 2CO_2$) over a RuO_2 catalyst into a reactor scale model using computational fluid dynamics (CFD). This higher-level model accounted for the changing concentration of reactants and products as the reaction mixture travelled along the reactor, enabling a prediction of what the product/reactant concentrations might be as a function of the position along the reactor bed. In this study, the product concentration gradient was found to increase along the reactor.[275] Whereas other similar studies have found reaction rates to vary dramatically with small changes in CO and O_2 concentrations for the oxidation of CO over RuO_2,[276] highlighting the need for further development in this area. Unfortunately, even the most advanced multiscale modelling techniques to date cannot accurately recreate the complex reaction environment of a heterogeneously catalysed reaction. This is due to the high degree of complexity associated with the interdependent variables which affect heterogeneous processes and further work is required in this area to provide models which accurately represent real-life reactions.[277,278]

Continuous flow reactors capable of nanoparticle catalysed reaction optimisation would overcome the need for pre-existing catalyst libraries while maintaining the ability to perform real-life experiments. These reactors could also lower the amount of waste produced, as they can adaptively search the design space avoiding the need to carry out experiments in non-optimal regions. However, to optimise the catalytic performance of nanoparticle catalysts they would need to observe the catalytic performance of nanoparticles in a reaction, requiring the reactor to have multiple stages.

5.1.3 Multistage flow synthesis and optimisation

Multistage flow reactors are currently the state of the art in flow reactor design. These reactors have proven capable of completing multistep organic synthesis procedures in a

single pass and have been used to synthesise a variety of pharmaceutical ingredients.[66,279,280] This has become possible due to advances in continuous flow technology which have enabled intermediate work-up steps such as liquid-liquid separations to be performed between different reactor stages.[281] As well as the advancement of a variety of real-time Process Analytical Technology (PAT) such as inline UV-vis spectroscopy, IR, NMR, online HPLC/GC, pH, pressure and temperature probes which can be placed within any stage of the reactor.[282]

The Jensen group have recently presented a paper which demonstrates a reconfigurable self-optimising multistage reactor which includes closed-loop optimisation, see Figure 124.[256] This system was made up of five discrete stages, each stage configurable by swapping out specially designed modules which allowed different reaction conditions within either: a photo (LED) reactor, heated/cooled reactor or packed bed reactor. Liquid-liquid separators or bypass modules could also be included to increase the versatility of the system. The output of the reactor was monitored with online HPLC and optimised using the SNOBFIT[106] algorithm.

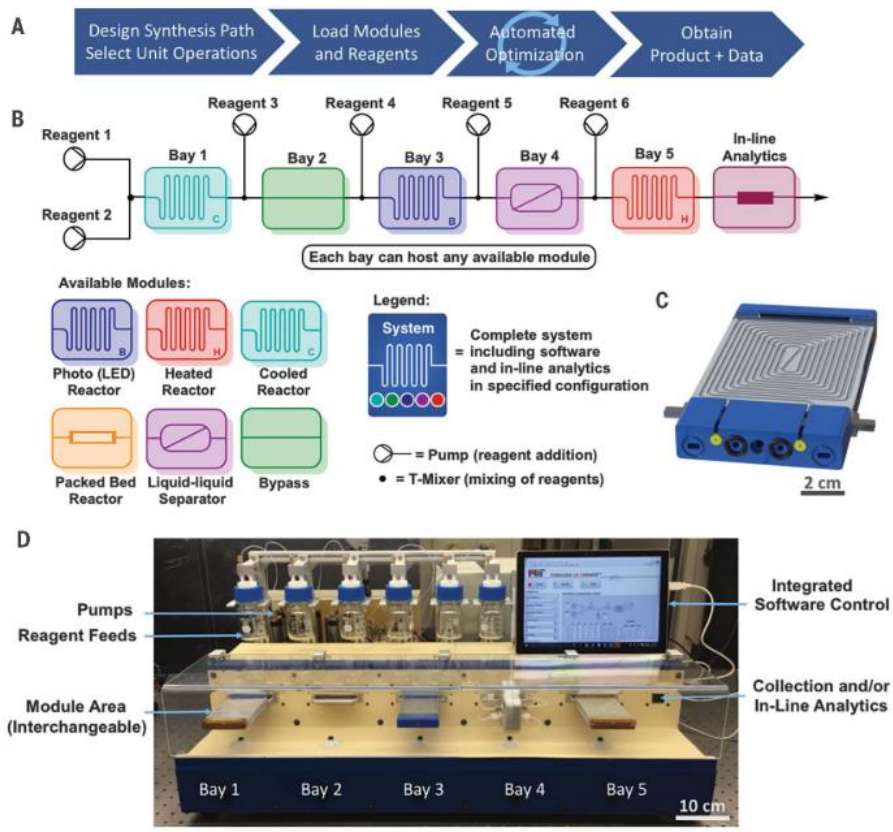

Figure 124. A reconfigurable multi-stage continuous synthesis and optimisation system (Reproduced with permission from ref.[256] Copyright 2018, American Association for the Advancement of Science. All rights reserved.)

The system was demonstrated by performing and optimising; a nucleophilic aromatic substitution (S_NAr), C-C cross-coupling, reductive amination, olefination, and photo redox catalysis reactions. The equivalence of the reaction reagents, residence time and reactor temperature was optimised in each case. The reactions are shown in Scheme 2.

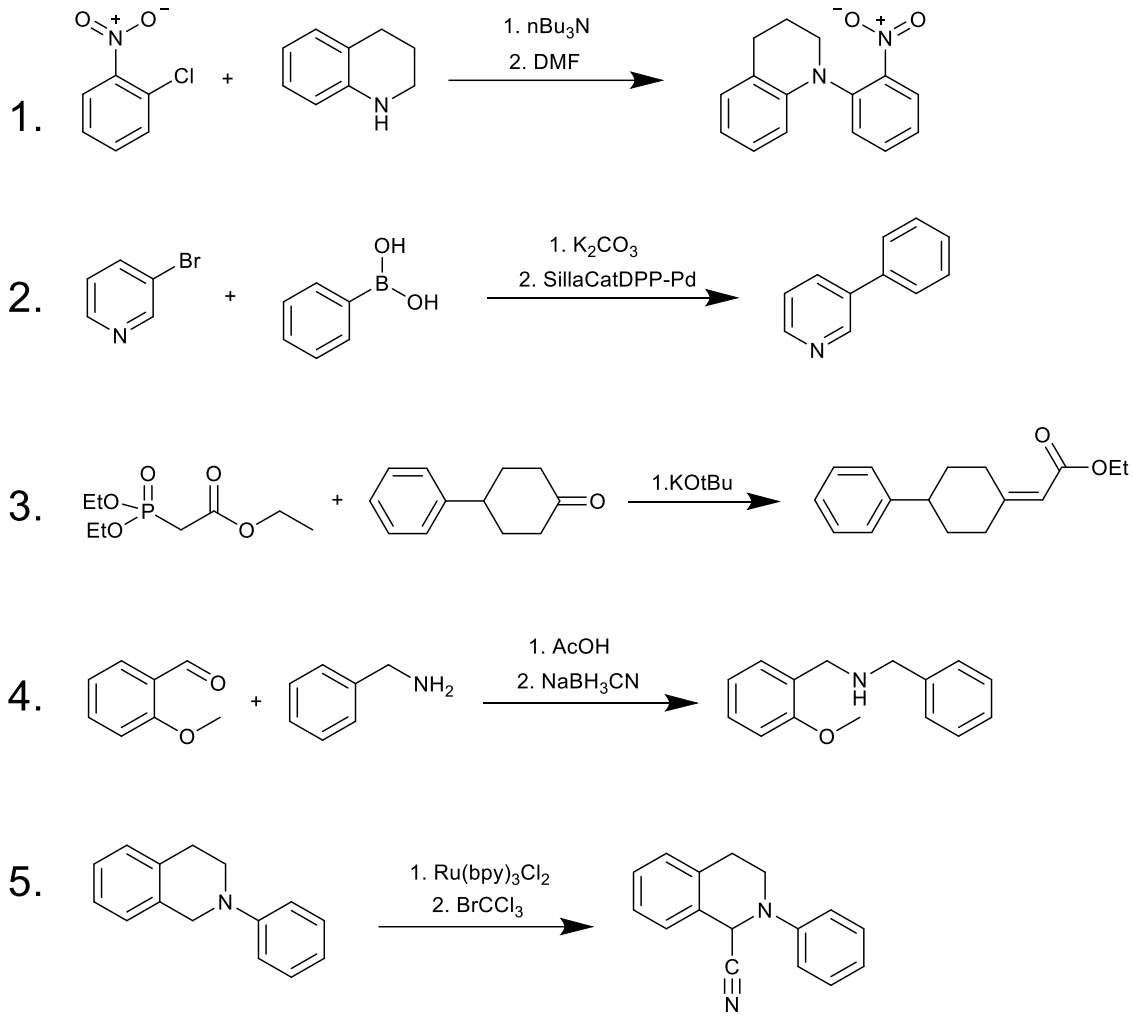

Scheme 2. Examples of the reactions optimised by the reconfigurable self-optimising multistage reactor. 1. Nucleophilic aromatic substitution (S_NAr), 2. C-C cross-coupling, 3. reductive amination, 4. olefination, and 5. photo redox catalysis, reproduced from.[256]

Yields of between 87-96% were achieved for each reaction and each optimisation required less than 50 experiments. The versatility of the system allowed a great variety of reactions to be performed under a wide range of conditions. Table 9 shows the number of optimisation experiments and the amount of time required to reach these yields for each reaction.

Table 9. A table showing the number of optimisation experiments and amount of time required to reach the reaction yields stated in the final column of each reaction, reproduced from.[256]

Reaction	No. of experiments	Optimisation time (hr)	Highest yield (%)
S_NAr	34	12	94
C-C cross-coupling	30	8	96
Reductive amination	33	14	87
Olefination	33	10	87
Photo redox catalysis	33	7	91

Despite the development of many continuous systems designed for the preparation of nanoparticle catalysts and nanoparticle purification, there has been far less progress in the area of continuous flow optimisation of nanoparticle catalysed reactions. Bawendi and Jensen *et. al.* have shown that excess capping agent can be removed from solutions containing CdSe QD or AuNPs by combining counter current flow with membrane separation.[191] This system was later used by Adpakpang and Weeranoppanant *et. al.* to design a multistage flow system capable of silver nanoparticle synthesis and purification demonstrating the viability of multistage nanoparticle synthesis systems.[190]

Trapp *et. al.* designed a continuous-flow HTS system for nanoparticle catalysed reactions. This involved flowing a reaction medium over palladium nanoparticles embedded within a polymer matrix on the first 2 cm of the walls of a gas chromatography capillary under different conditions. A wide range of hydrogenation reactions were then performed by varying the substrate, residence time and reaction temperatures within the column. This allowed over 5000 experiments to be completed within 40 hours and activation parameters to be obtained for each of the reactions,[258] with the kinetic parameters compared with other studies showing good agreement. Unfortunately, this reactor was limited by the fact that only one catalyst could be screened at a time, limiting its scope as a system for HTS of reaction conditions and not nanoparticle materials.

To the best of the author's knowledge, there are currently no examples of multistage reactors that couple continuous flow nanoparticle synthesis, with a nanoparticle

catalysed reaction within a single optimisation system, other than the system presented in this chapter.

5.2 Reactor development

5.2.1 Inline nitrophenol concentration monitoring

In this work nanoparticles containing mostly silver were found to absorb strongly within the same wavelength region as nitrophenol, it was therefore necessary to increase the detection range of the UV-vis detector to prevent inaccurate results due to sensor saturation. To achieve this a brighter light source (DH-2000) was employed and the shoulder of the absorption profile (475-450 nm) was monitored instead of the peak (375-425 nm). Figure 125 shows the wavelength absorption profiles taken for the nitrophenol calibration.

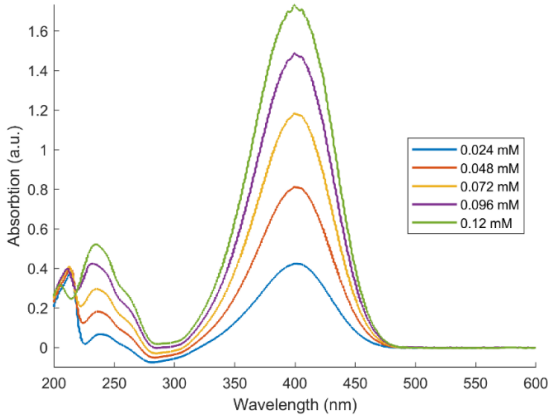

Figure 125. UV-vis absorption calibration for solutions of 4-nitrophenol between 0.024-0.12 mM.

Calibration values taken by integrating absorbance values between 375-425 nm resulted in a gradient of 12.60 with an R-squared value of 0.993, slight curvature of the calibration indicated that detector saturation at higher concentrations (Figure 126 (left)).

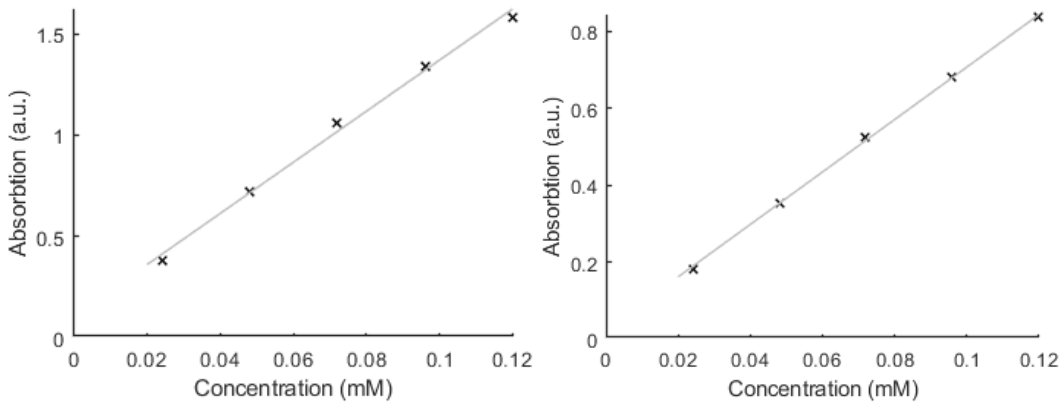

Figure 126. Calibration plots comparing calibrations taken between 375-425 nm (left) and 425-450 nm (right).

Alternatively, when the shoulder of the absorption profile between 425-450 nm was integrated to obtain the calibration values the calibration fell within a more linear range (Figure 126 (right)), confirmed by an increase in the R-squared value to 0.999 and a gradient of 6.81.

5.2.2 Spectra deconvolution

When the nanoparticles and nitrophenol were combined in solution, the constituent UV-vis absorption bands overlapped, resulting in an overall increase in absorbance and convoluted spectra. This increased the absorbance values measured to find the concentration of nitrophenol, leading to systematic error in the results. Therefore, it was necessary to analyse both stages of the reactor to enable deconvolution, by subtracting nanoparticle absorption from the overall spectrum.

In Section 2.3.3 a deconvolution procedure was applied to the reaction spectrum to improve the accuracy of the results.[133] A reference spectrum, scaled according to the concentration of nanoparticle solution, was then subtracted from the combined spectrum to deconvolute the absorption profile of each experiment. This was possible because the same nanoparticle solution was used to catalyse all of the reactions performed during the self-optimisation.

The same method could not be applied in this chapter, however, as each of the nanoparticle solutions in these automated experiments would have an individual UV-vis absorption profile, due to differences in metal composition. To deconvolute these spectra, it was necessary to record the UV-vis absorption profiles for each of the nanoparticle solutions used individually.

Figure 127 shows an example of the UV-vis absorption spectra before and after deconvolution, with the two underlying constituent components of the spectra for comparison. To deconvolute the combined spectra, the nanoparticle spectra were recorded and then scaled according to its concentration in the combined solution. The scaled spectrum was then subtracted from the overall spectrum to give a deconvoluted UV-vis absorption profile and more accurate nitrophenol concentration readings while enabling the same UV-vis instrument to analyse both stages of the reactor sequentially. This approach was further exploited to monitor each stage for steady-state, thus providing an efficient and robust control method for transitioning between each stage of the reactor.

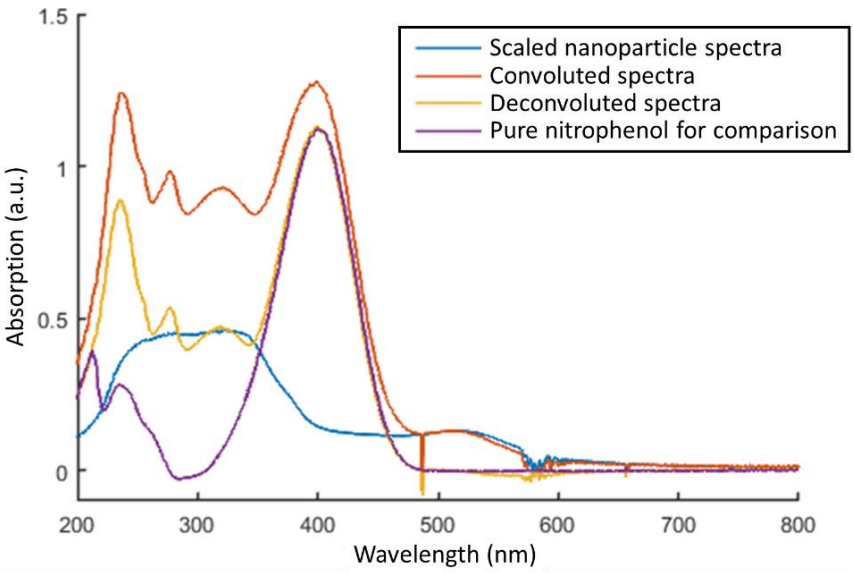

Figure 127. Plot showing UV-vis absorption spectra before and after deconvolution, a slight depression in absorption can be observed at 490 nm and ~580 nm, this is due to stronger light intensity provided in these areas from the stronger deuterium light source, this did not interfere with subsequent analysis as these regions of the spectrum were not analysed.

5.2.3 Two-stage reactor design

Figure 128 shows the initial design of the two-stage reactor developed in this chapter. This reactor was the product of combining the reactors developed in chapters 2 and 3. The addition of a nanoparticle storage coil allowed the flow rates of both reactor stages to be deconvoluted, which was imperative as the residence times of the two reactors were vastly different, this is explained in more detail below.

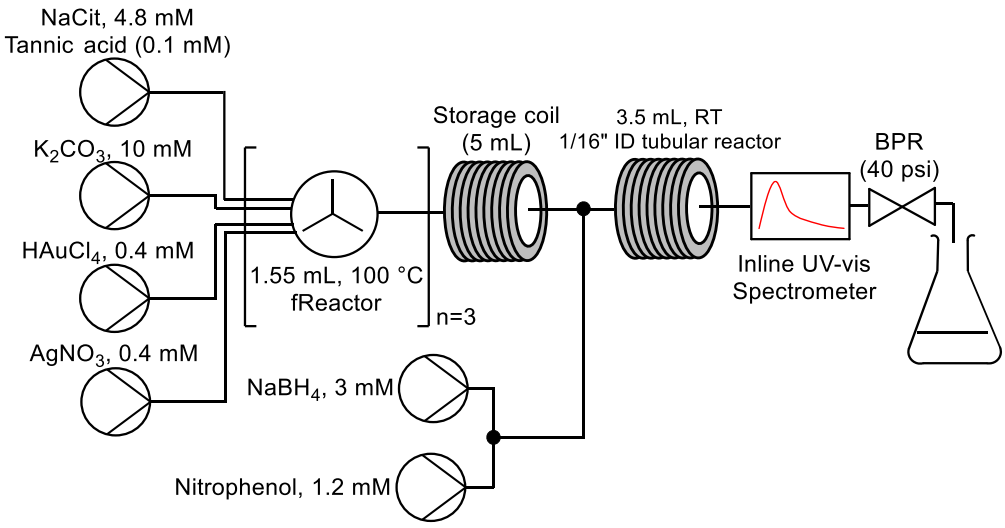

Figure 128. A diagram showing the initial two-stage reactor developed during this chapter of work.

The reactor used to produce nanoparticles operated at 4 mL/min, reaching steady-state after 5 minutes, upon reaching steady-state conditions a homogenous solution of

nanoparticles spanned across the entire volume of the nanoparticle storage coil. All of the pumps other than the K_2CO_3 pump were then turned off and the nanoparticle solution was pumped through the storage coil into the second reactor at flow rates between 0.18-2.1 mL/min controlled by the flow rate of the K_2CO_3 pump. The addition of a storage coil also allowed the temperature of the nanoparticle solution to equilibrate with room temperature, which was important as the nanoparticle solutions were heated to 100 °C in the CSTR reactors and could have affected the kinetics of the reaction in the second reactor if not allowed to equilibrate to the ambient temperatures.

The final design iteration of the two-stage optimisation system included a bypass route, for the nanoparticles synthesised during the first stage of an experiment to avoid the second reactor during initial analysis. Switching valves are commonly used in HPLC systems for fast and accurate solution handling.[283] 6-port switching valves are typically used in the configuration shown in Figure 129, to allow solutions of a precise volume to be accurately transferred from a high-pressure line into a chromatography column.

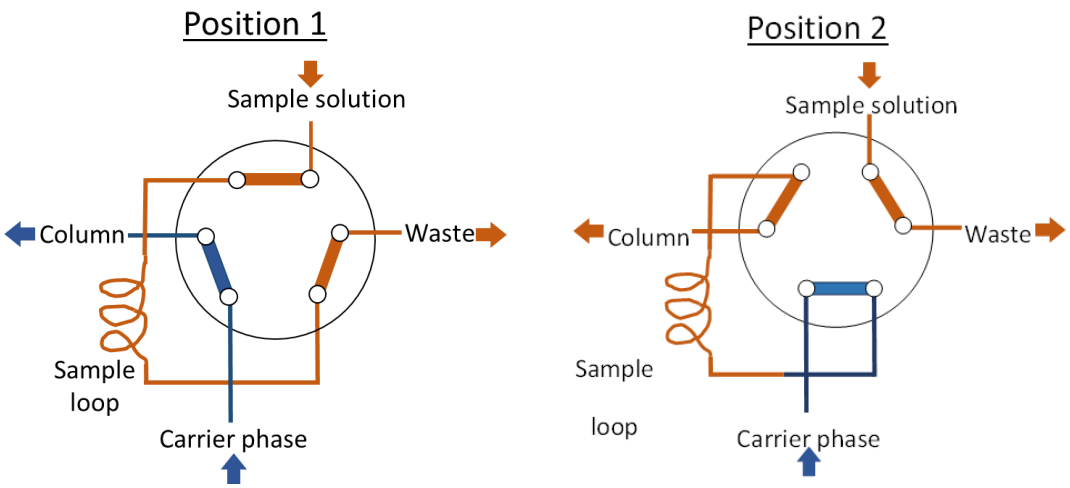

Figure 129. A diagram showing the conventional use of a six-way switching valve, when the switching valve is in Position 1 the sample flows through the sample loop while the carrier phase flows to the column. When the valve is switched to position 2, the sample solution contained within the sample loop is injected onto the column.

An automated 6-port switching valve was used in this flow reactor system to allow nanoparticle solutions from the first reactor to be pumped either, directly to the inline UV-vis spectrometer or through the second reactor to catalyse a reaction. Figure 130 presents a diagram showing how the reactor was configured. During stage one of each optimisation experiment, the $NaBH_4$ and nitrophenol pumps were turned off. The nanoparticle precursors, reducing and capping agent solutions were then pumped

directly to the inline UV-vis spectrometer, bypassing the second reactor. This saved both time and the amount of material required for the reactor to reach steady state.

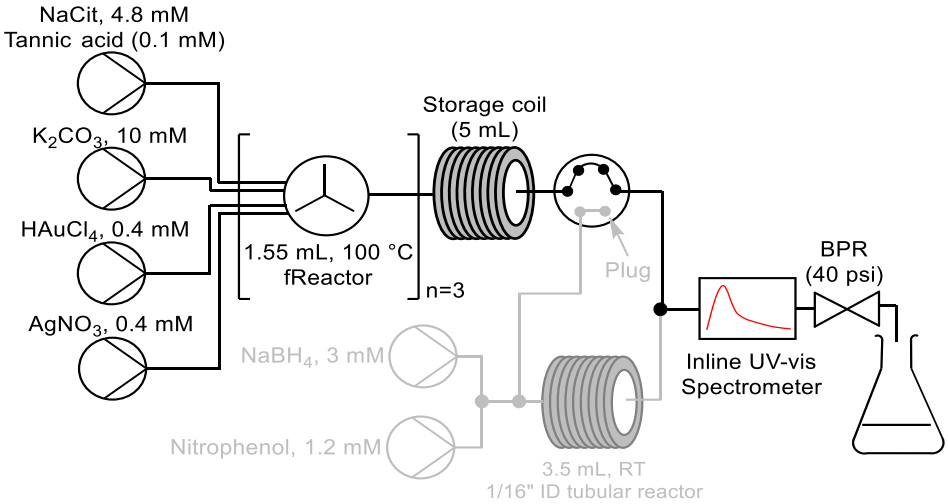

Figure 130. Diagram showing the reactor during stage one of an optimisation experiment, the secondary reactor is switched off and the nanoparticle stream bypasses the second reactor to save time and material.

During stage two (Figure 131), the second reactor pumps were turned on, the switching valve changed position to allow the nanoparticle solution made in stage one to then be pumped into the second reactor where they were used to catalyse a nitrophenol reduction reaction. 1.8 reactor volumes flowed through the reactor before steady state was reached and the reaction analysed. UV-vis spectroscopy was used to both monitor reaction conversion and confirm the reactor had reached steady-state. The data was then interpreted and fed to an optimisation algorithm for the iterative improvement of reaction conditions.

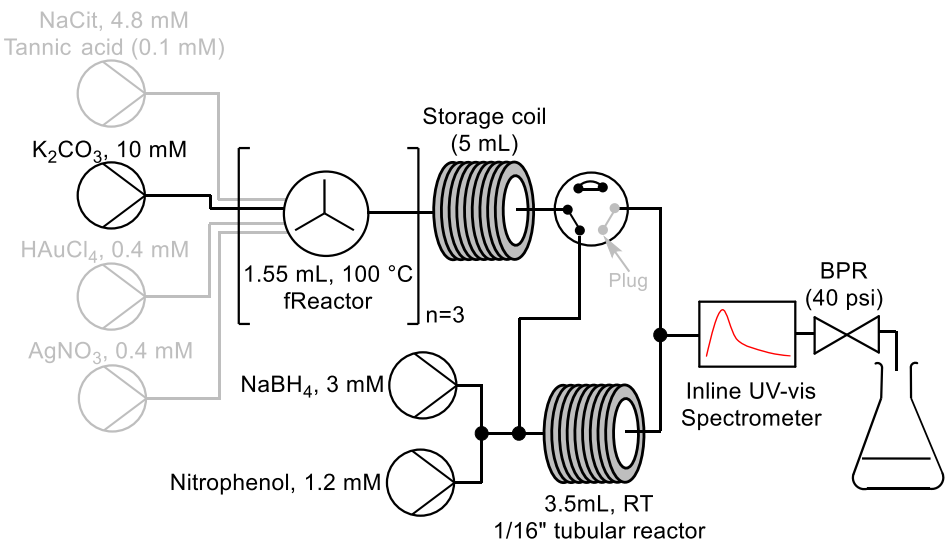

Figure 131. Diagram showing the reactor during stage two of on optimisation experiment, the switching valve changes position and the K_2CO_3 pump is used to pump nanoparticles into the second reactor.

5.2.4 Conditions generation function

During stage 1 of an optimisation, nanoparticles were synthesised with specific metal compositions, the total flow rate for the reactor was fixed with the K_2CO_3 pump set to 0.5 mL/min and the sodium citrate/tannic acid pump set to 1.5 mL/min. The combined flow rate of the $AgNO_3$ and $HAuCl_4$ pumps was fixed at 2 mL/min and the flow rate ratios of these pumps were varied to achieve the desired nanoparticle composition. The nitrophenol and $NaBH_4$ pumps were switched off during stage one.

The conditions generation method for Stage 2 was slightly more complex, the reactor residence time and nanoparticle to reducing agent solution ratios were varied between 0.03-0.3 and 0.5-2 min respectively during the optimisations. The sodium citrate/tannic acid, $AgNO_3$ and $HAuCl_4$ pumps were turned off during this stage of the optimisation and the flow rates of the remaining pumps were calculated as follows:

The total flow rate (FR) was calculated by dividing the reactor volume by the residence time equation (16).

$$Total\ FR = \frac{Reactor\ volume}{Residence\ time} \tag{16}$$

The starting concertation of the nitrophenol solution was 0.12 mM for every experiment. The nitrophenol stock solution concentration was 1.2 mM, therefore, the flow rate of nitrophenol could be calculated by multiplying the total reactor FR by 0.1 equation (17).

$$Nitrophenol\ FR = Total\ FR \times 0.1 \tag{17}$$

The ratio of $NaBH_4$ to nanoparticle solution in the reaction was varied during the optimisation, this was achieved using the following two equations (18) and (19).

$$Nanoparticle\ FR = Nanoparticle\ ratio \times Total\ FR \tag{18}$$

$$NaBH_4\ FR = Total\ FR - (Nanoparticle\ FR + Nitrophenol\ FR) \tag{19}$$

5.2.5 Reactor automation

The process was fully automated and operated with zero user intervention. This automated process is shown in Figure 132, and is split into two sections: the steps outlined in the blue box (left) describe the procedures undertaken to synthesise the nanoparticles during stage one of each optimisation experiment; the orange box (right) shows each step involved in the nanoparticle catalysed reaction.

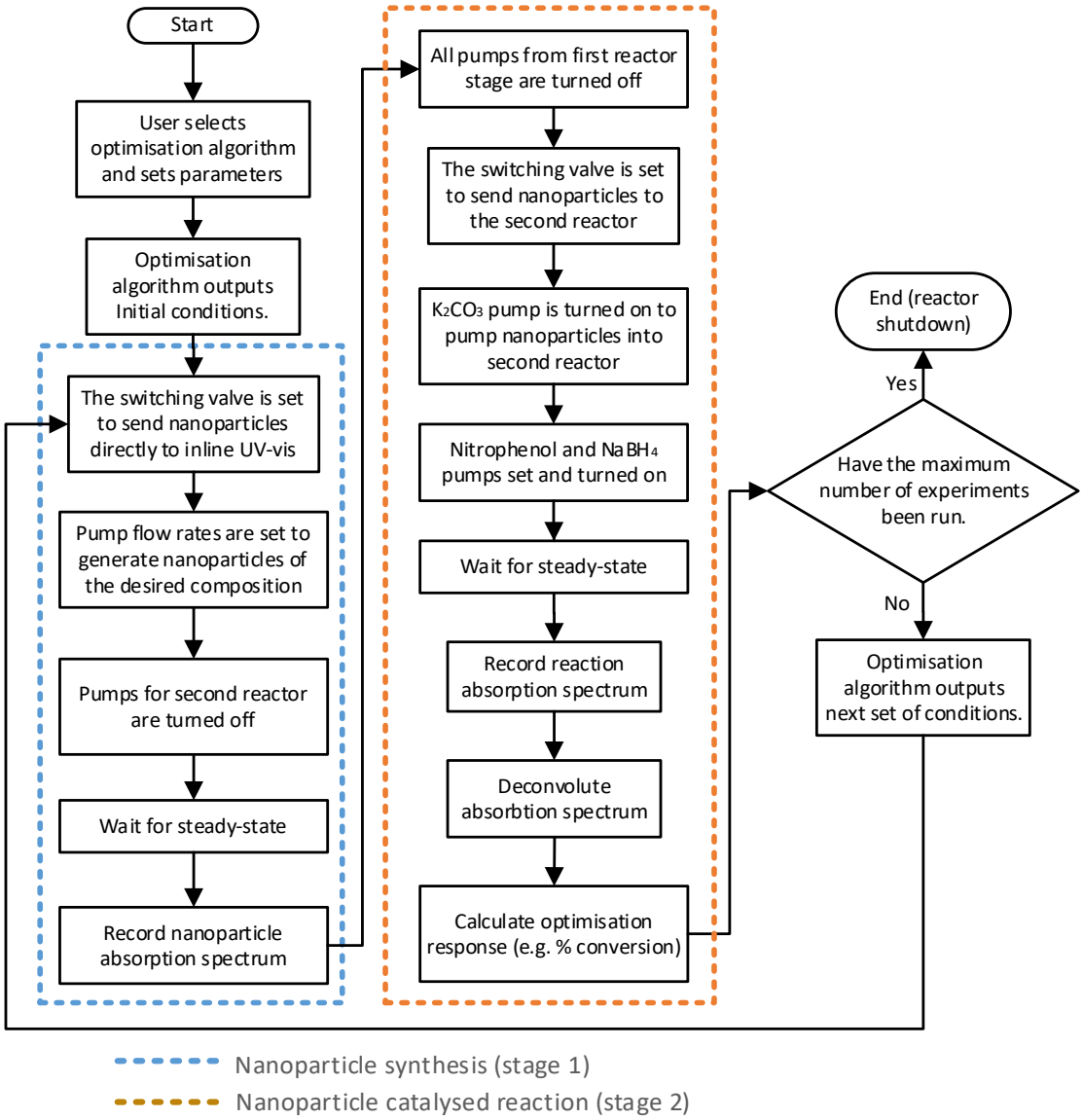

Figure 132. A flow diagram describing the automated processes by which the two-stage nanoparticle catalyst synthesis and screening reaction optimisation was performed.

Fixed wavelength (400 nm) inline UV-vis absorption spectroscopy was used to verify that steady-state conditions were reached during each experiment, see Figure 133. The blue lines indicate when the reactor was operating under stage one conditions

(nanoparticle synthesis). The orange lines indicate when the reactor was operating under stage two conditions (nanoparticle catalysed reaction optimisation).

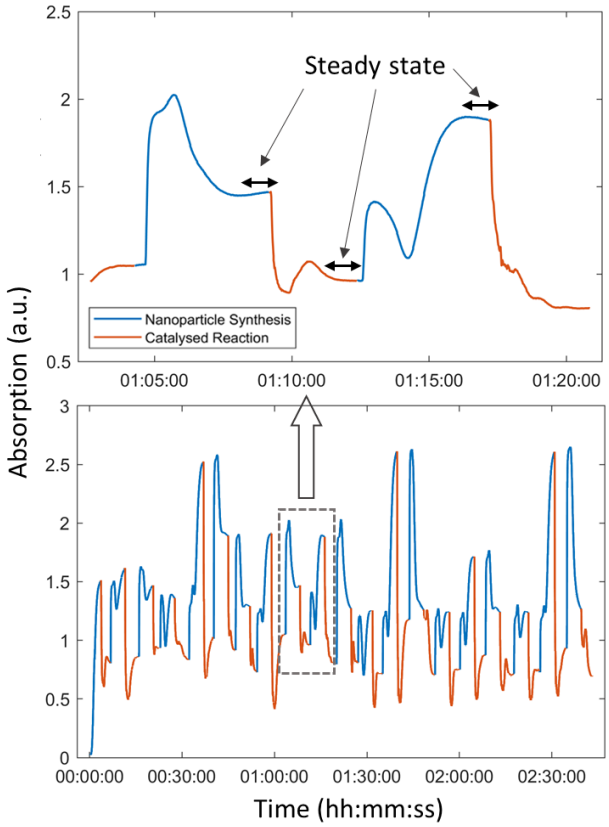

Figure 133. (bottom) A figure showing the changing fixed wavelength absorption @ 400 nm throughout the first 20 experiments of the optimisation experiment, described further in section 5.3.1. Blue lines indicate when nanoparticle synthesis was taking place, orange lines indicate when the catalysed reaction was being performed. (top) Expanded region to highlight when steady-state conditions were achieved.

5.3 Results

5.3.1 SNOBFIT optimisation

The stable noisy optimisation by branch and fit (SNOBFIT)[106] algorithm was initially selected, owing to its ability to locate the global optimum in the presence of experimental noise. Previous studies have found that alloying gold and silver can increase the catalytic performance of the nanoparticles for nitrophenol reduction reactions.[179,197,284] The optimisation design space was initially explored between 0.0:1.0 and 1.0:0.0 Au:Ag ratios, residence times between 0.5-1.5 min and NP:$NaBH_4$ ratios between 0.1-0.3 were also included as additional variables. The initial concentration of nitrophenol was kept constant for each experiment and pumped into the reactor at 10% vol/vol. The SNOBFIT algorithm also required a step size (dx) to be set for each optimisation, which was set to 0.01 for all variables to offer a near-continuous set of

conditions which could be explored by the algorithm. However, due to the limitations of the equipment, particularly the pump flow rate resolutions: 0.001 mL/min for Jasco HPLC pumps and 0.01 mL/min for SyrDos pumps, the actual achievable conditions were discrete, meaning instead the nearest possible conditions were set for each experiment. Table 10. shows the limits set for the first SNOBFIT optimisation performed by the system during the initial optimisation experiment.

Table 10. Design space for first SNOBFIT optimisation exploring all possible Au:Ag ratios.

	Au:Ag ratio	NP:$NaBH_4$ ratio	Residence time
Upper bound	1:0 - Au:Ag	0.3	1.5
Lower bound	0:1 - Au:Ag	0.1	0.5

The optimisation was terminated after 23 experiments taking 1.6 hours, with 5 minutes required to reach steady-state in the first reactor stage and between 1.35 and 4.05 min to reach steady-state in the second reactor stage per experiment. The results are shown in Figure 134 and tabulated in Appendix section 8.1.11.1. The highest conversion obtained was 56.78% obtained with 100% Au nanoparticle catalysts after 20 experiments (highlighted with a star in Figure 134), which occurred at a residence time of 1.2 min and a NP:$NaBH_4$ ratio of 0.27. This preliminary optimisation experiment provided useful information about the reaction design space, most notably that higher ratios of gold led to higher conversions.

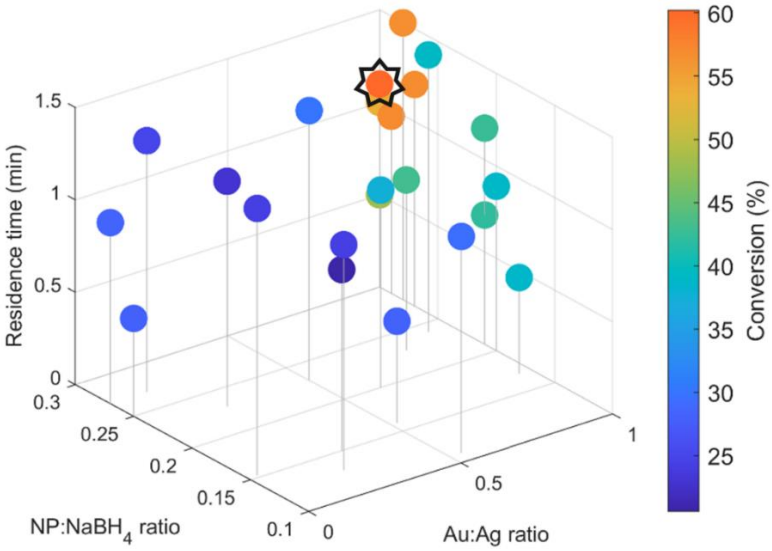

Figure 134. 3D plot showing results of a SNOBFIT optimisation exploring all possible Au:Ag ratios. The optimal reaction conditions identified in this optimisation are highlighted with a black star.

This optimisation experiment failed to identify any increase in catalytic performance with alloyed nanoparticles, this could have been due to the relatively small number of experiments carried out. To explore the region of space around these optimum conditions more thoroughly, the next optimisation experiment was limited to exploring Au:Ag metal ratios between 0.9:0.1 - 1.0:0.0 Au:Ag. The residence time was explored between 0.7 and 2 minutes, see Table 12.

Table 11. Design space for second SNOBFIT optimisation exploring Au:Ag ratios between 0.9-0.1 to 1.0-0.0.

	Au:Ag ratio	NP:$NaBH_4$ ratio	Residence time (min)
Upper bound	1.0:0.0 - Au:Ag	0.3	2
Lower bound	0.9:0.1 - Au:Ag	0.03	0.7

The results of this second optimisation are shown in Figure 135. The highest conversion was 66.58%, obtained after 3.2 hours, this occurred at the upper bounds of residence time (2.00 min) and NP:$NaBH_4$ ratio (0.3). Notably, the optimum Au:Ag ratio was 0.97:0.03, higher conversions were also observed at higher residence times and NP:$NaBH_4$ ratios.

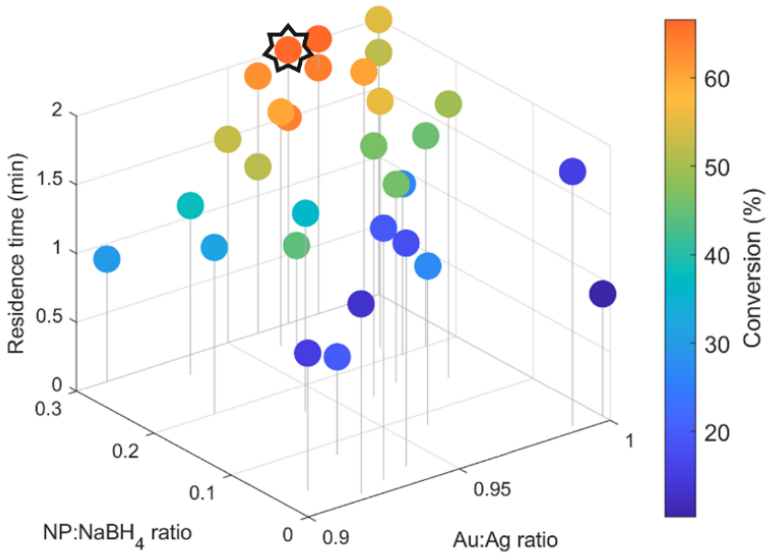

Figure 135. 3D plot showing results of second SNOBFIT optimisation exploring Au:Ag ratios between 0.9:0.1 and 1.0:0.0 Au:Ag with SNOBFIT. The optimal reaction conditions identified in this optimisation are highlighted with a black star.

This optimisation identified that a small amount of silver significantly increased the performance of the nanoparticle catalysts. Similar findings have been found in the literature for improved catalytic performance of AuNPs when alloyed with Ag in CO

oxidation reactions.[177] It has been theorised that combining both Au and Ag alters the electronic properties of the nanoparticles, resulting in a stronger tendency to lose electrons to the adsorbates. In CO oxidation this is advantageous as an electron transfer from the metal to the antibonding orbital of the O_2 molecule would weaken the O-O bond, lowering the energy barrier for CO oxidation.[285] He *et. al.* further investigated the synergistic effects of adding small amounts of silver to an alloyed gold nanoparticle catalyst in a simulated study, the authors simulated the formation of AuAgNP alloys with a variety of Wulff structure morphologies. They found that the Ag atoms segregated from the bulk Au phase along the edges of the nanoparticle structures. These lower coordinated Ag atoms were found to preferentially bind to and activate the O_2 molecules, which reacted with adjacent CO molecules selectively absorbed on the nanoparticle faces predominantly made up of Au atoms.[176]

The effect of adding small amounts of silver to the AuAgNPs was further investigated experimentally in this study by conducting a nanoparticle composition profile at the maximum residence time and NP:$NaBH_4$ ratio. This confirmed that an Au:Ag ratio of 0.97:0.03 was a "sweet spot" for this reaction, where any increase or decrease from this ratio resulted in a significant decrease in conversion, a plot showing this composition profile is shown in Figure 136.

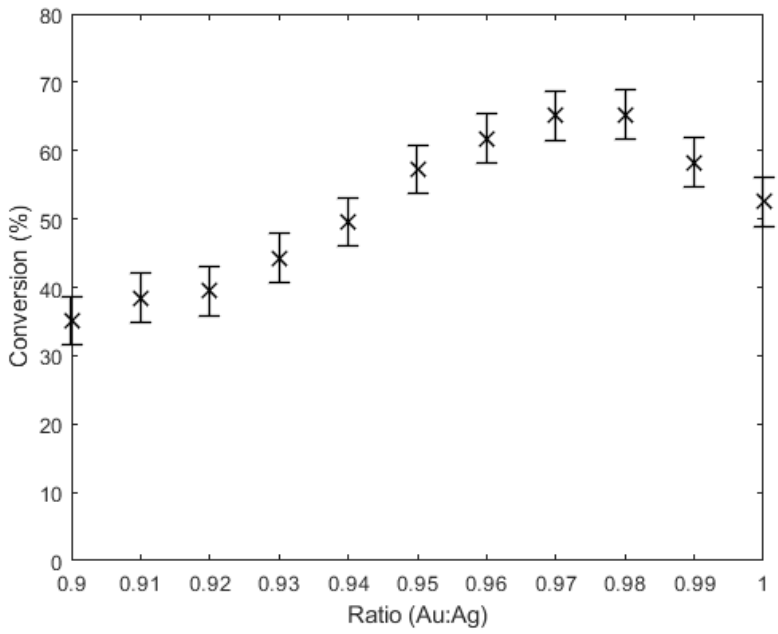

Figure 136. A line plot showing the effect of changing Au:Ag ratio between 0.9-0.1 to 1.0-0.0 Au:Ag, for the conversion of nitrophenol to aminophenol, the error bars are based on 3 repeats taken @ an Au:Ag ratio of 0.97:0.03 with a standard deviation of 3.58% quoted as the error.

The reactor system described so far has proven capable of accurately and reproducibly exploring a region of design space, obtaining the optimal Au/Ag nanoparticle composition and reaction conditions for a catalysed nitrophenol reduction reaction. To further improve this strategy, the efficiency of the closed-loop optimisation was improved through the use of a Bayesian optimisation algorithm.

5.3.2 Bayesian optimisation

As chemical systems are inherently expensive-to-evaluate due to material and time costs, minimising the number of experiments required is paramount. Bayesian optimisation algorithms are currently popular optimisation algorithms for expensive-to-evaluate chemical systems, these algorithms in general utilise Gaussian processes to maximise the expected improvement. One drawback of this approach is the requirement to predefine the hyperparameter for the trade-off between exploration and exploitation, meaning many optimisations are either over or under-explored – reducing either the efficiency or accuracy of the optimisation. Therefore, we investigated the use of a Bayesian Optimiser with Adaptive Expected Improvement (BOAEI), which dynamically adjusted its exploration hyperparameter as the optimisation proceeded. The same optimisation was repeated to directly compare the efficiency of SNOBFIT and BOAEI, the optimisation limits are shown in Table 12.

Table 12. A table outlining the design space for the BOAEI algorithm.

	Au:Ag ratio	NP:$NaBH_4$ ratio	Residence time (min)
Upper bound	0.1:0.0 - Au:Ag	0.3	2
Lower bound	0.9:0.1 - Au:Ag	0.03	0.7

Seven exploration experiments were generated using a Latin hypercube sampling method. After performing these experiments, the BOAEI optimisation located the same optimum as previously, but in a significantly reduced number of experiments with only 3 additional experiments required to find the optimal conditions. These were an Au:Ag metal ratio of 0.97:0.03; a NP:$NaBH_4$ ratio of 0.3 and a residence time of 2 minutes, discovered only 1.3 hours after the optimisation was initiated. In terms of efficiency, this represents a marked improvement over traditional nanoparticle optimisation methods, which require extensive characterisation of screening libraries. The results of this optimisation are shown in Figure 137, the experimental conditions which achieved the highest conversion are highlighted with a black star.

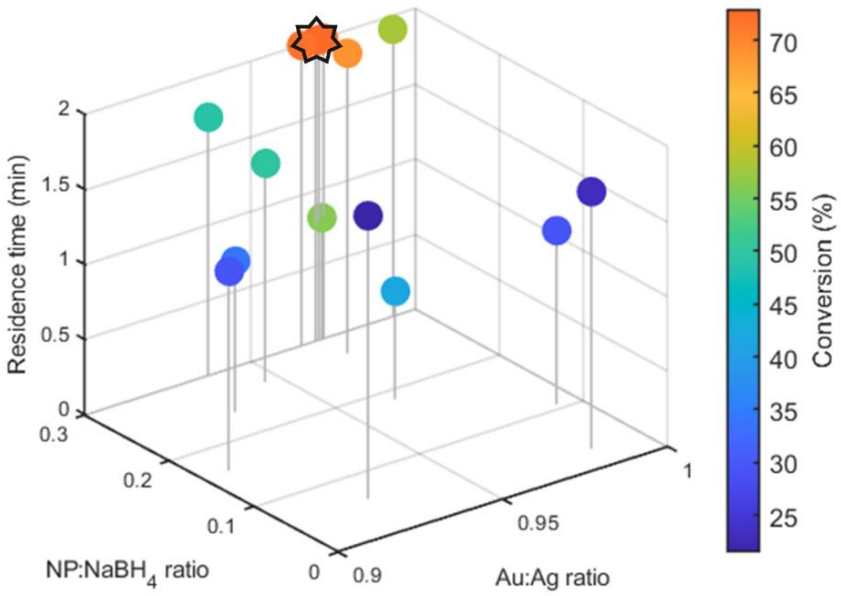

Figure 137. 3D plot showing results of the BOAEI algorithm optimisation exploring Au:Ag ratios between 0.9-0.1 to 1.0-0.0 Au:Ag. The optimal reaction conditions identified in this optimisation are highlighted with a black star.

A convergence plot comparing the SNOBFIT and BOAEI algorithms is presented in Figure 138. This increase in efficiency could be due to the BOAEI algorithm generating a more accurate singular model upon which to base its prediction of the best reaction conditions to carry out during the optimisation, whereas SNOBFIT generates multiple models in different areas of the design space to explore and optimise in parallel with less focus on narrowing down the optimal conditions.

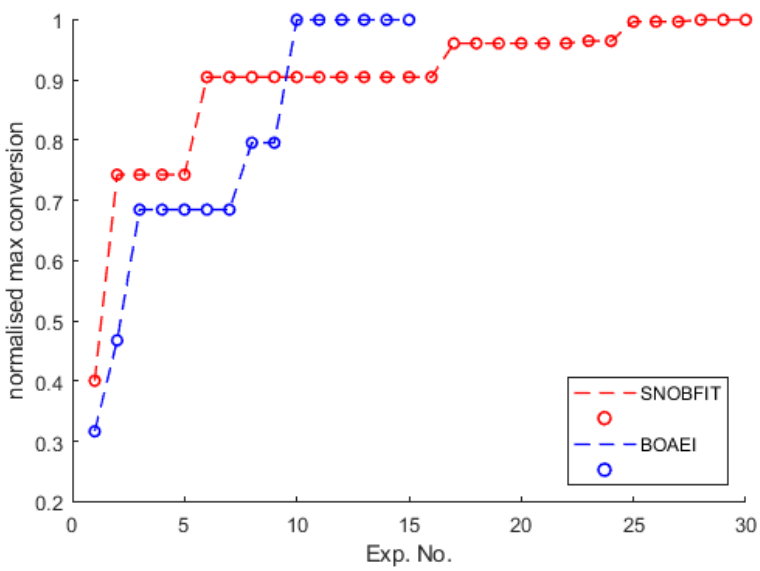

Figure 138. A convergence plot showing a comparison between the number of experiments taken to find the optimal conditions with the BOAEI and SNOBFIT algorithms.

5.3.3 TEM analysis

TEM analysis was used to compare the size distribution profiles of the nanoparticles within the optimal performance range. These were nanoparticle alloys with ratios of 0.96:0.04, 0.97:0.03, 0.98:0.00, 0.99:0.01 and 1.00:0.00 - Au:Ag. Representative TEM images are shown in Figure 139, further images and size analysis can be found in the Appendix section 8.1.4.

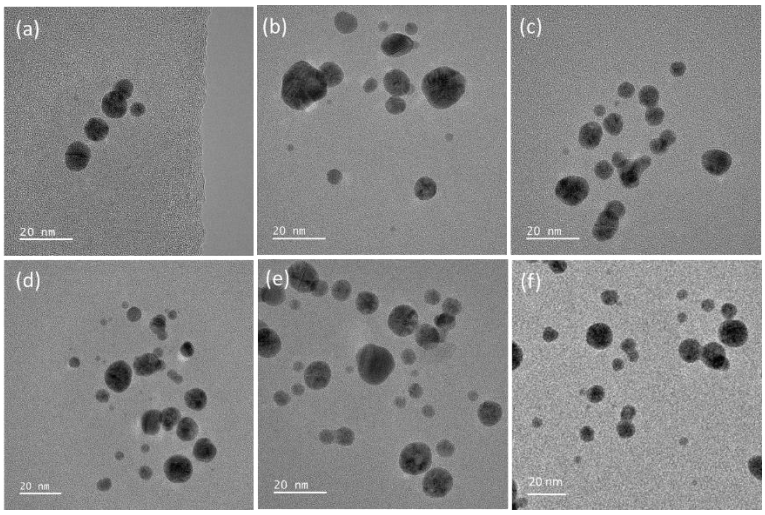

Figure 139. TEM images showing AuAgNP ratios of (a) 0.96:0.04,(b) 0.97:0.03, (c) 0.98:0.00,(d) 0.99:0.01(e) pure AuNPs and (f) 0.97:0.03 AuAgNPs after use in a catalytic reaction.

All of the nanoparticles analysed between 0.96:0.04 and 1.00:0.00 Au:Ag fell within a similar size range. The optimal nanoparticles 0.97:0.03 – Au:Ag were analysed before and after they were used to catalyse a reaction to confirm there was no significant change in size distribution (Figure 140). The average and standard deviation size ranges for the 6 most optimal catalyst ratios are shown in Figure 141.

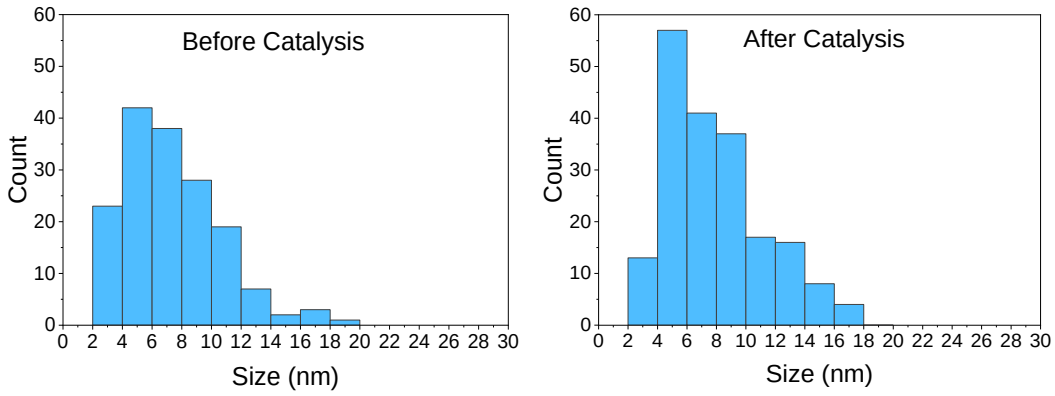

Figure 140. Histograms showing the size distribution of particle sizes for the optimal AuAgNPs with a ratio of 0.97:0.03 – Au:Ag

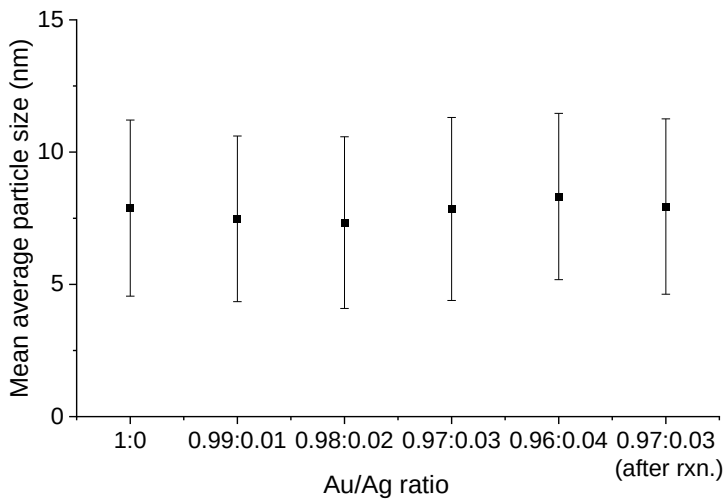

Figure 141. A plot showing the mean average and standard deviation range for the nanoparticles with Au:Ag ratios from 0.96:0.04 to 1.00:0.00 with steps of 0.01.

These results show that the nanoparticles within this range possessed very similar size distribution ranges. The average nanoparticle size for AuAgNPs nanoparticles containing between 0-4% Ag was 7.48 nm with a standard deviation of +/- 3.13. The nanoparticle size also showed no significant changes after they were used in a reaction. This supports the hypothesis that any increase in performance was due to changes in the nanoparticle composition rather than changes in the nanoparticle size.

These observations could have been due to the presence of Ag and Au surface sites which each preferentially adsorbed reacted and desorbed reactant molecules and intermediates during the reduction process. The increase in activity of the alloyed species could also be explained by the Sabatier principle which states that modulation of nanoparticle composition can lead to changes in the nanoparticle's electronic properties, causing reactant/product molecules such as the hydride ions from $NaBH_4$ or nitrophenol to bond neither too strongly nor too weakly to the metal surface promoting reactivity,[286] however further work would be required to verify these theories.

5.4 Summary

This chapter describes the first use of a performance directed nanocatalyst synthesis strategy, a two-stage continuous flow reactor coupled with closed-loop optimisation was used for the precise synthesis of bimetallic AuAgNPs with different metal compositions. This was accomplished using a modified version of the Turkovich protocol performed in a miniature CSTR cascade. The catalytic activity of the resulting AuAgNPs was then subsequently tested in the second stage of the system using the reduction of 4-nitrophenol as a model reaction.

An intermediary nanoparticle storage coil and 6-port switching valve enabled decoupling of the flow rates between the two stages, allowing nanocatalyst composition to be simultaneously optimised with other important reaction variables for the first time. Rapid analysis of the catalytic performance, nanoparticle characterisation and steady-state monitoring were all accomplished using a single inline UV-Vis spectrometer, using a flow bypass and spectral deconvolution approach.

The system was tested with two optimisation algorithms, SNOBFIT: a well-established and trusted optimisation algorithm for self-optimising reactors. The SNOBFIT algorithm was able to identify an area of maximum catalytic performance after 28 experiments in 4 hours. Compared with BOAEI, a newer optimisation algorithm with adaptive hyperparameter tuning, which identified the same region of maximum catalytic performance within just 10 experiments (1.3 hours). The ideal conditions in each case corresponded to a 0.97:0.03 AuAgNP ratio at the upper limits of residence time and 0.3 NP:$NaBH_4$ equivalents. Hence, this activity directed approach was successful in rapidly locating the optimum catalytic activity, notably corresponding to a non-intuitive nanoparticle composition. This strategy provides an unprecedented means by which to rapidly develop new fit-for-purpose nanoparticles with widespread potential applications.

Chapter 6
Conclusions and future work

The aim of this project, to design and develop an automated flow system for nanoparticle catalyst optimisation, has been fulfilled within this thesis. This approach is to the best of the authors knowledge, the first example of such a reactor. Overcoming issues associated with more traditional batch performance testing of nanoparticle catalysts, which is notoriously difficult as small changes to the reaction conditions can lead to significant differences in measured reaction kinetics.

Continuous flow methodologies were used to overcome these issues by synthesising nanoparticles in a controlled and reproducible manner then testing them within a consistent environment allowing fairer comparison of catalytic performance. Automation reduced the number of mistakes due to human error and application of the latest optimisation algorithms reduced the number of experiments required to determine the optimal conditions for both the catalyst and catalysed reaction.

The project was broken down into 4 distinct sections. Firstly, in chapter 2, a reactor was designed for the optimisation of a nitrophenol reduction reaction catalysed by gold nanoparticles in conditions flow. A major issue solved in this chapter was the elimination of gas evolution from reducing agent $NaBH_4$ used to reduce nitrophenol to aminophenol. This was overcome through pressurisation of the reactor, lowering the concentration range of $NaBH_4$ used in the reaction and raising the pH of $NaBH_4$ to prevent/slow down reactions with H^+ in aqueous solution. Once these challenges were overcome the reactor was then able to explore the effect of changing AuNP surface area, $NaBH_4$ concentration and residence time on the conversion of nitrophenol to aminophenol.

It was then possible to fit a kinetic model to these data using a kinetic fitting model developed by Taylor *et al.* Where ordinary differential equation (ODE) solvers were used to predict reaction progression under different conditions using the Langmuir Hinshelwood (LH) model. A genetic algorithm was used to determine the kinetic parameters within the LH model by maximising the convergence of the predicted reaction outcomes to experimental data. Upon identifying this kinetic information, it was possible to use the model to predict reaction conversion under different experimental conditions. The model was used to predict the reaction kinetics of a AuNP catalysed 4-NP reduction reaction performed in a batch reactor with a two-fold increase in 4-NP concentration, compared to the flow optimisation study. The resulting extrapolated reaction kinetics showed good agreement with the model prediction, with a residual error of only 1.85%.

Chapter 3 follows on from work published by… in this section of the project major challenges related to reactor fouling were overcome through carful choice of reactor materials and reaction conditions. Finally, chapter 5 showed how the reactors developed in chapters 2 and 3 could be combined to produce a powerful system capable of synthesising and optimising nanoparticles based on their performance in a specific reaction, this reaction was also optimised during the optimisation process.

Future work in this area could include the optimisation of other nanoparticle alloy catalysts such as PdPt,[81] RhAg,[61] or AuPd nanoparticles.[84] These catalysts are among the few systems which already have proven methods for continuous synthesis in flow, however, it is likely given time more continuous nanoparticle synthesis methods will appear in the literature and thus this represents a widely applicable route to optimisation.

In addition to composition size and shape have also been shown to influence the catalytic performance of these materials.[31,231,287] Incorporation of size analysis into a continuous system could employ a technique such as DLS, a recent study has shown that a flow cell combined with DLS can be used for real-time monitoring of nanoparticle size during synthesis, coupling this technique with the methods outlined in this thesis could provide more in depth understanding of these relationships in a variety of systems.[93]

Finally, other reactions such as the nanoparticle catalysed oxidation of alcohols,[87] click chemistry[288] and Suzuki-cross coupling reactions[22] could be optimised, while employing a more comprehensive array of in/online analytical techniques such as dynamic light scattering, nuclear magnetic resonance, mass spectroscopy, high-pressure liquid chromatography and gas chromatography to understand in even greater detail the structure property relationships which exist within a wide range of reaction systems.

Chapter 6 Materials and methods

All chemicals were sourced from commercial vendors and used without further purification. Solutions were made using type 1 ultra-pure water purified to a resistivity of 18.2 MΩ cm^{-1} with a Purelab Flex pure water system throughout this chapter.

Chloroauric acid

Supplier: Fisher Chemical, CAS: 16903-35-8, molecular formula: $HAuCl_4$, packaging: vial, quantity: 1 g, formula weight: 339.78 g/mol, physical form: orange solid.

Sodium citrate tribasic dihydrate

Supplier: Sigma Aldrich, CAS Number 6132-04-3, Bio Ultra, for molecular biology, >=99.5% (NT), physical form: white solid.

4-Nitrophenol

Supplier: Sigma Aldrich, CAS Number 100-02-7, molecular weight: 139.110 g/mol physical form: yellow solid.

Sodium borohydride

Supplier: Sigma Aldrich, CAS: 16940-66-2, molecular formula: $NaBH_4$, molecular weight: 37.83, physical form: white solid.

Silver Nitrate

Supplier: Sigma Aldrich, CAS no. 7761-88-8, formula weight: 169.87 g/mol, physical form: granular white crystals.

Tannic acid

Supplier: Sigma Aldrich, CAS: 1401-55-4, quantity: 100 g, formula weight: 1701.20 g/mol, physical form: brown powder.

Potassium carbonate

Supplier: Fisher Chemical, CAS: 584-08-7, quantity: 500 g, melting point: 891 °C, molecular formula: K_2CO_3, formula weight: 138.21 g/mol, physical form: white powder.

Aminophenol

Supplier: Fisher Chemical, CAS: 123-30-8, quantity 50g, melting point: 188°C.

7.1 Methods (chapter 2)

7.1.1 Reservoir solutions

7.1.1.1 Gold nanoparticle catalyst

The gold nanoparticle solution was synthesised using a Turkevich approach adapted from N.G. Bastus.[17] $HAuCl_4$ (aq.) (25 mM, 1 mL) was injected rapidly into a 3 necked 250 mL round-bottomed flask containing a stirred solution of sodium citrate (2.2 mM, 149 mL) at 95 °C with a reflux condenser for 30 minutes, the solution turned from pale yellow to greyish blue before turning pink then ruby red.

7.1.1.2 Nitrophenol (0.6 mM)

Nitrophenol (83.46 mg) was dissolved in 1000 mL of water.

7.1.1.3 $NaBH_4$ (10 mM)

To prevent hydrolysis of $NaBH_4$ and the generation of gas bubbles during the optimisation the $NaBH_4$ (aq.) reservoir was prepared as follows. $NaBH_4$ was dissolved in ice-cold water (600 mL) and maintained at 0 °C by placing the reservoir container in an insulated ice bath and adjusted to pH 10 by dropwise addition of sodium hydroxide solution (0.1 M). The $NaBH_4$ (aq.) solution was then passed through a heat exchange coil, so the $NaBH_4$ (aq.) solution reached room temperature before entering the reactor.

7.1.1.4 Water

Type 1 ultra-pure water purified to a resistivity of 18.2 MΩ cm^{-1} with a Purelab Flex pure water system.

7.1.2 Analytical methods

7.1.2.1 Preparation of aminophenol from batch reaction

$NaBH_4$ (18.91 mg) was added to a 10 mL stirred aqueous solution of nitrophenol (0.6 mM) and AuNPs 0.017 mM (see Section 7.1.1.1), the solution was then left to stir for 2 hours. After the reaction, the mixture was centrifuged, and syringe filtered (pore size – 25 µm).

7.1.2.2 HPLC method

5 µL of the filtered centrifuged reaction solution, was injected into an Agilent 1100 series HPLC system, with an Agilent Eclipse Plus C18 column (150 mm length 4.6 mm × 4.6 mm i.d., 5 µm particle size) and a gradient elution. The column temperature was

maintained at 30 °C and the UV detection wavelength set to 273 nm. The mobile phase consisted of a mixture of ultrapure deionised water (18 MΩ cm^{-1}) and HPLC grade acetonitrile, each containing 0.01% TFA, the gradient elution was performed at a constant flow rate of 1 mL/min as shown in Table 13 below.

Table 13. The solvent elution gradients used in the HPLC method to determine the extent of nitrophenol to aminophenol conversion.

Time (min)	Acetonitrile (%)	Water (%)
0	5	95
1	5	95
17	95	5
18	95	5
18.01	5	95
20	5	95

7.1.2.3 Preparation of calibration solutions

4-Aminophenol and 4-nitrophenol calibration standards were dissolved in deionized water (18 MΩ cm^{-1}) to produce 5 standard stock solutions between 0.15 and 0.75 mM. For both molecules calibration linearity was observed in a concentration range of 0.15 to 0.75 mM.

7.1.2.4 XPS method and sample preparation

AuNPs were synthesised in batch using the method described in section 7.1.1.1. For the pre-catalyst sample, nanoparticles were directly sampled after synthesis. For the post-catalysis sample, nanoparticles were sampled after the catalytic reduction of nitrophenol (method described in section 7.1.5.2), without further washing. For both samples, the original nanoparticle dispersions were concentrated via centrifugation-induced sedimentation (repeated centrifugation at 14,000 RPM for 5 min, with the supernatant from each run discarded and the tube refilled with more nanoparticle dispersion). The resulting concentrated AuNP dispersions were then drop-casted onto a silicon wafer and left to dry in air.

The spectra were obtained using a UHV-XPS system with a SPECS Phoibos 150 analyser with 1D-DLD detectors. The source was a monochromated Al anode (SPECS

XR-50M) with an energy of 1486.7 eV. The energy resolution was estimated to be 0.2 eV at a pass energy of 30 eV for the high-resolution spectra and 1 eV (step size) at a pass energy of 30 eV for the survey spectra.

The data were processed using CasaXPS software. The spectra were calibrated against the adventitious C 1s peak, which was set to a binding energy of 284.8 eV. An intensity calibration was also applied using a transmission function file obtained from the instrument operator. The angular distribution correction was set to 54.7 °.

Survey spectrum quantification was performed using the quantify tool in CasaXPS. Shirley-type backgrounds were applied to the elemental peaks and subsequent integration of the peaks enabled quantification of the atomic surface concentrations. Default RSF values for each element were used to scale the peak areas. A Shirley background was also defined for the high-resolution spectra, which were then subtracted before peak fitting. No constraints on peak width or position were required due to the symmetric nature of the Au $4f_{7/2}$ and $4f_{5/2}$ peaks.

7.1.2.5 AuNP UV-vis analysis

Reactor streams and batch samples were analysed with UV-vis spectroscopy using a CVF-Q-10 quarts flow cell (1 cm path length), in an OceanOptics CUV UV cuvette holder. The UV-vis spectra were obtained using a FLAME-S-US-VIS OceanOptics spectrometer (200-850 nm) with a DH-MINI deuterium tungsten halogen light source (200-2000 nm) and QP400-2-SR-BX 400 um premium fibre optic cables.

The inline spectra were monitored using ChemiView[130] software, time-stamped full spectrum readings were taken approximately every second and averaged over 100 scans, with the spectrometer integration time set to 7500. Absorption spectrum data was recorded in a text (.txt) file for further interpretation with code written in MATLAB.

7.1.2.6 AuNP DLS size distribution analysis

The AuNP solution (synthesis method described in Section 7.1.1.1) was added without dilution to a 1 cm path length disposable plastic cuvette. Dynamic light scattering (DLS) size distribution analysis was performed using a Nano series Malvern Zetasizer. Sample measurements were taken at 25 °C with an equilibration time of 120 seconds, 11 runs were performed per measurement each with an acquisition time of 10 seconds. DLS measurements were performed three times.

7.1.2.7 *Transmission electron microscopy (TEM) analysis*

TEM analysis was used to characterise the AuNPs (synthesis method described in Section 7.1.1.1), both before and after they were used to catalyse a nitrophenol reduction reaction. The samples for TEM were prepared by taking a solution of the AuNPs (5 drops dispersed in isopropanol (2 mL) using an ultrasonic bath) and depositing it on a holey carbon film-coated copper grid. TEM images were acquired on a FEI Tecnai TF20 field emission gun microscope operating at 200 kV. For both samples, the NP size distribution histograms in Figure 37 and Figure 38 were obtained from 120 different NPs assuming a spherical shape and with random distribution.

7.1.3 Reactor setup

A detailed reactor schematic is shown in Figure 142, reservoirs containing solutions of AuNPs, $NaBH_4$, nitrophenol and water were pumped through a 3.5 mL 1/32" ID tubular reactor; the reactor outlet was monitored with inline UV-vis. The pressure of the reactor was regulated at 40 psi with a cartridge BPR and monitored with a pressure sensor. A peristaltic pump was used to ensure the inline gas/liquid membrane separator was always wetted with $NaBH_4$ solution.

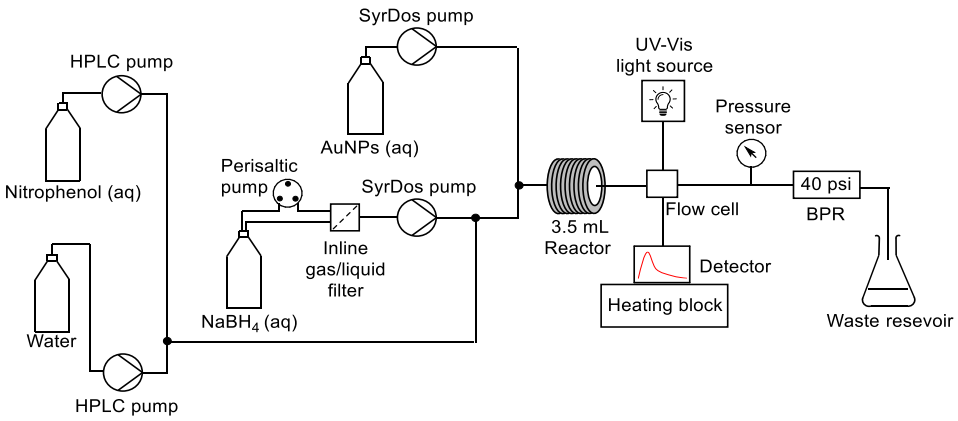

Figure 142. A reactor schematic describing in detail the reactor setup, the 4 pumps and the UV-vis detector in this schematic were connected to a computer to allow automated optimisation.

Figure 143 shows a photograph of the reactor setup, the components are numbered and described further in Table 14.

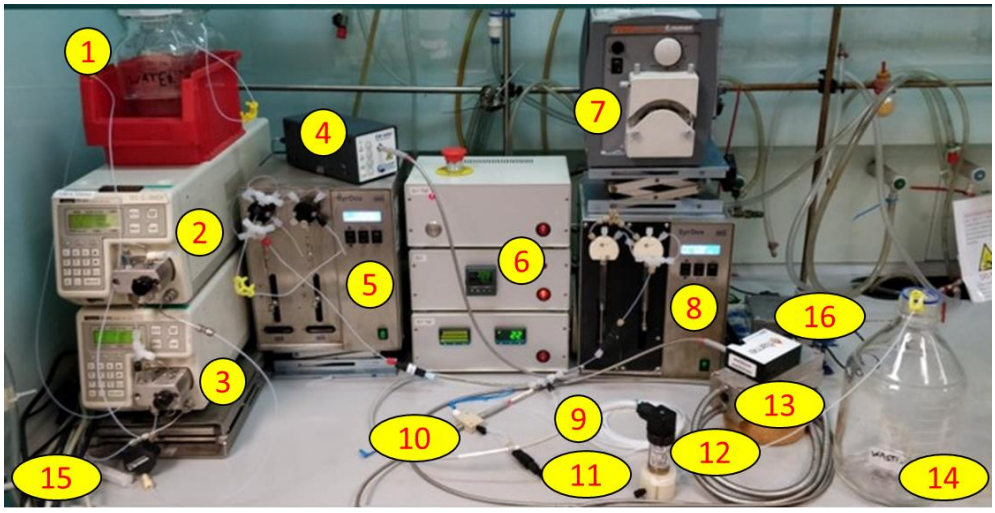

Figure 143. Photograph showing a configuration of the flow reactor platform for the optimisation of a gold nanoparticle catalysed nitrophenol reduction.

7.1.3.1 Table of components

Table 14. A table showing the name and purpose of the reactor components shown in Figure 143.

Number	Name	Purpose
1	Reagent reservoirs	Storage of solutions
2	HPLC pump	Nitrophenol pump
3	HPLC pump	Water pump
4	UV-vis light source	Inline analysis
5	SyrDos pump	AuNP pump
6	Eurotherm temperature controller	To keep spectrometer temperature constant
7	Peristaltic pump	To recirculate $NaBH_4$ solution through a gas/liquid separator
8	SyrDos pump	$NaBH_4$ pump
9	3.5 mL 1/32” ID PTFE tubing	Reactor
10	UV-vis flow cell	Inline analysis
11	Back pressure regulator (BPR)	Reactor pressure regulation
12	Pressure sensor	Pressure monitoring/overpressure protection
13	Heating block	UV-vis temperature regulation
14	Waste from reactor reservoir	Storage of reactor waste
15	Power/computer connection cables	Power and automated reactor control
16	UV-vis detector	Inline analysis

7.1.4 Reactor component details

Reactor: 7.07 m of 1/32” (ID) PTFE tubing (3.5 mL flow reactor)

Reagent pumps: Nitrophenol solution (0.6 mM): Jasco PU-980, pure water: Jasco PU-980, $NaBH_4$ (aq.) solution (10 mM): SyrDos2 and AuNP solution (0.167 mM): SyrDos1.

Reactor Unions: IDEX ETFE T-piece assemblies (part no. P-632)

Back Pressure Regulator: Spring-based (40 psi) IDEX (part no. P-761).

UV-Vis spectrometer: FLAME-S-US-VIS OceanOptics (200-850 nm), DH-MINI deuterium tungsten halogen light source (200-2000 nm), QP400-2-SR-BX 400 μm premium fibre optic cables and a CVF-Q-10 quarts flow cell (1 cm path length) in an OceanOptics CUV-UV cuvette holder.

Software: Automation code written in MATLAB 2018a was used to control the reactor pumps and determine the best reactor conditions using the optimisation algorithm SNOBFIT.

7.1.5 Experimental Methods

7.1.5.1 AuNP catalysed nitrophenol reduction (transient kinetic plot)

For the transient kinetic plot shown in Section 2.1, a solution of 4-nitrophenol (0.15 mg/mL, 1 mM, 2 mL) was measured into a UV cuvette, $NaBH_4$ (aq.) (0.4 mg/mL, 10 mM, 1 mL) and AuNP solution (300 μL, prepared using the standard protocol described in section 7.1.1.1) was then added the reaction mixture, shaken and monitored with UV-vis spectroscopy.

7.1.5.2 AuNP catalysed nitrophenol reduction (NP shape/structure control exp.)

To confirm there were no changes to the shape/structure of the AuNPs after they were used to catalyse a nitrophenol reduction. AuNPs (24 mL, synthesised using the method described in section 7.1.1.1) was added to a stirred solution of nitrophenol (50 mL of a 0.24 mM in water) in a 250 mL round-bottomed flask, additional water (20 mL) was added to make the solution up to 94 mL. The reaction was initiated by adding a portion of sodium borohydride solution (6 mL, 50 mM) to the stirred reaction mixture bringing the final total volume to 100 mL with the final concentrations: 0.12 mM nitrophenol, 0.04 mM AuNPs and 3 mM sodium borohydride, the reaction was left for 30 min.

7.2 Methods (Chapter 3)

7.2.1 Analytical methods

7.2.1.1 TEM-EDS analysis

Samples for TEM analysis were prepared by drop-casting nanoparticles suspensions produced using the reactor described in Section 3.3.9, (5 drops of nanoparticle solution dispersed in isopropanol (2 mL) using an ultrasonic bath) onto holey carbon film-coated 300 mesh copper grids.

TEM analysis was carried out using the FEI Titan Themis Cubed operated at 300 kV and fitted with a monochromator and Super-X EDX system with a windowless 4-detector design. Bright-field TEM images were collected using the Gatan OneView 16 Megapixel CMOS digital camera. GMS3 and Velox software was used to collect and process the data.

7.2.1.2 UV-vis spectroscopy

Reactor streams and batch samples were analysed with UV-vis absorption spectroscopy by flowing the nanoparticle solutions through a CVF-Q-10 quarts flow cell (1 cm path length), within an OceanOptics C-UV cuvette holder. The UV-vis absorption spectra were obtained using a FLAME-S-US-VIS OceanOptics spectrometer (200-850 nm) with a DH-MINI deuterium tungsten halogen light source (200-2000 nm) and QP400-2-SR-BX 400 um premium fibre optic cables.

The inline UV-vis absorption spectra were monitored using ChemiView[130] software and time-stamped full spectrum readings were taken approximately every second (averaged over 100 scans). UV-vis absorption data was recorded in a text (.txt) file post-processing of data was performed in MATLAB.

7.2.2 Experimental Methods

7.2.2.1 Batch synthesis AuAgNPs

AuAgNPs with different metal compositions were prepared in batch as follows. AuNP seed solution (5 mL) was added to water (90 mL, 95 °C), followed by sodium citrate (1 mL, 170 mM, 0.08 mol). Immediately after, gold (III) chloride hydrate (for volume see Table 15, 25 mM – stock solution made by dissolving $HAuCl_4$ (0.00294 mol, 1.00 g) in water (100 mL)) and $AgNO_3$ (for volume see Table 15, 25 mM – stock solution, made by dissolving $AgNO_3$ (0.618 mmol, 105 mg) in water (25 mL)) were added

simultaneously. The solutions were then heated and stirred for 1 hour. The resulting solutions were then analysed using UV-vis spectrometry.

Table 15. Volumes of metal precursor added to sodium citrate solution.

Ratio	$HAuCl_4$ (25 mM)	$AgNO_3$ (25 mM)
10:90	50	450
20:80	100	400
30:70	150	350
40:60	400	300
50:50	250	250
60:40	300	200
70:30	350	150
80:20	400	100
90:10	450	50

7.2.2.2 Flow synthesis AuNPs

The following aqueous stock solutions: 1. gold nanoparticle precursor $HAuCl_4$ (0.2 mM) and 2. reducing agent sodium citrate (4.8 mM) were pumped through a 5 mL PTFE tubular reactor in an oil bath heated to 100 °C. Both solutions were pumped through the reactor at the same flow rates with a total combined flow rate of 0.5 mL/min, the reaction was monitored with inline UV-vis absorption spectroscopy.

7.2.2.3 Batch seeded growth synthesis AuNPs

An aqueous solution of $HAuCl_4$ (25 mM, 1 mL) was injected into a stirred solution of sodium citrate (2.2 mM, 150 mL) heated to 95 °C, the subsequent formation of AuNPs was then monitored with online UV-vis spectroscopy, by continuously recirculating material through the reactor and a 600 µL capacity UV-vis flow cell at 5 mL/min with a peristaltic pump. A UV-vis absorption spectra were acquired and integrated between 500-550 nm once every 50 seconds, this time interval was chosen to give the best compromise between obtaining a high-resolution spectrum and a short interval time between scans. On addition of $HAuCl_4$, the solution turned light grey/blue, then ruby red after a few minutes indicating the formation of AuNPs.

The AuNP ‘seeds’ formed in the previous step were then grown by further additions of sodium citrate solution (60 mM, 1 mL) and $HAuCl_4$ (25 mM, 1 mL) at a lower

temperature (90 °C). The changing UV-vis spectrum was monitored after each further addition of precursor.

7.2.2.4 Continuous flow synthesis of AuNPs with AuNPs as catalyst solution

The following aqueous stock solutions were prepared: 1. gold nanoparticle precursor $HAuCl_4$ (0.2 mM), 2. reducing agent sodium citrate (4.8 mM) and 3. AuNP solution was prepared using the same method used to prepare the seed solution described in Section 7.2.2.3. The sodium citrate and $HAuCl_4$ solutions were pumped through a PFA tubular reactor (1/32" ID, internal volume 5 mL) in an oil bath heated to 100 °C, at the same flow rates with a total combined flow rate of 0.5 mL/min, while the pre-formed AuNPs were pumped into the same reactor with a flow rate of 0.2 mL/min. The reaction was monitored continuously with inline UV-vis absorption spectroscopy with adsorption spectra integrated between 500 and 550 nm to give time-series data.

7.2.2.5 Ascorbic acid reducing agent for flow synthesis of AuNPs

The following aqueous stock solutions were prepared: 1. gold nanoparticle precursor $HAuCl_4$ (0.2 mM), 2. reducing agent sodium citrate (4.8 mM) and ascorbic acid (0.2 mM). The sodium citrate and $HAuCl_4$ solutions were pumped through a PFA tubular reactor (1/32" ID, internal volume 5 mL) in an oil bath heated to 100 °C, at the same flow rates with a total combined flow rate of 0.5 mL/min. The reaction was monitored continuously with inline UV-vis absorption spectroscopy, the spectra were then integrated between 500 and 550 nm to give time-series data.

7.2.2.6 Sodium borohydride reducing agent for flow synthesis of AuNPs

The following aqueous stock solutions were prepared: 1. gold nanoparticle precursor $HAuCl_4$ (0.411 mM) and 2. reducing agent $NaBH_4$ (4.11 mM). The $NaBH_4$ and $HAuCl_4$ solutions were pumped through a room temperature PFA tubular reactor (1/32" ID, internal volume 0.5 mL) at the same flow rates, with a total combined flow rate of 6 mL/min. The reaction was monitored continuously with inline UV-vis absorption spectroscopy with adsorption spectra integrated between 500 and 550 nm to give time-series data.

7.2.2.7 Sodium borohydride reducing agent for flow synthesis of AuAgNPs

The following aqueous stock solutions were prepared: 1. gold nanoparticle precursor $HAuCl_4$ (0.411 mM), silver nanoparticle precursor solution $AgNO_3$ (0.411 mM)

and 3. reducing agent $NaBH_4$ (4.11 mM). The $HAuCl_4$, $AgNO_3$ and $NaBH_4$ solutions were pumped through a room temperature PFA tubular reactor (1/32" ID, internal volume 0.5 mL), with flow rates shown in Table 16.

Table 16. Flow rates of metal precursor and reducing agent used to synthesise AuAgNPs in 0.5 mL PFA reactor with sodium borohydride in continuous flow.

Ratio Au:Ag	**$HAuCl_4$ (0.411 mM) mL/min**	**$AgNO_3$ (0.411 mM) mL/min**	**$NaBH_4$ (4.11 mM) mL/min**
100:0	2	0	1
90:10	1.8	0.2	1
80:20	1.6	0.4	1
70:30	1.4	0.6	1
60:40	1.2	0.8	1
50:50	1.0	1.0	1
40:60	0.8	1.2	1
30:70	0.6	1.4	1
20:80	0.4	1.6	1
10:90	0.2	1.8	1
0:100	0	2.0	1

7.2.2.8 Tannic acid reducing agent for AuNP synthesis

The following aqueous stock solutions were prepared: 1. gold nanoparticle precursor $HAuCl_4$ (0.4 mM), 2. reducing agent sodium citrate (4.8 mM) and tannic acid (0.1 mM). The sodium citrate and $HAuCl_4$ solutions were pumped through a PFA tubular reactor (1/32" ID, internal volume 5 mL) in an oil bath heated to 100 °C, at the same flow rates with a total combined flow rate of 2 mL/min. The reaction was monitored continuously with inline UV-vis absorption spectroscopy, with adsorption spectra integrated between 500 and 550 nm to give inline time series data.

7.2.2.9 Batch synthesis of AuNPs with tannic acid

A gold nanoparticle precursor solution containing $HAuCl_4$ (0.4 mM, 25 mL) was heated to 100 °C, then added to a stirred solution containing 25 mL reducing agent sodium citrate (4.8 mM) and tannic acid (0.1 mM). A UV-vis absorption spectrum was recorded for the resulting sample.

7.2.2.10 AuNP synthesis in a fReactor with preheating

The following aqueous stock solutions were prepared: 1. gold nanoparticle precursor $HAuCl_4$ (0.4 mM), 2. reducing agents sodium citrate (4.8 mM) and tannic acid (0.1 mM). The solutions were pumped through two separate (pre-heating) fReactors each with an internal volume of 1.55 mL, heated to 100 °C on a hot plate, the solutions then flowed into a single fReactor, where a reduction reaction took place. Both solutions were pumped into the reactor at the same flow rates with a total combined flow rate of 2 mL/min. The reaction was monitored continuously with inline UV-vis absorption spectroscopy with adsorption spectra integrated between 500 and 550 nm to give time-series data.

7.2.2.11 fReactor flow rate experiment

The following aqueous stock solutions were prepared: 1. gold nanoparticle precursor $HAuCl_4$ (0.4 mM) and 2. reducing agents sodium citrate (4.8 mM) and tannic acid (0.1 mM). The solutions were pumped through 3 fReactors in series each with an internal volume of 1.55 mL, heated to 100 °C on a hot plate. AuNPs were synthesised using the flow rates shown in Table 17 below. Each set of conditions was run for 15 minutes before the next set of conditions was set. The reaction was monitored continuously with inline UV-vis absorption spectroscopy, with adsorption spectra integrated between 500 and 550 nm to give time-series data.

Table 17. Number of fReactors and the flow rates used to determine the requirements for steady-state conditions.

Number of fReactors	**$HAuCl_4$ (0.4 mM) mL/min**	**Sodium citrate (4.8 mM) and tannic acid (0.1 mM)**
3	0.5	0.5
3	1.5	1.5
3	2	2

7.2.2.12 Continuous flow synthesis of AuAgNPs

The following aqueous stock solutions were prepared: 1. gold nanoparticle precursor $HAuCl_4$ (0.4 mM), silver nanoparticle precursor $AgNO_3$ and 3. reducing agents sodium citrate (4.8 mM) and tannic acid (0.1 mM). The solutions were pumped through 3 consecutive fReactors each with an internal volume of 1.55 mL, heated to 100 °C on a hot plate. A full range of AuAgNPs were synthesised using the flow rates shown in Table 18 below. Each set of conditions was run for 15 minutes before the next set of

conditions was automatically set. The reaction was monitored continuously with inline UV-vis absorption spectroscopy, λ_{max} was tracked throughout the reaction.

Table 18. Flowrates of metal precursor and reducing agent used to synthesise AuAgNPs in continuous flow.

Ratio Au:Ag	$HAuCl_4$ (0.4 mM) mL/min	$AgNO_3$ (0.4 mM) mL/min	Sodium citrate (4.8 mM) and tannic acid (0.1 mM)
100:0	2	0	2
90:10	1.8	0.2	2
80:20	1.6	0.4	2
70:30	1.4	0.6	2
60:40	1.2	0.8	2
50:50	1.0	1.0	2
40:60	0.8	1.2	2
30:70	0.6	1.4	2
20:80	0.4	1.6	2
10:90	0.2	1.8	2
0:100	0	2.0	2

7.2.2.13 Batch kinetic study of AuNP, AgNP and AuAgNP formation

The experiments shown in Table 19 were performed by continuously monitoring a reaction mixture during nanoparticle formation, after injecting solutions of $AgNO_3$ (25 mM) and/or $HAuCl_4$ (25 mM) into a stirred solution of sodium citrate (2.4 mM) and tannic acid (0.05 mM) heated to 100 °C. Continuous monitoring was performed by recirculating the reaction mixture from the reactor through a 600 µL capacity UV-vis flow cell with a peristaltic pump (as described in Section 7.2.2.3), the reaction was monitored by integrating the absorption spectra between 400 and 450 mM.

Table 19. Table showing the volumes of precursor added to a tannic acid/sodium citrate solution.

Exp. No.	Au:Ag Ratio	Tannic acid (0.5 mM) & NaCit. (2.4 mM) mL	$AgNO_3$ (25 mM) mL	$HAuCl_4$ (25 mM) mL
1	0:100	148.8	0	1.2
2	15:85	148.8	0.18	1.02
3	50:50	148.8	0.6	0.6
4	85:15	148.8	1.02	0.18
5	100:0	148.8	1.2	0

7.3 Methods (chapter 4)

7.3.1 Experimental methods

7.3.1.1 Batch validation experiment

A batch validation reaction was performed as follows. AuNPs (24 mL, synthesised using the method described in Section 7.1.1.1) was added to a stirred solution of nitrophenol (50 mL of a 0.24 mM solution) and an additional portion of water (20 mL) was added. The reaction was initiated by adding freshly made sodium borohydride solution (6 mL of 50 mM) the final concentrations were: 0.12 mM nitrophenol, 0.04 mM AuNPs and 3 mM sodium borohydride. The reaction mixture was stirred and continuously monitored by recirculating through a quartz flow cell with a peristaltic pump.

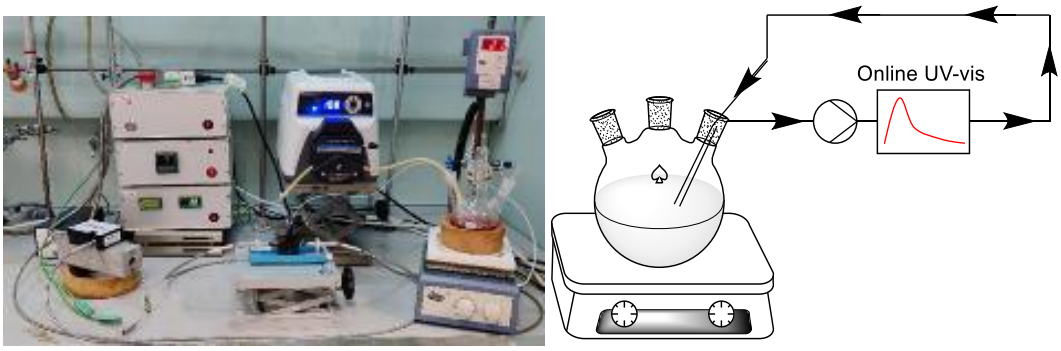

Figure 144. Left: a photograph showing a 250 mL round-bottomed flask containing a 100 mL stirred reaction solution was recirculated through a quartz flow cell for continuous monitoring. Right: a diagrammatic representation of this setup.

7.4 Methods (Chapter 5)

7.4.1 Reservoir solutions

7.4.1.1 Chloroauric acid (0.4 mM)

A premade solution of $HAuCl_4$ (25 mM, 16 mL) was made up to 1000 mL with water.

7.4.1.2 Silver nitrate (0.4 mM)

$AgNO_3$ (67.95 mg) was dissolved in water (1 L).

7.4.1.3 Sodium citrate (4.8 mM) and tannic acid (0.1 mM)

Sodium Citrate (1411.68 mg) and tannic acid (170.12 mg) were dissolved in 1000 mL of water.

7.4.1.4 K_2CO_3 (10 mM)

K_2CO_3 (1.38 g) was dissolved in water (1 L).

7.4.1.5 Nitrophenol (1.2 mM)

Nitrophenol (166.93 mg) was dissolved in water (1 L).

7.4.1.6 $NaBH_4$ (3 mM)

$NaBH_4$ (113.49 mg) was dissolved in ice-cold water (1 L) and maintained at 0 °C by placing in an insulated ice bath and adjusted to pH 10 by dropwise addition of sodium hydroxide solution (0.1 M). The cooled $NaBH_4$ solution was passed through a heat exchange coil (0.5 m, 1/32" ID PTFE tubing) and submerged in a water bath at room temperature.

7.4.2 Analytical methods

7.4.2.1 AuAgNP UV-vis analysis

Both the nanoparticle solutions and the reaction solutions were analysed with inline UV-vis spectroscopy by flowing the solutions through a CVF-Q-10 quarts flow cell (1 cm path length) in an OceanOptics CUV-UV cuvette holder. The UV-vis spectra were obtained using a FLAME-S-US-VIS OceanOptics spectrometer (200-850 nm) with a DH-2000 deuterium tungsten halogen light source (200-2000 nm) and QP400-2-SR-BX 400 um premium fibre optic cables.

The inline spectra were monitored using ChemiView[130] software, time-stamped full spectrum readings were taken approximately every second and averaged over 100 scans. Absorption spectrum data was recorded in a text (.txt) file for further deconvolution and interpretation with code written in MATLAB.

7.4.2.2 TEM analysis

Transmission electron microscopy (TEM) was used to characterise the AuAgNP solutions in this chapter. The samples for TEM were prepared by taking a solution of the AuAgNPs from the outlet stream of the reactor (5 drops dispersed in isopropanol (2 mL) using an ultrasonic bath) deposited on a holey carbon film-coated copper grid.

TEM analysis was carried out using the FEI Titan Themis Cubed operated at 300 kV. Bright-field TEM images were collected using a Gatan OneView 16 Megapixel CMOS digital camera. GMS3 and Velox software was used to collect and process the data. For

all samples, the NP size distribution histograms were obtained from at least 150 different NPs assuming a spherical shape and with random distribution.

7.4.3 Reactor setup

A detailed reactor diagram is shown in Figure 145, reservoirs containing solutions of $HAuCl_4$ (0.4 mM), $AgNO_3$ (0.4 mM), NaCit. (4.8 mM)/tannic acid (0.1 mM) and K_2CO_3 (10 mM) were all pumped through a three-part fReactor CSTR cascade with HPLC pumps except $HAuCl_4$ which was pumped through the reactor with a SyrDos pump. The CSTR cascade was heated to 100 °C within a custom-made stainless-steel heating mantel placed on top of a IKA hotplate, the nanoparticle solution was stored in a 5 mL (1/32" ID) storage coil, an Idex 2-position, 6-port switching valve was incorporated into the reactor design to save time/material. $NaBH_4$ (3 mM) and nitrophenol (1.2 mM) solutions were pumped through the reactor with SyrDos and HPLC pumps respectively. To prevent gas bubbles from entering the 3.5 mL (1/32" ID) reactor, a Waters inline gas/liquid membrane separator was placed in between the pump and the $NaBH_4$ reservoir, a peristaltic pump was used to ensure the inline gas-liquid separator was always wetted with $NaBH_4$ solution. Both stages of the reactor were monitored with the same UV-vis spectrometer, the spectrometer was maintained at a single temperature by placing on top of an aluminium heating block maintained at 35 °C with a Eurotherm PID temperature controller. In this final reactor design, 200 psi BPRs were placed after each pump to help identify the presence of gas bubbles in individual pump heads, this would be indicated by fluctuations in the pump internal pressure readings. The pressure of the reactor was regulated at 40 psi with a cartridge BPR and monitored with a pressure sensor.

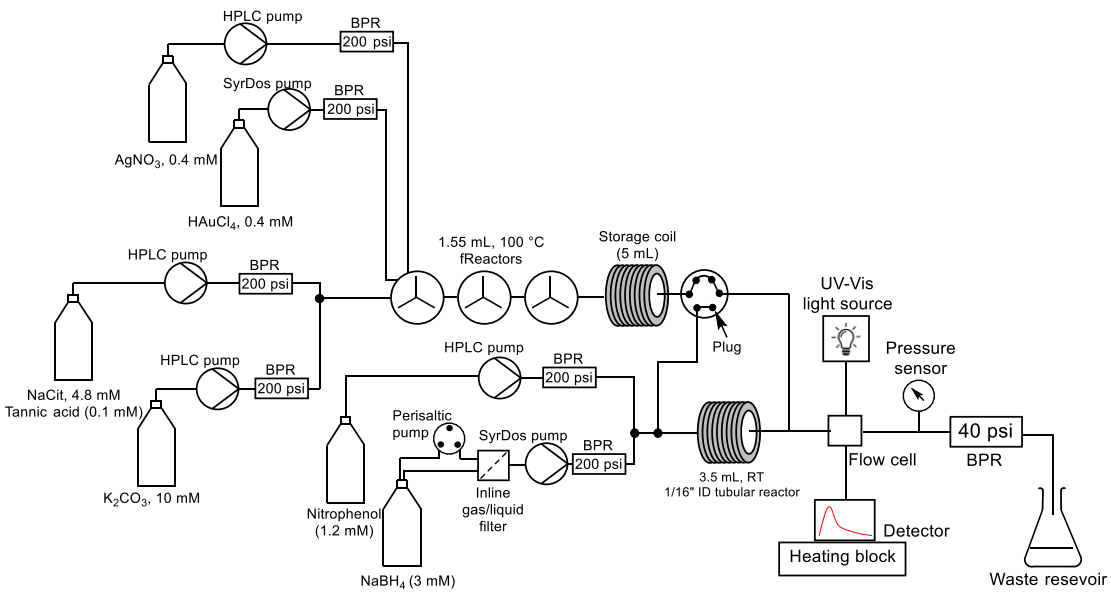

Figure 145. A reactor schematic describing in detail the reactor setup, the 6 pumps and the UV-vis detector in this schematic were connected to a computer to allow automated optimisation.

Figure 146 shows a photograph of the reactor setup, the components are numbered and described further in Table 20.

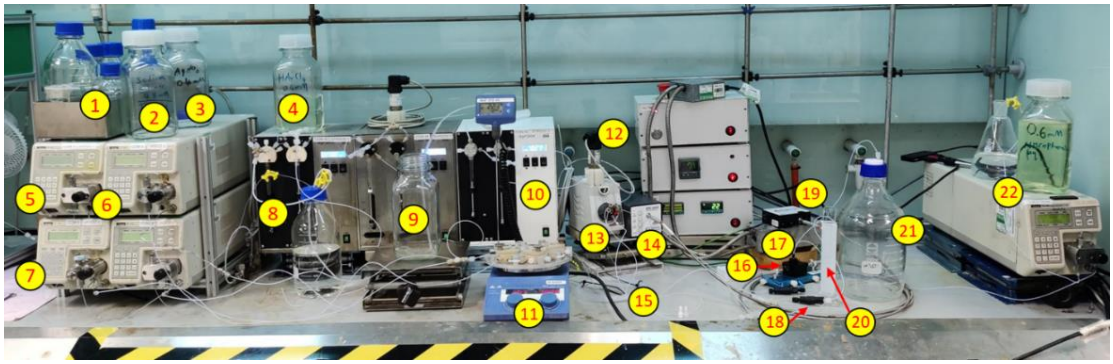

Figure 146. Photograph showing a configuration of the flow reactor platform for the optimisation of a AuNP, AgNP and AuAgNP catalysed nitrophenol reduction.

7.4.4 Table of components

Table 20. A table showing the name and purpose of the reactor components shown in Figure 144.

Number	Name	Purpose
1	Reagent reservoir	Potassium carbonate solution storage
2	Reagent reservoir	Sodium citrate & tannic acid solution storage
3	Reagent reservoir	Silver nitrate solution storage
4	HPLC pump	Potassium carbonate pump
5	HPLC pump	Sodium citrate & tannic acid pump

6	HPLC pump	Silver nitrate pump
7	Eurotherm temperature controller	To keep detector temp. constant
8	SyrDos pump	$HAuCl_4$ pump
9	Reagent reservoir	$NaBH_4$ solution storage
10	SyrDos pump	$NaBH_4$ pump
11	fReactor and hot plate	Synthesis of nanoparticles
12	Pressure sensor	Pressure monitoring/overpressure protection
13	6 port switching valve	Enable operation of 2 mode reactor
14	UV-vis light source	Inline analysis
15	5 mL 1/32” ID PTFE tubing	Nanoparticle solution storage
16	UV-vis flow cell	Inline analysis
17	Heating block	UV-vis temperature regulation
18	Back pressure regulator (BPR)	Reactor pressure regulation
19	UV-vis detector	Inline analysis
20	3.5 mL 1/32” ID PTFE tubing	Nitrophenol reduction reactor
21	Waste from reactor reservoir	Storage of reactor waste
22	HPLC pump and reservoir	Nitrophenol pump and solution storage

7.4.5 Reactor component details

Reactor (nitrophenol reduction): 7.07 m of 1/32” (ID) PTFE tubing (3.5 mL vol.).

Reactor (nanoparticle synthesis): A CSTR cascade comprised of 3 classic design fReactors joined with 1/16” ID tubing, the fReactors were heated within a purpose-built stainless-steel housing.

Hot plate: IKA 3810001 Digital Round-Top Stirring Hot Plate.

Nanoparticle storage coil: 10.1 m of 1/32” (ID) PFA tubing (5 mL vol.).

Switching valve: Idex MXP7900-000 Actuated Switching Valve, 2-Position, 6-Port, rated to 6000 psi.

Reagent pumps: $HAuCl_4$ (0.4 mM): SyrDos pump, $AgNO_3$ (0.4 mM): Jasco PU-980, NaCit. (4.8 mM)/tannic acid (0.1 mM): Jasco PU-980, K_2CO_3 (10 mM): Jasco PU-980, nitrophenol (0.6 mM): Jasco PU-980, $NaBH_4$ (10 mM): SyrDos pump.

Peristaltic pump: Masterflex UY-77916-20 Easy-Load II Pump.

Gas-liquid membrane separator: Whatman 6725-5002 In-Line Solvent Degasser.

Reactor Unions: IDEX ETFE T-piece assemblies (part no. P-632).

Fittings: IDEX ¼-28, Flat bottom, Flangeless Fitting, Standard Knurl ETFE fitting for 1/16” outer diameter tubing.

Back pressure regulator: Spring-based (40 psi) IDEX (part no. P-761).

UV-Vis spectrometer: FLAME-S-US-VIS OceanOptics (200-850 nm), DH2000 deuterium tungsten halogen light source (200-2000 nm), QP400-2-SR-BX 400 μm premium fibre optic cables and a CVF-Q-10 quarts flow cell (1 cm path length) in an OceanOptics CUV-UV cuvette holder.

Temperature controller: Eurotherm 3216 PID Temperature Controller.

Software: Automation code written in MATLAB 2018a was used to control the reactor pumps and determine the best reactor conditions using the optimisation algorithms SNOBFIT and BOAEI.

Appendix

8.1.1 TEM micrographs (before reaction)

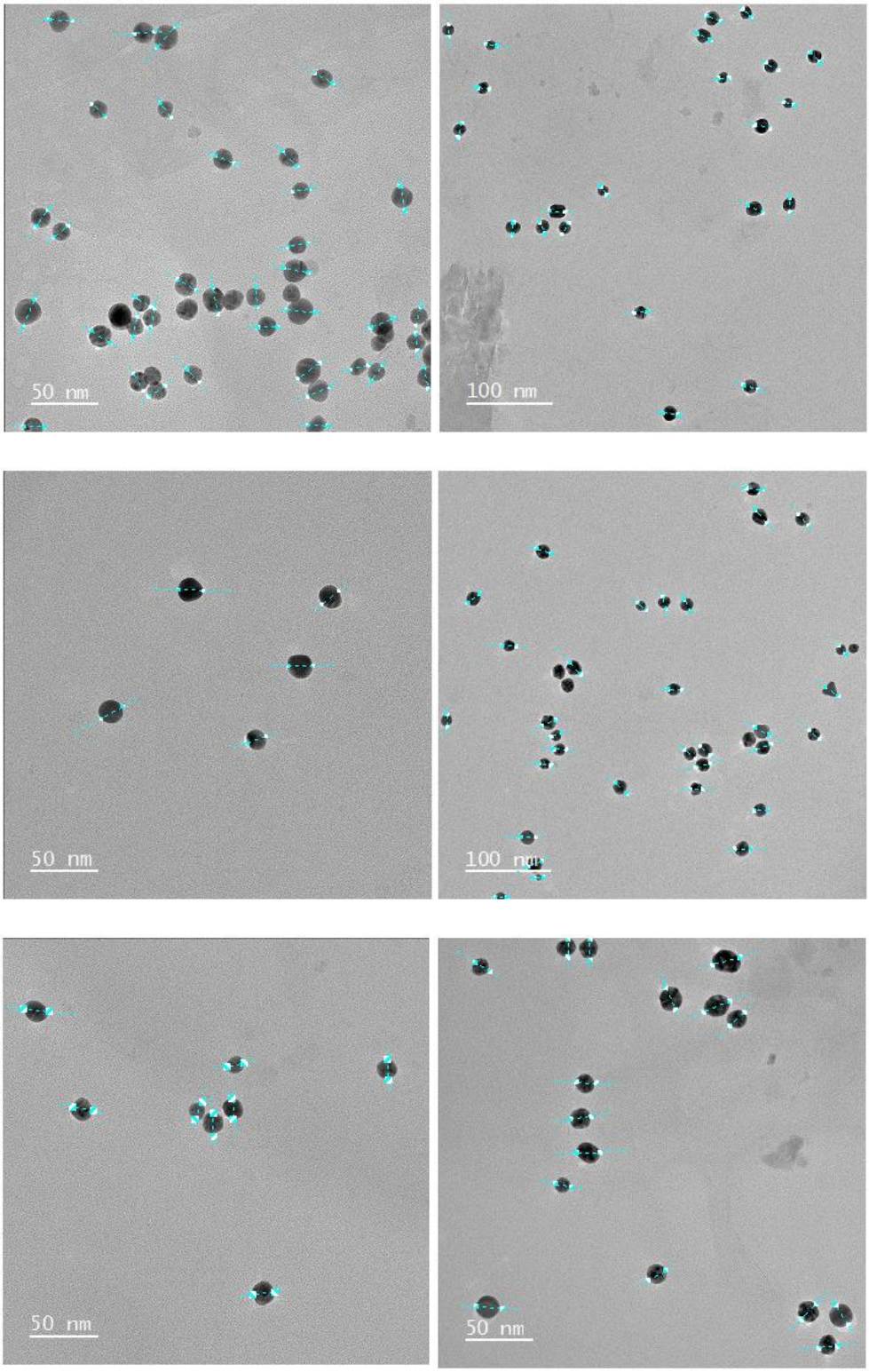

Figure 147. TEM images used to obtain the size distribution histogram shown in Figure 37 (before reaction).

8.1.2 TEM micrographs (after reaction)

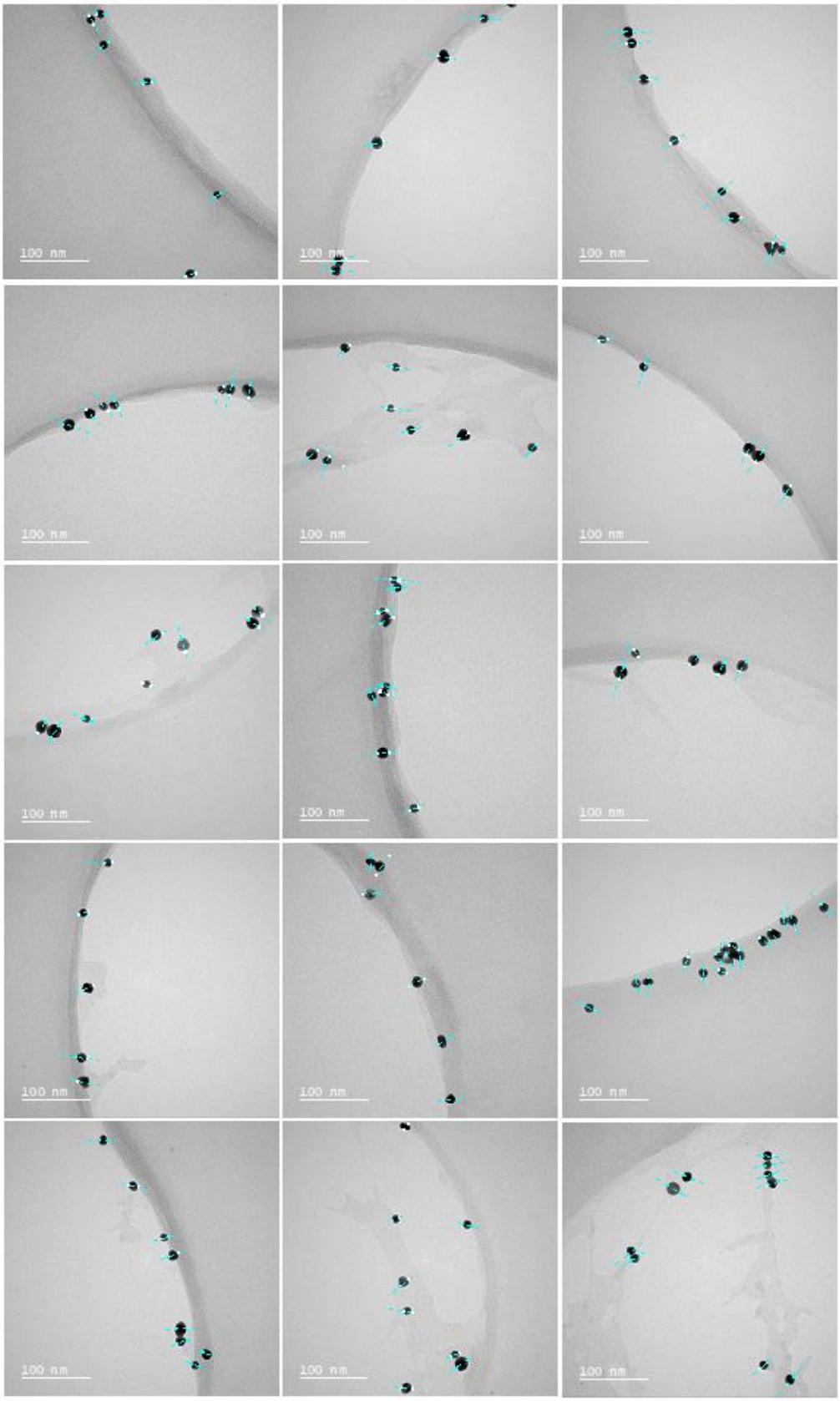

Figure 148. TEM images used to obtain the size distribution histogram shown in Figure 38 (after reaction).

8.1.3 Data from self-optimisation experiments

8.1.3.1 Initial optimisation experiment

Table 21. Table showing raw data for optimisation performed without conditions generation function.

Experiment	Water FR (mL/min)	$NaBH_4$ FR (mL/min)	Gold NP FR (mL/min)	Conversion (%)
1	0.125	1.375	0.275	61.728
2	1.7	1.9	0.325	21.491
3	0.5	0.3	0.1	61.199
4	1	1.2	0.1	23.503
5	0.85	1.95	0.2	31.965
6	2	1.2	0.1	13.828
7	1.025	0.625	0.35	52.406
8	1.475	1.275	0.5	34.533
9	0.1	0.3	0.5	103.63
10	1.3	1.55	0.2	24.053
11	0.1	0.25	0.5	98.295
12	0.3	1.7	0.175	56.035
13	0.675	1.4	0.35	45.99
14	1.65	0.25	0.1	23.618
15	0.1	0.975	0.5	85.798
16	1.65	1.775	0.125	19.286
17	0.1	0.925	0.2	76.646
18	0.5	0.575	0.4	80.861

8.1.3.2 Final optimisation experiment

Table 22. Table showing experiments performed during the optimisation.

ExperimentNumber.	$NaBH_4$ conc.	Gold NP SA. (m^2L^{-1})	Residence time	Conversion (%)
1	2.1294	0.06	2.2886	45.76
2	0.65	0.05	1.2	20.696
3	0.85	0.05	2.8	25.102
4	2	0.08	1.1	28.227
5	1.2	0.15	1.9	73.601
6	1.8	0.11	3	83.502
7	1.3	0.14	1.1	47.172
8	0.55	0.11	2.2	50.738
9	1.85	0.10	1.7	48.704
10	0.95	0.14	2.6	62.12
11	1.75	0.16	3	94.777
12	0.55	0.16	1.1	64.729
13	0.95	0.10	2.6	39.136
14	1.75	0.07	2.65	47.423
15	2.5	0.16	3	93.226
16	1.7	0.12	1.4	45.078
17	2.1	0.16	3	95.04
18	1	0.08	1.6	22.034
19	2.5	0.12	3	80.44
20	1.6	0.10	2.65	60.148
21	2	0.16	3	92.12
22	0.85	0.13	1.7	47.926
23	2.15	0.08	2.4	48.769
24	0.75	0.15	2.3	58.761
25	2.35	0.09	2.75	58.067
26	1.9	0.12	2.5	68.625
27	2.4	0.09	2.45	57.014
28	2.15	0.13	2.05	67.3722
29	2.5	0.16	2.5	87.2598

8.1.4 TEM micrographs and histograms for AuAgNPs

1.1.1.1 AgNPs

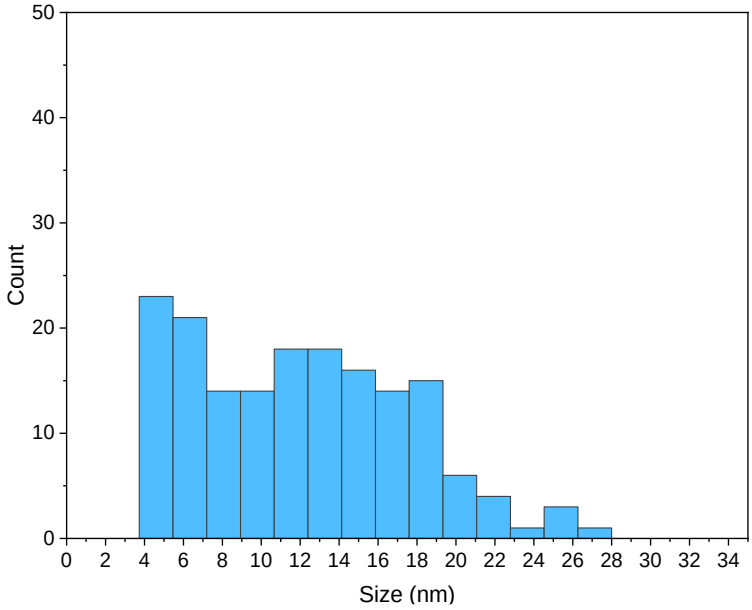

Figure 149. A histogram describing the distribution of particle sizes for AgNPs.

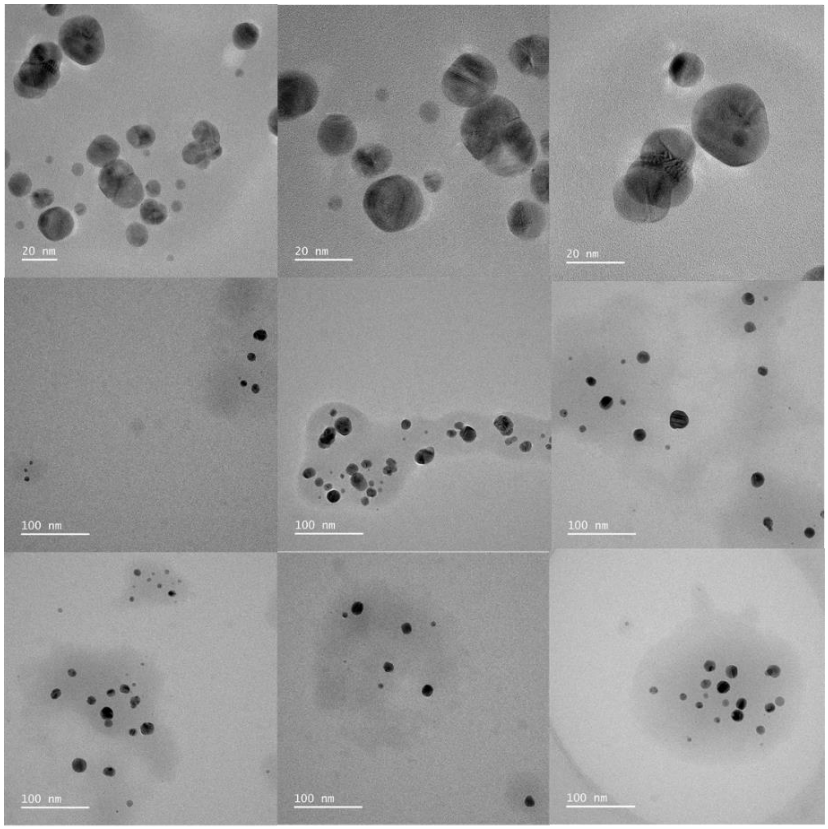

Figure 150. TEM micrographs showing AgNPs.

1.1.1.2 0.2:0.8 – Au:Ag

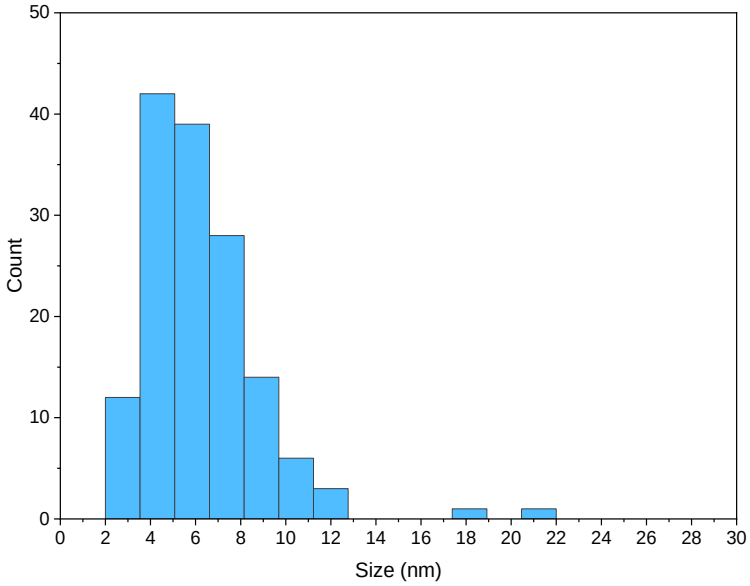

Figure 151. A histogram describing the distribution of particle sizes for AuAgNPs with the ratio 0.2:0.8 – Au:Ag.

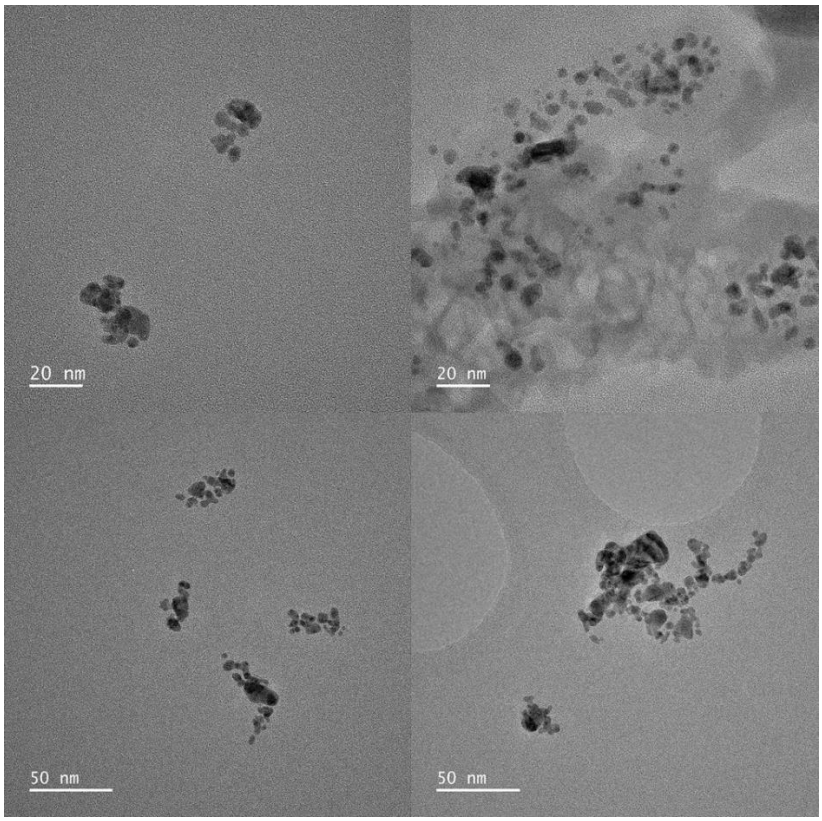

Figure 152. TEM micrographs showing AuAgNPs with the ratio with the ratio 0.2:0.8 – Au:Ag.

1.1.1.3 0.4:0.6 – Au:Ag

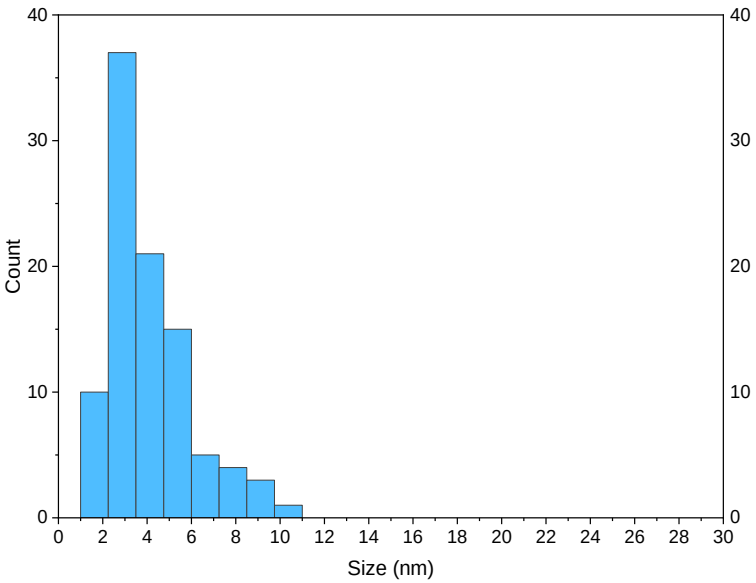

Figure 153. A histogram describing the distribution of particle sizes for AuAgNPs with the ratio 0.4:0.6 – Au:Ag.

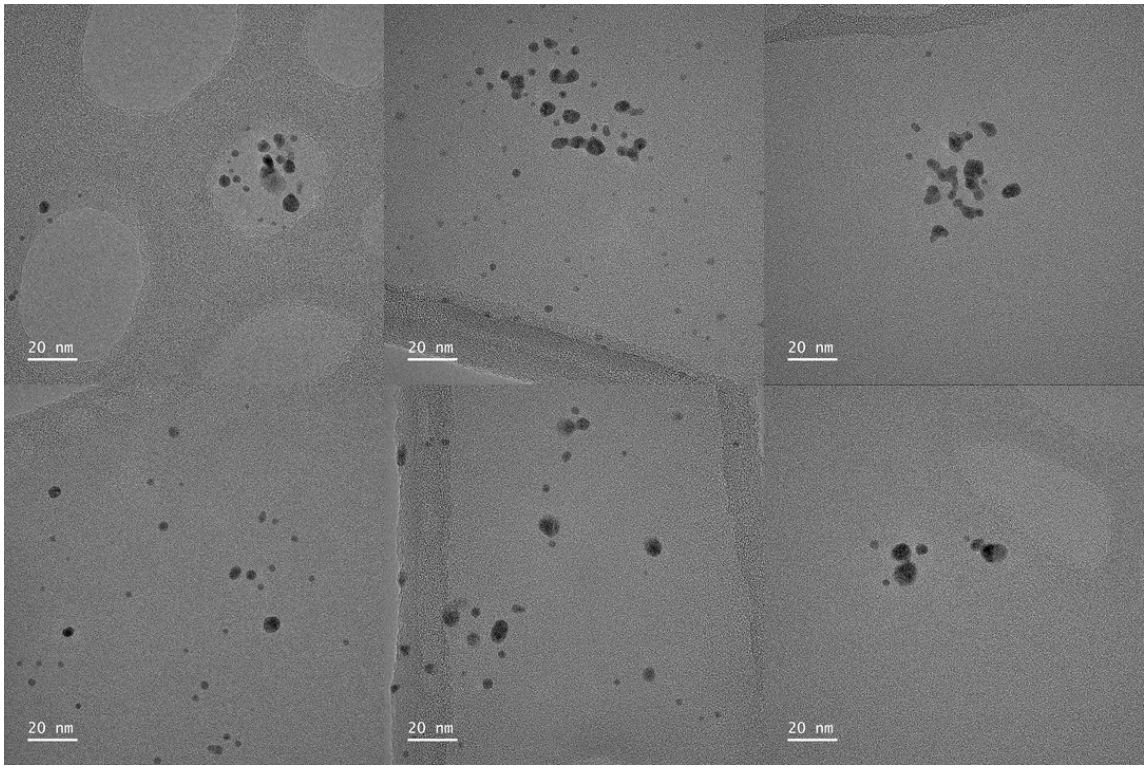

Figure 154. TEM micrographs showing AuAgNPs with the ratio with the ratio 0.4:0.6 – Au:Ag.

1.1.1.4 0.6:0.4 – Au:Ag

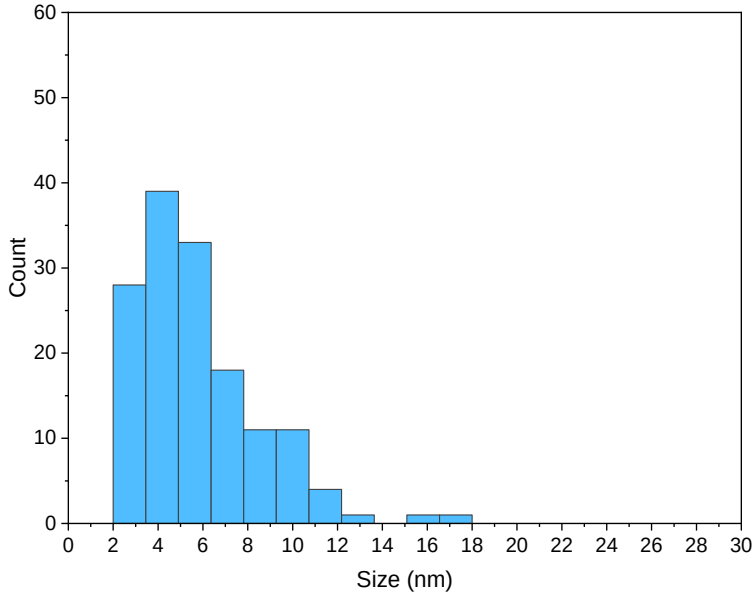

Figure 155. A histogram describing the distribution of particle sizes for AuAgNPs with the ratio 0.6:0.4 – Au:Ag.

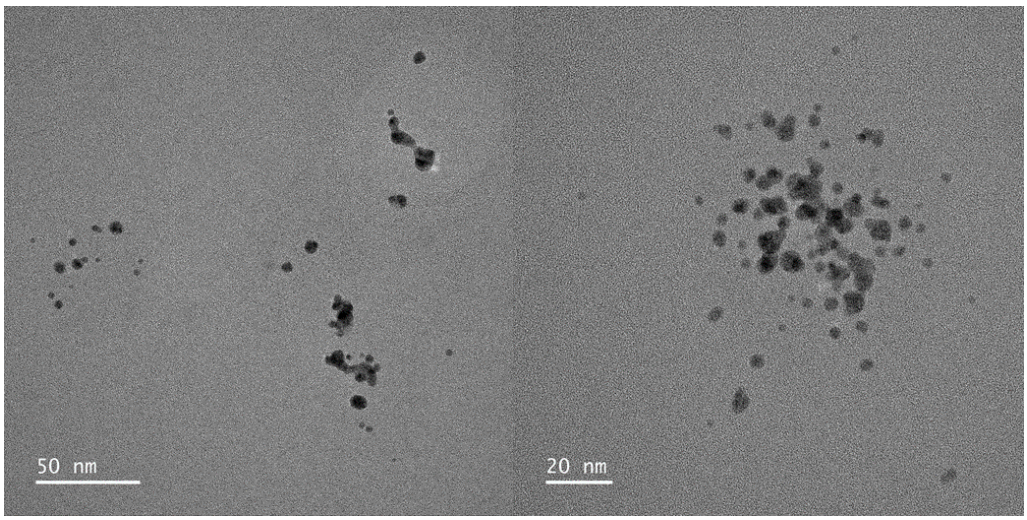

Figure 156. TEM micrographs showing AuAgNPs with the ratio with the ratio 0.6:0.4 – Au:Ag.

1.1.1.5 0.8:0.2 – Au:Ag

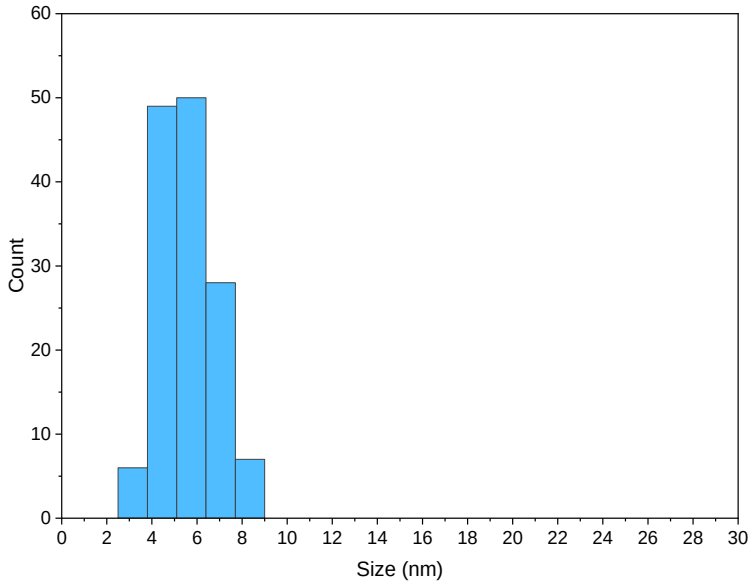

Figure 157. A histogram describing the distribution of particle sizes for AuAgNPs with the ratio 0.8:0.2 – Au:Ag.

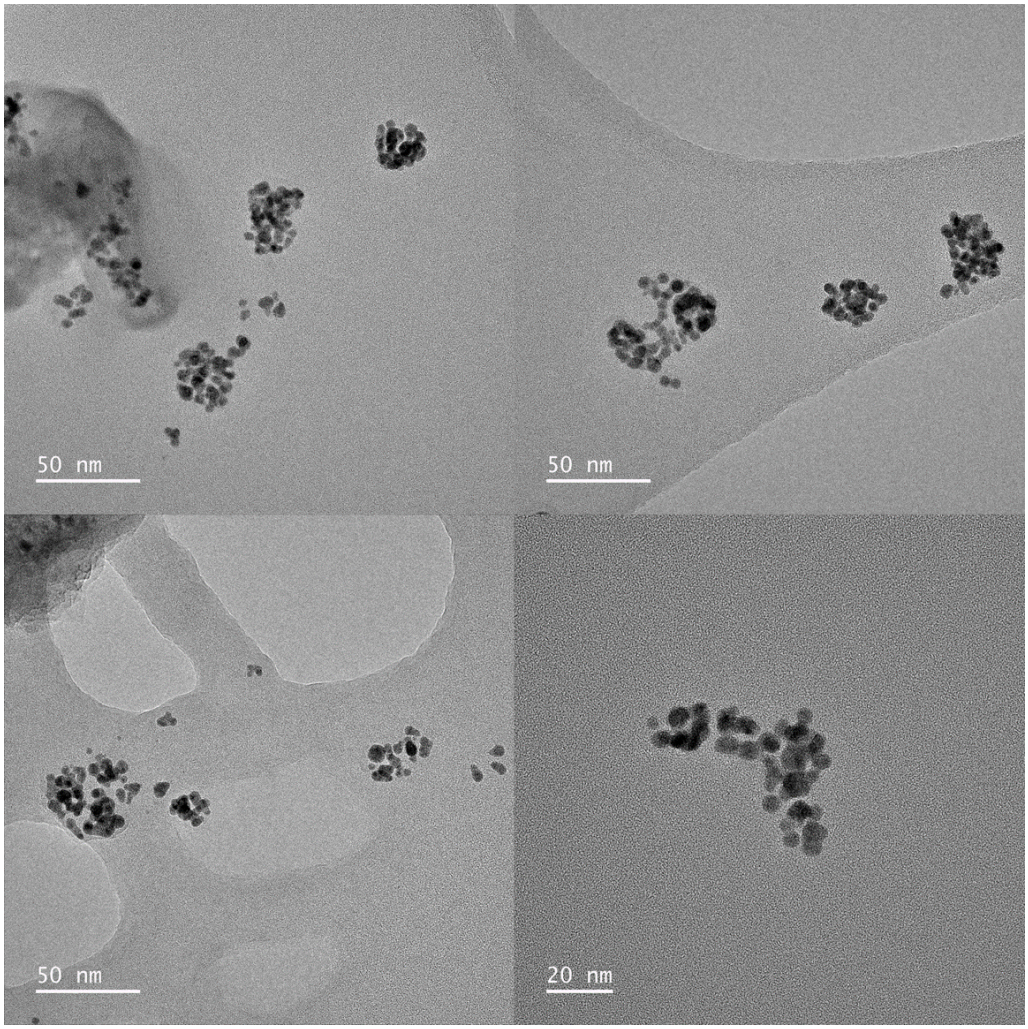

Figure 158. TEM micrographs showing AuAgNPs with the ratio with the ratio 0.8:0.2 – Au:Ag.

1.1.1.6 AuNPs

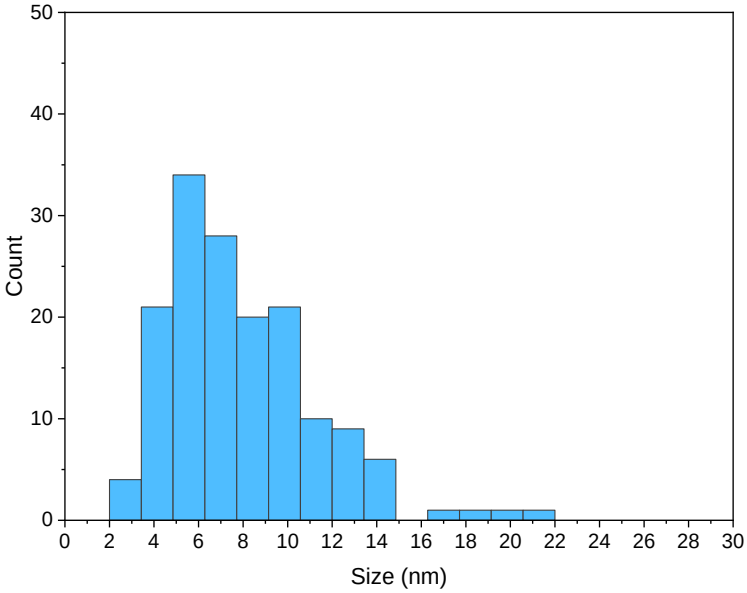

Figure 159. A histogram describing the distribution of particle sizes for AuNPs.

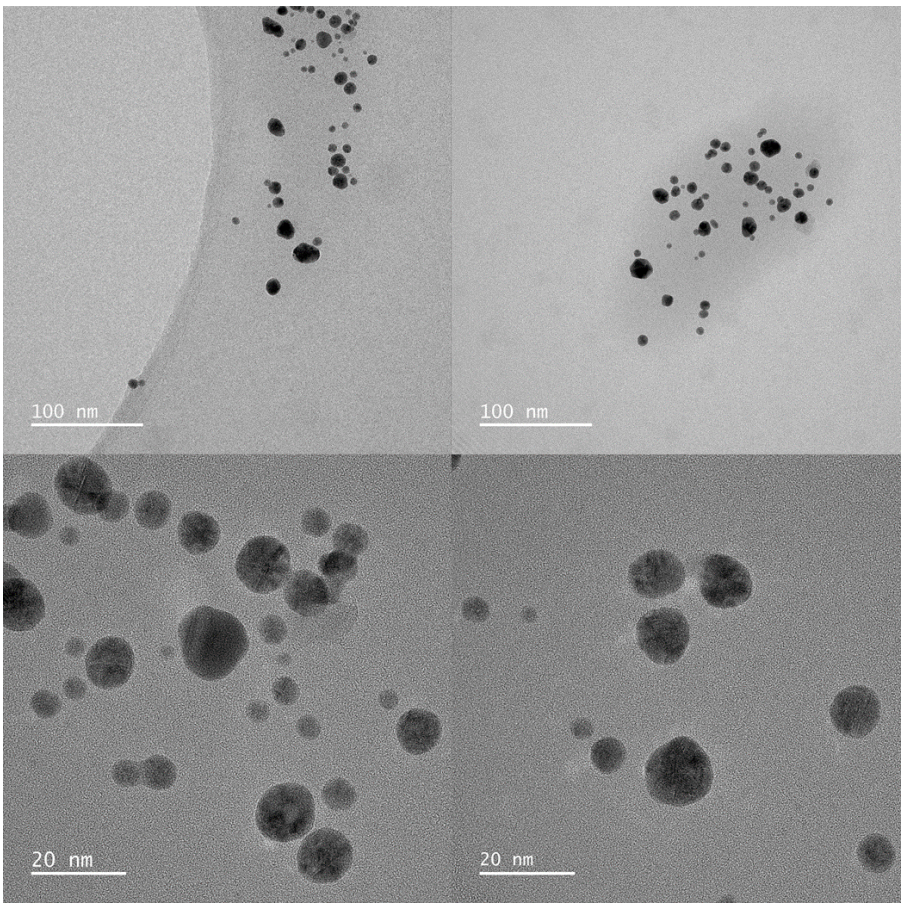

Figure 160. TEM micrographs showing AuNPs.

8.1.5 TEM-EDS analysis

1.1.1.7 0:1 – Au:Ag

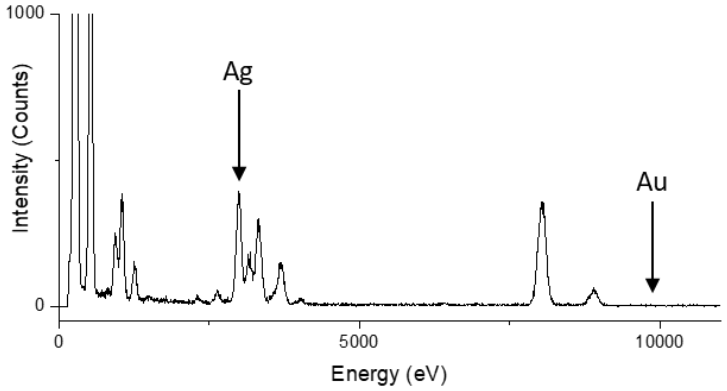

Figure 161. An EDS spectrum obtained from a AgNP sample.

1.1.1.8 0.2:0.8 – Au:Ag

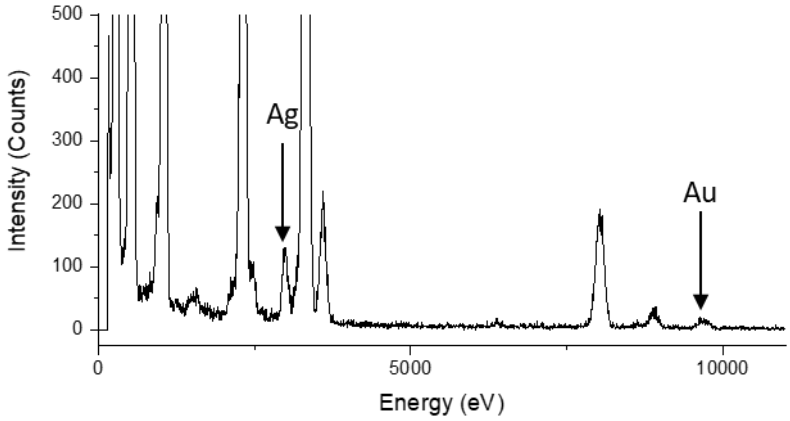

Figure 162. An EDS spectrum obtained from a 20:80 AuAgNP sample.

1.1.1.9 0.4:0.6 – Au:Ag

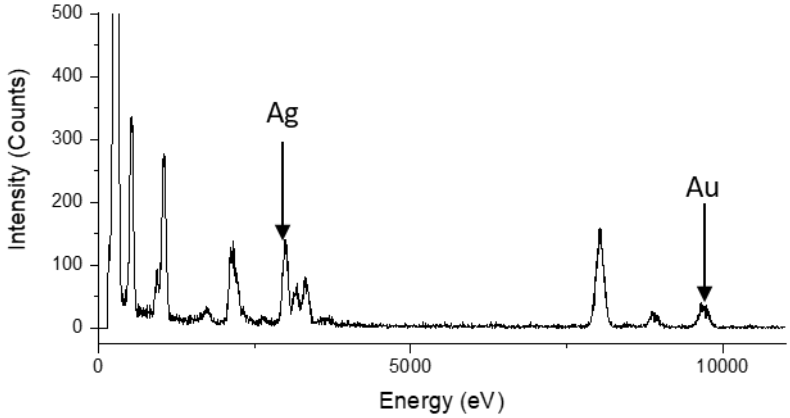

Figure 163. An EDS spectrum obtained from a 40:60 AuAgNP sample.

1.1.1.10 0.6:0.4 – Au:Ag

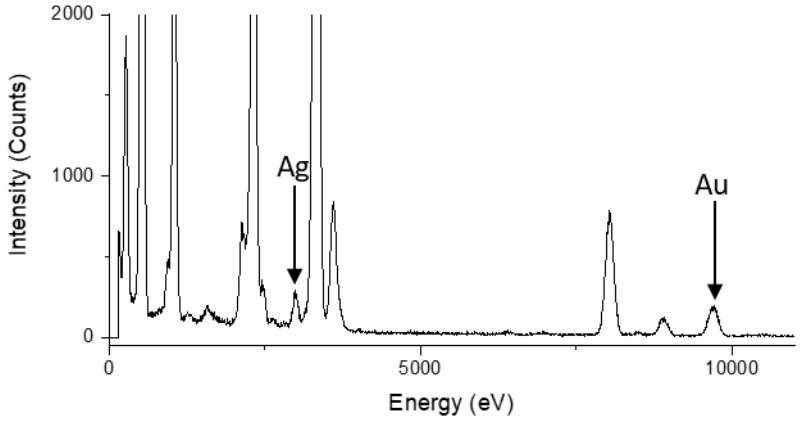

Figure 164. An EDS spectrum obtained from a 60:40 AuAgNP sample.

1.1.1.11 0.8:0.2 – Au:Ag

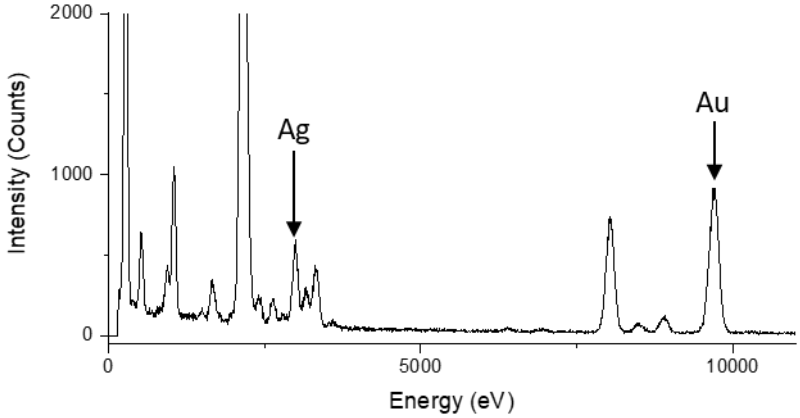

Figure 165. An EDS spectrum obtained from an 80:20 AuAgNP sample.

1.1.1.12 1:0 – Au:Ag

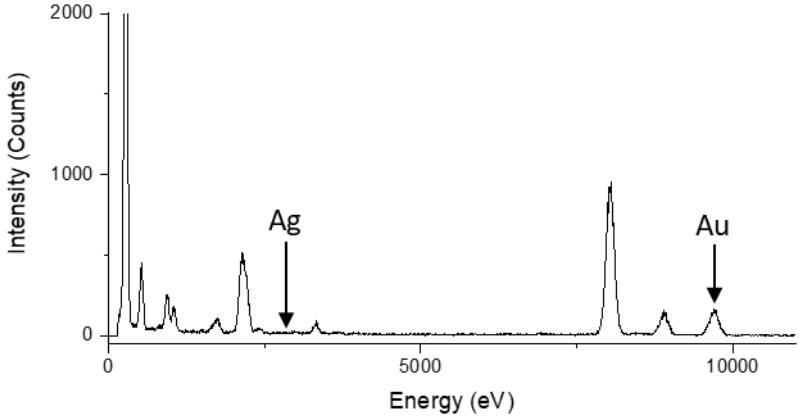

Figure 166. An EDS spectrum obtained from a AuNP sample.

8.1.6 Simulated test problem single objective optimisation comparison

Table 23. A list of simulated experiments based on a LH kinetic model. Showing mean average changes in reaction efficiency (20 runs) for the BOAEI and genetic algorithms and a single run for the SNOBFIT algorithm.

	Average Reaction efficiency (%)		
Experiment	**Genetic**	**SNOBFIT**	**BOAEI**
1	76.83	59.46	61.8
2	73.34	28.84	77.42
3	76.14	68.90	64.97
4	71.46	35.78	91.59
5	66.24	73.86	54.22
6	74.39	89.64	99.9
7	63.81	65.65	99.91
8	74.47	90.14	99.9
9	56.13	91.43	99.91
10	83.65	75.98	99.91
11	58.74	94.38	99.9
12	74.29	47.64	99.91
13	76.41	94.94	99.91
14	75.86	0.63	99.91
15	75.58	81.26	99.91
16	77.51	98.73	99.91
17	76.77	99.79	99.91
18	77.01	95.74	99.91
19	71.84	90.45	99.91
20	-26.32	0.24	99.91
21	79.54	80.17	64.55
22	77.89	95.90	99.9
23	76.10	92.73	99.87
24	80.20	97.87	99.9
25	62.39	76.09	99.89
26	77.82	92.69	99.9
27	76.95	90.75	80.75
28	77.58	96.49	91.07
29	79.25	12.89	99.9
30	72.02	98.93	99.8
31	74.55	96.54	99.88

32	74.54	99.18	99.9
33	76.03	87.13	99.89
34	70.26	97.11	98.06
35	75.60	99.60	99.9
36	78.50	2.21	99.9
37	78.94	77.50	99.89
38	78.01	98.42	97.18
39	80.95	0.63	99.9
40	97.74	99.80	99.9
41	78.32	69.36	95.88
42	83.92	99.87	96.23
43	72.41	90.94	69.01
44	80.96	77.82	99.9
45	86.37	67.33	99.87
46	86.76	84.93	99.89
47	90.96	98.44	99.91
48	89.74	96.36	99.89
49	76.57	99.09	99.89
50	82.71	91.12	99.91
51	91.36	99.49	99.91
52	81.13	91.19	99.9
53	76.96	81.69	99.85
54	80.97	80.62	99.9
55	78.96	98.49	90.08
56	79.11	99.72	99.9
57	80.63	99.08	99.89
58	87.53	94.36	99.61
59	91.83	67.93	54.61
60	98.22	97.77	98.33
61	81.19	99.37	83.15
62	87.85	91.13	98.71
63	89.97	98.95	98.13
64	84.99	38.89	82.8
65	84.45	98.14	0.43
66	85.55	80.51	93.74
67	90.66	99.01	72.59
68	92.23	99.65	88.48

69	89.91	66.15	90.95
70	80.99	95.12	80.66
71	91.10	98.94	-34.87
72	90.67	0.42	99.86
73	87.85	55.29	99.9
74	94.01	99.90	99.9
75	89.20	93.37	99.75
76	75.26	96.76	99.9
77	90.64	26.40	99.9
78	92.13	98.98	97.37
79	91.58	95.23	99.41
80	98.93	96.10	99.9
81	81.19	20.48	-0.9
82	87.85	99.56	99.8
83	89.97	97.23	53.14
84	84.99	94.95	85.55
85	84.45	62.67	99.19
86	85.55	99.82	97.78
87	90.66	98.58	98.82
88	92.23	97.21	99.39
89	89.91	96.19	78.41
90	80.99	95.67	99.63
91	91.10	99.79	95.1
92	90.67	62.90	88.52
93	87.85	81.21	94.5
94	94.01	87.79	69.19
95	89.20	99.71	-51.03
96	75.26	96.74	91.6
97	90.64	99.03	-2.38
98	92.13	88.85	94.49
99	91.58	92.73	61.86
100	98.93	93.15	93.82

8.1.7 Design of experiments

Table 24. A table showing the initial conditions and reaction efficiencies for a FFD exploring the upper and lower limits of residence time, AuNP SA on reaction efficiency.

Exp. no.	AuNP SA (m^2L^{-1})	Res. time (min)	Reaction efficiency (%)
1	0	0	0.0
2	0	10.00	0.0
3	0.6000	0	0.0
4	0.6000	10.00	41.96
5	0.3000	5.00	94.32

Table 25. A table showing the initial condition and reaction efficiencies for a FFD with additional experiments along the axis of the design exploring the upper and lower limits of residence time, AuNP SA on reaction efficiency.

Exp. no.	AuNP SA (m^2L^{-1})	Res. time (min)	Reaction efficiency (%)
1	0	0	0
2	0	10.00	0
3	0.6000	0	0
4	0.6000	10.00	41.96
5	0.3000	5.00	94.32
6	0.3000	10.00	68.84
7	0	5.00	0
8	0.6000	5.00	68.83
9	0.3000	0	0

8.1.8 Single objective optimisation comparison with added noise

Table 26. A list of simulated experiments based on a LH kinetic model. Showing mean average changes in reaction efficiency (20 runs) for the BOAEI and genetic algorithms and a single run for the SNOBFIT algorithm with added white Gaussian noise.

	Average reaction efficiency (%)		
Exp. No.	**SNOBFIT**	**GA**	**BOAEI**
1	58.3938	60.42423	76.52517
2	65.18606	68.55858	59.17977

3	77.71974	77.749	60.83220
4	59.19558	81.19783	28.24913
5	64.82476	87.62103	28.91953
6	89.64616	80.31418	0.26550
7	73.4546	55.7877	91.13700
8	72.3845	91.14708	82.98750
9	79.70052	76.1234	88.56270
10	80.82802	-22.0409	89.02850
11	60.83266	47.05743	73.79790
12	69.61632	85.93925	88.25327
13	73.8411	82.23888	44.16330
14	85.75972	78.0818	58.20273
15	90.8557	80.18	75.10147
16	89.30842	56.60283	32.79080
17	87.41068	83.89985	78.41197
18	90.79514	91.18223	95.47403
19	80.06014	82.02085	98.16200
20	95.41008	95.45213	96.74043
21	94.40322	95.2476	94.94210
22	84.3245	92.63608	95.30363
23	80.94906	73.54953	94.25970
24	94.39626	94.3223	97.24733
25	72.75934	93.43383	96.10363
26	85.33212	67.14148	97.64360
27	77.6349	95.00908	96.73310
28	95.54454	90.93265	96.72790
29	90.63478	81.0462	96.78510
30	94.79524	95.43308	92.83250
31	87.91092	91.73633	96.34317
32	97.0217	96.39755	97.10617
33	90.64228	94.7829	96.73537
34	90.35928	88.12123	-0.63037
35	82.52586	66.9986	98.90040
36	92.31274	95.37148	95.31313
37	90.48778	91.9265	96.46603
38	94.64838	94.77068	96.27027
39	88.08332	74.54173	95.71690

40	68.21462	95.46023	96.65760
41	76.51096	91.73633	86.31210
42	94.71974	96.39755	97.74340
43	87.30416	94.7829	97.67510
44	87.37576	88.12123	97.68260
45	94.39288	66.9986	97.48110
46	88.81212	95.37148	97.69380
47	86.26742	91.9265	97.55310
48	91.31538	94.77068	97.46393
49	82.2889	74.54173	97.44993
50	90.79514	95.46023	97.60627

8.1.9 TS-EMO multi-objective optimisation

Table 27. A table showing the reaction conditions, STY and E-factors for experiments performed during the multi-objective TS-EMO optimisation.

Exp. no.	AuNP SA (m^2L^{-1})	Res. time (min)	STY (mmol mL^{-1} min^{-1})	E-Factor
1	0.4803	2.194187	0.264	0.2137
2	0.5166	8.081008	0.0743	0.2218
3	0.0791	3.853363	0.105	0.0504
4	0.5215	6.093033	0.0985	0.224
5	0.3486	2.246638	0.247	0.1619
6	0.0668	6.675568	0.0712	0.0362
7	0.1831	3.38773	0.1556	0.0895
8	0.301	7.092788	0.0845	0.1295
9	0.5674	7.297062	0.0823	0.2436
10	0.5908	7.645388	0.0785	0.2537
11	0.1116	5.255688	0.0988	0.0554
12	0.5983	1.076937	0.494	0.2898
13	0.5625	2.787635	0.2135	0.2436
14	0.2739	9.351723	0.0641	0.1177
15	0.4675	2.024468	0.2825	0.2107
16	0.1001	8.688255	0.065	0.0457
17	0.2449	6.155342	0.0966	0.1062
18	0.5294	9.919532	0.0605	0.2273
19	0.4595	0.924362	0.5056	0.2534
20	0.5801	5.112015	0.1174	0.2492

21	0.372	1.403095	0.3578	0.191
22	0.0378	9.864383	0.045	0.022
23	0.5047	0.26644	0.926	0.5272
24	0.5467	7.679172	0.0782	0.2347
25	0.3744	8.434103	0.0712	0.1608
26	0.4377	8.888572	0.0675	0.1879
27	0.4119	1.17363	0.4171	0.2168
28	0.2398	4.499362	0.1291	0.1064
29	0.3665	3.305957	0.1775	0.161
30	0.122	8.281273	0.0696	0.0545
31	0.3993	4.901532	0.1221	0.172
32	0.0301	9.275413	0.0418	0.02
33	0.1789	2.49099	0.191	0.0969
34	0.0449	3.469053	0.0788	0.0423
35	0.0651	1.988702	0.1206	0.07
36	0.4891	1.799643	0.3145	0.2228
37	0.3895	8.98869	0.0668	0.1672
38	0.198	6.568183	0.0898	0.0865
39	0.5569	6.344755	0.0946	0.2391
40	0.0345	1.8744	0.0744	0.0637
41	0.2515	8.737217	0.0686	0.1082
42	0.2331	6.692768	0.0889	0.1009
43	0.4446	4.047363	0.1476	0.1917
44	0.4664	5.930558	0.1012	0.2004
45	0.1248	4.611262	0.112	0.0623
46	0.2768	0.793773	0.428	0.21
47	0.255	3.024083	0.183	0.1187
48	0.353	1.523083	0.3326	0.1796
49	0.4072	2.64677	0.2194	0.1807
50	0.4291	3.079152	0.1917	0.1874
51	0.171	4.803108	0.1165	0.0788
52	0.3822	0.571643	0.5921	0.291
53	0.3592	9.155032	0.0656	0.1542
54	0.1173	9.654935	0.0604	0.0518
55	0.0752	5.641935	0.0828	0.0415
56	0.2832	5.547513	0.1073	0.1226
57	0.5845	3.937632	0.1522	0.2513
58	0.2091	9.110018	0.0657	0.0901

59	0.3369	4.24759	0.1396	0.1464
60	0.1361	1.500815	0.2168	0.1078
61	0.42	8.046822	0.0746	0.1803
62	0.1599	4.387783	0.1237	0.0759
63	0.2873	3.186518	0.1787	0.1301
64	0.3924	4.669755	0.128	0.1692
65	0.5124	1.303933	0.4115	0.2461
66	0.5753	1.67653	0.3419	0.2586
67	0.3081	9.56508	0.0627	0.1323
68	0.0915	9.70929	0.0584	0.0416
69	0.1062	6.47475	0.0834	0.0507
70	0.1666	0.654087	0.3242	0.2025
71	0.5008	2.917135	0.2034	0.2175
72	0.1554	4.113313	0.1291	0.0754
73	0.4753	8.616385	0.0697	0.2041
74	0.1431	0.403245	0.3148	0.2905
75	0.5379	0.495503	0.7627	0.3668
76	0.212	2.38324	0.2085	0.1099
77	0.1308	7.017523	0.0812	0.0592
78	0.1515	7.442947	0.0784	0.0669
79	0.3407	6.94	0.0864	0.1465
80	0.2683	5.360658	0.1106	0.1166
81	0.2228	6.270448	0.0944	0.097
82	0.4913	3.634182	0.1644	0.2119
83	0.3303	7.502333	0.0799	0.142
84	0.313	2.759135	0.2045	0.143
85	0.531	7.189623	0.0835	0.228
86	0.1905	2.49419	0.1952	0.1008
87	0.434	4.1763	0.1431	0.1872
88	0.421	6.846472	0.0876	0.1809
89	0.2241	7.895553	0.0757	0.0967
90	0.3183	1.019493	0.4091	0.1966
91	0.0595	9.424135	0.0544	0.0299
92	0.0534	7.769233	0.0596	0.0297
93	0.2933	5.435268	0.1096	0.1269
94	0.4548	5.002078	0.1198	0.1956
95	0.5508	5.16455	0.1162	0.2366
96	0.0886	3.757805	0.1123	0.0541

97	0.3217	5.766037	0.1037	0.1387
98	0.2595	5.87451	0.1012	0.1125
99	0.0229	8.521755	0.0371	0.0186
100	0.2029	8.22757	0.0725	0.0877
101	0.5858	0.391108	0.8888	0.4343
102	0.6	0.32351	0.9733	0.4911
103	0.6	0.699295	0.6649	0.3326
104	0.2633	1.307762	0.3278	0.1583
105	0.1762	1.21616	0.2753	0.1356
106	0.6	0.476732	0.8221	0.3946
107	0.3835	0.760437	0.5208	0.2496
108	0.6	0.371332	0.921	0.4522
109	0.3694	0.867283	0.478	0.2296
110	0.6	0.276557	1.0297	0.543
111	0.5788	0.602913	0.7146	0.3462
112	0.4952	0.646187	0.641	0.3081
113	0.6	0.285635	1.0181	0.5317
114	0.4483	0.721837	0.577	0.2774
115	0.1333	2.651072	0.1635	0.0793
116	0.1972	1.602843	0.2571	0.1233
117	0.252	0.922683	0.3805	0.185
118	0.02	4.206657	0.0412	0.0297
119	0.6	0.440433	0.854	0.4112
120	0.5041	0.581548	0.6826	0.3273
121	0.412	0.745912	0.5448	0.2613
122	0.2479	1.013573	0.3616	0.1743
123	0.1044	3.221265	0.1316	0.0635
124	0.6	0.296922	1.0044	0.5185
125	0.6	0.505837	0.7981	0.3831
126	0.02	6.585327	0.037	0.0212
127	0.2305	1.438337	0.293	0.141
128	0.6	0.576422	0.7445	0.3604
129	0.6	0.345783	0.9482	0.4716
130	0.3257	0.87298	0.448	0.2146

8.1.10 TEM micrographs and histograms for AuAgNPs

8.1.10.1 0.96:0.04 – Au:Ag

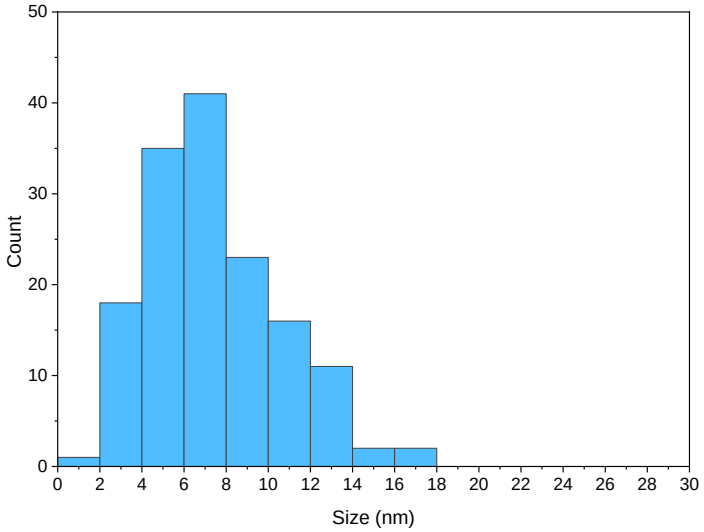

Figure 167. A histogram describing the distribution of particle sizes for AuAgNPs with the ratio 0.96:0.04 – Au:Ag.

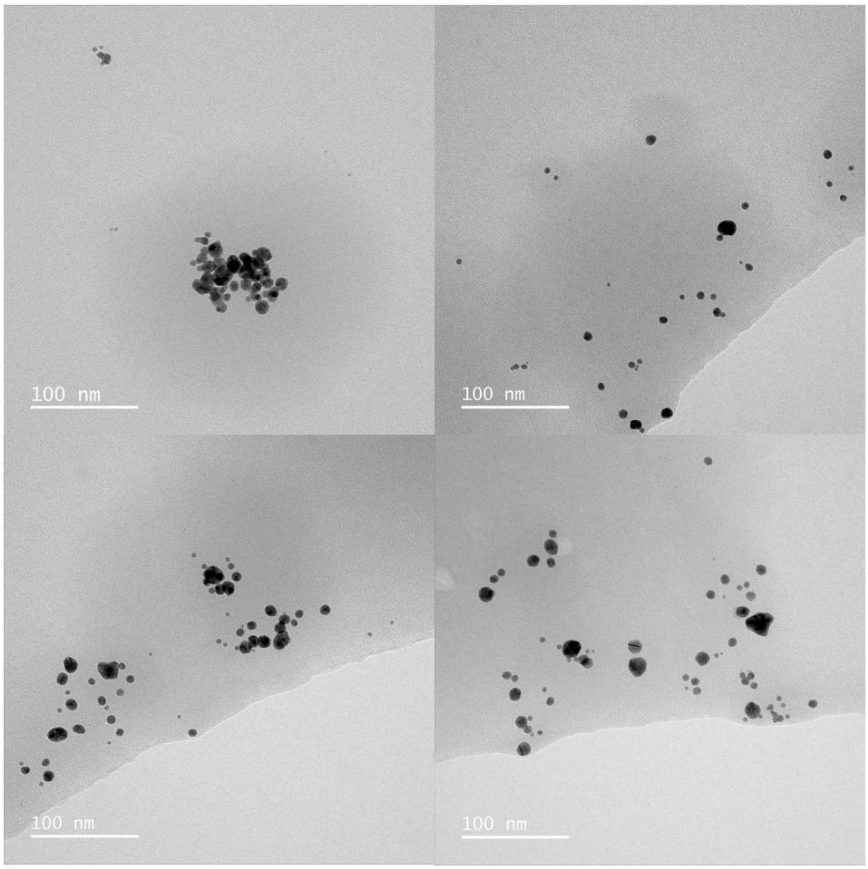

Figure 168. TEM micrographs showing AuAgNPs with the ratio 0.96:0.04 – Au:Ag.

8.1.10.2 0.97:0.03 – Au:Ag

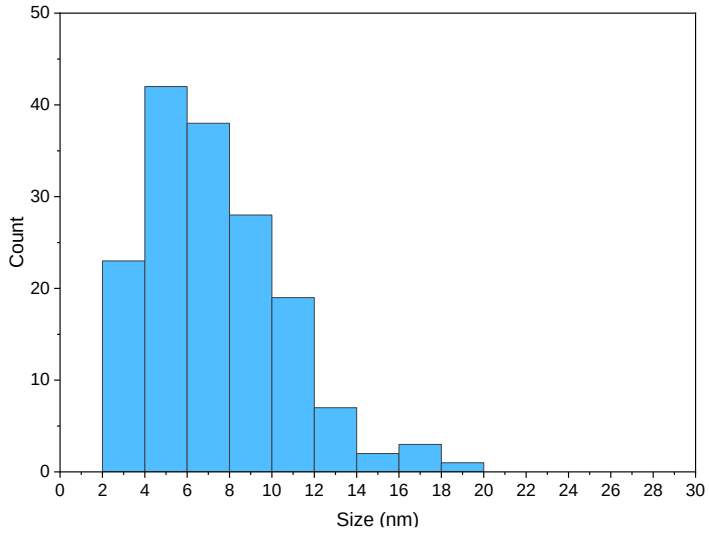

Figure 169. A histogram describing the distribution of particle sizes for AuAgNPs with the ratio 0.97:0.03 – Au:Ag.

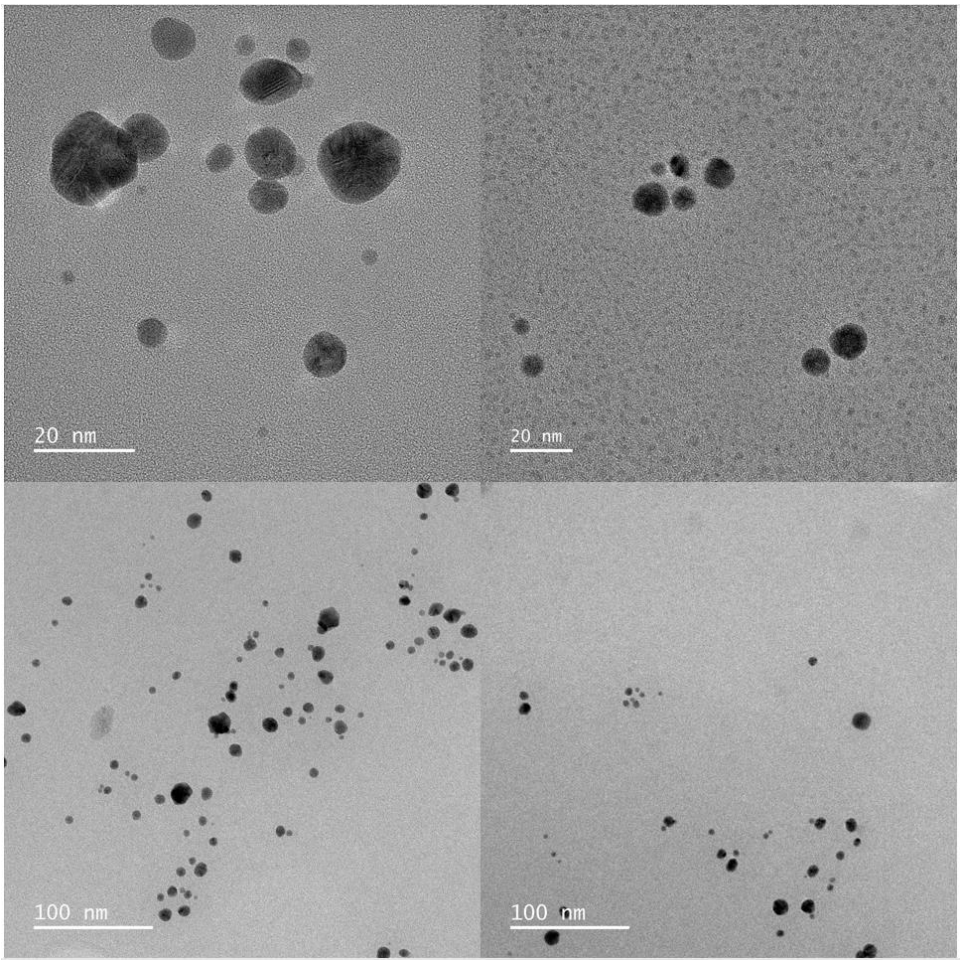

Figure 170. TEM micrographs showing AuAgNPs with the ratio with the ratio 0.97:0.03 – Au:Ag.

8.1.10.3 0.98:0.02 – Au:Ag

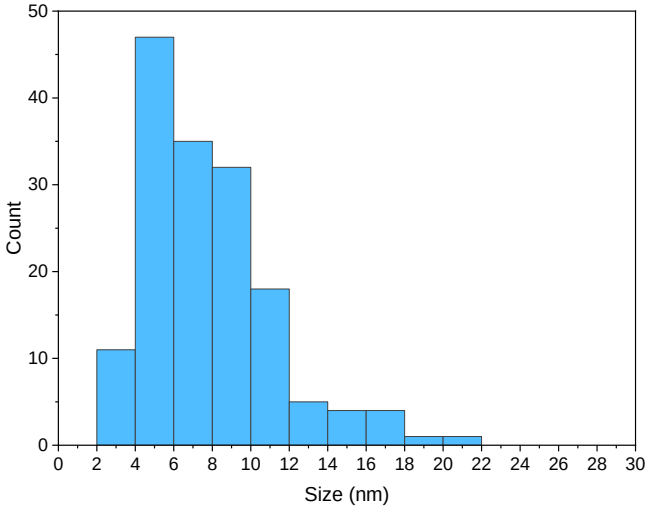

Figure 171. A histogram describing the distribution of particle sizes for AuAgNPs with the ratio 0.98:0.02 – Au:Ag.

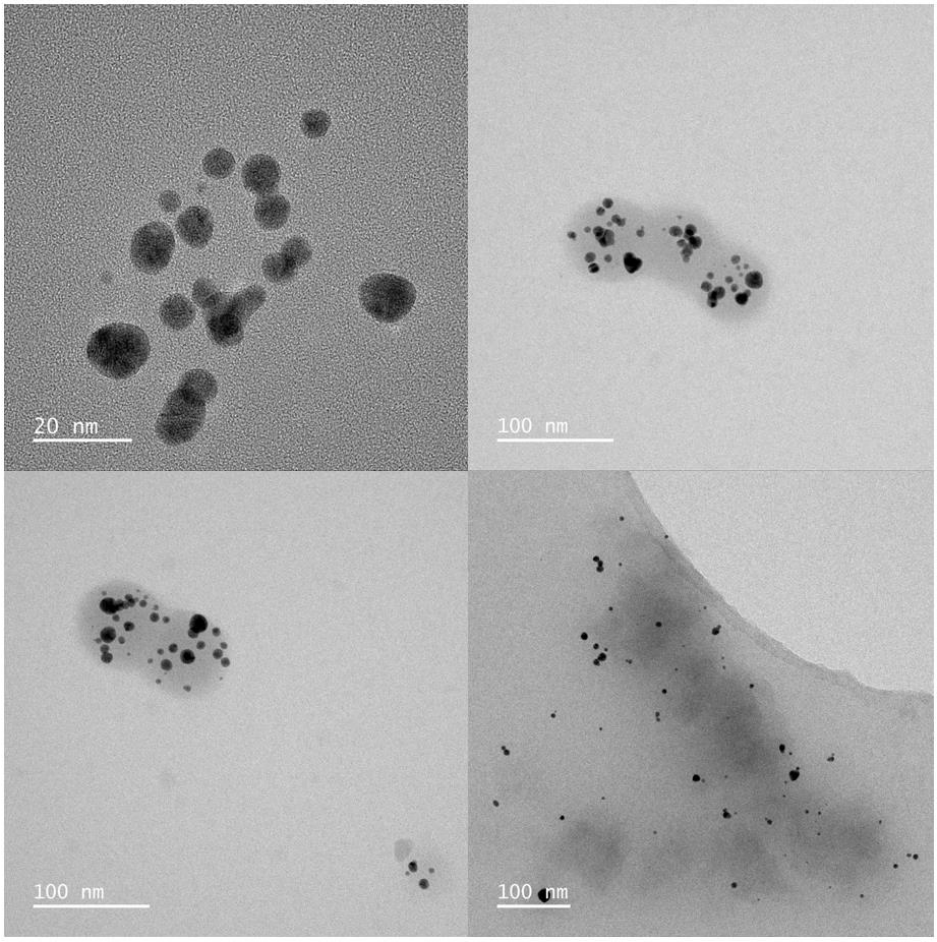

Figure 172. TEM micrographs showing AuAgNPs with the ratio with the ratio 0.98:0.02 – Au:Ag.

8.1.10.4 0.99:0.01 – Au:Ag

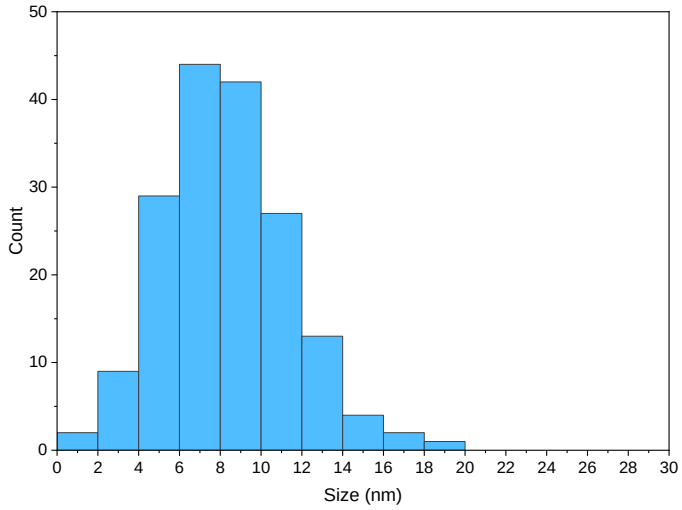

Figure 173. A histogram describing the distribution of particle sizes for AuAgNPs with the ratio 0.99:0.01 – Au:Ag.

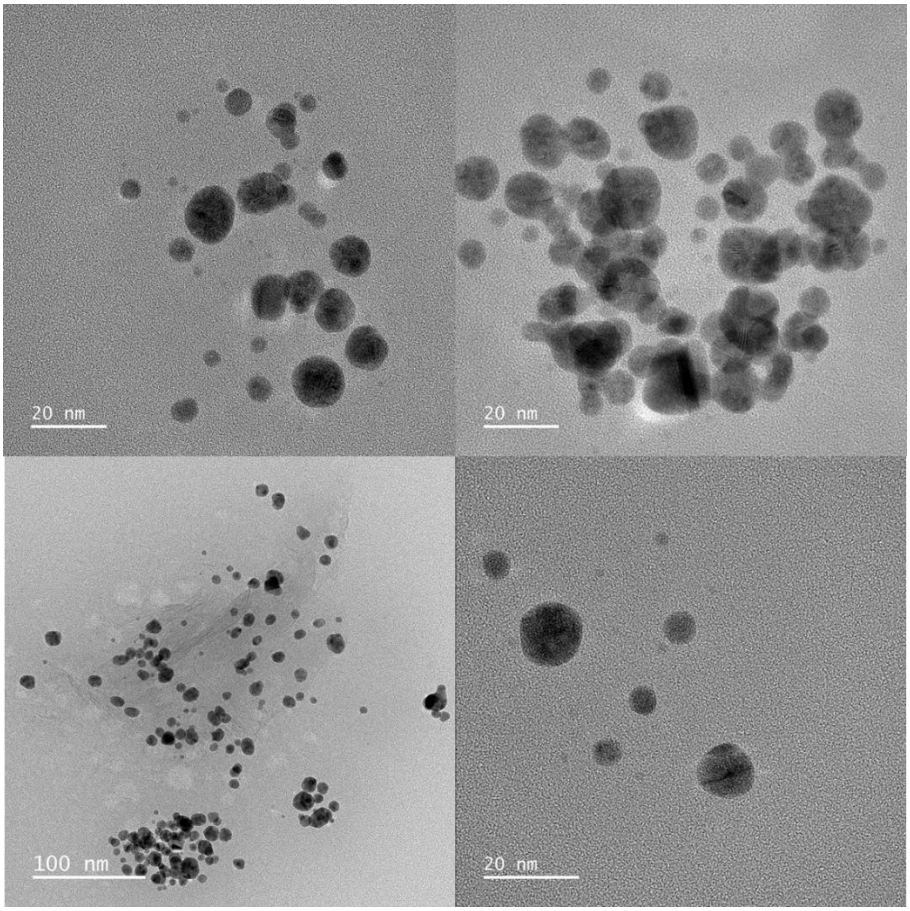

Figure 174. TEM micrographs showing AuAgNPs with the ratio with the ratio 0.99:0.01 – Au:Ag.

8.1.10.5 AuNPs

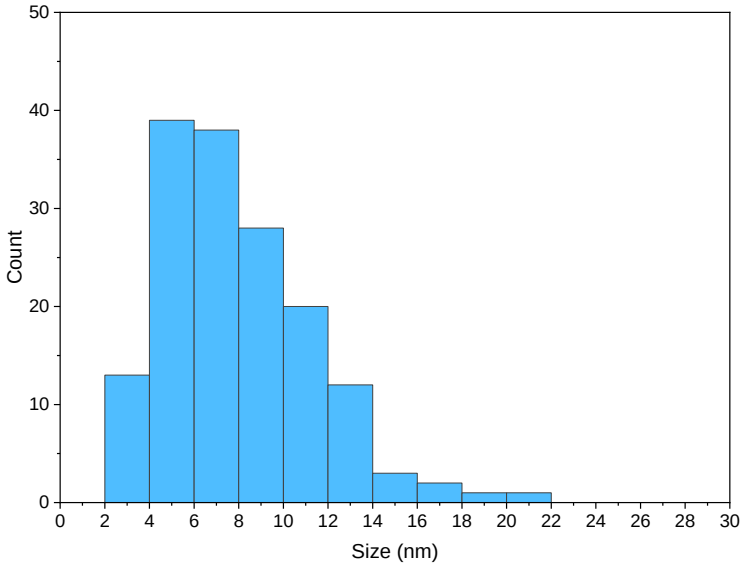

Figure 175. A histogram describing the distribution of particle sizes for AuNPs.

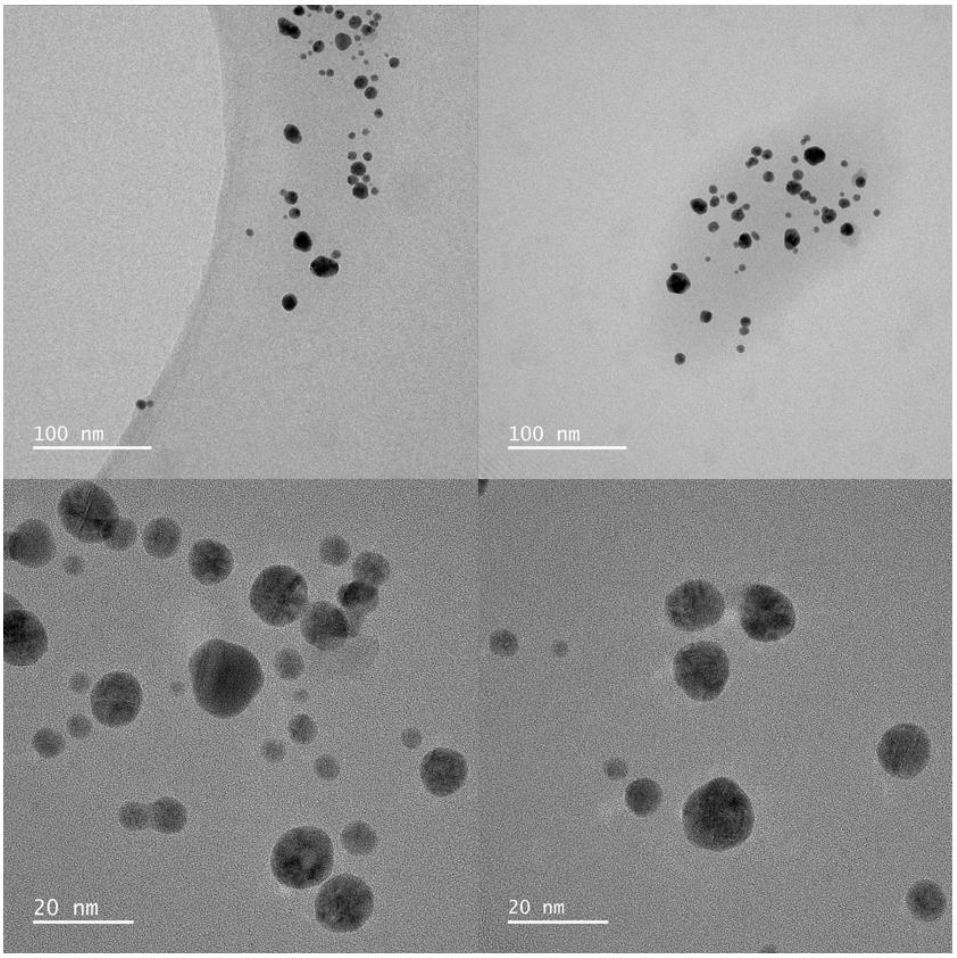

Figure 176. TEM micrographs showing AuNPs.

8.1.10.6 Optimal (0.97:0.03 – Au:Ag) AuAgNP catalysts after reaction

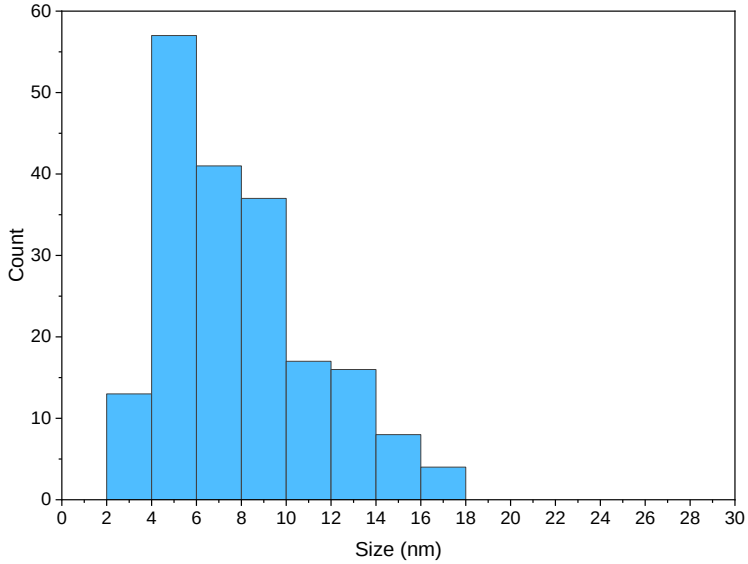

Figure 177. A histogram describing the distribution of particle sizes for AuAgNPs with the ratio 0.97:0.03 – Au:Ag after use in a catalysed reaction.

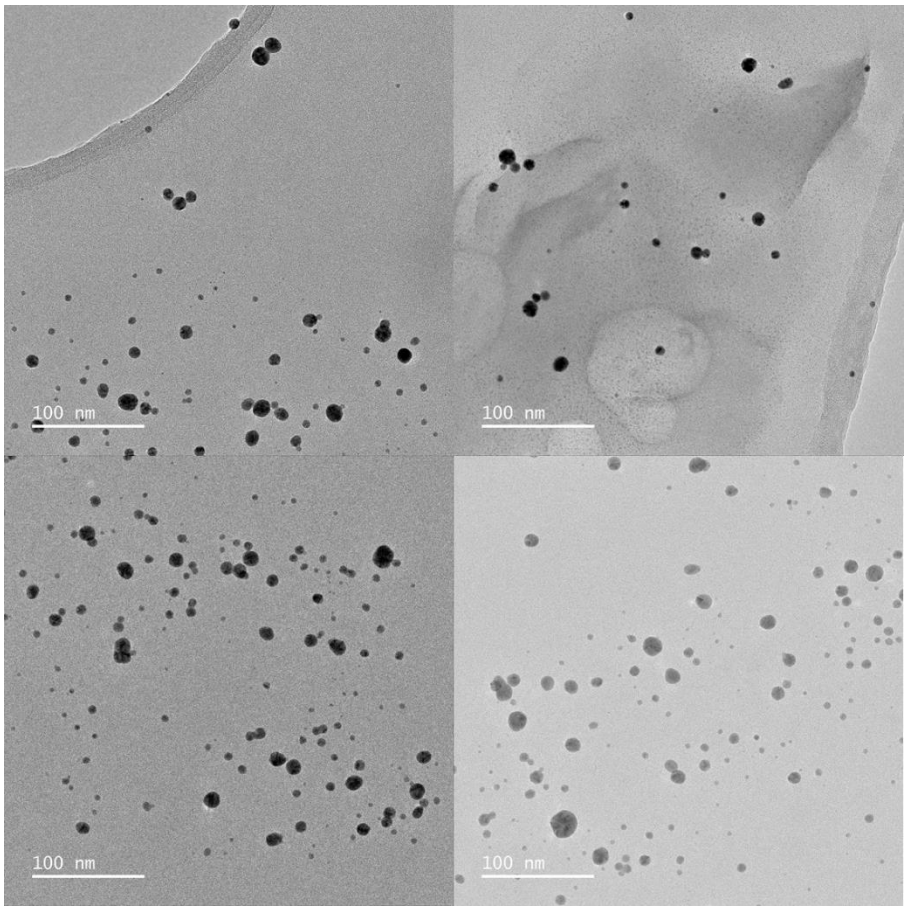

Figure 178. TEM micrographs showing AuAgNPs with the ratio 0.97:0.03 – Au:Ag after use in a catalysed reaction.

8.1.11 Data from self-optimisation experiments

8.1.11.1 Optimisation of full AuAgNP range (0.0:1.0 – 1.0:0.0, Au:Ag)

Table 28. Table showing raw data for optimisation performed with AuAgNP range (0.0:1.0 – 1.0:0.0, Au:Ag).

Experiment	Au:Ag ratio	AuAgNP:$NaBH_4$ ratio	Residence time (min)	Conversion (%)
1	0.81	0.23	0.92	43.07
2	0.03	0.15	1.44	24.29
3	0.00	0.25	0.53	27.90
4	0.93	0.24	1.50	39.23
5	0.30	0.15	0.98	20.57
6	0.52	0.16	0.55	28.20
7	0.96	0.17	0.52	38.71
8	0.50	0.23	1.46	30.15
9	0.00	0.27	0.98	28.43
10	0.54	0.11	1.17	29.42
11	1.00	0.30	0.50	48.22
12	1.00	0.29	0.96	57.02
13	0.23	0.23	1.22	22.93
14	1.00	0.30	1.10	60.22
15	1.00	0.30	1.00	53.56
16	0.62	0.20	1.07	37.57
17	1.00	0.28	1.50	56.53
18	1.00	0.21	1.17	42.63
19	0.23	0.13	1.22	24.40
20	1.00	0.27	1.20	56.78
21	1.00	0.20	0.89	39.05
22	0.12	0.27	1.36	24.98
23	1.00	0.21	0.70	42.18

8.1.11.2 Optimisation of narrow AuAgNP range (0.9:0.1 – 1.0:0.0, Au:Ag)

Table 29. Table showing experiments performed with AuAgNP range (0.9:0.1 – 1.0:0.0, Au:Ag) using the SNOBFIT algorithm.

Experiment	Au:Ag ratio	AuAgNP:$NaBH_4$ ratio	Residence time (min)	Conversion (%)
1	0.98	0.20	1.25	26.67
2	0.98	0.14	1.99	49.50
3	0.93	0.08	0.71	19.91
4	0.94	0.03	1.62	17.92
5	0.91	0.04	1.00	15.17
6	0.99	0.28	1.75	60.25
7	0.91	0.30	0.89	29.75
8	0.95	0.30	1.48	52.67
9	0.92	0.01	1.38	13.33
10	0.93	0.02	1.83	19.58
11	1.00	0.01	0.89	10.33
12	1.00	0.30	2.00	54.92
13	0.94	0.16	1.44	36.42
14	0.99	0.01	1.85	15.42
15	1.00	0.30	1.76	52.00
16	0.93	0.27	1.23	37.83
17	0.97	0.30	1.50	64.00
18	0.96	0.30	1.87	62.33
19	0.92	0.20	1.21	31.67
20	0.96	0.30	1.21	51.75
21	0.96	0.27	1.70	59.92
22	0.96	0.25	0.79	44.42
23	0.98	0.30	1.79	64.25
24	0.97	0.16	1.44	46.08
25	0.98	0.30	2.00	66.42
26	0.96	0.15	1.82	46.58

27	0.96	0.08	1.16	27.08
28	0.97	0.30	2.00	66.58
29	0.98	0.22	1.79	55.58
30	0.99	0.20	1.53	45.67

8.1.11.3 Line profile AuAgNP range (0.9:0.1 – 1.0:0.0, Au:Ag)

Table 30. Table showing line profile experiments performed between a AuAgNP range of 0.9:0.1 – 1.0:0.0, Au:Ag.

Experiment	Au:Ag ratio	AuAgNP:$NaBH_4$ ratio	Residence time (min)	Conversion (%)
1	0.90	0.30	2.00	35.07
2	0.91	0.30	2.00	38.44
3	0.92	0.30	2.00	39.42
4	0.93	0.30	2.00	44.29
5	0.94	0.30	2.00	49.58
6	0.95	0.30	2.00	57.29
7	0.96	0.30	2.00	61.79
8	0.97	0.30	2.00	65.14
9	0.98	0.30	2.00	65.24
10	0.99	0.30	2.00	58.29
11	1.00	0.30	2.00	52.49

The quoted error of 3.58% was based on 3 repeats taken @ an Au:Ag ratio of 0.97:0.03 with a standard deviation of as the error.

8.1.11.4 Optimisation of narrow AuAgNP range (0.9:0.1 – 1.0:0.0, Au:Ag)

Table 31. Table showing experiments performed with AuAgNP range (0.9:0.1 – 1.0:0.0, Au:Ag) with a Bayesian optimisation algorithm (BOAEI)

Experiment	Au:Ag ratio	AuAgNP:$NaBH_4$ ratio	Residence time (min)	Conversion (%)
1	0.98	0.03	1.72	23.10
2	0.93	0.24	1.00	34.15
3	0.95	0.27	1.45	49.99
4	0.96	0.18	0.72	41.74
5	0.99	0.10	1.16	29.47
6	0.90	0.16	1.33	29.45
7	0.92	0.06	1.89	21.48
8	0.99	0.30	1.91	58.04
9	0.94	0.30	1.72	49.14
10	0.97	0.30	2.00	72.95
11	0.97	0.30	0.81	56.09
12	0.97	0.30	2.00	71.93
13	0.97	0.27	2.00	68.90
14	0.97	0.30	2.00	71.99
15	0.97	0.3	2.00	72.62

References

1. Verena Fath, Norbert Kockmann, Jürgen Otto & Thorsten Röder. Self-optimising processes and real-time-optimisation of organic syntheses in a microreactor system using Nelder–Mead and design of experiments. *React. Chem. Eng.* **5**, 1281–1299 (2020).

2. Narayan, N., Meiyazhagan, A. & Vajtai, R. Metal nanoparticles as green catalysts. *Materials (Basel).* **12**, 1–12 (2019).

3. Lester, E. H., Dunne, P. W., Munn, A. S., Starkey, C. L. & Huddle, T. A. Continuous-flow hydrothermal synthesis for the production of inorganic nanomaterials. *Phil.Trans.R.Soc.* **373**, 1–35 (2015).

4. Clayton, A. D. *et al.* Algorithms for the self-optimisation of chemical reactions. *React. Chem. Eng.* **4**, 1545–1554 (2019).

5. Holmes, N. *et al.* Self-optimisation of the final stage in the synthesis of EGFR kinase inhibitor AZD9291 using an automated flow reactor. *React. Chem. Eng.* **1**, 366–371 (2016).

6. Pramanik, A. *et al.* The rapid diagnosis and effective inhibition of coronavirus using spike antibody attached gold nanoparticles. *Nanoscale Adv.* **3**, 1588–1596 (2021).

7. Phillips, R. L., Miranda, O. R., You, C.-C., Rotello, V. M. & Bunz, U. H. F. Rapid and Efficient Identification of Bacteria Using Gold-Nanoparticle–Poly(para-phenyleneethynylene) Constructs. *Angew. Chemie Int. Ed.* **47**, 2590–2594 (2008).

8. Mocan, T. *et al.* Development of nanoparticle-based optical sensors for pathogenic bacterial detection. *J. Nanobiotechnology* **15**, 25 (2017).

9. Naja, G., Hrapovic, S., Male, K., Bouvrette, P. & Luong, J. H. T. Rapid detection of microorganisms with nanoparticles and electron microscopy. *Microsc. Res. Tech.* **71**, 742–748 (2008).

10. Pissuwan, D., Niidome, T. & Cortie, M. B. The forthcoming applications of gold nanoparticles in drug and gene delivery systems. *J. Control. Release* **149**, 65–71 (2011).

11. Duncan, B., Kim, C. & Rotello, V. M. Gold nanoparticle platforms as drug and biomacromolecule delivery systems. *J. Control. Release* **148**, 122–127 (2010).

12. Kumar, A., Zhang, X. & Liang, X.-J. J. Gold nanoparticles: Emerging paradigm for targeted drug delivery system. *Biotechnol. Adv.* **31**, 593–606 (2013).

13. Lim, Z.-Z. J., Li, J.-E. J., Ng, C.-T., Yung, L.-Y. L. & Bay, B.-H. Gold nanoparticles in cancer therapy. *Acta Pharmacol. Sin.* **32**, 983–90 (2011).

14. Campisi, S. *et al.* Untangling the Role of the Capping Agent in Nanocatalysis: Recent Advances and Perspectives. *Catalysts* **6**, 185 (2016).

15. Han, J., Liu, Y. & Guo, R. Facile Synthesis of Highly Stable Gold Nanoparticles and Their Unexpected Excellent Catalytic Activity for Suzuki-Miyaura Cross-Coupling Reaction in Water. *JACS* **131**, 2060–2061 (2009).

16. Amendola, V. & Meneghetti, M. Size Evaluation of Gold Nanoparticles by UV-vis Spectroscopy. *J. Phys. Chem.* **113**, 4277–4285 (2009).

17. Bastus, N. G. *et al.* Kinetically Controlled Seeded Growth Synthesis of Citrate-Stabilized Gold Nanoparticles of up to 200 nm: Size Focusing versus Ostwald Ripening. *Langmuir* **27**, 11098–11105 (2011).

18. Ríos-Corripio, M. A., García-Pérez, B. E., Jaramillo-Flores, M. E., Gayou, V. L. & Rojas-López, M. UV–Visible intensity ratio (aggregates/single particles) as a measure to obtain stability of gold nanoparticles conjugated with protein A. *J. Nanoparticle Res. 2013 155* **15**, 1–7 (2013).

19. Wang, Q. & Domen, K. Particulate Photocatalysts for Light-Driven Water Splitting: Mechanisms, Challenges, and Design Strategies. *Chem. Rev* **120**, 919–985 (2019).

20. Mitsudome, T. & Kaneda, K. Gold nanoparticle catalysts for selective hydrogenations. *Green Chem.* **15**, 2636–2654 (2013).

21. Mallat, T. & Baiker, A. Potential of Gold Nanoparticles for Oxidation in Fine Chemical Synthesis. *Annu. Rev. Chem. Biomol. Eng.* **3**, 11–28 (2012).

22. Fihri, A., Bouhrara, M., Nekoueishahraki, B., Basset, J. M. & Polshettiwar, V. Nanocatalysts for Suzuki cross-coupling reactions. *Chem. Soc. Rev.* **40**, 5181–5203 (2011).

23. Molleman, B. & Hiemstra, T. Size and shape dependency of the surface energy of metallic nanoparticles: unifying the atomic and thermodynamic approaches †. *Phys. Chem. Chem. Phys* **20**, 20575–20587 (2018).

24. Ganapuram, B. R. *et al.* Catalytic reduction of methylene blue and Congo red dyes using green synthesized gold nanoparticles capped by salmalia malabarica gum. *Int. Nano Lett.* **5**, 215–222 (2015).

25. Biondi, I., Laurenczy, G., Dyson, P. J., Abor Laurenczy, G. & Dyson, P. J. Synthesis of Gold Nanoparticle Catalysts Based on a New Water-Soluble Ionic Polymer. *Inorg. Chem.* **50**, 8038–8045 (2011).

26. Moma, J. A., Ntho, T. A. & Scurrell, M. Gold-Catalysed Reactions. in *Catalytic Application of Nano-Gold Catalysts* (InTech, 2016). doi:10.5772/64103.

27. Tsunoyama, H., Sakurai, H., Ichikuni, N., Negishi, Y. & Tsukuda, T. Colloidal Gold Nanoparticles as Catalyst for Carbon-Carbon Bond Formation: Application to Aerobic Homocoupling of Phenylboronic Acid in Water. *Langmuir* **20**, 11293–11296 (2004).

28. Zhou, X., Xu, W., Liu, G., Panda, D. & Chen, P. Size-Dependent Catalytic Activity and Dynamics of Gold Nanoparticles at the Single-Molecule Level. *JACS* **132**, 138–146 (2010).

29. Deraedt, C. *et al.* Sodium borohydride stabilizes very active gold nanoparticle catalysts. *Chem. Commun* **50**, 14194–14196 (2014).

30. Negishi, Y. & Tsukuda, T. One-Pot Preparation of Subnanometer-Sized Gold Clusters via Reduction and Stabilization by *meso* -2,3-Dimercaptosuccinic Acid. *J. Am. Chem. Soc.* **125**, 4046–4047 (2003).

31. Lin, C. *et al.* Size effect of gold nanoparticles in catalytic reduction of p-nitrophenol with NaBH4. *Molecules* **18**, 12609–12620 (2013).

32. Roberts, E. J., Karadaghi, L. R., Wang, L., Malmstadt, N. & Brutchey, R. L. Continuous Flow Methods of Fabricating Catalytically Active Metal Nanoparticles. *ACS Appl. Mater. Interfaces* **11**, 27479−27502 (2019).

33. Piella, J., Bastúsbastús, N. G. & Puntes, V. Size-Controlled Synthesis of Sub-10-nanometer Citrate-Stabilized Gold Nanoparticles and Related Optical Properties. (2016) doi:10.1021/acs.chemmater.5b04406.

34. Li, L., Zhang, G., Wang, B., Yang, T. & Yang, S. Electrochemical formation of PtRu bimetallic nanoparticles for highly efficient and pH-universal hydrogen evolution reaction. *J. Mater. Chem. A* **8**, 2090–2098 (2020).

35. Chen, X. *et al.* Simultaneous SAXS/WAXS/UV−Vis Study of the Nucleation and Growth of Nanoparticles: A Test of Classical Nucleation Theory. *Langmuir* **31**, 11678−11691 (2015).

36. LaMer, V. K. & Dinegar, R. H. Theory, Production and Mechanism of Formation of Monodispersed Hydrosols. *Am. Chem. Soc.* **72**, 4847–4854 (1950).

37. Turkevich, J., Stevenson, P. C. & Hillier, J. A study of the nucleation and growth processes in the synthesis of colloidal gold. *Discuss. Faraday Soc.* **11**, 55 (1951).

38. Rg Polte, J. *et al.* Mechanism of Gold Nanoparticle Formation in the Classical Citrate Synthesis Method Derived from Coupled In Situ XANES and SAXS Evaluation. *JACS* **132**, 1296–1301 (2010).

39. Sengani, M., Grumezescu, A. M. & Rajeswari, V. D. Recent trends and methodologies in gold nanoparticle synthesis – A prospective review on drug delivery aspect. *OpenNano* **2**, 37–46 (2017).

40. Richardson, J. C. and J. F. *Coulson and Richardson's Chemical Engineering*. (Butterworth-Heinemann, 2017).

41. Hartman, R. L., McMullen, J. P. & Jensen, K. F. Deciding Whether To Go with the Flow: Evaluating the Merits of Flow Reactors for Synthesis. *Angew. Chemie Int. Ed.* **50**, 7502–7519 (2011).

42. Levenspiel, O. *Chemical Reaction Engineering*. (John Wiley & Sons, Ltd, 1999).

43. Du Toit, H., Macdonald, T. J., Huang, H., Parkin, I. P. & Gavriilidis, A. Continuous flow synthesis of citrate capped gold nanoparticles using UV induced nucleation †. *RSC Adv.* **7**, 9632 (2017).

44. Huang, H. *et al.* Continuous flow synthesis of ultrasmall gold nanoparticles in a microreactor using trisodium citrate and their SERS performance. *Chem. Eng. Sci. J.* **189**, 422–430 (2018).

45. Carino, A., Walter, A., Testino, A. & Hofmann, H. Continuous Synthesis of Gold Nanoparticles Using the Segmented Flow Tubular Reactor (SFTR). *Chim. Int. J.*

Chem. **70**, 457–457 (2016).

46. Pallipurath, A. R., Flandrin, P. B., Wayment, L. E., Wilson, C. C. & Robertson, K. In situ non-invasive Raman spectroscopic characterisation of succinic acid polymorphism during segmented flow crystallisation. *Mol. Syst. Des. Eng.* **5**, 294–303 (2020).

47. Levenstein, M. A. *et al.* Dynamic Crystallization Pathways of Polymorphic Pharmaceuticals Revealed in Segmented Flow with Inline Powder X-ray Diffraction. *Anal. Chem.* **92**, 7754–7761 (2020).

48. Nightingale, A. M. & deMello, J. C. Segmented Flow Reactors for Nanocrystal Synthesis. *Adv. Mater.* **25**, 1813–1821 (2013).

49. Chow, E. *et al.* Flow-controlled synthesis of gold nanoparticles in a biphasic system with inline liquid–liquid separation. *React. Chem. Eng.* **5**, 356–366 (2020).

50. Hone, C. A., Holmes, N., Akien, G. R., Bourne, R. A. & Muller, F. L. Rapid multistep kinetic model generation from transient flow data. *Cite this React. Chem. Eng* **2**, 103–108 (2017).

51. Mcmullen, J. P. & Jensen, K. F. Rapid Determination of Reaction Kinetics with an Automated Microfluidic System. *Org. Process Res. Dev* **15**, 398–407 (2011).

52. Aroh, K. C. & Jensen, K. F. Efficient kinetic experiments in continuous flow microreactors. *React. Chem. Eng* **3**, 94–101 (2018).

53. Nagy, K. D., Shen, B., Jamison, T. F. & Jensen, K. F. Mixing and Dispersion in Small-Scale Flow Systems. *Process. Dev.* **16**, 976−981 (2012).

54. Taylor, G. I. Dispersion of soluble matter in solvent flowing slowly through a tube. *Proc. R. Soc. London. Ser. A. Math. Phys. Sci.* **219**, 186–203 (1953).

55. Aris, R. On the dispersion of a solute in a fluid flowing through a tube. *Proc. R. Soc. London. Ser. A. Math. Phys. Sci.* **235**, 67–77 (1956).

56. Tajbl, D. G., Simons, J. B. & Carberry, J. J. Heterogeneous Catalysis in Continuous Stirred Tank Reactor. *Ind. Eng. Chem. Fundam.* **5**, 171–175 (2002).

57. Chapman, M. R. *et al.* Simple and Versatile Laboratory Scale CSTR for Multiphasic Continuous-Flow Chemistry and Long Residence Times. *Org.*

Process Res. Dev. **21**, 1294–1301 (2017).

58. Lignos, I. *et al.* A high-temperature continuous stirred-tank reactor cascade for the multistep synthesis of InP/ZnS quantum dots. *React. Chem. Eng.* **6**, 459–464 (2021).

59. Wu, K.-J., Gao, Y. & Torrente-Murciano, L. Continuous synthesis of hollow silver– palladium nanoparticles for catalytic applications. *Faraday Discuss.* **208**, 427–441 (2018).

60. Wu, K.-J., De Varine Bohan, G. M. & Torrente-Murciano, L. Synthesis of narrow sized silver nanoparticles in the absence of capping ligands in helical microreactors. *React. Chem. Eng.* **2**, 116–128 (2017).

61. Kunal, P. *et al.* Continuous Flow Synthesis of Rh and RhAg Alloy Nanoparticle Catalysts Enables Scalable Production and Improved Morphological Control. *Chem. Mater.* **29**, 4341–4350 (2017).

62. McMullen, J. P. *et al.* An Integrated Microreactor System for Self-Optimization of a Heck Reaction: From Micro-to Mesoscale Flow Systems**. *Angew. Chemie* **49**, 7076 –7080 (2010).

63. Yang, C. *et al.* Catalytic hydrogenation of N-4-nitrophenyl nicotinamide in a micro-packed bed reactor. *Green Chem.* **20**, 886–893 (2018).

64. Arndt, D., Thöming, J. & Bäumer, M. Improving the quality of nanoparticle production by using a new biphasic synthesis in a slug flow microreactor. *Chem. Eng. J.* **228**, 1083–1091 (2013).

65. Stucchi, M. *et al.* Synergistic effect in Au-Cu bimetallic catalysts for the valorization of Lignin-Derived compounds. *Catalysts* **10**, 332 (2020).

66. Bloemendal, V. R. L. J., Janssen, M. A. C. H., Hest, J. C. M. van & Rutjes, F. P. J. T. Continuous one-flow multi-step synthesis of active pharmaceutical ingredients. *React. Chem. Eng.* **5**, 1186–1197 (2020).

67. Hartlieb, K. J., Saunders, M., Jachuck, R. J. J. & Raston, C. L. Continuous flow synthesis of small silver nanoparticles involving hydrogen as the reducing agent. *Green Chem* **12**, 1012–1017 (2010).

68. Holvey, C. P., Roberge, D. M., Gottsponer, M., Kockmann, N. & Macchi, A.

Pressure drop and mixing in single phase microreactors: Simplified designs of micromixers. *Chem. Eng. Process. Process Intensif.* **50**, 1069–1075 (2011).

69. Feng, H. *et al.* Multilayered Pd nanocatalysts with nano-bulge structure in a microreactor for multiphase catalytic reaction. *Chem. Eng. Res. Des.* **138**, 190–199 (2018).

70. Wang, N., Matsumoto, T., Ueno, M., Miyamura, H. & Kobayashi, S. A gold-immobilized Microchannel flow reactor for oxidation of alcohols with molecular oxygen. *Angew. Chemie - Int. Ed.* **48**, 4744–4746 (2009).

71. Wagner, J. & Köhler, J. M. Continuous Synthesis of Gold Nanoparticles in a Microreactor. *NANO Lett.* **5**, 685–691 (2005).

72. Tsunoyama, H., Ichikuni, N. & Tsukuda, T. Microfluidic synthesis and catalytic application of pvp-stabilized, ∼1 nm gold clusters. *Langmuir* **24**, 11327–11330 (2008).

73. Ke, S., Wu, J. & Torrente-Murciano, L. Continuous synthesis of tuneable sized silver nanoparticles via a tandem seed-mediated method in coiled flow inverter reactors. *React. Chem. Eng* **3**, 267–276 (2018).

74. Baber, R., Mazzei, L., Thi, N., Thanh, K. & Gavriilidis, A. An engineering approach to synthesis of gold and silver nanoparticles by controlling hydrodynamics and mixing based on a coaxial flow reactor †. *Nanoscale* **9**, 14149 (2017).

75. Bandulasena, M. V., Vladisavljević, G. T., Odunmbaku, O. G. & Benyahia, B. Continuous synthesis of PVP stabilized biocompatible gold nanoparticles with a controlled size using a 3D glass capillary microfluidic device. *Chem. Eng. Sci.* **171**, 233–243 (2017).

76. Amiri Delouei, A., Sajjadi, H., Izadi, M. & Mohebbi, R. The simultaneous effects of nanoparticles and ultrasonic vibration on inlet turbulent flow: An experimental study. *Appl. Therm. Eng.* **146**, 268–277 (2019).

77. Panariello, L. *et al.* Highly reproducible, high-yield flow synthesis of gold nanoparticles based on a rational reactor design exploiting the reduction of passivated Au(iii). *React. Chem. Eng.* **5**, 663–676 (2020).

78. Sebastian, V., Basak, S. & Jensen, K. F. Continuous synthesis of palladium nanorods in oxidative segmented flow. *AIChE J.* **62**, 373–380 (2016).

79. Köhler, J. M., Abahmane, L., Wagner, J., Albert, J. & Mayer, G. Preparation of metal nanoparticles with varied composition for catalytical applications in microreactors. *Chem. Eng. Sci.* **63**, 5048–5055 (2008).

80. Knauer, A. *et al.* Au/Ag/Au double shell nanoparticles with narrow size distribution obtained by continuous micro segmented flow synthesis. *Chem. Eng. J.* **166**, 1164–1169 (2011).

81. Pekkari, A. *et al.* Continuous Microfluidic Synthesis of Pd Nanocubes and PdPt Core-Shell Nanoparticles and Their Catalysis of NO 2 Reduction. *ACS Appl. Mater. Interfaces* **11**, 36196–36204 (2019).

82. Liu, H. *et al.* Continuous-flow biosynthesis of Au–Ag bimetallic nanoparticles in a microreactor. *J. Nanoparticle Res.* **16**, 1–9 (2014).

83. Zhou, Y. *et al.* A scalable synthesis of ternary nanocatalysts for a high-efficiency electrooxidation catalysis by microfluidics. *Nanoscale* **12**, 12647–12654 (2020).

84. Cattaneo, S. *et al.* Synthesis of highly uniform and composition-controlled gold–palladium supported nanoparticles in continuous flow. *Nanoscale* **11**, 8247–8259 (2019).

85. Nikam, A. V., Kulkarni, A. A. & Prasad, B. L. V. Microwave-assisted batch and continuous flow synthesis of palladium supported on magnetic nickel nanocrystals and their evaluation as reusable catalyst. *Cryst. Growth Des.* **17**, 5163–5169 (2017).

86. Kunal, P. *et al.* Continuous Flow Synthesis of Rh and RhAg Alloy Nanoparticle Catalysts Enables Scalable Production and Improved Morphological Control. *Chem. Mater.* **29**, 4341–4350 (2017).

87. Cattaneo, S. *et al.* Continuous Flow Synthesis of Bimetallic AuPd Catalysts for the Selective Oxidation of 5-Hydroxymethylfurfural to 2,5-Furandicarboxylic Acid. *ChemNanoMat* **6**, 420–426 (2020).

88. Silva, H. *et al.* Supercritical flow synthesis of PtPdFe alloyed nanoparticles with enhanced low-temperature activity and thermal stability for propene oxidation under lean exhaust gas conditions. *Catal. Sci. Technol.* **9**, 6691–6699 (2019).

89. Cabeza, S., Kuhn, S., Kulkarni, A. A. & Jensen, K. F. Size-Controlled Flow Synthesis of Gold Nanoparticles Using a Segmented Flow Microfluidic Platform. *Langmuir* **28**, 7007−7013 (2018).

90. Sagmeister, P., Williams, J. D., Hone, C. A. & Kappe, C. O. Laboratory of the future: a modular flow platform with multiple integrated PAT tools for multistep reactions. *React. Chem. Eng.* **4**, 1571–1578 (2019).

91. Carter, C. F. *et al.* ReactIR Flow Cell: A New Analytical Tool for Continuous Flow Chemical Processing. *Org. Process Res. Dev.* **14**, 393–404 (2010).

92. Giraudeau, P. & Felpin, F. X. Flow reactors integrated with in-line monitoring using benchtop NMR spectroscopy. *React. Chem. Eng.* **3**, 399–413 (2018).

93. Meulendijks, N. *et al.* Flow Cell Coupled Dynamic Light Scattering for Real-Time Monitoring of Nanoparticle Size during Liquid Phase Bottom-Up Synthesis. *Appl. Sci. Commun.* **8**, 108 (2018).

94. Tao, H. *et al.* Nanoparticle synthesis assisted by machine learning. *Nat. Rev. Mater.* **6**, 701–716 (2021).

95. Wang, L., Karadaghi, L. R., Brutchey, R. L. & Malmstadt, N. Self-optimizing parallel millifluidic reactor for scaling nanoparticle synthesis. *Chem. Commun.* **56**, 3745–3748 (2020).

96. Epps, R. W. *et al.* Artificial Chemist: An Autonomous Quantum Dot Synthesis Bot. *Adv. Mater.* **32**, 1–9 (2020).

97. S. Krishnadasan, a R. J. C. Brown, b A. J. deMelloa and J. C. deMello*a. Intelligent routes to the controlled synthesis of nanoparticles. *Lab Chip* **7**, 1377–1612 (2007).

98. Abdel-Latif, K. *et al.* Facile Room-Temperature Anion Exchange Reactions of Inorganic Perovskite Quantum Dots Enabled by a Modular Microfluidic Platform. *Adv. Funct. Mater.* **29**, 1–13 (2019).

99. Salley, D. *et al.* A nanomaterials discovery robot for the Darwinian evolution of shape programmable gold nanoparticles. *Nat. Commun. 2020 111* **11**, 1–7 (2020).

100. Wang, J., Yan, T., Tang, Y. & Miao, Y. High Efficient Aldol Condensation

Reaction Utilizing Modified Calcium Oxide as Stable Solid Base Catalyst 1. *Kinet. Catal.* **57**, 439–445 (2016).

101. Taylor, C. J. *et al.* Flow chemistry for process optimisation using design of experiments. *J. Flow Chem.* **11**, 75–86 (2021).

102. Weissman, S. A. & Anderson, N. G. Design of Experiments (DoE) and Process Optimization. A Review of Recent Publications. *Org. Process Res. Dev.* **19**, 1605–1633 (2014).

103. Spendley, W., Hext, G. R. & Himsworth, F. R. Sequential Application of Simplex Designs in Optimisation and Evolutionary Operation. *Technometrics* **4**, 441–461 (1962).

104. J. A. Nelder, R. M. A Simplex Method for Function Minimization. *Comput. Journal*, **7**, 308–313 (1965).

105. Goldberg, D. E. & Holland, J. H. Genetic Algorithms and Machine Learning. *Mach. Learn. 1988 32* **3**, 95–99 (1988).

106. Huyer, W. & Neumaier, A. *Snobfit-Stable Noisy Optimization by Branch and Fit*.

107. Holmes, N. *et al.* Online quantitative mass spectrometry for the rapid adaptive optimisation of automated flow reactors. *React. Chem. Eng.* 96–100 (2016) doi:10.1039/C5RE00083A.

108. Jeraal, M. I., Holmes, N., Akien, G. R. & Bourne, R. A. Enhanced process development using automated continuous reactors by self-optimisation algorithms and statistical empirical modelling. *Tetrahedron* **74**, 3158–3164 (2018).

109. Walker, B. E., Bannock, J. H., Nightingale, A. M. & Demello, J. C. Tuning reaction products by constrained optimisation. *React. Chem. Eng.* **2**, 785–798 (2017).

110. Cherkasov, N., Bai, Y., Expósito, A. J. & Rebrov, E. V. OpenFlowChem – a platform for quick, robust and flexible automation and self-optimisation of flow chemistry. *React. Chem. Eng.* **3**, 769–780 (2018).

111. Shields, B. J. *et al.* Bayesian reaction optimization as a tool for chemical synthesis. *Nat. 2021 5907844* **590**, 89–96 (2021).

112. Roshan Joseph, V. & Hung, Y. ORTHOGONAL-MAXIMIN LATIN HYPERCUBE DESIGNS. *Stat. Sin.* **18**, 171–186 (2008).

113. Frazier, P. I. A Tutorial on Bayesian Optimization. *arXiv:1807.02811v1* 1–22 (2018).

114. Gunantara, N. A review of multi-objective optimization: Methods and its applications. *Cogent Eng.* **5**, 1–16 (2018).

115. Clayton, A. D. *et al.* Automated self-optimisation of multi-step reaction and separation processes using machine learning. *Chem. Eng. J.* **384**, 123340 (2020).

116. Auger, A., Bader, J., Brockhoff, D. & Zitzler, E. Hypervolume-based multiobjective optimization: Theoretical foundations and practical implications. *Theor. Comput. Sci.* **425**, 75–103 (2012).

117. Travis, A. S. Manufacture and uses of the Anilines: A Vast Array of Processes and Products. in *The Chemistry of Anilines* 715–782 (John Wiley & Sons, Ltd, 2007). doi:10.1002/9780470871737.ch13.

118. Booth, G. Nitro Compounds, Aromatic. in *Ullmann's Encyclopedia of Industrial Chemistry* 301–349 (Wiley-VCH Verlag GmbH & Co. KGaA, 2000). doi:10.1002/14356007.a17_411.

119. Hervés, P. *et al.* Catalysis by metallic nanoparticles in aqueous solution: Model reactions. *Chem. Soc. Rev.* **41**, 5577–5587 (2012).

120. Wunder, S., Lu, Y., Albrecht, M. & Ballauff, M. Catalytic activity of faceted gold nanoparticles studied by a model reaction: Evidence for substrate-induced surface restructuring. *ACS Catal.* **1**, 908–916 (2011).

121. Baghbamidi, S. E., Hassankhani, A., Sanchooli, | Esmael, Seyed, | & Sadeghzadeh, M. The reduction of 4-nitrophenol and 2-nitroaniline by palladium catalyst based on a KCC-1/IL in aqueous solution. *Appl. Org. Chem.* **32**, 4251 (2017).

122. Aditya, T., Pal, A. & Pal, T. Nitroarene reduction: A trusted model reaction to test nanoparticle catalysts. *Chemical Communications* vol. 51 9410–9431 (2015).

123. Pradhan, N., Pal, A. & Pal, T. Silver nanoparticle catalyzed reduction of aromatic

nitro compounds. *Colloids Surfaces A Physicochem. Eng. Asp.* **196**, 247–257 (2002).

124. *Ocean Optics, Catalog of Products*. (2012).

125. Radnik, J., Mohr, C. & Claus, P. On the origin of binding energy shifts of core levels of supported gold nanoparticles and dependence of pretreatment and material synthesis. *Phys. Chem. Chem. Phys.* **5**, 172–177 (2003).

126. Tchaplyguine, M., Mikkelä, M. H., Zhang, C., Andersson, T. & Björneholm, O. Gold oxide nanoparticles with variable gold oxidation state. *J. Phys. Chem. C* **119**, 8937–8943 (2015).

127. Casaletto, M. P., Longo, A., Martorana, A., Prestianni, A. & Venezia, A. M. XPS study of supported gold catalysts: the role of Au0 and Au+δ species as active sites. *Surf. Interface Anal.* **38**, 215–218 (2006).

128. Spreadborough, J. & Christian, J. W. High-temperature X-ray diffractometer. *J. Sci. Instrum.* **36**, 116–118 (1959).

129. Sutherland, T. I. *et al.* Effect of ferrous ion concentration on the kinetics of radiation-induced iron-oxide nanoparticle formation and growth. *Phys. Chem. Chem. Phys* **19**, 695–708 (2017).

130. Avila C. ChemiView V3.4. http://chemiview.leeds.ac.uk.

131. Wunder, S., Polzer, F., Lu, Y., Mei, Y. & Ballauff, M. Kinetic analysis of catalytic reduction of 4-nitrophenol by metallic nanoparticles immobilized in spherical polyelectrolyte brushes. *J. Phys. Chem. C* **114**, 8814–8820 (2010).

132. Scholder, P., Hafner, M., Hassel, A. W. & Nischang, I. Gold Nanoparticle@Polyhedral Oligomeric Silsesquioxane Hybrid Scaffolds in Microfluidic Format - Highly Efficient and Green Catalytic Platforms. *Eur. J. Inorg. Chem.* **2016**, 951–955 (2016).

133. Hall, B. L. *et al.* Autonomous optimisation of a nanoparticle catalysed reduction reaction in continuous flow. *Chem. Commun.* **57**, 4926–4929 (2021).

134. Link, S., Wang, Z. L. Z. & El-Sayed, M. A. Alloy Formation of Gold−Silver Nanoparticles and the Dependence of the Plasmon Absorption on Their Composition. *J. Phys. Chem. B* **103**, 3529–3533 (1999).

135. Cao, Y.-Q. *et al.* Co-Pt bimetallic nanoparticles with tunable magnetic and electrocatalytic properties prepared by atomic layer deposition. *Chem. Commun* **56**, 8675–8678 (2020).

136. Chen, T. & Rodionov, V. O. Controllable Catalysis with Nanoparticles: Bimetallic Alloy Systems and Surface Adsorbates. *ACS Catal.* **6**, 4025−4033 (2016).

137. Liu, X., Wang, D. & Li, Y. Synthesis and catalytic properties of bimetallic nanomaterials with various architectures. *Nano Today* **7**, 448–466 (2012).

138. Zaleska-Medynska, A., Marchelek, M., Diak, M. & Grabowska, E. Noble metal-based bimetallic nanoparticles: The effect of the structure on the optical, catalytic and photocatalytic properties. *Adv. Colloid Interface Sci.* **229**, 80–107 (2016).

139. Sharma, G. *et al.* Novel development of nanoparticles to bimetallic nanoparticles and their composites: A review. *J. King Saud Univ. - Sci.* **31**, 257–269 (2019).

140. Abu-Dief, A. M. & Abdel-Fatah, S. M. Development and functionalization of magnetic nanoparticles as powerful and green catalysts for organic synthesis. *Beni-Suef Univ. J. Basic Appl. Sci.* **7**, 55–67 (2018).

141. Jun, Y., Choi, J. & Cheon, J. Heterostructured magnetic nanoparticles: their versatility and high performance capabilities. *Chem. Commun.* 1203–1214 (2007).

142. Jang, Y. *et al.* Simple one-pot synthesis of Rh–Fe3O4 heterodimer nanocrystals and their applications to a magnetically recyclable catalyst for efficient and selective reduction of nitroarenes and alkenes. *Chem. Commun.* **47**, 3601–3603 (2011).

143. Gawande, M. B. *et al.* Core–shell nanoparticles: synthesis and applications in catalysis and electrocatalysis. *Chem. Soc. Rev.* **44**, 7540–7590 (2015).

144. Singh, A. K. & Xu, Q. Synergistic Catalysis over Bimetallic Alloy Nanoparticles. *ChemCatChem* **5**, 652–676 (2013).

145. Wu, J. *et al.* Surface lattice-engineered bimetallic nanoparticles and their catalytic properties. *Chem. Soc. Rev.* **41**, 8066–8074 (2012).

146. Nørskov, J. K., Bligaard, T., Rossmeisl, J. & Christensen, C. H. *Towards the*

computational design of solid catalysts. *Nature Chemistry* vol. 1 37–46 (Nature Publishing Group, 2009).

147. Greeley, J., Jaramillo, T. F., Bonde, J., Chorkendorff, I. & Nørskov, J. K. Computational high-throughput screening of electrocatalytic materials for hydrogen evolution. *Nat. Mater.* **5**, 909–913 (2006).

148. Strmcnik, D. *et al.* Improving the hydrogen oxidation reaction rate by promotion of hydroxyl adsorption. *Nat. Chem. 2013 54* **5**, 300–306 (2013).

149. Ahsan, M. A. *et al.* Tuning of Trifunctional NiCu Bimetallic Nanoparticles Confined in a Porous Carbon Network with Surface Composition and Local Structural Distortions for the Electrocatalytic Oxygen Reduction, Oxygen and Hydrogen Evolution Reactions. *J. Am. Chem. Soc.* **142**, 14688–14701 (2020).

150. Ji, X. *et al.* Nanocrystalline intermetallics on mesoporous carbon for direct formic acid fuel cell anodes. *Nat. Chem. 2010 24* **2**, 286–293 (2010).

151. Chang, S. C., Ho, Y. & Weaver, M. J. Applications of real-time infrared spectroscopy to electrocatalysis at bimetallic surfaces. I. Electrooxidation of formic acid and methanol on bismuth-modified Pt(111) and Pt(100). *Surf. Sci.* **265**, 81–94 (1992).

152. Casado-Rivera, E. *et al.* Electrocatalytic Oxidation of Formic Acid at an Ordered Intermetallic PtBi Surface. *ChemPhysChem* **4**, 193–199 (2003).

153. Casado-Rivera, E. *et al.* Electrocatalytic Activity of Ordered Intermetallic Phases for Fuel Cell Applications. *J. Am. Chem. Soc.* **126**, 4043–4049 (2004).

154. Rice, C., Ha, S., Masel, R. I. & Wieckowski, A. Catalysts for direct formic acid fuel cells. *J. Power Sources* **115**, 229–235 (2003).

155. Li, J. & Sun, S. Intermetallic Nanoparticles: Synthetic Control and Their Enhanced Electrocatalysis. *Acc. Chem. Res.* **52**, 2015–2025 (2019).

156. Chaudhuri, R. G. & Paria, S. Core/Shell Nanoparticles: Classes, Properties, Synthesis Mechanisms, Characterization, and Applications. *Chem. Rev.* **112**, 2373–2433 (2011).

157. Lv, Y., Duan, S. & Wang, R. Structure design, controllable synthesis, and application of metal-semiconductor heterostructure nanoparticles. *Prog. Nat. Sci.*

Mater. Int. **30**, 1–12 (2020).

158. Rioux, D. & Meunier, M. Seeded Growth Synthesis of Composition and Size-Controlled Gold-Silver Alloy Nanoparticles. *J. Phys. Chem. C* **119**, 13160–13168 (2015).

159. Feng, L. *et al.* Optical properties and catalytic activity of bimetallic gold-silver nanoparticles. *Nano Biomedicine and Engineering* vol. 2 258–267 (2010).

160. Monga, A. & Pal, B. Improved catalytic activity and surface electro-kinetics of bimetallic Au-Ag core-shell nanocomposites. *New J. Chem.* **39**, 304–313 (2015).

161. Shore, M. S., Wang, J., Johnston-Peck, A. C., Oldenburg, A. L. & Tracy, J. B. Synthesis of Au(Core)/Ag(Shell) Nanoparticles and their Conversion to AuAg Alloy Nanoparticles. *Small* **7**, 230–234 (2011).

162. Rodríguez-González, B., Burrows, A., Watanabe, M., Kiely, C. J. & Marzán, L. M. L. Multishell bimetallic AuAg nanoparticles: synthesis, structure and optical properties. *J. Mater. Chem.* **15**, 1755–1759 (2005).

163. Li, J. *et al.* Fe Stabilization by Intermetallic L10-FePt and Pt Catalysis Enhancement in L10-FePt/Pt Nanoparticles for Efficient Oxygen Reduction Reaction in Fuel Cells. *J. Am. Chem. Soc.* **140**, 2926–2932 (2018).

164. Li, J. *et al.* Hard-Magnet L10-CoPt Nanoparticles Advance Fuel Cell Catalysis. *Joule* **3**, 124–135 (2019).

165. Sun, S., Murray, C. B., Weller, D., Folks, L. & Moser, A. Monodisperse FePt nanoparticles and ferromagnetic FePt nanocrystal superlattices. *Science (80-.).* **287**, 1989–1992 (2000).

166. Kim, J., Lee, Y. & Sun, S. Structurally Ordered FePt Nanoparticles and Their Enhanced Catalysis for Oxygen Reduction Reaction. *J. Am. Chem. Soc.* **132**, 4996–4997 (2010).

167. Wang, D. *et al.* Structurally ordered intermetallic platinum–cobalt core–shell nanoparticles with enhanced activity and stability as oxygen reduction electrocatalysts. *Nat. Mater.* **12**, 81–87 (2012).

168. Jonathan W. Lekse, Tristan J. Stagger, A. & Aitken*, J. A. Microwave Metallurgy: Synthesis of Intermetallic Compounds via Microwave Irradiation.

Chem. Mater. **19**, 3601–3603 (2007).

169. Lei, W. *et al.* Halide Ion-Mediated Synthesis of L10-FePt Nanoparticles with Tunable Magnetic Properties. *Nano Lett.* **18**, 7839–7844 (2018).

170. Wang, H. *et al.* One-Step Synthesis of High-Coercivity L10-FePtAg Nanoparticles: Effects of Ag on the Morphology and Chemical Ordering of FePt Nanoparticles. *Chem. Mater.* **25**, 2450–2454 (2013).

171. Amandeep K. Sra, Trevor D. Ewers, A. & Schaak*, R. E. Direct Solution Synthesis of Intermetallic AuCu and AuCu3 Nanocrystals and Nanowire Networks. *Chem. Mater.* **17**, 758–766 (2005).

172. Kim, D. *et al.* Electrochemical Activation of CO2 through Atomic Ordering Transformations of AuCu Nanoparticles. *J. Am. Chem. Soc.* **139**, 8329–8336 (2017).

173. Wang, C., Chen, D. P., Sang, X., Unocic, R. R. & Skrabalak, S. E. Size-Dependent Disorder–Order Transformation in the Synthesis of Monodisperse Intermetallic PdCu Nanocatalysts. *ACS Nano* **10**, 6345–6353 (2016).

174. Yan, Y. *et al.* Intermetallic Nanocrystals: Syntheses and Catalytic Applications. *Adv. Mater.* **29**, 1–29 (2017).

175. Chen, P. C. *et al.* Polyelemental nanoparticle libraries. *Science (80-.).* **352**, 1565–1569 (2016).

176. He, X., Zhang, S. E., Cheng, F. & Chen, Z. X. The region-specific segregation and catalytic activity of gold-silver nanoparticles. *Chem. Commun.* **54**, 638–641 (2018).

177. Yen, C.-W. *et al.* CO Oxidation Catalyzed by Au-Ag Bimetallic Nanoparticles Supported in Mesoporous Silica. *J. Phys. Chem. C* **113**, 17831–17839 (2009).

178. Jouve, A. *et al.* Gold-silver catalysts: Effect of catalyst structure on the selectivity of glycerol oxidation. *J. Catal.* **368**, 324–335 (2018).

179. Berahim, N., Basirun, W., Leo, B. & Johan, M. Synthesis of Bimetallic Gold-Silver (Au-Ag) Nanoparticles for the Catalytic Reduction of 4-Nitrophenol to 4-Aminophenol. *Catalysts* **8**, 1–15 (2018).

180. Gonzalez, C. M., Liu, Y. & Scaiano, J. C. Photochemical Strategies for the Facile

Synthesis of Gold−Silver Alloy and Core−Shell Bimetallic Nanoparticles. *J. Phys. Chem. C* **113**, 11861–11867 (2009).

181. Liu, S., Chen, G., Prasad, P. N. & Swihart, M. T. Synthesis of Monodisperse Au, Ag, and Au–Ag Alloy Nanoparticles with Tunable Size and Surface Plasmon Resonance Frequency. *Chem. Mater.* **23**, 4098–4101 (2011).

182. Zhang, Q., Xie, J., Liang, J. & Lee, J. Y. Synthesis of Monodisperse AgAu Alloy Nanoparticles with Independently Tunable Morphology, Composition, Size, and Surface Chemistry and Their 3-D Superlattices. *Adv. Funct. Mater.* **19**, 1387–1398 (2009).

183. Pal, U., Sánchez-Ramírez, J. F., Nolasco-Hernández, L., Mendoza-Álvarez, J. & Pescador-Rojas, J. A. Synthesis and optical properties of Au-Ag alloy nanoclusters with controlled composition. *J. Nanomater.* 1–9 (2008).

184. Mallin, M. P. & Murphy, C. J. Solution-Phase Synthesis of Sub-10 nm Au-Ag Alloy Nanoparticles. *Nano Lett.* **2**, 1235–1237 (2002).

185. Link, S., Wang, Z. L. & El-Sayed, M. A. Alloy Formation of Gold-Silver Nanoparticles and the Dependence of the Plasmon Absorption on Their Composition. *J. Phys. Chem.* **103**, 3529–3533 (1999).

186. Rg Polte, J. *et al.* Mechanism of Gold Nanoparticle Formation in the Classical Citrate Synthesis Method Derived from Coupled In Situ XANES and SAXS Evaluation. *JACS* **132**, 1296–1301 (2010).

187. Watzky, M. A. & Finke, R. G. Gold Nanoparticle Formation Kinetics and Mechanism: A Critical Analysis of the Redox Crystallization Mechanism. **3**, (2018).

188. Jana, N. R., Gearheart, L. & Murphy, C. J. Evidence for Seed-Mediated Nucleation in the Chemical Reduction of Gold Salts to Gold Nanoparticles. (2001).

189. Pan, L.-J. *et al.* Lab on a Chip CRITICAL REVIEW Controllable synthesis of nanocrystals in droplet reactors. *Lab Chip* **18**, 41–56 (2018).

190. Khositanon, C., Adpakpang, K., Bureekaew, S. & Weeranoppanant, N. Continuous-flow purification of silver nanoparticles and its integration with flow synthesis. *J. Flow Chem.* **10**, 353–362 (2020).

191. Shen, Y. *et al.* Multistage extraction platform for highly efficient and fully continuous purification of nanoparticles. *Nanoscale* **9**, 54 (2017).

192. Adishev, A. *et al.* Control of catalytic nanoparticle synthesis: general discussion. *Faraday Discuss.* **208**, 471–495 (2018).

193. Długosz, O. & Banach, M. Inorganic nanoparticle synthesis in flow reactors – applications and future directions. *React. Chem. Eng.* **5**, 1619–1641 (2020).

194. Kim, H. seok *et al.* Concentration Effect of Reducing Agents on Green Synthesis of Gold Nanoparticles: Size, Morphology, and Growth Mechanism. *Nanoscale Res. Lett.* **11**, 230 (2016).

195. Pinho, B. & Torrente-Murciano, L. Continuous manufacturing of silver nanoparticles between 5 and 80 nm with rapid online optical size and shape evaluation. *React. Chem. Eng.* **5**, 342–355 (2020).

196. Wrigglesworth, E. G. & Johnston, J. H. The use of dual reductants in gold nanoparticle syntheses. *RSC Adv.* **7**, 45757 (2017).

197. Larm, N. E., Thon, J. A., Vazmitsel, Y., Atwood, J. L. & Baker, G. A. Borohydride stabilized gold-silver bimetallic nanocatalysts for highly efficient 4-nitrophenol reduction. *Nanoscale Adv.* **1**, 4665–4668 (2019).

198. Mühlpfordt, H. The preparation of colloidal gold particles using tannic acid as an additional reducing agent. *Experientia* **38**, 1127–1128 (1982).

199. Mo, Y. & Jensen, K. F. A miniature CSTR cascade for continuous flow of reactions containing solids. *Cite this React. Chem. Eng* **1**, 501 (2014).

200. Lignos, I. *et al.* Continuous Multistage Synthesis and Functionalization of Sub-100 nm Silica Nanoparticles in 3D-Printed Continuous Stirred-Tank Reactor Cascades. *ACS Appl. Mater. Interfaces* **12**, 6699–6706 (2020).

201. Mann, D. *et al.* The Influence of Particle Size Distribution and Shell Imperfections on the Plasmon Resonance of Au and Ag Nanoshells. *Plasmonics* **12**, 929–945 (2017).

202. Godfrey, I. J., Dent, A. J., Parkin, I. P., Maenosono, S. & Sankar, G. Structure of Gold–Silver Nanoparticles. *J. Phys. Chem. C* **121**, 1957–1963 (2017).

203. Vanýsek, P. *Handbook of Chemistry and Physics*. (CRC Press, 2012).

204. Tiwari, A. *et al.* Survey on the use of computational optimisation in UK engineering companies. *J. Manuf. Sci. Technol.* **9**, 57–68 (2015).

205. Manikowski, P. L. *et al.* Multi-Objective Optimisation of the Benchmark Wind Farm Layout Problem. *J. Mar. Sci. Eng. 2021, Vol. 9, Page 1376* **9**, 1376 (2021).

206. Helbig, M. & Engelbrecht, A. P. Benchmarks for dynamic multi-objective optimisation algorithms. *ACM Comput. Surv.* **46**, 1–39 (2014).

207. Beiranvand, V., Hare, W. & Lucet, Y. Best practices for comparing optimization algorithms. *Optim. Eng.* **18**, 815–848 (2017).

208. Karaboga, D. & Basturk, B. A powerful and efficient algorithm for numerical function optimization: artificial bee colony (ABC) algorithm. *J. Glob. Optim. 2007 393* **39**, 459–471 (2007).

209. Arora, S. & Singh, S. Butterfly optimization algorithm: a novel approach for global optimization. *Soft Comput.* **23**, 715–734 (2019).

210. Yang, X. S. & Deb, S. Cuckoo search: recent advances and applications. *Neural Comput. Appl. 2013 241* **24**, 169–174 (2013).

211. Storn, R. & Price, K. Differential Evolution – A Simple and Efficient Heuristic for global Optimization over Continuous Spaces. *J. Glob. Optim. 1997 114* **11**, 341–359 (1997).

212. Yang, X. S. Firefly Algorithm, Lévy Flights and Global Optimization. in *Research and Development in Intelligent Systems XXVI: Incorporating Applications and Innovations in Intelligent Systems XVII* 209–218 (Springer, London, 2010). doi:10.1007/978-1-84882-983-1_15.

213. Wang, G. G., Deb, S. & Cui, Z. Monarch butterfly optimization. *Neural Comput. Appl.* **31**, 1995–2014 (2019).

214. Eberhart, R. C. & Shi, Y. Particle swarm optimization: developments, applications and resources. in *Proceedings of the 2001 Congress on Evolutionary Computation* vol. 1 81–86 (IEEE, 2001).

215. Shilane, D., Martikainen, J., Dudoit, S. & Ovaska, S. J. A general framework for statistical performance comparison of evolutionary computation algorithms. *Inf. Sci. (Ny).* **178**, 2870–2879 (2008).

216. Wolpert, D. H. & Macready, W. G. No free lunch theorems for optimization. *IEEE Trans. Evol. Comput.* **1**, 67–82 (1997).

217. Nelder, J. A., Mead, R. & J. A. Nelder, R. M. A Simplex Method for Function Minimization. *Comput. Journal*, **7**, 308–313 (1965).

218. Paleyes, A. Gaussian Process Optimization using GPy. https://github.com/SheffieldML/GPyOpt (2020).

219. Häse, F., Aldeghi, M., Hickman, R. J., Roch, L. M. & Aspuru-Guzik, A. Gryffin: An algorithm for Bayesian optimization of categorical variables informed by expert knowledge. *Appl. Phys. Rev.* **8**, 1–35 (2020).

220. Bradford, E., Schweidtmann, A. M. & Lapkin, A. Efficient multiobjective optimization employing Gaussian processes, spectral sampling and a genetic algorithm. *J. Glob. Optim.* **71**, 407–438 (2018).

221. Zhou, Z., Li, X. & Zare, R. N. Optimizing Chemical Reactions with Deep Reinforcement Learning. *ACS Cent. Sci.* **3**, 1337–1344 (2017).

222. Felton, K. C., Rittig, J. G., Alexei, P. & Lapkin, A. Summit: Benchmarking Machine Learning Methods for Reaction Optimisation. *Univ. Cambridge, ChemRxiv* 1–20 (2020) doi:10.26434/CHEMRXIV.12939806.V2.

223. Lo, C. T. F., Karan, K. & Davis, B. R. Kinetic Studies of Reaction between Sodium Borohydride and Methanol, Water, and Their Mixtures. *Ind. Eng. Chem. Res.* **46**, 5478–5484 (2007).

224. Venkatesan, P. & Santhanalakshmi, J. Kinetics of oxidation of L-leucine by mono- and bimetallic gold and silver nanoparticles in hydrogen peroxide solution. *Chinese J. Catal.* **33**, 1306–1311 (2012).

225. Zaborenko, N., Bedore, M. W., Jamison, T. F. & Jensen, K. F. Kinetic and Scale-Up Investigations of Epoxide Aminolysis in Microreactors at High Temperatures and Pressures. *Org. Process Res. Dev.* **15**, 131–139 (2011).

226. Girisuta, B., Janssen, L. P. B. M. & Heeres, H. J. A kinetic study on the decomposition of 5-hydroxymethylfurfural into levulinic acid. *Green Chem.* **8**, 701–709 (2006).

227. Scheithauer, A. *et al.* Online 1 H NMR Spectroscopic Study of the Reaction

Kinetics in Mixtures of Acetaldehyde and Water Using a New Microreactor Probe Head. *I&EC Res.* **53**, 17589−17596 (2014).

228. Pérez-Ramírez, J., Berger, R. J., Mul, G., Kapteijn, F. & Moulijn, J. A. *The six-flow reactor technology A review on fast catalyst screening and kinetic studies*. *Catalysis Today* vol. 60 http://www.tekim.undip.ac.id/staf/istadi/files/2010/03/ramirez_cattd2000_catalreactdimension.pdf (2000).

229. Taylor, C. J. *et al.* Rapid, Automated Determination of Reaction Models and Kinetic Parameters. *Chem. Eng. J.* 127017 (2020) doi:10.1016/j.cej.2020.127017.

230. Duan, X. *et al.* An automated flow platform for accurate determination of gas-liquid-solid reaction kinetics †. *React. Chem. Eng.* **5**, 1751–1758 (2020).

231. Suchomel, P. *et al.* Simple size-controlled synthesis of Au nanoparticles and their size-dependent catalytic activity. *Sci. Rep.* **8**, 4589 (2018).

232. Thawarkar, S. R., Thombare, B., Munde, B. S. & Khupse, N. D. Kinetic investigation for the catalytic reduction of nitrophenol using ionic liquid stabilized gold nanoparticles. *RSC Adv.* **8**, 38384–38390 (2018).

233. Seo, Y. S. *et al.* Catalytic reduction of 4-nitrophenol with gold nanoparticles synthesized by caffeic acid. *Nanoscale Res. Lett.* **12**, 1–11 (2017).

234. Kohantorabi, M. & Gholami, M. R. Fabrication of novel ternary Au/CeO2@g-C3N4 nanocomposite: kinetics and mechanism investigation of 4-nitrophenol reduction, and benzyl alcohol oxidation. *Appl. Phys. A* **124**, 1–17 (2018).

235. Eley, D. D. & Rideal, E. K. Parahydrogen Conversion on Tungsten. *Nature* **146**, 401–402 (1940).

236. Khalavka, Y., Becker, J. & Sönnichsen, C. Synthesis of Rod-Shaped Gold Nanorattles with Improved Plasmon Sensitivity and Catalytic Activity. *J. Am. Chem. Soc.* **131**, 1871–1875 (2009).

237. Layek, K. *et al.* Gold nanoparticles stabilized on nanocrystalline magnesium oxide as an active catalyst for reduction of nitroarenes in aqueous medium at room temperature. *Green Chem.* **14**, 3164–3174 (2012).

238. MATLAB. *ga (R2020b)*. (The MathWorks Inc., 2020).

239. Taylor, C. J. Compunetics. (2020).

240. Fitzpatrick, D. E., Battilocchio, C. & Ley, S. V. A Novel Internet-Based Reaction Monitoring, Control and Autonomous Self-Optimization Platform for Chemical Synthesis. *Org. Process Res. Dev.* **20**, 386–394 (2016).

241. Bourne, R. A., Skilton, R. A., Parrott, A. J., Irvine, D. J. & Poliakoff, M. Adaptive Process Optimization for Continuous Methylation of Alcohols in Supercritical Carbon Dioxide. *Org. Process Res. Dev* **15**, 932–938 (2011).

242. Abolhasani, M., Epps, R. W., Volk, A. A. & Reyes, K. G. Accelerated AI development for autonomous materials synthesis in flow. *Chem. Sci.* **12**, 6025–6036 (2021).

243. Kreutz, J. E. *et al.* Evolution of catalysts directed by genetic algorithms in a plug-based microfluidic device tested with oxidation of methane by oxygen. *J Am Chem Soc.* **132**, 3128–3132 (2010).

244. Kreutz, J. E. *et al.* Evolution of Catalysts Directed by Genetic Algorithms in a Plug-Based Microfluidic Device Tested with Oxidation of Methane by Oxygen. *J. Am. Chem. Soc.* **132**, 3128–3132 (2010).

245. Chatterjee, S. & Bhattacherjee, A. Genetic algorithms for feature selection of image analysis-based quality monitoring model: An application to an iron mine. *Eng. Appl. Artif. Intell.* **24**, 786–795 (2011).

246. Hornby, G. S., Globus, A., Linden, D. S. & Lohn, J. D. Automated antenna design with evolutionary algorithms. in *Session: SPS-6: Enabling Technology for Realizing the Value Proposition* vol. 1 445–452 (American Institute of Aeronautics and Astronautics Inc., 2006).

247. Bullen, T. & Katchabaw, M. *USING GENETIC ALGORITHMS TO EVOLVE CHARACTER BEHAVIOURS IN MODERN VIDEO GAMES*. *University of Western Ontario, Department of Computer Science* (2008).

248. Emiabata-Smith, D. F., Crookes, D. L. & Owen, M. R. A Practical Approach to Accelerated Process Screening and Optimisation. *Org. Process Res. Dev.* **3**, 281–288 (1999).

249. Murray, P. M., Tyler, S. N. G. & Moseley, J. D. Beyond the Numbers: Charting Chemical Reaction Space. *Org. Process Res. Dev.* **17**, 40–46 (2013).

250. Bacchi, S., Yahyah, M., Carangio, A., Ribecai, A. & Oliveros, M. C. C. Fit for Purpose Experimental Designs and Analyses in Chemical Development. *Org. Process Res. Dev.* **14**, 332–338 (2010).

251. Liang, Q. *et al.* Benchmarking the Performance of Bayesian Optimization across Multiple Experimental Materials Science Domains. *NPJ Comput. Mater.* **7**, 1–10 (2021).

252. Melton, T. The Benefits of Lean Manufacturing: What Lean Thinking has to Offer the Process Industries. *Chem. Eng. Res. Des.* **83**, 662–673 (2005).

253. Artur M.Schweidtmannab, Adam D.Claytonc, NicholasHolmes, cEricBradfordad, Richard A.Bournec, A. A. L. Machine learning meets continuous flow chemistry: Automated optimization towards the Pareto front of multiple objectives. *Chem. Eng. J.* **352**, 277–282 (2018).

254. Li, R., Greenchem, / & Sheldon, R. A. The E factor 25 years on: the rise of green chemistry and sustainability. *Green Chem.* **19**, 18–43 (2017).

255. Pereira, S. R. M. *et al.* Effect of the Genetic Algorithm Parameters on the Optimisation of Heterogeneous Catalysts. *QSAR Comb. Sci.* **24**, 45–57 (2005).

256. Bédard, A. C. *et al.* Reconfigurable system for automated optimization of diverse chemical reactions. *Science (80-.).* **361**, 1220–1225 (2018).

257. Clayton, A. D. Multi-Objective, Multiphasic and Multi-Step Self-Optimising Continuous Flow Systems. (University of Leeds, 2020).

258. Trapp, O., Weber, S. K., Bauch, S. & Hofstadt, W. High-Throughput Screening of Catalysts by Combining Reaction and Analysis. *Angew. Chemie Int. Ed.* **46**, 7307–7310 (2007).

259. Roldan Cuenya, B. Synthesis and catalytic properties of metal nanoparticles: Size, shape, support, composition, and oxidation state effects. *Thin Solid Films* **518**, 3127–3150 (2010).

260. Coley, C. W. *et al.* A robotic platform for flow synthesis of organic compounds informed by AI planning. *Science (80-.).* **365**, 1–9 (2019).

261. Baumgartner, L. M. *et al.* Optimum catalyst selection over continuous and discrete process variables with a single droplet microfluidic reaction platform. *React. Chem. Eng* **3**, 301–311 (2018).

262. Mohamed, D. K. B., Yu, X., Li, J. & Wu, J. Reaction screening in continuous flow reactors. *Tetrahedron Letters* vol. 57 3965–3977 (2016).

263. Epps, R. W., Felton, K. C., Coley, C. W. & Abolhasani, M. Automated microfluidic platform for systematic studies of colloidal perovskite nanocrystals: Towards continuous nano-manufacturing. *Lab Chip* **17**, 4040–4047 (2017).

264. Abdel-Latif, K. *et al.* Self-Driven Multistep Quantum Dot Synthesis Enabled by Autonomous Robotic Experimentation in Flow. *Adv. Intell. Syst.* **3**, 2000245 (2021).

265. Santanilla, A. B. *et al.* Nanomole-scale high-throughput chemistry for the synthesis of complex molecules. *Science (80-.).* **347**, 49–53 (2015).

266. Welch, C. J. High throughput analysis enables high throughput experimentation in pharmaceutical process research. *React. Chem. Eng.* **4**, 1895–1911 (2019).

267. Shevlin, M. Practical High-Throughput Experimentation for Chemists. *ACS Med. Chem. Lett.* **8**, 601–607 (2017).

268. Catalyst Screening Solution. https://www.chemspeed.com/news/chemspeed-catalyst-screening-solution-6-months-roi-astrazeneca/ (Date accessed: 25.10.2022).

269. Tovey, I. High-throughput Agrochemical Formulation: Easing the Route to Commercial Manufacture. *Syngenta* (2017).

270. Weidenhof, B. *et al.* High-Throughput Screening of Nanoparticle Catalysts Made by Flame Spray Pyrolysis as Hydrocarbon/NO Oxidation Catalysts. *J. Am. Chem. Soc.* **131**, 9207–9219 (2009).

271. Yu, Y.-X. *et al.* High-Throughput Screening of Alloy Catalysts for Dry Methane Reforming. *ACS Catal.* **11**, 8881–8894 (2021).

272. Li, Z., Wang, S., Chin, W. S., Achenie, L. E. & Xin, H. High-throughput screening of bimetallic catalysts enabled by machine learning. *J. Mater. Chem. A* **5**, 24131–24138 (2017).

273. Bruix, A., Margraf, J. T., Andersen, M. & Reuter, K. First-principles-based multiscale modelling of heterogeneous catalysis. *Nature Catalysis* vol. 2 659–670 (2019).

274. Yang, L., Karim, A. & Muckerman, J. T. Density functional kinetic monte carlo simulation of water-gas shift reaction on Cu/ZnO. *J. Phys. Chem. C* **117**, 3414–3425 (2013).

275. Sutton, J. E. *et al.* Electrons to Reactors Multiscale Modeling: Catalytic CO Oxidation over RuO2. *ACS Catal.* **8**, 5002–5016 (2018).

276. Reuter, K., Frenkel, D. & Scheffler, M. The steady state of heterogeneous catalysis, studied by first-principles statistical mechanics. *Phys. Rev. Lett.* **93**, 116105 (2004).

277. Sabbe, M. K., Reyniers, M.-F. & Reuter, K. First-principles kinetic modeling in heterogeneous catalysis: an industrial perspective on best-practice, gaps and needs. *Catal. Sci. Technol.* **2**, 2010–2024 (2012).

278. Kalz, K. F. *et al.* Future Challenges in Heterogeneous Catalysis: Understanding Catalysts under Dynamic Reaction Conditions. *ChemCatChem* **9**, 17–29 (2017).

279. Joshua Britton & L. Raston, C. Multi-step continuous-flow synthesis. *Chem. Soc. Rev.* **46**, 1250–1271 (2017).

280. Webb, D. & Jamison, T. F. Continuous flow multi-step organic synthesis. *Chem. Sci.* **1**, 675–680 (2010).

281. Ley, S. V., Fitzpatrick, D. E., Ingham, R. J. & Myers, R. M. Organic Synthesis: March of the Machines. *Angew. Chemie Int. Ed.* **54**, 3449–3464 (2015).

282. Sagmeister, P. *et al.* Advanced Real-Time Process Analytics for Multistep Synthesis in Continuous Flow**. *Angew. Chemie Int. Ed.* **60**, 8139–8148 (2021).

283. Heftmann, E. *Chromatography : fundamentals and applications of chromatography and related differential migration methods. Fundamentals and techniques*. (2004).

284. Koga, H., Umemura, Y. & Kitaoka, T. In Situ Synthesis of Bimetallic Hybrid Nanocatalysts on a Paper-Structured Matrix for Catalytic Applications. *Catalysts* **1**, 69–82 (2011).

285. Wang, A. Q., Chang, C. M. & Mou, C. Y. Evolution of Catalytic Activity of Au−Ag Bimetallic Nanoparticles on Mesoporous Support for CO Oxidation. *J. Phys. Chem. B* **109**, 18860–18867 (2005).

286. Medford, A. J. *et al.* From the Sabatier principle to a predictive theory of transition-metal heterogeneous catalysis. *J. Catal.* **328**, 36–42 (2015).

287. Sanjeeva Gandhi, M. & Mok, Y. S. Shape-dependent plasma-catalytic activity of ZnO nanomaterials coated on porous ceramic membrane for oxidation of butane. *Chemosphere* **117**, 440–446 (2014).

288. Alonso, F., Moglie, Y. & Radivoy, G. Copper Nanoparticles in Click Chemistry. *ACS Accounts* **48**, 2516−2528 (2015).